University of Ljubljana
Faculty of mathematics and physics
Department of Physics

Gregor Vidmar

The influence of Tunneling on Eigenvalue Statistics and Dynamics in the Mixed-Type Systems

Doctoral thesis

ADVISER: Prof. Dr. Marko Robnik

Ljubljana, 2008

Univerza v Ljubljani
Fakulteta za matematiko in fiziko
Oddelek za fiziko

Gregor Vidmar

Vpliv tuneliranja na statistiko in dinamiko energijskih stanj sistema mešanega tipa

Doktorska disertacija

MENTOR: prof. dr. Marko Robnik

Ljubljana, 2008

This PhD thesis has been performed at the
CAMTP - Center for Applied Mathematics and Theoretical Physics,
University of Maribor

CAMTP

To doktorsko delo je bilo izdelano na
CAMTP - Centru za uporabno matematiko in teoretično fiziko
Univerze v Mariboru

Abstract

In this thesis we have studied dynamical tunneling and random matrix theory in the field of quantum chaos.
First, we have considered the spectra of quantum Hamilton systems characterised by the mixed-type classical dynamics. In the semiclassical limit the Berry-Robnik (BR) statistics applies whereas at larger values of $\hbar_{\text{eff}}$ one can notice deviations from BR due to localisation and tunneling effects. We have derived a 2-level random matrix model which can be treated analytically and the N-level random matrix model which has been treated numerically. Both models describe tunneling effects. The coupling between the regular and the chaotic levels due to tunneling is assumed to be Gaussian distributed. The results are predicted to apply in mixed-type systems at low energies. The two-level model describes many features of large matrices. The proposed 2 and the N level spacing distributions have two parameters, the BR parameter ρ, characterising the classical phase space, and the coupling parameter σ. The same procedure has been followed for the all-to-all couplings as well.
Second, we have studied the mushroom billiard introduced by Bunimovich, especially in terms of its level spacing distribution, avoided crossing distribution and dynamical tunneling rates. The mushroom billiard has a nice property of sharply divided phase space into precisely one regular and one chaotic region. By changing the appropriate parameter one can easily identify the regular or the chaotic states without considering the Wigner functions. First we have studied the level spacing distribution to test the random matrix model and, then, we have focused on the avoided crossings appearing between the regular and the chaotic states. The splittings, appearing at such avoided crossings, indicate the strength of dynamical tunneling. Larger splitting presuppose stronger tunneling effect. With the help of Fermi's golden rule we have calculated the dynamical tunneling rates for each regular state of the mushroom billiard. We have compared the results from the microwave experiment and those from the expanded boundary integral numerical method with the already-existing analytic prediction derived by Ketzmerick and his co-workers. We have observed excellent agreement in the accessible regime of low energies.
Third, we have discussed various ensembles of real symmetric matrices with the dimensions $N = 2$ to $N = \infty$ for a variety of distributions of matrix elements. For $N = 2$ there exist the exact analytic results obtained by Grossmann and Robnik whereas for $N = \infty$ one can rely on the theoretical findings by Hackenbroich and Weidenmüller (HW). According to these findings the local spectral fluctuations are exactly described by the GOE if the limiting distribution of the eigenvalues is smooth and restricted to a finite interval. We have numerically shown, according to HW, that such a transition to the universal behaviour is pretty fast and that it does really not occur if one or both of the conditions from the theory mentioned are not fulfilled. We have tested this findings for the box, the exponential, the Cauchy-Lorentz and the singular (power law times exponential) distribution function of matrix elements.

PACS numbers:

02.50.Cw	Probability theory
02.70.Pt	Boundary-integral methods
03.65.Sq	Semiclassical theories and applications in quantum mechanics
03.65.Xp	Tunneling, traversal time, quantum Zeno dynamics
05.45.-a	Nonlinear dynamics and nonlinear dynamical systems
05.45.Mt	Quantum chaos; semiclassical methods
05.45.Pq	Numerical simulations of chaotic systems

Keywords: dynamical tunneling, regular, chaotic, mixed-type system, energy levels, level spacing distribution, level dynamics, mushroom billiard, avoided crossings, tunneling rates, random matrix theory, microwave experiments

Povzetek

V tej disertaciji študiramo dinamično tuneliranje in teorijo naključnih matrik na področju kvantnega kaosa.
Najprej obravnavamo energijske spektre kvantnega Hamiltonskega sistema z mešano klasično dinamiko. V semiklasični limiti, ko je efektivna Planckova konstanta $\hbar_{\text{eff}}$ dovolj majhna, velja statistika Berryja in Robnika (BR), medtem ko pri večjih vrednostih $\hbar_{\text{eff}}$ (manjših energijah) vidimo odstopanja od BR zaradi lokalizacije in tunelskih efektov. Izpeljemo 2-nivojski model naključnih matrik, ki ga lahko obravnavamo analitično in N-nivojski model naključnih matrik, ki ga obravnavamo numerično. Oba modela opisujeta tunelske efekte. Predpostavljamo Gaussovo, eksponentno ali škatlasto porazdelitev tunelske sklopitve med regularnimi in kaotičnimi nivoji. Rezultati se predvidoma uporabljajo v mešanih sistemim pri nizkih energijah. Dvonivojski model opisuje večino lastnosti večjih matrik. Predlagani 2- in N-nivojski porazdelitvi po razmikih med sosednjimi nivoji imata dva parametra, BR parameter ρ, ki opisuje klasični fazni prostor, in sklopitveni parameter σ. Isti postopek naredimo tudi v primeru sklopitve vseh nivojev z vsemi.
Nadalje eksperimentalno in numerično študiramo gobasti biljard, ki ga je vpeljal Bunimovich, posebej porazdelitev po razmikih med sosednjimi nivoji, porazdelitev izognjenih križanj in koeficiente dinamičnega tuneliranja. Gobasti biljard ima to lepo lastnost, da je fazni prostor ostro ločen v natanko eno regularno in eno kaotično komponento. S spreminjanjem ustreznega parametra razvrstimo stanja v regularna in kaotična brez računanja Wignerjevih funkcij. Najprej se osredotočimo na porazdelitev po razmikih med sesednjimi nivoji z namenom testiranja modela naključnih matrik, potem pa na izognjena križanja med regularnimi in kaotičnimi stanji. Razcep v izognjenem križanju nam pove o velikosti dinamičnega tuneliranja in posledično o stabilnosti določenega regularnega stanja. Večji razcep pomeni večje tuneliranje. Z upoštevanjem Fermijevega zlatega pravila smo dobili koeficiente dinamičnega tuneliranja za vsako regularno stanje gobastega biljarda. Primerjamo rezultate mikrovalovnega ekperimenta in numeričega računa z razširjeno metodo integriranja po robu z že obstoječo analitično teorijo Ketzmericka in sodelavcev. Našli smo zelo dobro ujemanje v dosegljivem območju nizkih energij.
Nazadnje obravnavamo ansamble realnih simetričnih matrik dimenzij $N = 2$ do $N = \infty$ za različne porazdelitve matričnih elementov. Za $N = 2$ imamo eksaktne analitične rezultate Grossmanna in Robnika, medtem ko imamo za $N = \infty$ teorijo Hackenbroicha in Weidenmüllerja (HW). Ta pravi, da so lokalne fluktuacije spektrov natančno popisane z GOE, če je limitna porazdelitev lastnih vrednosti gladka in omejena na končen interval. Numerično pokažemo, da je tak prehod k univerzalnemu obnašanju, ki ga napoveduje HW, zelo hiter in da se dejansko ne zgodi, če ena ali druga predpostavka v HW ni izpoljena. To testiramo za škatlasto, eksponentno, Cauchy-Lorentzovo in singularno (potenčna pomnožimo z eksponentno) porazdelitev matričnih elementov.

PACS števila:

02.50.Cw Verjetnostna teorija
02.70.Pt Metoda integriranja po robu
03.65.Sq Semiklasične teorije in aplikacije v kvantni mehaniki
03.65.Xp Tuneliranje, čas prečenja, kvantna Zeno dinamika
05.45.-a Nelinearna dinamika in nelinearni dinamični sistemi
05.45.Mt Kvantni kaos; semiklasične metode
05.45.Pq Numerične simulacije kaotičnih sistemov

Ključne besede: dinamično tuneliranje, regularno, kaotično, sistem mešanega tipa, energijski nivoji, porazdelitev po razmikih med sosednjimi nivoji, dinamika stanj, gobasti biljard, izognjena križanja, koeficienti tuneliranja, teorija naključnih matrik, mikrovalovni eksperimenti

Acknowledgement

I would like to thank my supervisor Marko Robnik for all his effort, organisation and support during all the years of my research presented in this thesis.
I would also like to thank Hans-Jürgen Stöckmann for his cooperation, great ideas and remarks.
I am also grateful to Ulrich Kuhl for his great and invaluable help in the experiments and for many answers to my numerous questions.
I would also like to thank Marko Vraničar, Igor Mozetič and Valery Romanovski for their unselfish help at CAMTP.
I am also grateful to Roland Ketzmerich and his team from Dresden, Helena M. David and Ruven Höhmann for their excellent cooperation. I would like to express my gratitude to Tomaž Prosen and, especially, to Gregor Veble for all their advice and software assistance.
In the end, I would like to thank Brigita Retar and Petra Pučnik for proofreading the English and the Slovenian part of the present thesis.

Zahvala

Rad bi se zahvalil mentorju Marku Robniku za ves trud, organizacijo in podporo vsa leta raziskovanja, ki je sedaj predstavljeno v tej disertaciji.
Potem bi se rad zahvalil Hans-Jürgenu Stöckmannu za zelo dobro sodelovanje, ideje in komentarje.
Rad bi se zahvalil Ulrichu Kuhlu za veliko in prijazno pomoč v času bivanj v Marburgu, za vso podporo pri eksperimentalnem delu in izvrednotenju podatkov ter za odgovore na veliko mojih vprašanj.
Rad bi se zahvalil tudi Marku Vraničarju, Igorju Mozetiču in Valeriju Romanovskemu za nesebično pomoč na CAMTP-ju ter skupini Rolanda Ketzmericka iz Dresdena, Heleni M. David in Ruvenu Höhmannu za dobro sodelovanje. Zahvala gre tudi Tomažu Prosenu in posebej Gregorju Vebletu za koristne diskusije in programsko pomoč.
Na koncu bi se rad zahvalil Brigiti Retar in Petri Pučnik za lektoriranje angleškega in slovenskega dela te disertacije.

Dedication

I dedicate this thesis to my family.

Posvetilo

Disertacijo posvečam svoji družini.

Contents

1 Introduction **1**
- 1.1 Billiards . . . 1
- 1.2 Quantum chaos . . . 2
- 1.3 Dynamical tunneling . . . 3
- 1.4 Random matrix theory and level statistics . . . 5
- 1.5 Non-Gaussian RMT . . . 7

2 The distorted Berry-Robnik level spacing distribution **9**
- 2.1 The Berry-Robnik level spacing distribution . . . 9
- 2.2 General distortion of the general level spacing distribution . . . 10
- 2.3 Gaussian distortion of the BR distribution . . . 12
- 2.4 Analytical studies of the distorted Berry-Robnik distribution . . . 22
  - 2.4.1 Small S behaviour of $P^A_{DBR}(S)$ . . . 22
  - 2.4.2 Large S behaviour of $P^A_{DBR}(S)$ and $P^T_{DBR}(S)$ . . . 23
- 2.5 Simulations with random matrices . . . 24
  - 2.5.1 The antenna distorted BR distribution (all-to-all couplings) . . . 24
  - 2.5.2 The tunneling distorted BR distribution . . . 31
- 2.6 Improvements on the tunneling-distorted BR distribution . . . 34
- 2.7 Dependence of the model on the matrix element statistics . . . 38

3 Dynamical tunneling in mushroom billiards **41**
- 3.1 Mushroom billiard - classical . . . 41
- 3.2 Mushroom billiard - quantum . . . 43
- 3.3 Microwave experiments . . . 45
  - 3.3.1 The similarity between QM and ED . . . 45
  - 3.3.2 Resonances . . . 46
  - 3.3.3 Harmonic inversion . . . 48
- 3.4 Level Statistics . . . 50
  - 3.4.1 Level dynamics . . . 51
  - 3.4.2 The level spacing distribution - comparison with the RMT prediction 53
  - 3.4.3 Absorber in the foot . . . 53
- 3.5 Expanded boundary integral method . . . 53
  - 3.5.1 Corners and the accuracy of EBIM . . . 57
  - 3.5.2 Level dynamics - increasing the depth l . . . 61
  - 3.5.3 The level spacing distribution - comparison with the RMT prediction 64
- 3.6 Avoided crossings . . . 64
- 3.7 Tunneling rates . . . 72

3.7.1 Fermi's golden rule . . . 73
3.7.2 Tunneling rates - the experiment . . . 75
3.7.3 Tunneling rates - the numerics . . . 80

4 Numerical studies of non-Gaussian real symmetric random matrices 85
4.1 2D real symmetric random matrices . . . 85
4.1.1 Box (uniform) distribution . . . 85
4.1.2 Exponential distribution . . . 86
4.1.3 Cauchy-Lorentz distribution . . . 86
4.1.4 Singular times exponential distribution . . . 87
4.1.5 Comparison with numerics . . . 87
4.2 Numerical calculations with higher dimensional non-Gaussian random matrices . . . 88
4.2.1 Box (uniform) distribution . . . 89
4.2.2 Exponential distribution . . . 89
4.2.3 Cauchy-Lorentz distribution . . . 89
4.2.4 Singular times exponential distribution . . . 92

5 Summary and conclusions 95

Bibliography 98

Appendices 105

A ρ_1 calculation for the mushroom billiard 107

B Theoretical analysis of the tunneling rates in the mushroom billiard 111

C Numerics with particular solutions for the tunneling rates in the mushroom billiard 115

Daljši slovenski povzetek 117
i Deformirana porazdelitev Berryja in Robnika po razmikih med sosednjimi nivoji . . . 118
ii Simulacije z naključnimi matrikami . . . 120
iii Gobasti biljard . . . 123
iv Mikrovalovni eksperimenti in numerična metoda EBIM . . . 125
v Dinamika lastnih energij gobastega biljarda . . . 126
vi Izognjena križanja in tuneliranje . . . 127
vii Numerična študija negausovskih realno simetričnih matrik . . . 131

Chapter 1

Introduction

In classical mechanics there exist two types of motion - regular and chaotic. In an integrable system regular motion is stable quasiperiodic or periodic and takes place on the N-dimensional invariant tori in the classical phase space of $2N$ dimensions where N is the number of degrees of freedom. Since chaotic orbits are characterised by the exponential divergence of nearby orbits, they have positive Lyapunov exponents. The K-system is characterised by the chaotic region in the classical phase space with positive Lyapunov exponents and with a positive Liouville measure. If the system is ergodic as well, i.e. if almost any orbit can visit an arbitrarily small neighbourhood of any other point on the $(2N-1)$-dimensional energy surface, we say that the system is fully chaotic. However, in nature the generic (or typical) systems are neither integrable (regular) nor fully chaotic but they are of mixed type. Their motion is regular on invariant tori for certain initial conditions and chaotic for complementary ones.

1.1 Billiards

The difference between the two types of motion can easily be demonstrated in billiards. The 2D closed billiard system is characterised by a free-point particle elastically bouncing off the boundary of a given Euclidean domain. The 2D billiard is integrable, if apart from the energy there exists another constant of motion. The invariant tori on the surface of section appear as one dimensional. All the orbits are stable. The only billiards, proven to be integrable, are the circular, the rectangular and the elliptic one. In the circular billiard there appears the angular momentum as the additional constant of motion. Thus, the invariant tori in this case can be either rational (resonant) or not, depending on the reflection angle selected. If the reflection angle is a rational multiple of π, the torus is resonant and all the orbits on this torus are periodic. If, on the other hand, the reflection angle is an irrational multiple of π, the orbits on the torus are quasiperiodic whereas the motion is ergodic on this torus. In the case of the semicircular billiard the second constant of motion is the absolute value of the angular momentum. In the rectangular billiard the constants of motion are the absolute values of momenta parallel to the walls of the billiard in question. The phase portrait of the elliptic billiard reminds one of the mathematical pendulum. Apart from the total energy the constant of motion is the product of the angular momenta about both foci of the ellipse.

On the other hand the Sinai billiard was the first proven fully chaotic billiard (Sinai, 1970), whose disk (a circular obstacle) is located in the rectangle. At that time it was

believed that the exponential divergence of orbits can only be achieved with the help of a non-convex boundary in a billiard. A few years later L. A. Bunimovich invented the stadium billiard (Bunimovich, 1974) and proved, that it is ergodic, that it has a mixing property and that it is a K system, which means that it is fully chaotic. The next fully chaotic billiard is the cardioid billiard whose chaoticity is proven in (Markarian, 1993). So far these are the only three rigourously proven chaotic billiards. At this point one should mention the family of Robnik billiards as an example of 'practically' chaotic billiards (Robnik, 1983) for $\lambda \geq \frac{1}{4}$. This billiard family is described by the complex conformal map of the unit circle, $w = z + \lambda z^2$ which determines the boundary (for $\lambda = \frac{1}{2}$ one gets the cardioid billiard). [1] Another interesting example of chaotic billiards comes from the family of Africa billiards (Berry and Robnik, 1986) for $\lambda \geq 0.2$, defined as a conformal map of the circle as well: $w = z + \lambda z^2 + \lambda z^3 e^{i\frac{\pi}{3}}$.

The most frequent mixed-type systems are KAM systems in which fractal structures of the islands of stability coexist with the chaotic sea. The Robnik and the Africa billiards are KAM systems which are characterised by a continuous transition from an integrable to a fully chaotic billiard with the continuously changing (shape) parameter λ. There are other examples of KAM billiards, from cosine billiard to annular billiard (Bohigas et al., 1993a), etc. However there exists a mixed-type billiard which does not share the complex structures of many regular islands surrounded by the chaotic sea. This billiard, which is characterised by a sharply divided phase space, is called the mushroom billiard. It was invented by L. A. Bunimovich and it was classically treated in (Bunimovich, 2001; Altmann et al., 2005, 2006; Dietz et al., 2006; Tanaka and Shudo, 2006). This thesis discusses the characteristics of the mushroom billiard and its quantum mechanical counterpart.

1.2 Quantum chaos

In quantum mechanics classical behaviour is related to various quantum objects, from wave functions to energy spectra of the corresponding counterparts, etc. The field in physics, which deals with chaos in quantum mechanics, is termed quantum chaos. One should emphasize the fact that in quantum mechanics chaos does not exist in the time domain since the Schrödinger equation is a linear equation. Therefore, quantum chaos was originally meant to be a study of quantum mechanics of classically chaotic systems. Some recent developments have proved that certain quantum integrable or chaotic systems, such as the spin chains which are presented in (Prosen, 1998b; Pineda and Prosen, 2007), are unique and do not have a classical limit. There arises a question of criteria distinguishing between regular and chaotic quantum systems. Apart from the Wigner or the Husimi functions of eigenstates lying in the quantum phase space, the most significant aspects are the statistical properties of the spectra of bound (Hamiltonian or Floquet) systems. These statistical properties are universal. The energy levels of integrable quantum systems are uncorrelated and possess the Poissonian statistics whereas in chaotic systems the neighbouring levels repel each other, which results in energy level repulsion.

On the basis of the so-called Principle of Uniform Semiclassical Condensation (PUSC) of Wigner functions in the true semiclassical limit one can identify two types of eigenstates in mixed-type quantum systems, i.e. those of the regular and the chaotic type

[1] The so-called Pascal snail curve (i.e. Pascal limaçon) only resembles the Robnik billiard, but it is not the same as this billiard.

(Percival, 1973), depending on where they 'live' in the quantum phase space. But in order to achieve such a clear classification and uniform extendedness (no localisation) of the Wigner functions, one should really be in the semiclassical limit: otherwise, there can emerge the so-called hierarchial states (Ketzmerick et al., 2000), 'living' in the chaotic sea in the vicinity of the hierarchy of the regular islands. This can happen if the value of the effective Planck constant is not small enough.

Due to the formal similarity of the Schrödinger equation to other wave equations of physics the concept of quantum chaos can be generalized to the field of wave chaos. In these systems one may observe many similarities between wave mechanics and a suitably defined 'classical' mechanics - ray dynamics. One should also study the morphology of the eigenfunctions and eigenmodes of the underlying wave equation. In Napoleon times there existed certain pictures named after E. F. Chladni (1756-1827). Chladni pictures (Stöckmann, 1999) show the nodal lines of the first randomly-distributed dust on vibrating glass or metal plates; this phenomenon is shown qualitatively. Regular nodal patterns are typical for the integrable systems whereas the random ones appear in the chaotic systems of the underlying ray dynamics. To obtain more precise results people have used water surface waves, vibrating blocks, ultrasonic fields in water-filled cavities and microwave cavities. The Schrödinger equation of the 2D billiard system and the wave equation, which describes the electrical field of the low frequency modes in a thin microwave resonator of the same planar shape, are equivalent from the point of view of mathematical physics. The great advantage of microwave cavities is in their size which is in the range of about one meter, compared to the real implementations of quantum billiards (i.e. quantum dots, quantum wells, quantum corrals) with the range of μm or even nm (for a review see (Stöckmann, 1999)). In the last fifteen years microwave cavities have become the main experimental research tool in the field of quantum chaos. In this research the cavity is mushroom billiard-shaped.

1.3 Dynamical tunneling

Classically, individual regions of regular and chaotic motion are separated from one other. However, from the perpective of quantum mechanics they are coupled by tunneling. This process has been termed 'dynamical tunneling' (Davis and Heller, 1981) since it occurs across a dynamically generated barrier in phase space. The dynamical tunneling effect differs greatly from the majority of the familiar cases of quantum mechanical tunneling which involve tunneling through a classically forbidden region between two separate regions of coordinate space. The EBK (Einstein-Brillouin-Keller) quantized tori do not intersect in phase space, but their projections onto the coordinate space usually overlap, so there is no spatial separation of the two wavefunctions participating in the dynamical tunneling process. One can remark that if one treats the problem strictly mathematically, one can notice that such dynamically forbidden regions are connected by complex classical trajectories. Of course, complex algebra is needed in this case. Although the tunneling phenomena have been systematically studied in the context of quantum chaos for more than twenty years, we still have not managed to explain them completely.

Dynamical tunneling was first discussed in (Davis and Heller, 1981) where the authors treated the 2D anharmonic model potential and its eigenstates and they also tried to explain certain splittings in the vibrational states of molecules. They also showed that

symmetry breaking increases the splittings of the doublets. A few years later some important general considerations of the tunneling between the tori in phase space (Wilkinson, 1986) and the narrowly avoided crossings (Wilkinson, 1987) have been presented. Dynamical tunneling between symmetry related regular regions has been studied in many systems: in a driven anharmonic oscillator and in a driven double well oscillator (Lin and Ballentine, 1990, 1992), in coupled quartic oscillators (Bohigas et al., 1990, 1993b; Tomsovic and Ullmo, 1994; Leyvraz and Ullmo, 1996), in annular billiard (Doron and Frischat, 1995; Frischat and Doron, 1998; Dembowski et al., 2000), in certain experiments with cold atoms (Steck et al., 2001; Hensinger et al., 2001; Mouchet et al., 2001), in the time periodic kicked Harper system (Brodier et al., 2001, 2002; Eltschka and Schlagheck, 2005), etc. In such systems there exist the so-called quasi-modes (Arnold, 1989) lying on the symmetric tori in phase space.

Quasi-modes are wavefunctions which are constructed on a single torus. These functions fulfill the Schrödinger equation and would degenerate if tunneling was not present. But they are not eigenstates because they do not fulfill symmetry claims, 'real' eigenstates are constructed via the linear combination of the quasi-modes lying on symmetry related tori. Therefore, if a quasi-mode, which is constructed on one of the tori, develops for a long period of time, it eventually evolves into its symmetric partner whereas its classical trajectories forever remain trapped on a single torus. While quasi-modes also emerge within the familiar 1D tunneling across the barrier, they are often surrounded by the chaotic sea in the context of dynamical tunneling. Thus, the presence of chaotic states increases the tunneling rates and causes an extreme sensitivity to external parameter variation. This process is called chaos-assisted tunneling (CAT). The tunneling, thus, annihilates the degeneracies and creates the splittings. Energy splitting is semiclassically given by

$$\Delta E = A\,\exp(-S/\hbar) = A\,\exp\left(-\frac{1}{\hbar}\int_B \mathbf{p}d\mathbf{q}\right), \tag{1.1}$$

where A is a constant associated with the energy of a quasi-mode, which weakly and mostly algebraically depends on $\hbar$, whereas S is the classical action for the trajectories from the 'forbidden' region along the path B. A special role in this semiclassical treatment is performed by the tori, fulfilling the EBK quantisation conditions, where the action integrals calculated for the N independent closed paths C_j on the torus are given by

$$J_j = \oint_{C_j} \mathbf{p}d\mathbf{q} = 2\pi\hbar\left(n_j + \frac{\nu_j}{4}\right). \tag{1.2}$$

Here n_j is the quantum number, $j = 1 \ldots N$ where N is the number of degrees of freedom of the system whereas ν_j is the Maslov index which counts the number of caustics encountered on the path C_j. Thus, in the far semiclassical limit, where the actions are very large, the level splittings decrease, which reduces the tunneling between the two symmetric EBK levels (1.2) according to (1.1).

For the sake of clarity one should emphasise that without any chaos involved, there always exists a direct tunneling between symmetry related quasi-modes. But if chaos is present, tunneling is usually much stronger and this is the reason why CAT is so important. We can see this clearly if the rate of chaoticity is treated as a perturbation, as it can be observed in the case of the model of two coupled quartic oscillators in (Tomsovic

and Ullmo, 1994). Direct tunneling is preferred for smaller couplings whereas CAT is preferred in the case of larger couplings. In this process, which can be best described as a 3-level mechanism, two regular states (the doublet) and one chaotic state (which is not part of the doublet) function as the media in the neigbourhood of the two quasi-degeneracies. The reason why CAT is often preferred to direct tunneling lies in the fact that chaotic orbits from the chaotic region between two tori connect these tori classically and, thus, this type of classical transport supports quantum tunneling.

Tunneling rates also increase in the case of resonance-assisted tunneling. This type of tunneling occurs if in regular islands the complex KAM structure of resonant tori becomes important (Brodier et al., 2001, 2002; Eltschka and Schlagheck, 2005).

Dynamical tunneling has also been studied from a single regular region to the chaotic sea: in the kicked rotor (Hanson et al., 1984), in the kicked rotors with complex classical dynamics (Shudo and Ikeda, 1995) and via localisation suppression of the tunneling effects (Ishikawa et al., 2007), in the ionisation of hydrogen atoms in polarized microwaves (Zakrzewski et al., 1998), during the decay of quantum accelerator modes (Sheinman et al., 2006), in electronic quantum transport through nanowires (Feist et al., 2006), etc. Tunneling is essential whenever two eigenvalues, one from the chaotic and one from the regular region, are degenerate. Due to tunneling there emerges a quantum-mechanical mixture of the respective eigenfunctions ψ_C and ψ_R, so the degeneracy vanishes. This type of dynamical tunneling is widely discussed in the present thesis, but also CAT emerges in a slightly different way from the one presented above.

Unlike the 1D tunneling through a barrier, it is extremely difficult to quantitatively predict dynamical tunneling. Results have only been found for specific systems or system classes so far, most recently for 2D quantum maps. The latter has been studied with the help of a fictitious integrable system (Bäcker et al., 2008b). However, a precise knowledge of tunneling rates is of great importance. Apart from our spectral statistics model in systems characterised by the mixed phase space recently studied examples are the eigenstates affected by the flooding of regular islands (Bäcker et al., 2005, 2007) and emission properties of optical micro-cavities (Wiersig and Hentschel, 2008). So far the dynamical tunneling rates have not been fully quantitatively predicted since they require fitting by the factor of about 6 in the case of the annular billiard (Frischat and Doron, 1998) and by the factor of about 100 in the case of the mushroom billiard (Barnett and Betcke, 2007).

In Chap. 3 we have presented a combined experimental, theoretical, and numerical investigation into the tunneling rates in mushroom billiards. The tunneling rates were calculated with the help of Fermi's golden rule of time perturbation theory applying to the avoided crossings between the regular and the chaotic eigenstates. The most important results have been published in (Bäcker et al., 2008a). Although the theoretical and one of the numerical parts of the research have not been provided by the author of the present thesis they are also briefly presented and discussed for the sake of completeness. Another significant topic is avoided-crossing distribution for the mushroom billiard (which is presented in Chap. 3).

1.4 Random matrix theory and level statistics

Random matrix theory (RMT) (Mehta, 1991; Guhr et al., 1998) has important applications in many branches of physics such as elementary particle physics, nuclear physics,

atomic physics, molecular physics, solid state physics, and, especially, in quantum wells (Narimanov and Stone, 1999). In quantum chaos RMT has proved to be an excellent model for the statistical properties of energy spectra of chaotic Hamiltonian systems. It goes back to the original paper (Casati et al., 1980) and to the classic paper (Bohigas et al., 1984) where the conjecture about the universality of RMT for classically fully chaotic systems was formulated. The conjecture has been theoretically supported by the dynamical and the semiclassical theory of spectral rigidity (Berry, 1985). The next important step beyond this approximation has been achieved in (Sieber and Richter, 2001), followed by the development of an expanded semiclassical theory (Müller et al., 2004; Heusler et al., 2004; Müller et al., 2004).

Classically integrable quantum systems show the Poissonian statistics, which is well known and corroborated by numerous analytical and numerical works (Berry and Tabor, 1977; Robnik and Veble, 1998). In chaotic systems spectral fluctuations obey the statistics of the Gaussian orthogonal (GOE), the unitary (GUE) or the simplectic (GSE) ensembles (depending on the existence of antiunitary symmetry (Robnik, 1986) and on an internal degree of freedom - spin). Usually the well known Wigner surmise, Eq. (2.4), well describes the level spacing distribution for the infinite dimensional GOE level spacing distribution. For higher-order level spacing distributions of chaotic systems useful approximate closed form formulae have been derived in (Abul-Magd and Simbel, 2000).

The spectral statistics in mixed-type systems rests upon the PUSC of the Wigner functions, upon the theoretical foundations in (Berry, 1977), and upon the theory of superposition of the so-called $E(k, L)$ statistics (Berry and Robnik, 1984). $E(k, L)$ statistics is the probability of having exactly k levels in an interval of the length L after unfolding, where the level spacing distribution $P(S)$ is the second derivative of the gap probability $E(0, S)$. The theory states that the $E(k, L)$ statistics factorise in the strict semiclassical limit of a sufficiently small effective Planck constant $\hbar_{\text{eff}}$, where the factorisation is a direct consequence of the statistical independence of the sequences of the regular and the irregular levels.

The Berry-Robnik (BR) theory and its resulting formulae have been verified in many different systems in the asymptotic semiclassical regime: in the 'far' semiclassical limit of quantised standard map on the torus (Prosen and Robnik, 1994a,b), in the periodically pulsed spin system (Jacquod and Amiet, 1995), in the 2D semiseparable oscillator (Prosen, 1995), in the quartic generic KAM billiard with the border described by $r(\phi) = 1 + a\cos(4\phi)$ with the simple phase space structures reflected in the lower transition point (Prosen, 1998a), in the $E(k, L)$ statistics for the standard map on the torus and the quartic billiard (Prosen and Robnik, 1999), in the $E(k, L)$ statistics with a generalised Wigner surmise tested on the Hénon-Hiles potential (Abul-Magd and Simbel, 2000), in the system with a sharply divided phase space of kicked-rotor-type map in the 'near' semiclassical regime (Malovrh and Prosen, 2002), in the Andreev billiard (Kaufmann et al., 2006), etc. There have been a number of attempts in literature to describe correctly the level statistics in the mixed-type systems and all these approaches interpolate between the RMT and the Poissonian statistics, but, unlike the BR, they are not based on sound physical grounds, and they have not been confirmed in the semiclassical limit. For a review see Chapter 3.2.2 of (Stöckmann, 1999).

If the semiclassical limit is not reached, one observes deviations from the BR behaviour which emerge due to both the localisation effects and the tunneling between the regular and the chaotic regions in the quantum phase space of the Wigner functions of the eigen-

states. This results in the linear behaviour of $P(S)$ at small S, as predicted qualitatively in (Berry and Robnik, 1984), and in the fractional power law level repulsion (which was first presented in (Prosen and Robnik, 1994b)) for S between the linear level repulsion regime and the BR tail. Presumably, the main reason for the fractional power law level repulsion lies in the localisation effects (for more details see (Izrailev, 1989, 1990)).

Here, we would like to offer a new random matrix model in order to generalise the BR level spacing distribution by including the tunneling effects between eigenstates. We will not consider localisation effects, except for the special case where ρ can be replaced by some effective ρ_{eff}; for example in the case of flooding (Bäcker et al., 2005, 2007) or in the case of hierarchical states (Ketzmerick et al., 2000). So, we will assume that the PUSC is fulfilled and the level splittings are affected by tunneling mechanisms which couple two regular and two chaotic levels and also regular-chaotic levels through the chaotic levels functioning as the intermediary. Thus, our purpose is to mimic tunneling by means of a two-level random matrix model where the non-diagonal elements correspond to the tunneling matrix elements.

Following some recent advances in the non-Gaussian and the non-normal random matrices in (Grossmann and Robnik, 2007a,b) we will try to verify to what extent the properties of the matrix ensemble remain structurally stable, i. e. robust, against certain variations of the model properties such as the statistics of the matrix elements. Finally, we will use the theoretical results to describe the level spacing distribution of the eigenvalues of a various configurations of the mushroom billiard, both on the basis of the experimental data for the microwave cavities as well as on the basis of the numerical data obtained by the expanded boundary integral method.

This work, published in (Vidmar et al., 2007), is presented in Chap. 2 and, partially, in Chap. 3 of the present thesis.

1.5 Non-Gaussian RMT

The last part (Chap. 4) of the thesis, also presented in (Robnik et al., 2007), contains the eigenvalue calculations for different random matrix ensembles where the distribution of the matrix elements is non-Gaussian. The importance of the Gaussian ensembles of the RMT has been corroborated by theory in (Hackenbroich and Weidenmüller, 1995), where the authors have considered other random matrix ensembles than the Gaussian ones (GOE, GUE and GSE). They have proved (using the supersymmetric techniques) that the local spectral fluctuations (after spectral unfolding) obey universal statistical laws described by the Gaussian ensembles in the limit of the infinite dimension $N \to \infty$, independent of the distribution of the matrix elements, provided that two conditions are fulfilled: **(i)** the energy level distribution function in this limit should be smooth, and **(ii)** it should be confined to a finite interval. Thus, this important finding is some kind of a central limit theorem for all the spectral fluctuations of random matrices.

Usually the renowned Wigner formula (Mehta, 1991) well describes the infinite dimensional GOE (or also GUE and GSE) level spacing distribution. Recently in (Grossmann and Robnik, 2007a) the authors have also studied 2D non-normal Gaussian matrices (with asymmetric variance) and a number of non-Gaussian ensembles of 2D real symmetric random matrices in (Grossmann and Robnik, 2007b) where explicit analytic results for level spacing distribution have been obtained. It has been shown there that the level repulsion

is a very robust phenomenon, which only depends on the behaviour of the distribution of the matrix elements, i.e. on its regularity at zero value. If the distribution functions of the diagonal and the off-diagonal matrix elements are regular and nonzero at zero value, there always appears the linear level repulsion. If the distribution functions in question are regular and at least one of them is zero at zero value, then the level repulsion is quadratic. If the distribution of the matrix elements is singular at zero value (e.g. an integrable power law times exponential), there appears the fractional power law level repulsion (Prosen and Robnik, 1994b; Prosen, 1995). The Cauchy-Lorentz distribution is also interesting, since it does not contain a finite first moment and produces $P(S)$ which is not normalisable to the unit first moment (mean level spacings).

It is straightforward, interesting and important to generalise these analytic 2D results to the higher dimensional case $N > 2$ where analytical results are practically impossible. Our extensive numerical calculations have shown that for regular matrix ensembles there applies the HW theorem. In the last two singular cases (mentioned earlier) all the assumptions from HW theory are not fulfilled, i.e. condition (ii) is not realised and, due to this, the systems strongly violate the GOE behaviour permitted by the HW theorem which is presented in Chap. 4.

Chapter 2

The distorted Berry-Robnik level spacing distribution

2.1 The Berry-Robnik level spacing distribution

Gap probability $E(0,S)$ is the probability that there are no levels on the interval of the length S after spectral unfolding. The level spacing distribution $P(S)$ for an unfolded spectrum is equal to the second derivative of gap probability: $P(S) = d^2E(0,S)/dS^2$. Gap probability factorises upon a statistically independent superposition of independent level sequences. From here onwards gap probability is denoted by $E(S)$. The basic finding in the Berry-Robnik (BR) picture (Berry and Robnik, 1984) is that the $E(S)$ for the total spectrum of a mixed-type system is the product of all the gap probabilities whose arguments must be weighted by the classical parameters ρ_i measuring the relative volume of the phase space of the regular component ($i = 1$), of the largest chaotic component $i = 2$, of the next largest chaotic component ($i = 3$), etc. We have focused on the simple (and usually sufficient) approximation of only two components, i.e. the regular component $i = 1$, with $\rho_1 \equiv \rho$, and the chaotic component one $i = 2$, with $\rho_2 = 1 - \rho$, so that $\rho_1 + \rho_2 = 1$. Thus, gap probability for the entire spectrum equals $E(S) = E_1(\rho_1 S)E_2(\rho_2 S)$. The BR level spacing distribution can be presented by

$$P_{BR}(S) = \frac{d^2}{dS^2}\ E_1(\rho_1 S)\ E_2(\rho_2 S). \tag{2.1}$$

Here we have introduced two quantities related to $E(S)$. The first one, $F(S)$, indicates the probability that the level spacing is larger than S. The second one is the cumulative level spacing distribution which equals: $W(S) = \int_0^S P(x)dx$. The relations between two quantities can be represented as: $F(S) = -dE/dS = 1 - W(S)$. Now the BR level spacing distribution (2.1) can be rewritten thus

$$P_{BR}(S) = \rho_1^2 P_1 E_2 + 2\rho_1\rho_2 F_1 F_2 + \rho_2^2 E_1 P_2\ , \tag{2.2}$$

where the argument of each quantity with the index i equals $x_i = \rho_i S$, $i = 1, 2$. For the chaotic case we have to apply the GOE (GUE, GSE) results for infinite matrices, for which there exist no closed form expressions. For the analytical case the Wigner distribution, which is an exact GOE result for the 2×2 matrices (while the GUE and the GSE are not treated here), is often used as an excellent approximation. The discrepancy between the

Wigner distribution and the exact result for the infinite matrices is only up to 2%, so the Wigner approximation is suitable for many practical and, especially, for many analytical purposes. In the regular case, $i = 1$, we will use the Poissonian statistics (Berry and Tabor, 1977)

$$E_1(x_1) = F_1(x_1) = P_1(x_1) = e^{-x_1}, \tag{2.3}$$

whereas in the chaotic case, $i = 2$, we will employ the Wigner (2D GOE) approximation; see (Mehta, 1991).

$$P_2(x_2) = \frac{\pi x_2}{2} \exp\left(-\frac{\pi x_2^2}{4}\right), \quad F_2(x_2) = 1 - W_2(x_2) = \exp\left(-\frac{\pi x_2^2}{4}\right), \tag{2.4}$$

and

$$E_2(x_2) = 1 - \mathrm{erf}\left(\frac{\sqrt{\pi}x_2}{2}\right) = \mathrm{erfc}\left(\frac{\sqrt{\pi}x_2}{2}\right), \tag{2.5}$$

where $\mathrm{erf}(x) = \frac{2}{\sqrt{\pi}} \int_0^x e^{-u^2}\, du$ is the error integral whereas $\mathrm{erfc}(x) = 1 - \mathrm{erf}(x)$ represents its complement. With (2.3) - (2.5) the BR level spacing distribution function (2.2) can be written as (Berry and Robnik, 1984)

$$P_{BR}(S) = e^{-\rho_1 S}\left\{e^{-\frac{\pi\rho_2^2 S^2}{4}}\left(2\rho_1\rho_2 + \frac{\pi\rho_2^3 S}{2}\right) + \rho_1^2 \mathrm{erfc}\left(\frac{\sqrt{\pi}\rho_2 S}{2}\right)\right\}. \tag{2.6}$$

The P_{BR} and its first moment are normalised. The second moment $\langle S^2\rangle = 2\int_0^\infty E(S)\, dS$ can sometimes be useful as well. For the BR level spacing distribution the second moment can be expressed in a closed form

$$\langle S^2\rangle_{BR} = \frac{2}{\rho_1}\left\{1 - e^{\frac{\rho_1^2}{\pi\rho_2^2}} \mathrm{erfc}\left(\frac{\rho_1}{\sqrt{\pi}\rho_2}\right)\right\}. \tag{2.7}$$

In case of the Poissonian statistics ($\rho_1 = 1,\ \rho_2 = 0$) $\langle S^2\rangle$ equals 2, while in the case of the Wigner distribution ($\rho_1 = 0,\ \rho_2 = 1$) $\langle S^2\rangle$ equals $4/\pi$.

2.2 General distortion of the general level spacing distribution

Let us consider 2×2 real symmetric matrices $A = (A_{ij})$ where $i, j = 1$ or 2. Only the difference between the eigenvalues is of relevance in the present context. Without any loss of generality (Grossmann and Robnik, 2007a) one may assume that the trace of A vanishes

$$A = \begin{pmatrix} a & b \\ b & -a \end{pmatrix}, \tag{2.8}$$

where a and b are real. Thus, for the eigenvalues of A one obtains

$$\lambda_{1,2} = \pm\sqrt{a^2 + b^2}\,, \tag{2.9}$$

where the difference $\lambda_1 - \lambda_2$ between the both eigenvalues equals $2\sqrt{a^2+b^2}$. Thus, the level spacing distribution is given by

$$P(S) = \int_{-\infty}^{+\infty} \int_{-\infty}^{+\infty} da\ db\ \delta\left(S - 2\sqrt{a^2+b^2}\right) g_a(a)\ g_b(b), \tag{2.10}$$

where $\delta(x)$ is the Dirac delta function whereas $g_a(a)$ and $g_b(b)$ are the normalised probability densities of the diagonal and the off-diagonal matrix elements a and b respectively. In the above construction $P(S)$ is defined for $S \geq 0$.

$P(S)$ is automatically normalised,

$$\begin{aligned} \int_0^{\infty} P(S)\ dS &= \int_{-\infty}^{+\infty} \int_{-\infty}^{+\infty} \int_0^{\infty} da\ db\ dS\ \delta\left(S - 2\sqrt{a^2+b^2}\right) g_a(a)\ g_b(b) \\ &= \int_{-\infty}^{+\infty} g_a(a)\ da \int_{-\infty}^{+\infty} g_b(b)\ db \int_0^{\infty}\ \delta\left(S - 2\sqrt{a^2+b^2}\right)\ dS \\ &= 1\ , \end{aligned} \tag{2.11}$$

but this is not true for its first moment; in general $\int_0^{\infty} S\ P(S)\ dS \neq 1$.

If we now introduce the polar coordinates

$$a = r\cos\varphi, \quad b = r\sin\varphi \tag{2.12}$$

where $r \in [0, \infty)$ and $0 \leq \varphi \leq 2\pi$, we can do the r-integration and obtain the general formula (Grossmann and Robnik, 2007b)

$$P(S) = \frac{S}{4} \int_0^{2\pi} d\varphi\ g_a\left(\frac{S}{2}\cos\varphi\right)\ g_b\left(\frac{S}{2}\sin\varphi\right). \tag{2.13}$$

If $g_a(a)$ and $g_b(b)$ are regular and nonzero at $a, b = 0$, then the integrand at $S = 0$ is just a nonzero number equal to $g_a(0)g_b(0)$. For small S we then obtain

$$P(S) \approx \frac{\pi S}{2} g_a(0) g_b(0). \tag{2.14}$$

Thus, in cases where both $g_a(a)$ and $g_b(b)$ are regular and non-zero at $a, b = 0$, there appears the linear level repulsion. It is very robust since it only depends on the regularity properties of the distribution functions of the diagonal and the off-diagonal matrix elements at zero value. For the regular distribution functions $g_a(a), g_b(b)$ higher-order corrections in S to this formula can be obtained from the Taylor expansions of $g_a(a)$ and $g_b(b)$ around $a, b = 0$. If either $g_a(a)$ or $g_b(b)$ is zero at $a, b = 0$, the level repulsion is no longer linear but of a higher order, which depends on the behaviour of $g_a(a)$ and $g_b(b)$ at $a, b = 0$. One also notices that the level repulsion is not linear in S if $g_a(0)$ and $g_b(0)$ do not exist, provided that the distributions $g_a(a)$ and $g_b(b)$ are singular at $a, b = 0$. In the case of the fractional power singularity (Grossmann and Robnik, 2007b) one obtains the fractional power law level repulsion, which was discovered and studied in detail in (Prosen and Robnik, 1993a,b) where the repulsion exponent is between 0 and 1. At this point we conclude the discussion about the general level spacing distribution and its distortion and continue with it in Chap. 4. Now, the thesis continues by applying the BR distribution as the distribution $g_a(a)$.

2.3 Gaussian distortion of the BR distribution

Eq. (2.13) can be applied to arbitrary distributions of the diagonal and the off-diagonal matrix elements of matrix A. We have assumed that in the absence of the off-diagonal elements level spacing distribution of A is given by Eq. (2.6). $P_{BR}(S)$ is normalised, $\langle 1 \rangle_{BR} = 1$ with the unit mean level spacing, $\langle S \rangle_{BR} = 1$. If there are no off-diagonal elements, this means $b = 0$ or that, equivalently, $g_b(b) = \delta(b)$. By using Eq. (2.8) we get

$$\begin{aligned} P_{BR}(S) &= \int_{-\infty}^{+\infty} da\ \delta\left(S - 2\,|a|\right) g_a(a) \\ &= \frac{1}{2}\int_{-\infty}^{+\infty} dt\ \delta\left(S - |t|\right) g_a\left(\frac{t}{2}\right) \\ &= \frac{1}{2}\left[\int_{0}^{+\infty} dt\ \delta(t-S) g_a\left(\frac{t}{2}\right) + \int_{-\infty}^{0} dt\ \delta(t+S) g_a\left(\frac{t}{2}\right)\right] \\ &= \frac{1}{2}\left[g_a\left(\frac{S}{2}\right) + g_a\left(-\frac{S}{2}\right)\right] \\ &= g_a\left(\frac{S}{2}\right), \end{aligned} \tag{2.15}$$

where g_a was assumed to be an even function of its argument. Eq. (2.15) defines the $g_a(a)$ distribution function.

In the presence of the off-diagonal matrix elements b the BR level spacing distribution is distorted. If we first assume that the off-diagonal matrix elements exist between *all* the pairs of eigenstates, then there appear the so-called *all-to-all* level couplings. An example of this can be found in the spectra obtained in a microwave experiment due to the presence of an antenna (Šeba et al., 1997). [1] Thus, in this context we can also use the term *antenna-distorted* distribution. For the sake of simplicity we will follow the usual practice in RMT and assume the normalised Gaussian distribution for the off-diagonal elements b, which has already been suggested in (Tomsovic and Ullmo, 1994)

$$g_b(b) = \frac{1}{\sigma\sqrt{2\pi}} \exp\left(-\frac{b^2}{2\sigma^2}\right). \tag{2.16}$$

The standard deviation σ can be considered as a measure for the strength of the physical coupling between the coupled states. If $\sigma = 0$ we get $g_b(b) = \delta(b)$, which corresponds to vanishing coupling. At nonzero values of σ there appear nonzero bs functioning as level coupling. Eventually (see Sec. 2.5) it turns out that the 2D theory, parameterized by the value of σ, is in very good agreement with the numerical simulations of the level spacing distributions for large matrices, provided that σ is not too large.

At this point one should comment on the choice of the statistics of the off-diagonal elements. In the case of arbitrary non-Gaussian N-dimensional random matrix ensembles it has been shown in (Hackenbroich and Weidenmüller, 1995), using Efetov's supersymmetric techniques, that the RMT statistics of the local spectral fluctuations is universal for all of them, provided that the limiting level distribution $N \to \infty$ is smooth and confined to

[1] All the eigenvalues also acquire imaginary parts due to the presence of the antenna, which is not considered in this thesis.

a finite interval. In general, this universal behaviour enables one to choose the Gaussian matrix element distributions in any further large matrix simulations. But, our ensemble is different because on the diagonal there appear the BR distribution and the off-diagonal elements are obtained from some other general ensemble. Intuitively, one expects that the final result will mainly depend only on the standard deviation σ of the off-diagonal matrix elements. This is true to some extent; nevertheless, there appear some deviations from the Gaussian case if the off-diagonal matrix element distribution is replaced by the exponential or the box (the uniform) distribution with the same σ. However, the 2D analytic theory is always in agreement with the higher dimensional counterpart (with the same statistical model), so that the results do not actually depend on the size of the matrix. This is discussed in more detail in Sec. 2.7 where we show the results of our analytic and numerical studies.

Now, we will continue with Eq. (2.16) where we have chosen the Gaussian distribution of the off-diagonal matrix elements. We should emphasise that the variance σ^2 represents the strength of the all-to-all coupling between the eigenstates. Using the fact that both g_a and g_b are even functions, the resulting level spacing distribution is represented as

$$P^A_{DBR}(S) = \frac{S}{\sigma\sqrt{2\pi}} \int_0^{\pi/2} d\varphi \; P_{BR}\left(S\cos\varphi\right) \; \exp\left(-\frac{S^2\sin^2\varphi}{8\sigma^2}\right), \tag{2.17}$$

which was termed as the antenna-distorted Berry-Robnik (DBR) distribution. One can easily verify that for $\sigma \to 0$ one returns to $P^A_{DBR} = P_{BR}$, as expected. Since we have not used special properties of the BR distribution so far, this formula is valid for any prescribed level spacing distribution function $P_0(S)$ instead of $P_{BR}(S)$. Moreover, other g_bs can be used instead of (2.16)(see Sec. 2.7). As known (see Sec. 2.1) the $P_{BR}(S)$ has one parameter $\rho = \rho_1$ which measures the fraction of the regular part of the classical phase space.

In Sec. 2.4 we will evaluate the antenna-distorted level spacing distribution by inserting the explicit form of the BR distribution function $P_{BR}(S)$ into (2.17). At this point we will briefly discuss the main features of the new distribution function $P^A_{DBR}(S)$. At small values of S, provided that $P_{BR}(0) \neq 0$, the level repulsion is linear

$$P^A_{DBR}(S) \approx \frac{S\sqrt{\pi}P_{BR}(0)}{2\sigma\sqrt{2}}. \tag{2.18}$$

The steepness of the linear rise is inversely proportional to σ. Thus, the smaller the coupling effects, modelled by the off-diagonal elements, the steeper $P^A_{DBR}(S)$ increases with S due to the level coupling. The smaller σ, the closer $g_b(b)$ approaches the delta function, i. e. the vanishing distortion. Concerning the completely chaotic systems $P_{BR}(S)$ reduces to the GOE level spacing distribution (2.4) (reminding $x \propto S$), so that $P_{BR}(0) = 0$ and $P_{BR}(S)$ is linear in S for small values of S. Consequently, in accordance with (2.18), the $P^A_{DBR}(S)$ is quadratic in S for small S. The distorted level distance distribution, therefore, has the quadratic level repulsion. The same quadratic level repulsion has been observed in the experimental spectra from the Sinai microwave billiard (Šeba et al., 1997).

Let us stress that this quadratic level repulsion has nothing to do with the breaking of the time reversal (antiunitary) symmetry in the system (Robnik and Berry, 1986) since only time reversal symmetric systems are treated in this thesis.

At very large S/σ the main contribution to the integral (2.17) comes from $\varphi \approx 0$. In this case we can make the approximation $\sin\varphi \approx \varphi$, and $\cos\varphi \approx 1$, where the integration

interval can be extended from 0 to ∞, thereby committing only an exponentially small error. To the leading order in S/σ we find

$$P^A_{DBR}(S) \approx P_{BR}(S), \tag{2.19}$$

which means that $P^A_{DBR}(S)$ has precisely the BR tail. We will present more analytical aspects of (2.17) in the following section.

The antenna-distorted BR distribution, which is defined by (2.17), is normalised by construction whereas this is not true for the first moment. If we want to use it as the model distribution for real, experimental spectra after the spectral unfolding, it has to be normalised to the unit mean level spacing $\langle S\rangle = 1$. This normalised distribution is denoted by $P^{An}_{DBR}(S)$. It can easily be obtained if one rescales the argument of $P^A_{DBR}(S)$ by a factor B_A,

$$P^{An}_{DBR}(S) = B_A\ P^A_{DBR}(B_A S), \quad \text{with} \quad B_A = \int_0^\infty x\ P^A_{DBR}(x)\ dx. \tag{2.20}$$

For each particular set of parameters (ρ, σ) we have numerically evaluated the integral from Eq. (2.17) together with the integral from Eq. (2.20) in order to obtain the constant B_A and, thus, the resulting $P^{An}_{DBR}(S)$, which is plotted in Figs. 2.1 - 2.6 with the full orange curve. For the sake of reference each figure includes the BR level spacing distribution (dashed line) with the same ρ, which shows the effect of level coupling very clearly. In each picture one clearly sees the linear level repulsion and the later overshooting. Asymptotically, at large values of S, the distribution $P^{An}_{DBR}(S)$ behaves like the stretched BR distribution, which is more visible at larger σ.

The resulting B_As for the same set of parameters (ρ, σ) are shown in the third column of Tab. 2.1. We see that B_As lie in the interval $[1, 1.2]$ for the parameters selected. In Sec. 2.5 we will compare the 2×2 and the $N \times N$ RMT results whereas in Sec. 3.5.3 the RMT results will be compared with the spectra of real physical systems.

Let us now assume that there are tunneling processes which only couple the integrable and the chaotic parts of the spectrum. In this case the off-diagonal matrix elements only appear between the regular and the chaotic states and not between two regular or two chaotic states. We should again emphasise that ρ_1 and $\rho_2 = 1 - \rho_1$, where ρ_1 and ρ_2 are the relative densities of the regular and the chaotic levels respectively. The number of pairs of states participating in the tunneling equals $1 - \rho_1^2 - \rho_2^2 = 2 \cdot \rho_1 \cdot \rho_2 = 2\rho(1-\rho)$, which is, in fact, the complement of the regular-regular and the chaotic-chaotic pairings. The distribution function, presented by Eq. (2.16), has to be modified into

$$g_b(b) = 2\rho(1-\rho)\frac{1}{\sigma\sqrt{2\pi}} \exp\left(-\frac{b^2}{2\sigma^2}\right) + [1 - 2\rho(1-\rho)]\delta(b). \tag{2.21}$$

Here σ measures the tunneling strength between the regular and the chaotic states whereas ρ measures the relative fraction of the available regular tunneling partners. The number of pairs coupled by tunneling is described by 2 times the number of regular states times the number of chaotic states. With this $g_b(b)$ we now obtain the resulting tunneling-distorted Berry-Robnik distribution function

$$P^T_{DBR}(S) = 2\rho(1-\rho)P^A_{DBR}(S) + [1 - 2\rho(1-\rho)]P_{BR}(S). \tag{2.22}$$

ρ	σ	B_A	B_T
0.10	0.05	1.0083	1.0015
0.25	0.05	1.0097	1.0036
0.35	0.05	1.0106	1.0048
0.50	0.05	1.0116	1.0058
0.65	0.05	1.0124	1.0057
0.75	0.05	1.0128	1.0048
0.90	0.05	1.0132	1.0024
0.10	0.10	1.0287	1.0052
0.25	0.10	1.0321	1.0120
0.35	0.10	1.0341	1.0155
0.50	0.10	1.0367	1.0184
0.65	0.10	1.0387	1.0176
0.75	0.10	1.0397	1.0149
0.90	0.10	1.0406	1.0073
0.10	0.15	1.0579	1.0104
0.25	0.15	1.0631	1.0237
0.35	0.15	1.0662	1.0301
0.50	0.15	1.0703	1.0351
0.65	0.15	1.0735	1.0334
0.75	0.15	1.0751	1.0281
0.90	0.15	1.0764	1.0138
0.10	0.20	1.0938	1.0169
0.25	0.20	1.1006	1.0377
0.35	0.20	1.1047	1.0476
0.50	0.20	1.1101	1.0550
0.65	0.20	1.1143	1.0520
0.75	0.20	1.1164	1.0437
0.90	0.20	1.1183	1.0213
0.10	0.30	1.1809	1.0326
0.25	0.30	1.1900	1.0712
0.35	0.30	1.1956	1.0890
0.50	0.30	1.2030	1.1015
0.65	0.30	1.2091	1.0951
0.75	0.30	1.2121	1.0796
0.90	0.30	1.2149	1.0387
0.50	0.01	1.0007	1.0004
0.50	0.02	1.0024	1.0012
0.50	0.03	1.0049	1.0024
0.50	0.04	1.0080	1.0040

Table 2.1: Numerically calculated normalisation constants B_A and B_T from Eqs. (2.20) and (2.23) respectively, used for various parameters (ρ, σ).

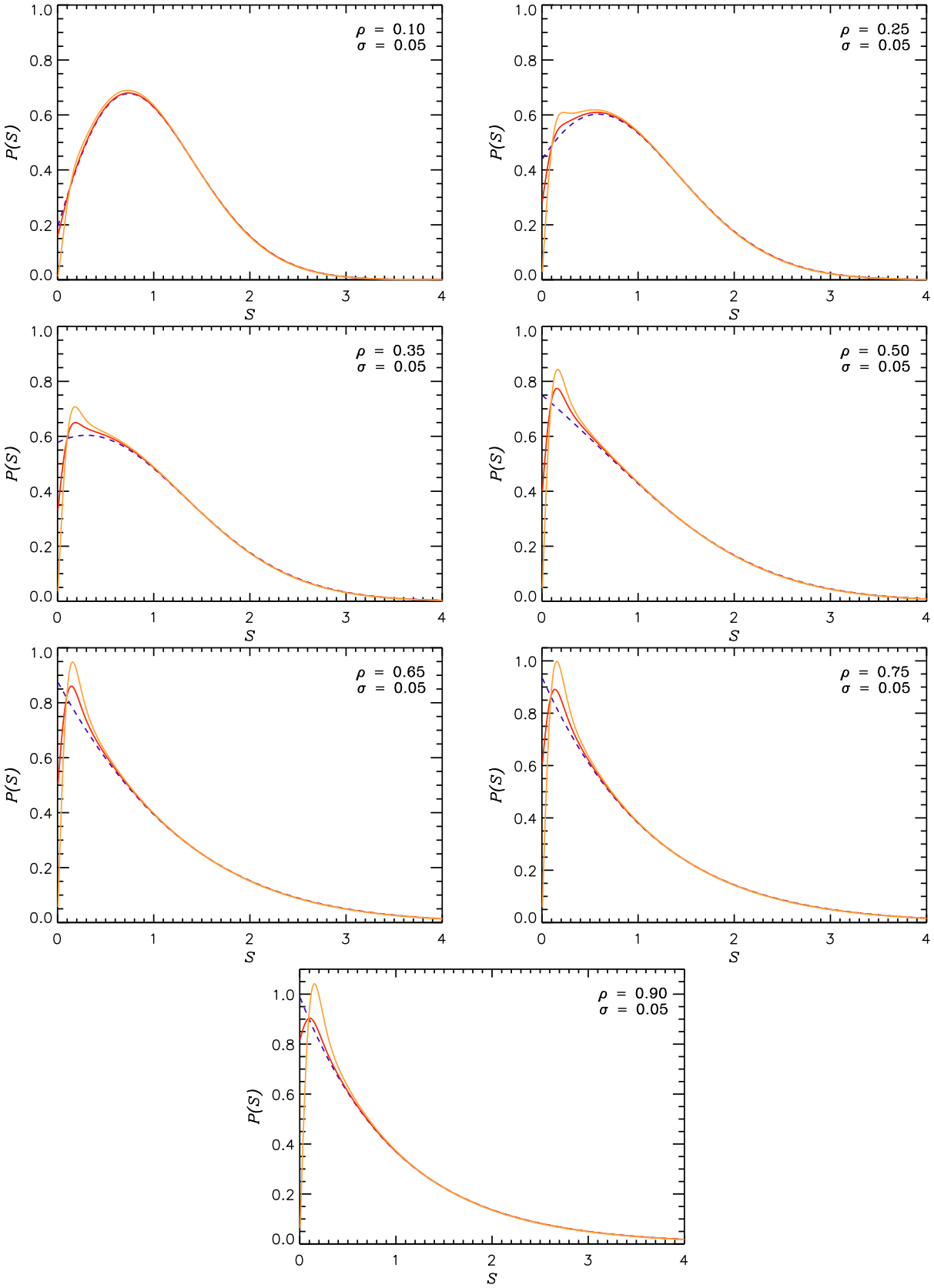

Figure 2.1: The antenna-distorted level spacing distribution (orange), Eq. (2.20), and the tunneling-distorted level spacing distribution (red), Eq. (2.23), for the level coupling parameter $\sigma = 0.05$ and for various values of the regular fraction $\rho = 0.10, 0.25, 0.35, 0.50, 0.65, 0.75, 0.90$. The dashed (blue) curve represents the BR distribution which deviates noticeably. Both curves (the red and the orange one as well) are calculated using the exact evaluation of the GOE gap probability.

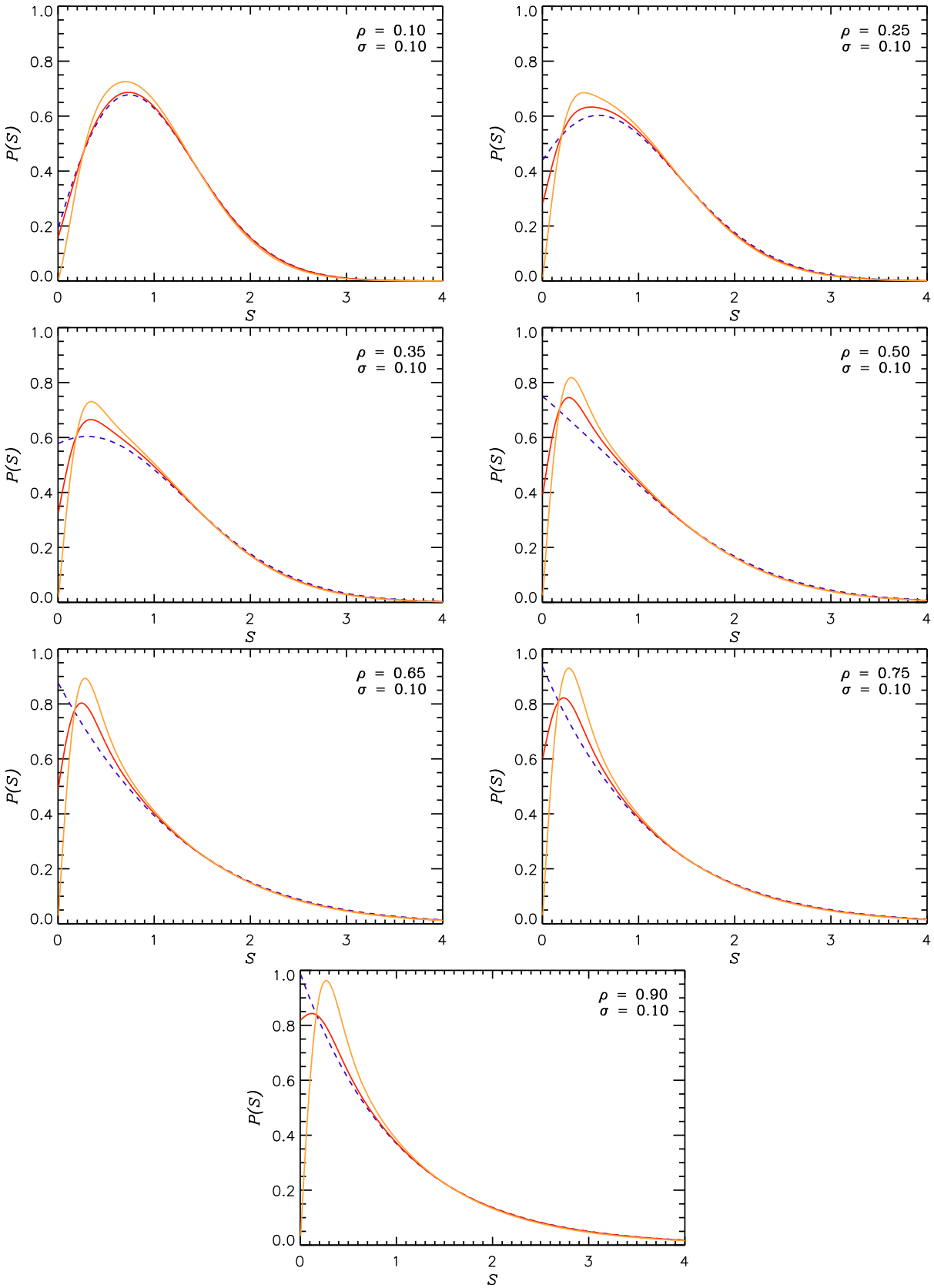

Figure 2.2: The same as Fig. 2.1 for the level coupling parameter $\sigma = 0.1$ and for various values of the regular fraction $\rho = 0.10, 0.25, 0.35, 0.50, 0.65, 0.75, 0.90$.

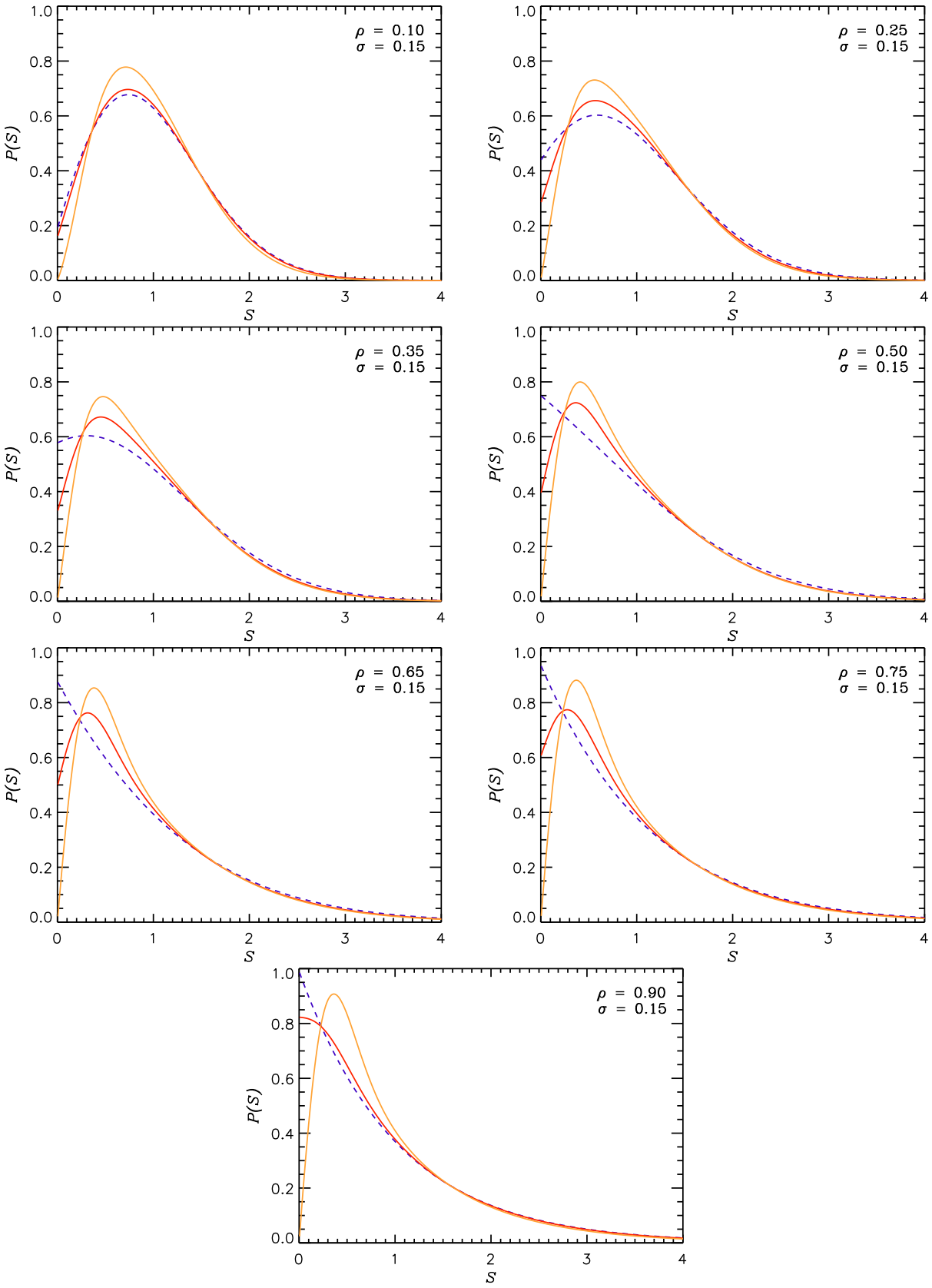

Figure 2.3: The same as Figs. 2.1 - 2.2 for the level coupling parameter $\sigma = 0.15$ and for various values of the regular fraction $\rho = 0.10, 0.25, 0.35, 0.50, 0.65, 0.75, 0.90$.

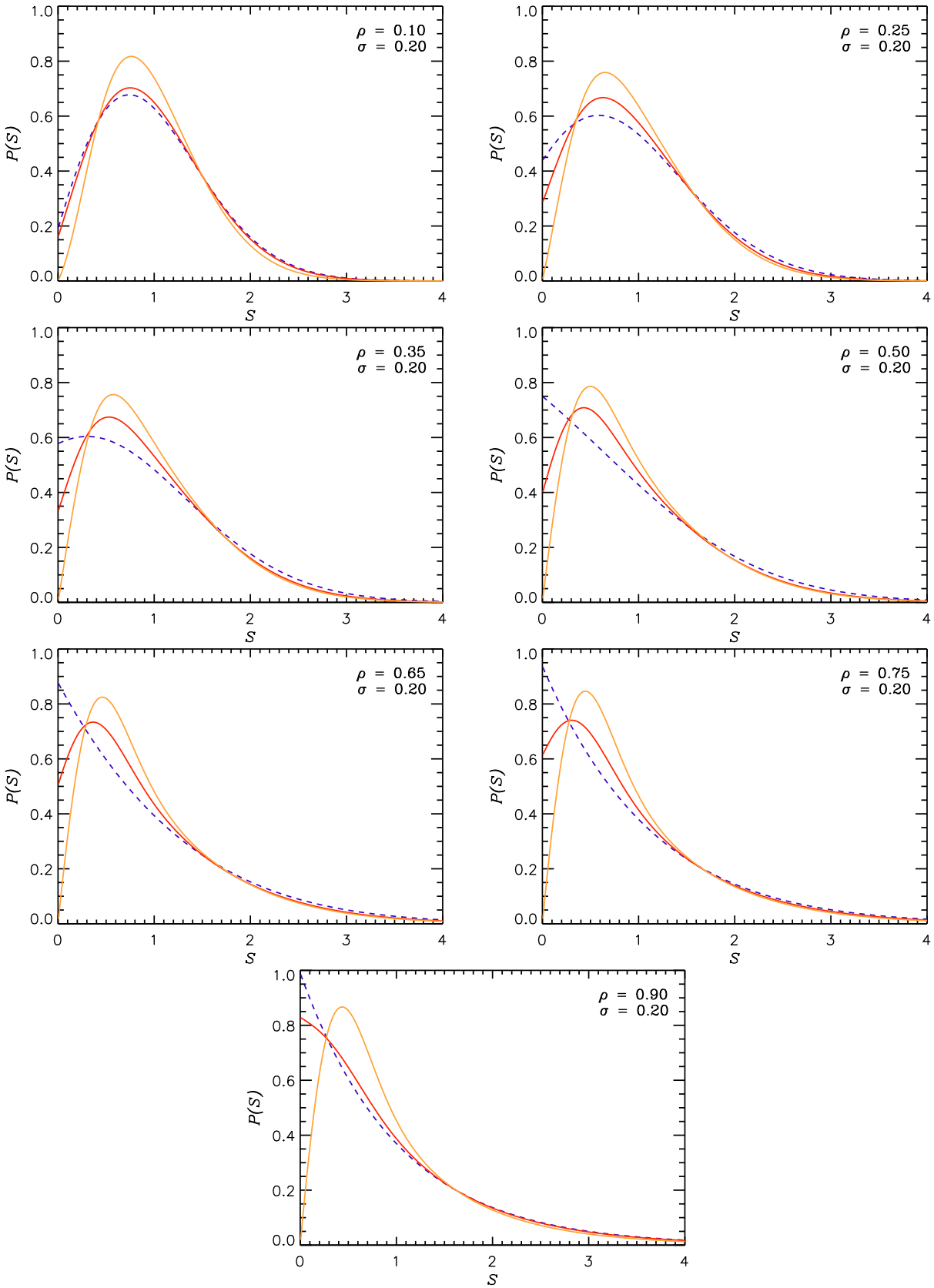

Figure 2.4: The same as Figs. 2.1 - 2.3 for the level coupling parameter $\sigma = 0.2$ and for various values of the regular fraction $\rho = 0.10, 0.25, 0.35, 0.50, 0.65, 0.75, 0.90$.

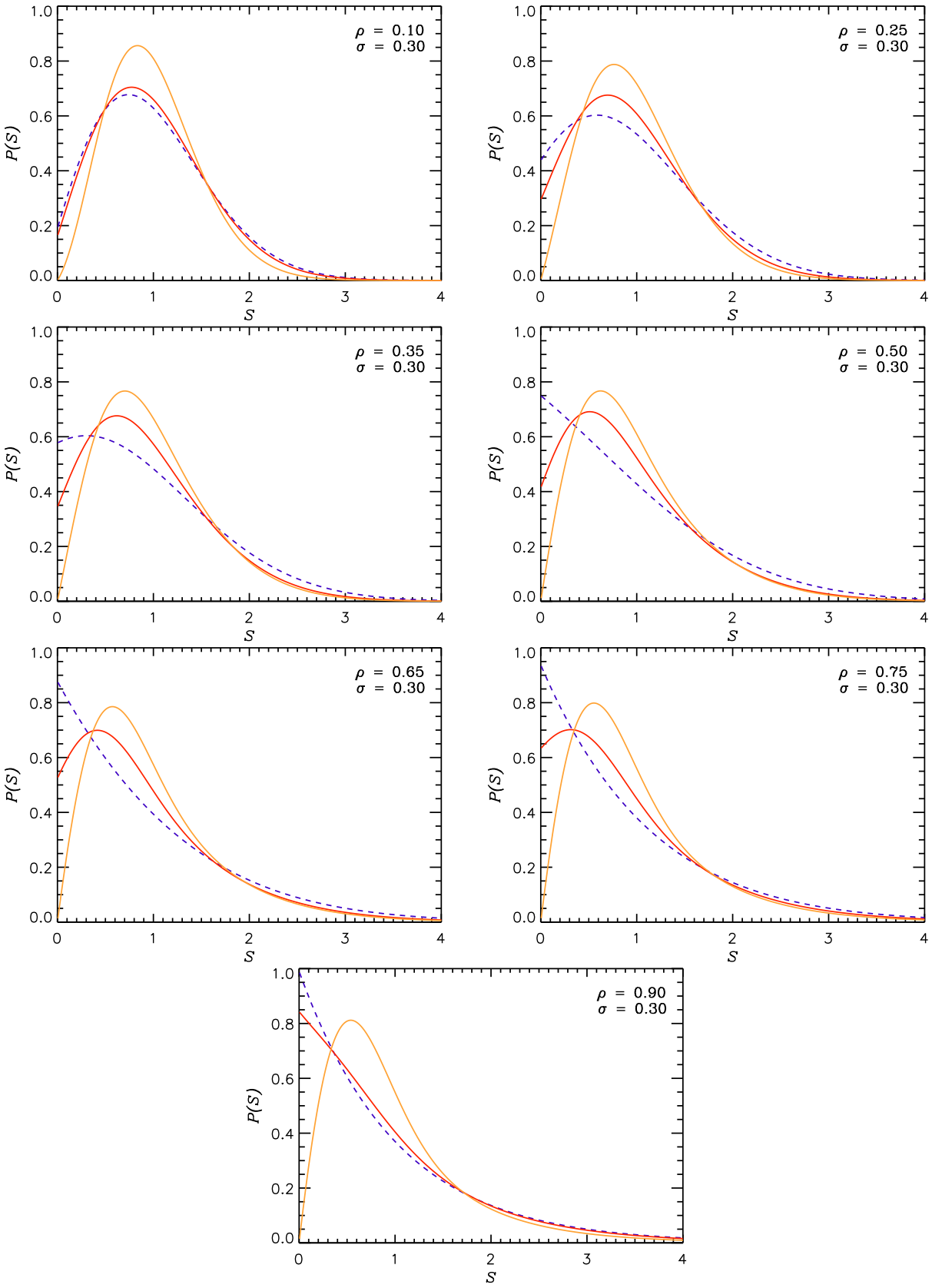

Figure 2.5: The same as Figs. 2.1 - 2.4 for the level coupling parameter $\sigma = 0.3$ and for various values of the regular fraction $\rho = 0.10, 0.25, 0.35, 0.50, 0.65, 0.75, 0.90$.

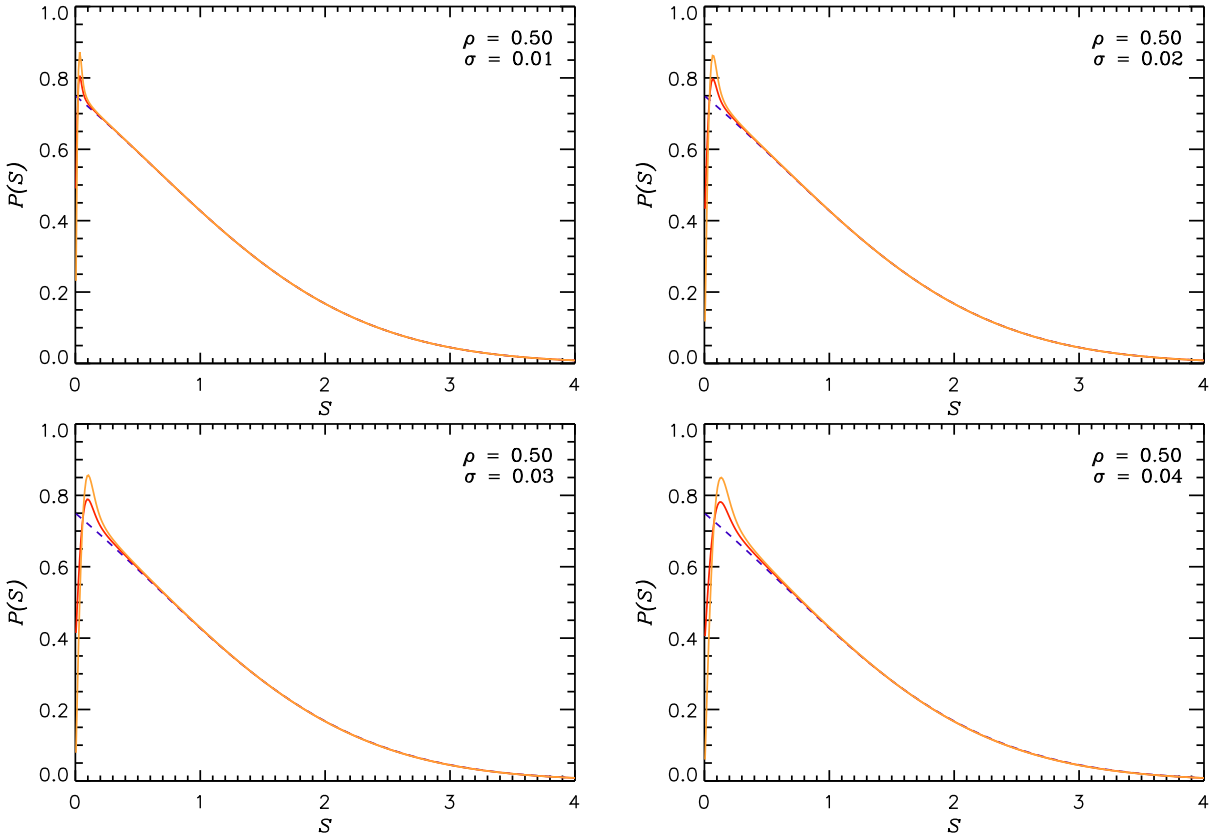

Figure 2.6: The same as Figs. 2.1 - 2.5 presenting the regular fraction $\rho = 0.5$ and various values of the level coupling parameter $\sigma = 0.01, 0.02, 0.03, 0.04$.

This is, in fact, the weighted mean of the undistorted and the antenna-distorted (distorted by the all-to-all couplings) BR distributions. For both limiting cases $\rho = 0$ and $\rho = 1$ the original GOE and PE (the Poissonian ensemble) level spacing distributions are recovered as expected. One should note that the tunneling-distorted BR distribution (2.22) is normalised to unity whereas its first moment (i.e. the mean level spacing) is not. In order to compare the theoretical level spacing distribution with the level spacing distribution from the real data (experimental or numerical ones) the rescaling, or the normalisation of the first moment to one, has to be performed exactly as suggested in Eq. (2.20). In the end we obtain the final theoretical tunneling-distorted BR distribution function by using the rescaling factor B_T

$$P^{Tn}_{DBR}(S) = B_T \; P^{T}_{DBR}(B_T S), \quad \text{with} \quad B_T = \int_0^\infty x \; P^{T}_{DBR}(x) \; dx. \tag{2.23}$$

The B_Ts for the set of parameters (ρ, σ) are shown in the forth column of Tab. 2.1. They appear in the range $[1, 1.1]$ for the parameters selected.

Again, for each set of parameters (ρ, σ) the integrals in Eqs. (2.23) and (2.17) are evaluated numerically. The resulting $P^{Tn}_{DBR}(S)$s are plotted in Figs. 2.1 - 2.6 with the full red curve. One can clearly see that there are no examples of repulsion. Why does this happen? For mathematical reasons $P^{Tn}_{DBR}(S)$ is a superposition of $P^{A}_{DBR}(S)$ and $P_{BR}(S)$ where the latter has this property. This feature is discussed in more detail in the Subsec. 2.5.2. At larger values of S of the distribution $P^{Tn}_{DBR}(S)$ one also notices the overshooting and,

asymptotically, $P^{Tn}_{DBR}(S)$ also behaves like the stretched BR distribution.

2.4 Analytical studies of the distorted Berry-Robnik distribution

We will calculate analytical approximations for the antenna-distorted BR level spacing distribution P^{A}_{DBR} given in Eq. (2.17), i.e. for small S and for large S, by using (2.6) for P_{BR} in the general expression (2.17).

2.4.1 Small S behaviour of $P^{A}_{DBR}(S)$

Let us expand $P_{BR}(x)$ from (2.6) into the Taylor series at small x,

$$P_{BR}(x) = \sum_{k=0}^{\infty} a_k x^k. \tag{2.24}$$

Then $P^{A}_{DBR}(S)$ is given by the series, from Eqs. (2.17) and (2.24),

$$P^{A}_{DBR}(S) = \frac{S}{\sigma\sqrt{2\pi}} \sum_{k=0}^{\infty} a_k S^k \int_0^{\pi/2} \cos^k\varphi \quad \exp\left(-\frac{S^2\sin^2\varphi}{8\sigma^2}\right) d\varphi \ , \tag{2.25}$$

which should be a good approximation for small S. The relevant integrals can be calculated using the relation

$$\int_0^{\pi/2} \cos^k\varphi \quad \exp\left(-\alpha\sin^2\varphi\right) d\varphi = \frac{\sqrt{\pi}\Gamma(\frac{1+k}{2})}{k\Gamma(\frac{k}{2})} \quad {}_1F_1\left(\frac{1}{2}, 1+\frac{k}{2}, -\alpha\right) \ , \tag{2.26}$$

where ${}_1F_1(x)$ is the confluent hypergeometric function. In our case $\alpha = S^2/8\sigma^2$. The confluent hypergeometric function can be further expressed in terms of the certain special functions as follows:

$$k=0: \quad {}_1F_1\left(\frac{1}{2}, 1, -\alpha\right) = e^{-\alpha/2} I_0\left(\frac{\alpha}{2}\right), \tag{2.27}$$

$$k=1: \quad {}_1F_1\left(\frac{1}{2}, \frac{3}{2}, -\alpha\right) = \frac{\sqrt{\pi}}{2\sqrt{\alpha}}\,\mathrm{erf}(\sqrt{\alpha}), \tag{2.28}$$

$$k=2: \quad {}_1F_1\left(\frac{1}{2}, 2, -\alpha\right) = e^{-\alpha/2}\left[I_0\left(\frac{\alpha}{2}\right) + I_1\left(\frac{\alpha}{2}\right)\right]. \tag{2.29}$$

I_0 and I_1 are the modified Bessel functions of the first kind, of the zero and the first order respectively. The terms $k = 3$ are not presented here since these are complicated combinations of exponential and error functions and their complexity even increases if one increases k. The coefficients in the Taylor expansion (2.24) can be presented as follows

$$a_0 = \rho_1^2 + 2\rho_1\rho_2, \tag{2.30}$$

$$a_1 = -\rho_1^3 - 3\rho_1^2\rho_2 + \frac{\pi\rho_2^3}{2}, \tag{2.31}$$

$$a_2 = \frac{1}{2}(\rho_1^4 + 4\rho_1^3\rho_2 - 2\pi\rho_1\rho_2^3), \tag{2.32}$$

$$a_3 = \frac{1}{24}(-4\rho_1^5 - 20\rho_1^4\rho_2 + 20\pi\rho_1^2\rho_2^3 - 3\pi^2\rho_2^5). \tag{2.33}$$

The hypergeometric function can be expanded into the Taylor series in terms of $\alpha = S^2/8\sigma^2$ so, accordingly, we can calculate all the terms up to and including the cubic term in S. For small S we get

$$\begin{aligned} P^A_{DBR}(S) &\approx \frac{S}{\sigma\sqrt{2\pi}}\Big\{\frac{\pi}{2}\left(\rho_1^2 + 2\rho_1\rho_2\right) + \left(-\rho_1^3 - 3\rho_1^2\rho_2 + \frac{\pi\rho_2^3}{2}\right)S \\ &+ \frac{\pi}{4}\left(a_2 - \frac{a_0}{8\sigma^2}\right)S^2 + \frac{1}{3}\left(-\frac{a_1}{8\sigma^2} + 2a_3\right)S^3\Big\} + O(S^5)\ . \end{aligned} \tag{2.34}$$

One sees that the antenna-distorted level spacing distribution $P^A_{DBR}(S)$ is linear at $S = 0$ if $\rho_1 \neq 0$, i.e.

$$P^A_{DBR}(S) \approx \frac{\sqrt{\pi}}{2\sigma\sqrt{2}}(\rho_1^2 + 2\rho_1\rho_2)S. \tag{2.35}$$

If the regular part is missing ($\rho_1 = 0$) and only the chaotic part contributes ($\rho_2 = 1$), there appears the quadratic level repulsion with the leading term

$$P^A_{DBR}(S) \approx \frac{\sqrt{\pi}}{2\sigma\sqrt{2}}S^2, \tag{2.36}$$

which, as mentioned earlier, is expected due to the assumption that all the pairs of levels are coupled, namely the regular and the chaotic ones as well as the two chaotic (chaotic-chaotic) and the two regular (regular-regular) ones; obviously, only chaotic-chaotic couplings are of relevance in this case (Haake et al., 1996).

We have verified the accuracy of the approximation (2.34) numerically and compared it with the exact evaluation of $P^A_{DBS}(S)$. It has turned out that the quadratic and the cubic terms in the curly brackets, which emerge due to the expansion of the confluent hypergeometric function ${}_1F_1$, do not significantly improve the quality of the approximation for small S values. In fact, the region of agreement with the exact formula within about a few percent extends up to $S \leq 0.4$, provided that only the first two terms from Eq. (2.34) are taken into account, and up to $S \leq 0.7$ if all the terms from Eq. (2.34) are considered.

2.4.2 Large S behaviour of $P^A_{DBR}(S)$ and $P^T_{DBR}(S)$

We again use Eq. (2.17) and calculate $P^A_{DBR}(S)$ at a large $S/\sigma \gg 1$. The main contribution to the integral comes from the interval close to $\varphi = 0$. Therefore, we can make the approximations $\sin\varphi \approx \varphi$ and $\cos\varphi \approx 1 + \epsilon \equiv 1 - \varphi^2/2$. Then we can apply the Taylor expansion $P_{BR}(S + \epsilon S) = P_{BR}(S) + \epsilon S dP_{BR}/dS$ in Eq. (2.17) and extend the

upper integration limit to ∞, thereby committing only an exponentially small error. Now the integrals can be done in a closed form, so that we obtain

$$P^A_{DBR}(S) \approx P_{BR}(S) - \frac{2\sigma^2}{S}\frac{dP_{BR}(S)}{dS}. \tag{2.37}$$

The derivative $\frac{dP_{BR}(S)}{dS}$ can be calculated explicitly from Eq. (2.6), i.e.

$$\begin{aligned}\frac{dP_{BR}(S)}{dS} &= -\frac{1}{4}\exp\left(-\rho_1 S - \frac{\pi}{4}\rho_2^2 S^2\right) \\ &\times \left\{12\rho_1^2\rho_2 - 2\pi\rho_2^3 + 6\pi\rho_1\rho_2^3 S + \pi^2\rho_2^5 S^2 + 4\rho_1^3 \exp\left(\frac{\pi}{4}\rho_2^2 S^2\right)\mathrm{erfc}\left(\frac{\sqrt{\pi}\rho_2}{2}S\right)\right\}.\end{aligned} \tag{2.38}$$

It means that, asymptotically, $P^A_{DBR}(S)$ has exactly the same tail as $P_{BR}(S)$ and its first lowest correction is described in terms of the first derivative of $P_{BR}(S)$. Its higher-order corrections increase in complexity, but they can be worked out if necessary.

Using Eqs. (2.37) and (2.22) we can also represent the asymptotic behaviour of the tunneling-distorted BR distribution (here $\langle S\rangle$ is not normalised yet) at large S, namely

$$P^T_{DBR}(S) \approx P_{BR}(S) - [1 - 2\rho(1-\rho)]\frac{2\sigma^2}{S}\frac{dP_{BR}(S)}{dS}. \tag{2.39}$$

The normalised distributions $P^{An}_{DBR}(S)$ and $P^{Tn}_{DBR}(S)$ are then calculated using the rescaling procedure as defined in Eqs. (2.20) and (2.23). Due to the rescaling factor B_T the tail of $P^{Tn}_{DBR}(S)$ is not exactly the BR distribution but, rather, the stretched BR distribution according to Eq. (2.23), unless $B_T = 1$. The same reasoning applies to $P^{An}_{DBR}(S)$ with the rescaling factor B_A.

One should notice that the Wigner approximation (2.4), (2.5) is very suitable for analytical studies as it includes all the important features of the BR as well as those of the distorted BR level spacing distribution. However, to get the precise expression for the BR distribution as defined in Eqs. (2.1) and (2.2), and, consequently, for the antenna-distorted BR distribution from Eq. (2.17), the exact GOE results from the large dimension limit for P_2, F_2, E_2 should be applied in precise numerical calculations and analysis. This is indeed what we have done in our numerical studies where we used the Padé approximations from Section 4.11 (p69-78) from the reference (Haake, 2001) for the quantity $W_2(S) = 1 - F_2(S)$, from which $P_2(S)$ is obtained by differentiation whereas $E_2(S)$ is obtained by integration (for more details see 2.1).

If the Wigner approximation were used instead, one would notice statistically significant deviations (within one percent or so) of the two-level formula from $P^{An}_{DBRN}(S)$, provided that the ρ_1 values were not too large (i.e. $\rho_1 \leq 0.35$) while for larger ρ_1 the Wigner approximation would be precise enough. This is important for the applications presented in the next section.

2.5 Simulations with random matrices

2.5.1 The antenna distorted BR distribution (all-to-all couplings)

Let us start with the assumption that there exist the Gaussian distributed off-diagonal matrix elements for all the pairs of eigenvalues. As stated above, this corresponds to

microwave cavities (i.e. "quantum billiard systems") in the presence of an antenna (see Sec. 3.3). This is not exactly true since, normally, the matrix elements are *not* Gaussian distributed in this case. For a delta-like scatterer the off-diagonal matrix element, which couples two states n and m, is proportional to $\psi_n\psi_m$ where ψ_n and ψ_m correspond to the values of the wave functions of the unperturbed cavity at the antenna position; for more details see Chap. 6 in (Stöckmann, 1999). If both ψ_n and ψ_m are Gaussian distributed at the antenna positions (which is the case if both states n and m belong to the chaotic part of the phase space) the distribution of the product $\psi_n\psi_m$ is described by the modified Bessel function, i. e. it is *non*-Gaussian! Thus, for regular eigenstates there exists no universal distribution for the wave function amplitudes (needed at the antenna positions), which consequently implies that the distribution of matrix elements (coupling chaotic and regular as well as two regular states) is non-universal as well.

But, since this chapter mainly deals with the modification of the Berry-Robnik formula resulting from the tunneling, we have applied a pragmatic approach and chosen the Gaussian distributions with the same variance for *all* the off-diagonal matrix elements. In Sec. 2.7 we will study how the type of the statistics of the off-diagonal matrix elements influences the results obtained in the research.

At this point we will introduce the normalized N-level antenna-distorted BR level spacing distribution function denoted by P^{An}_{DBRN} where N is the dimension of the matrix. This, after unfolding, is the level spacing distribution of a random matrix ensemble whose diagonal has the BR distributed eigenvalues (taking the exact large N limit distance distribution for the GOE part) with the given and fixed-value parameters ρ_i, $i = 1, 2, \ldots$, whereas all the off-diagonal elements are Gaussian distributed (see Eq. (2.16)) with the same variance σ^2.

In cases where the chaotic components smaller than the dominating one are ignored (as presented by the 2×2 model), there remain only two parameters: the BR parameter $\rho_1 = \rho$ together with $\rho_2 = 1 - \rho$, and the coupling parameter σ. We expect that this two-parameter level spacing distribution function adequately describes the level spacings of real quantum dynamical systems of the mixed type.

We have done extensive numerical calculations for the two-parameter distribution function $P^{An}_{DBRN}(S)$, with $N = 1000$. The diagonal spectrum was generated by the block random matrix with the Poissonian block of the relative size ρ, and with the remaining chaotic block of the relative size $1 - \rho$ with the GOE statistics. Spectral unfolding was performed with the help of the Wigner semicircular level density rule for the chaotic part. After sorting all the eigenvalues, one obtains the BR spectrum. One should also emphasise that random numbers were calculated using the procedure based on *ran1* from (Press et al., 1986).

Then the distorted BR matrix of the dimension $N = 1000$ (indicated by $DBRN$) was constructed for $M = 1000$ realisations of the same ensemble and diagonalised as well. In this way each histogram contains one million objects, which results in high statistical significance manifested in small fluctuations of the histogram around the expected smooth theoretical curve. The resulting spectrum was unfolded each time with the help of the phenomenological rule determining the local density of levels (or local mean level spacing) - we have averaged the nearest **unf** = 30 levels, (15 neighbouring levels up and 15 down).

The results are presented in Figs. 2.7 - 2.9 where the numerical histograms for $P^{An}_{DBRN}(S)$, $N = 1000$ are compared with the 2D prediction of $P^{An}_{DBR}(S)$ for a variety of different values of ρ and σ. We must emphasise that no curve fitting was applied in this case. The

N	**unf**	M	**stat**	$\chi^2/(\mathbf{stat}\,\Delta S)$
1000	6	1000	999000	0.4333
1000	8	1000	999000	0.1188
1000	10	1000	999000	0.0629
1000	12	1000	999000	0.0450
1000	14	1000	999000	0.0307
1000	16	1000	999000	0.0303
1000	18	1000	999000	0.0274
1000	20	1000	999000	0.0276
1000	**30**	**1000**	**999000**	**0.0254**
1000	40	1000	999000	0.0279
1000	50	1000	999000	0.0348
1000	60	1000	999000	0.0291
1000	70	1000	999000	0.0304
1000	80	1000	999000	0.0334
1000	90	1000	999000	0.0307
1000	100	1000	999000	0.0319
1000	200	1000	999000	0.0312
50	10	20000	980000	0.0369
50	12	20000	980000	0.0232
50	14	20000	980000	0.0285
50	16	20000	980000	0.0258
50	18	20000	980000	0.0208
50	20	20000	980000	0.0302
100	20	10000	990000	0.0219
200	20	5000	995000	0.0237
500	30	2000	998000	0.0278

Table 2.2: Numerically calculated χ^2 for matrices with different sizes of N and with various number of points **unf** subjected to the unfolding procedure. The number of repetitions for each matrix is indicated by M whereas **stat** is the number of all the objects (spacings) forming the histograms: $\mathbf{stat} = (N-1) \times M$ and ΔS is the bin size. All the calculations have been done with the parameters $\rho = 0.25$, $\sigma = 0.1$. The chosen configuration for the simulations shown in Figs. 2.7 - 2.13, 2.15, 2.16 is marked in bold.

agreement for small variance σ^2 and for all the regular part fractions ρ is very good.

In higher dimensions (i.e. for the large N) we expect the GOE level spacing distribution, $\rho = 0$, maps to the distorted GOE level spacing distribution, for σ larger than the characteristic σ_c. The transition is slow and can be seen in Fig. 2.10 for 4 different coupling parameters: i.e. $\sigma = 0.1, 0.2, 0.3, 0.4$.

It is obvious that the two-level approximation is suitable only in the cases where the off-diagonal elements are small compared to the mean level spacing (i.e. if $\sigma \ll 1$). To illustrate this, Fig. 2.7 compares the results obtained from the simulation $P^{An}_{DBRN}(S)$ with the results from the two-level expression (2.20) for $P^{An}_{DBR}(S)$ for $\sigma = 0.05$ and for a number of ρ values which measure the relative contribution of the regular states. An

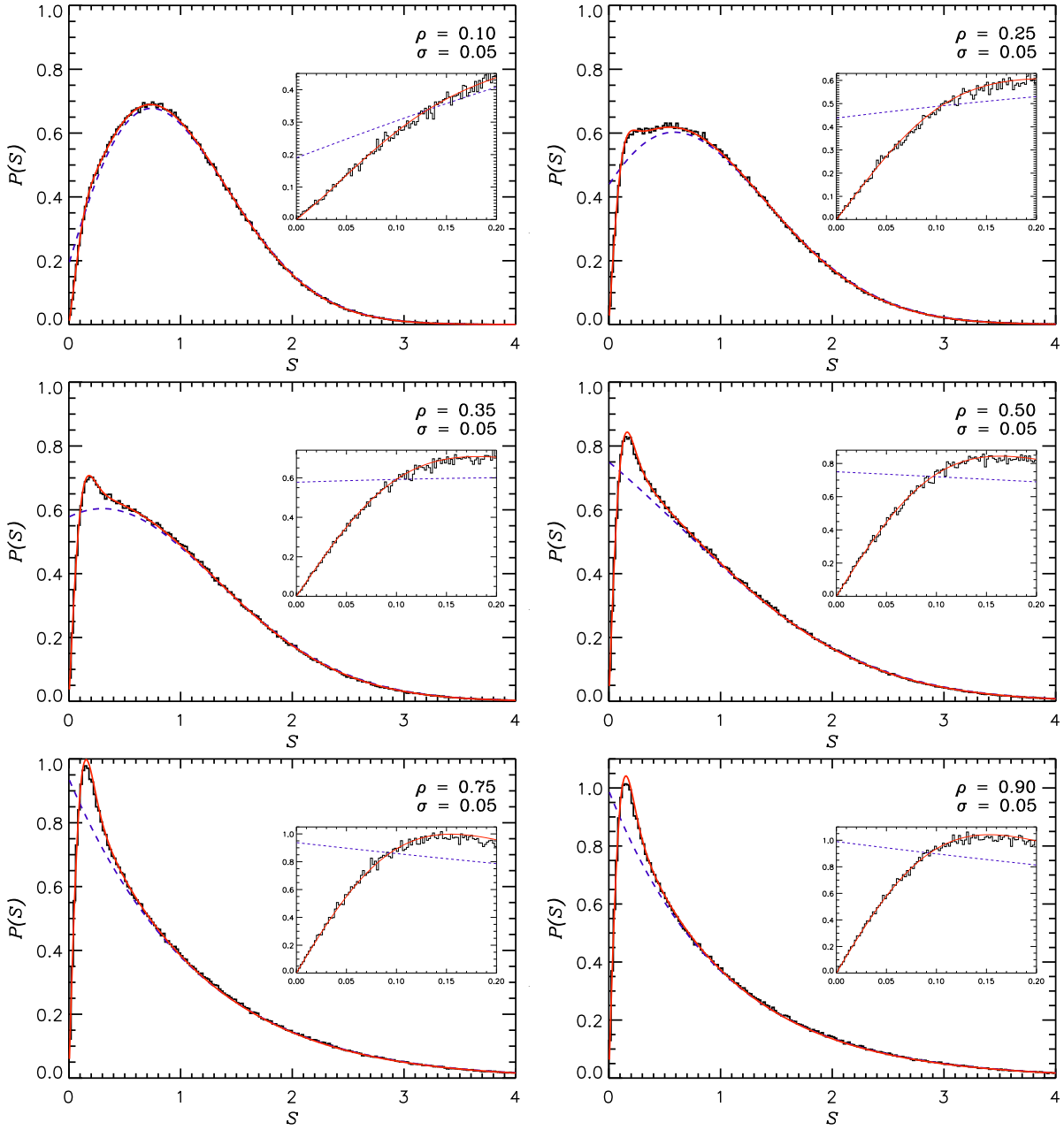

Figure 2.7: The numerical histogram for the N-level ($N = 1000$) antenna-distorted BR level spacing distribution $P^{An}_{DBRN}(S)$ is compared with the $P^{An}_{DBR}(S)$ from the 2-level model (2.20), for the level coupling parameter $\sigma = 0.05$ and for various values of the regular fraction $\rho = 0.10, 0.25, 0.35, 0.50, 0.75, 0.90$. All the eigenvalues are coupled here. The solid red line indicates the analytical 2D-matrix plot from Eq. (2.20) whereas the dashed blue curve represents the BR distribution. The numerical and the analytical results are almost indistinguishable, but the BR curve deviates noticeably. Both curves are calculated using the exact evaluation of the GOE gap probability rather than with the help of the Wigner approximation. The insets show the small S behaviour for all the three curves.

excellent agreement is found for all the ρ values. For larger values of σ the simulation and analytical curve (2.20) well agree with each other, as evident from Fig. 2.8 where $P^{An}_{DBR}(S)$ and $P^{An}_{DBRN}(S)$ are shown for $\sigma = 0.10$ and for a set of ρ values. Fig. 2.9 compares the

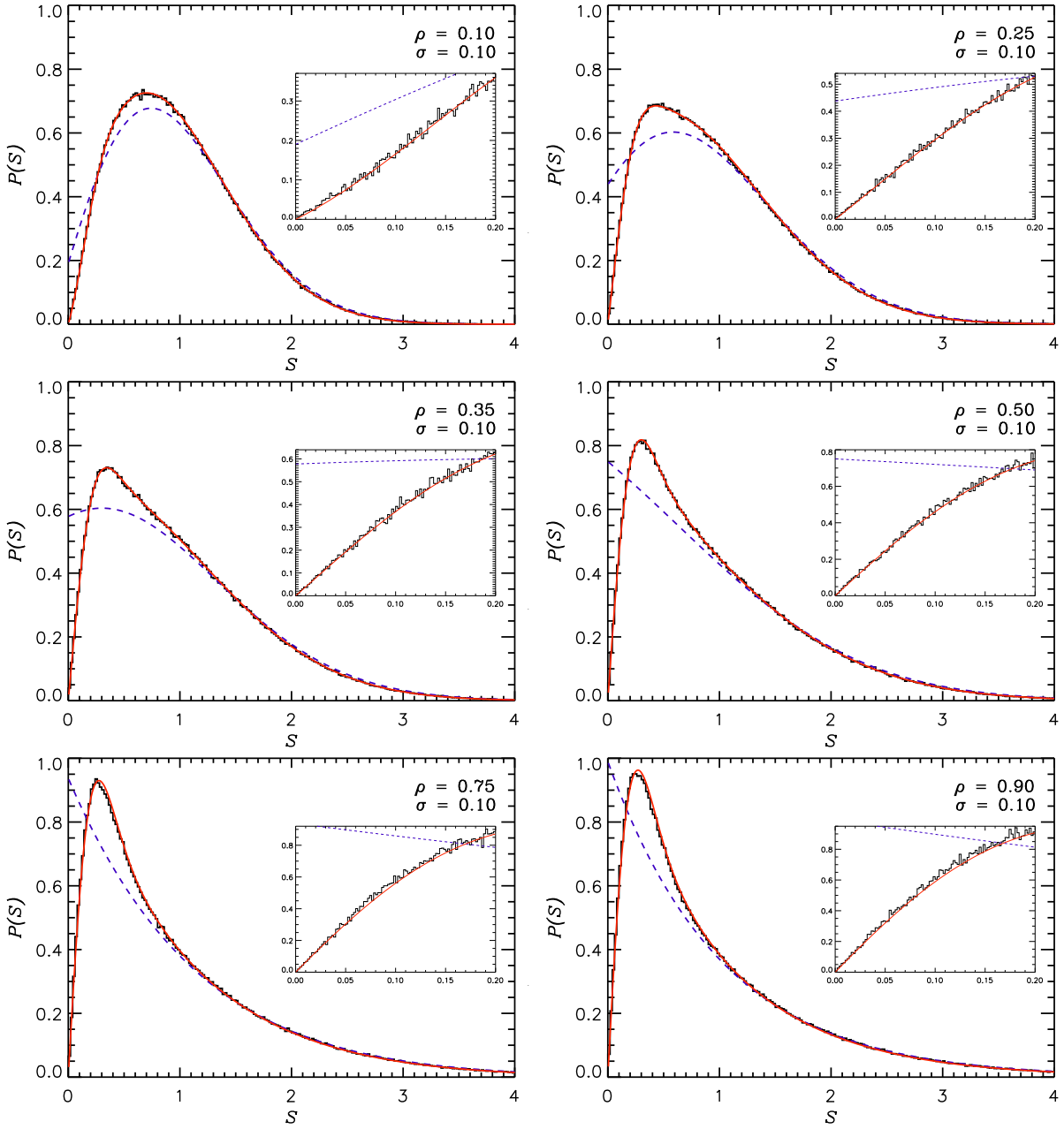

Figure 2.8: The same as Fig. 2.7 with the doubled (but still small) coupling parameter $\sigma = 0.10$ and with various values of $\rho = 0.10, 0.25, 0.35, 0.50, 0.75, 0.90$. All the eigenvalues are coupled in this figure as well.

results for the fixed $\rho = 0.5$ and for varying coupling strength $\sigma = 0.01, 0.02, 0.03, 0.04$; the agreement is very good in the case of all the weak couplings while for larger coupling values $\sigma = 0.20$ and $\sigma = 0.30$ one can notice small deviations (as expected from the theory).

Let us now study the dependence of the model on the size of the matrices N and the number of points **unf** subjected to the unfolding procedure. For the statistical measure we use the χ^2 statistics [2], defined as

[2]There are different definitions of the χ^2 statistic. This thesis employs the definition from (Press et al., 1986), p. 470.

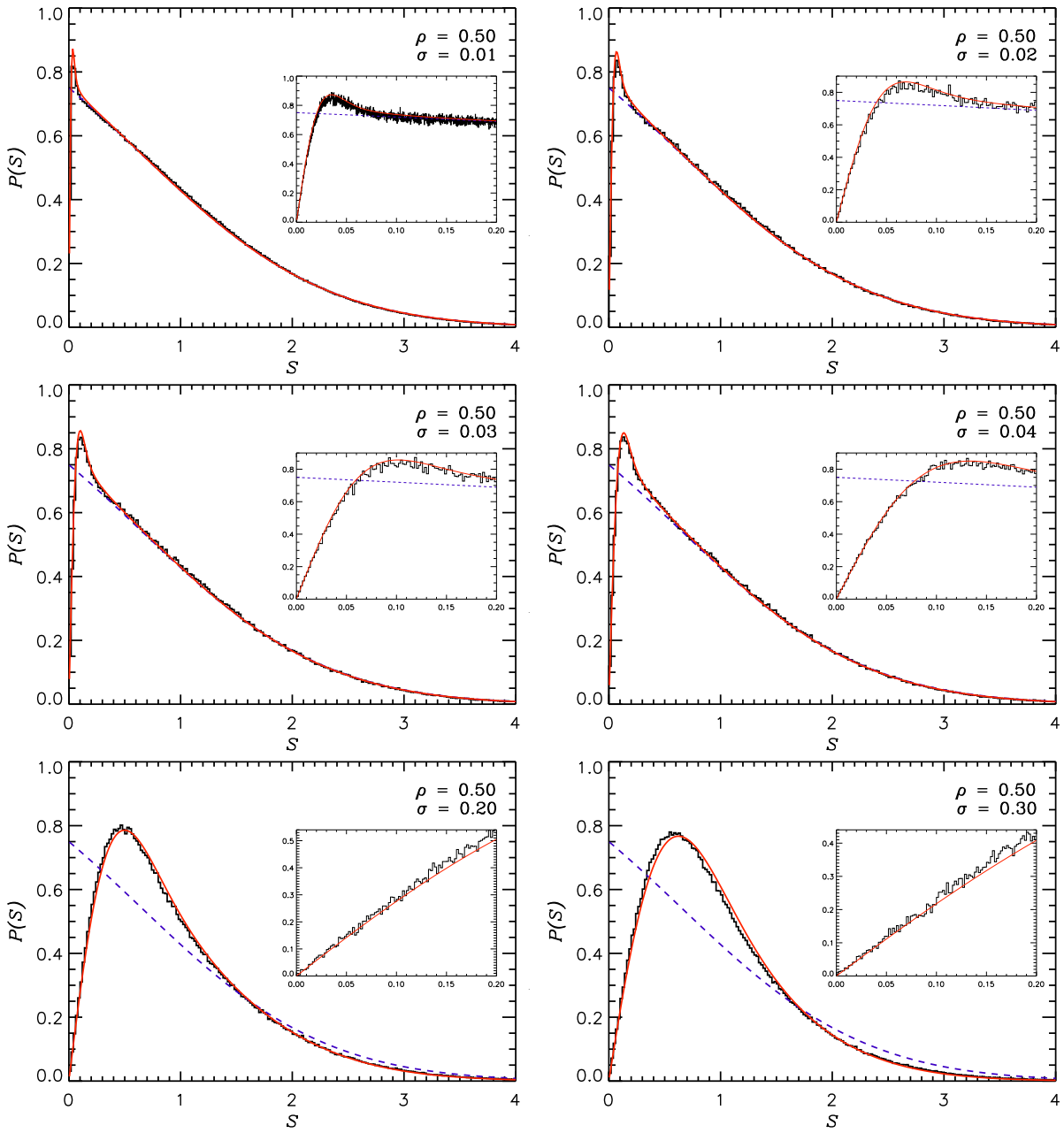

Figure 2.9: The same as in Figs. 2.7 and 2.8 but for the fixed $\rho = 0.5$ corresponding to equally large regular and chaotic regions and various strengths σ of the all-to-all level coupling, i.e. for small values $\sigma = 0.01, 0.02, 0.03, 0.04$ as well as for large values $\sigma = 0.2$, 0.3. All the eigenvalues are coupled in this figure. At large values of σ one can notice small deviations of the numerical simulations from the 2D theoretical model. At large values of $\sigma = 0.2$, 0.3 the tail of the distribution (2.20) (for the solid red curve and for the numerical histogram as well) behaves like the stretched BR distribution rather than like the 'true' BR distribution represented by the dashed curve. At smaller values of σ this effect cannot be visible since the stretching factor B_A is very close to 1. For the upper left plot with $\sigma = 0.01$ there appear 10 times more objects in the statistics.

$$\chi^2 \equiv \mathbf{stat}\, \Delta S \sum_{i=1}^{N_{bins}} \frac{\left(P^{An}_{DBRN}(S_i) - P^{An}_{DBR}(S_i)\right)^2}{P^{An}_{DBR}(S_i)}, \tag{2.40}$$

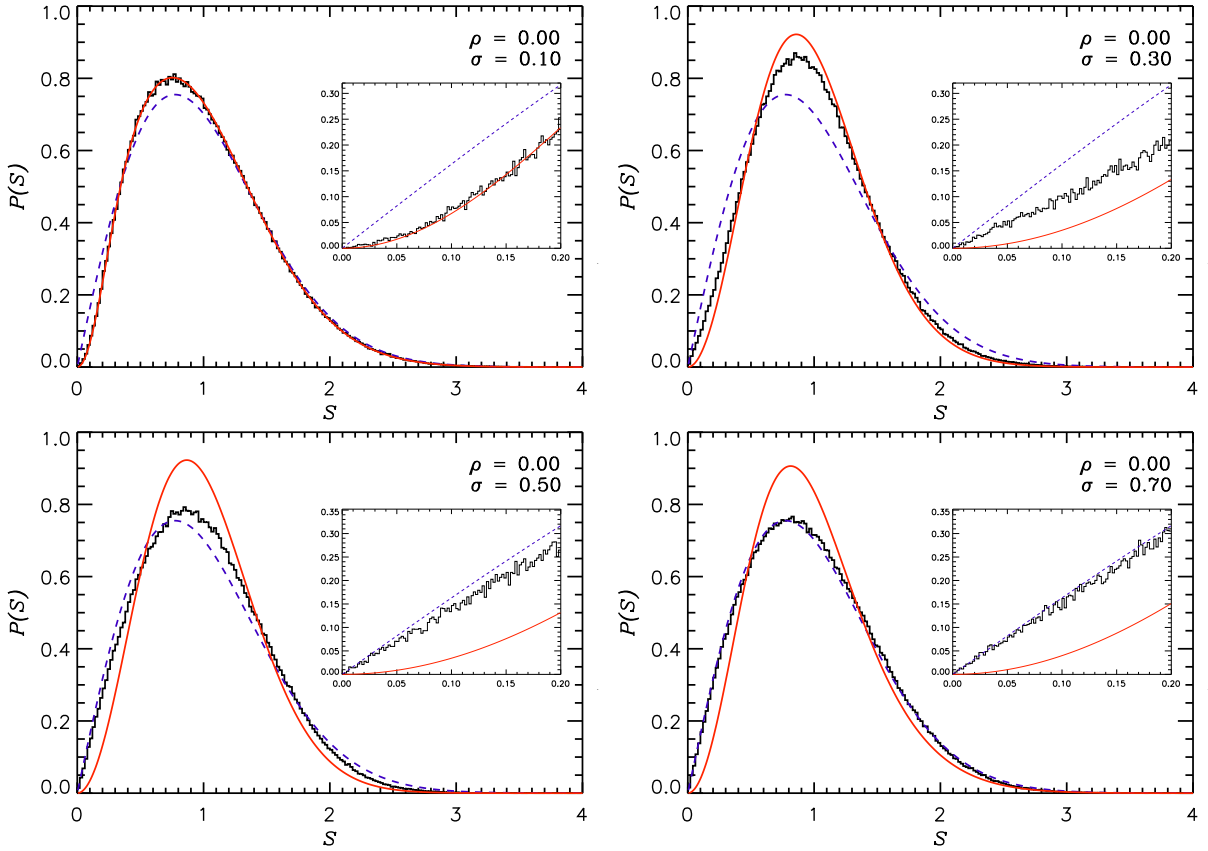

Figure 2.10: The same as Figs. 2.7 - 2.9 but for the fixed $\rho = 0$ corresponding to the fully chaotic system and to various strengths σ of the all-to-all level coupling, i.e. $\sigma = 0.1, 0.3, 0.5, 0.7$. All the eigenvalues are coupled in this case. One clearly sees the transition from the distorted GOE (solid red curve) at $\sigma = 0.1$ to the 'true' GOE (dashed blue curve) at $\sigma = 0.7$.

where $\Delta S = S_{i+1} - S_i$ is the bin size (all bins have the same size) whereas **stat** indicates the number of objects appearing in the histogram (see Tab. 2.2), N_{bins} is the number of bins of the histogram, $P^{An}_{DBRN}(S_i)$ is the value of N-dimensional statistics in the i-th bin, and $P^{An}_{DBR}(S_i)$ is the value of 2D statistical function in the center S_i of the i-th bin. The results are presented in Tab. 2.2. The smallest χ^2 for $N = 1000$ appears at **unf** $= 30$, which justifies our choice of **unf** $= 30$ in all the simulations shown in Figs. 2.7 - 2.13, 2.15, 2.16. However, one notices that there exists a wide region of possible unfolding points for a fixed N, so for $N = 1000$ and **unf** ≥ 14 all the results are practically the same. We have also tested matrices with $N = 50$ (and smaller) and observed a very good agreement as well. Therefore, we believe that the results of the model do not depend on the dimension of the matrices, so, for instance, the option $N = 100$ and **unf** $= 20$ would be equally or (even) slightly more appropriate, as indicated in Tab. 2.2.

We have also tested the phenomenological rule with **unf** (for $N = 1000$) by using the GOE random matrices ($\rho = 0$, $\sigma = 0$) where the optimal agreement with the exact unfolding (using the Wigner semicircle rule) has been sought. The results confirm the ones obtained from the χ^2 test, which means that **unf** $= 30$ is the best possible choice in this case where the **unf** does not influence the results to such a large extent.

If we consider the results of $P^{An}_{DBR}(S)$ and $P^{An}_{DBRN}(S)$ for sufficiently small values of σ, we notice one interesting feature: smaller spacings are affected to much a larger extent

than bigger ones (for the non-normalised distributions the effect would be even greater). For the 2D model this can be explained in the following way: the spacing $S = E_{n+1} - E_n$ of the coupled system, which is expressed in terms of the spacing of the uncoupled system $S_0 = E_{n+1,0} - E_{n,0} = 2a \geq 0$ as well as in terms of the coupling b (for the definition of matrix elements a and b see Eq. (2.8)), is given by

$$S = \sqrt{S_0^2 + 4\,b^2} \tag{2.41}$$

If $E_{n,0}$ and $E_{n+1,0}$ are equal (i.e. $a = 0$), then $S = 2\,b$, otherwise $S = S_0\sqrt{1 + \frac{4\,b^2}{S_0^2}}$. If σ is small, which we have assumed here, the coupling b is small as well, i.e. $b \ll S_0$. Thus, we can only take the first order in the Taylor expansion and get

$$S \cong S_0 + 2\,\frac{b^2}{S_0}. \tag{2.42}$$

The S_0 from the denominator explains why smaller spacings change to much a larger extent than bigger ones. It seems that the two-level process dominates in the N-dimensional model as well.

2.5.2 The tunneling distorted BR distribution

In order to describe the tunneling between the regular and the chaotic phase space regions in physical systems we will assume that the non-zero off-diagonal matrix elements only occur between the regular and the chaotic states but not within the regular or the chaotic block itself. In the cross coupling case the two-level approximation expresses the tunneling-distorted Berry-Robnik formula $P^{Tn}_{DBR}(S)$ which is a weighted mean of the antenna-distorted and the undistorted Berry-Robnik formula which is normalised to $\langle S\rangle = 1$, as presented in Eqs. (2.22) and (2.23). Fig. 2.11 shows the results from the simulations of $P^{Tn}_{DBRN}(S)$ and from the two-level expression for $P^{Tn}_{DBR}(S)$, for $\sigma = 0.05$ (as also applied for the all-to-all couplings) and for a number of ρ values. Fig. 2.12 represents $P^{Tn}_{DBRN}(S)$ and the $P^{Tn}_{DBR}(S)$ for $\sigma = 0.1$ and for a number of ρ values. Fig. 2.13 displays the results for $\rho = 0.5$ and $\sigma = 0.01, 0.02, 0.03, 0.04$. In all the cases the agreement between the N-level simulation and the two-level analytical formula (2.22) is rather encouraging. The agreement is better for larger values of ρ where the regular part dominates.

Although the general agreement for $\sigma = 0.05$ is still good, there appear significant deviations between the two-level approximation and the results from the N-dimensional simulations for small values of S. In the N-dimensional simulation the linear level repulsion is always observed in cases of small values of S while the two-level approximation starts with a non-zero value at $S = 0$. For a steep linear level repulsion the region in S, which should appear within an exponentially small interval $\propto \exp(-const./\hbar_{eff})$ typical of tunneling phenomena, is indeed very small (see the insets in Figs. 2.11 - 2.13). This reflects that the accidental degeneracies, which occur generically in the regular part of the spectrum, are not lifted in the case of the two-level approximation. In the N-dimensional simulations, on the other hand, *all* the degeneracies are lifted in the regular block although there are no direct tunneling matrix elements; there only appears the second order tunneling which couples two regular states indirectly, i.e. via one or more chaotic ones. Here the two-level approximation is certainly not appropriate. [3]

[3] Here the term 'degeneracies' also includes nearby lying states, i.e. the so-called quasi-degeneracies.

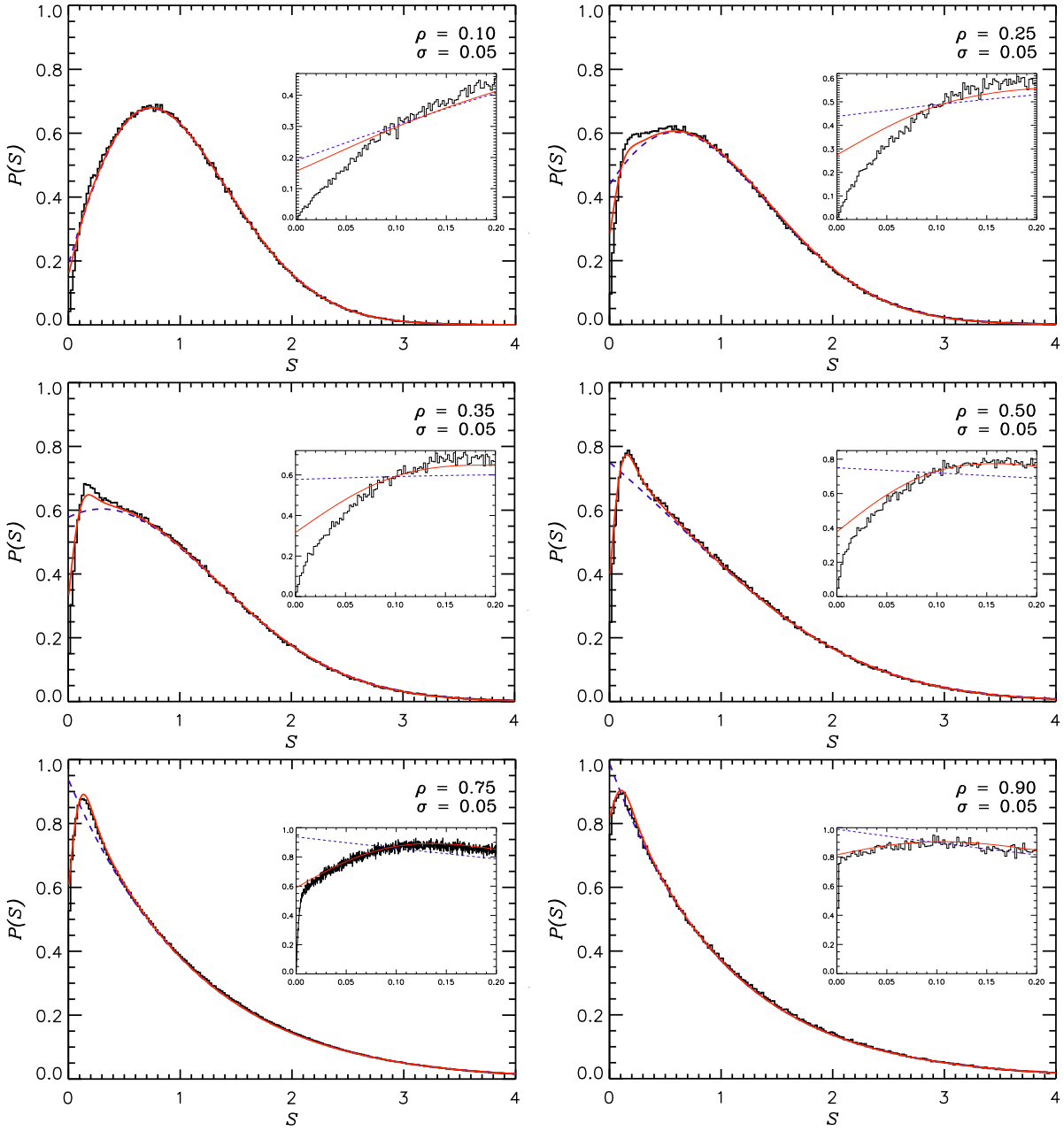

Figure 2.11: The numerical histogram for the N-level ($N = 1000$) tunneling distorted BR level spacing distribution $P^{Tn}_{DBRN}(S)$ is compared with the $P^{Tn}_{DBR}(S)$ from the 2-level model (2.23) for the fixed coupling parameter $\sigma = 0.05$ and for various sizes of the regular regions $\rho = 0.10, 0.25, 0.35, 0.50, 0.75, 0.90$. For the sake of comparison the blue dashed line represents the BR distribution with the same ρ. Only the couplings between the regular and the chaotic eigenvalues are allowed in this case; couplings cannot occur between two regular states or two chaotic ones. The insets show the small S behaviour of all the three curves plotted. The tunneling formula (2.23) is in good agreement with the numerical simulations. For the lower left plot with $\rho = 0.75$ there are 10 times more objects in the statistics.

We should also mention that neither localisation (Leyvraz and Ullmo, 1996; Ishikawa et al., 2007) nor flooding effects (Bäcker et al., 2005, 2007) have been treated so far. Typically, localisation of chaotic states (as a deviation from the PUCS-uniformity) would

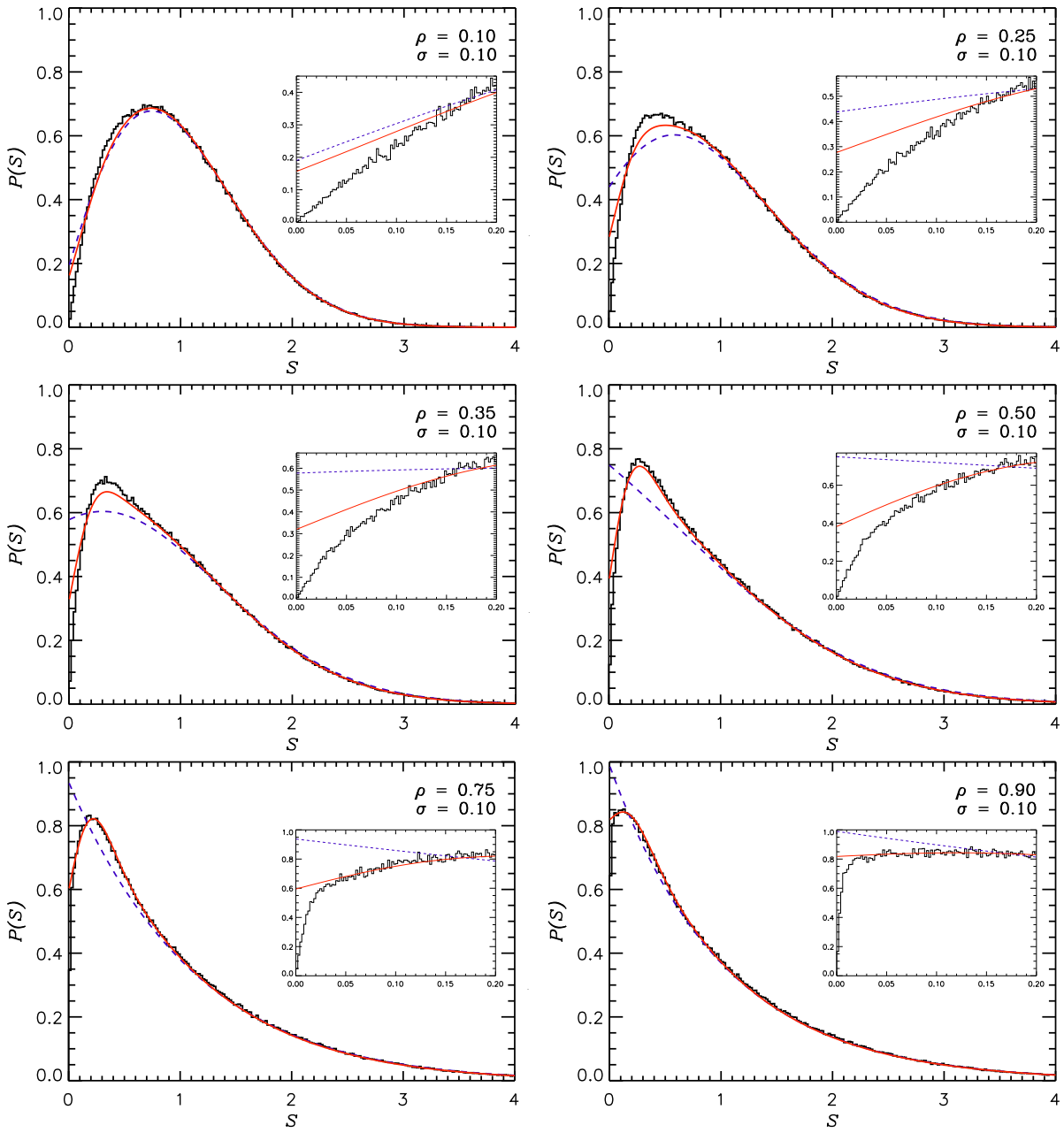

Figure 2.12: The same as in Fig. 2.11 but for the doubled cross-coupling (tunneling) strength $\sigma = 0.10$ and for various values of the relative size of the regular regions $\rho = 0.10, 0.25, 0.35, 0.50, 0.75, 0.90$. Again only cross couplings of the integrable with the chaotic states are allowed here; couplings cannot occur between two regular states or two chaotic ones. All the plots have the same number of objects in the statistics.

be modelled by the suppression of tunneling between certain basis-states. Localisation near regular (stability) islands (classically stickiness) would be modelled by replacing ρ with some larger effective ρ_{eff}, whereas (partial) flooding of regular (stability) islands would be modelled by some smaller effective ρ_{eff}.

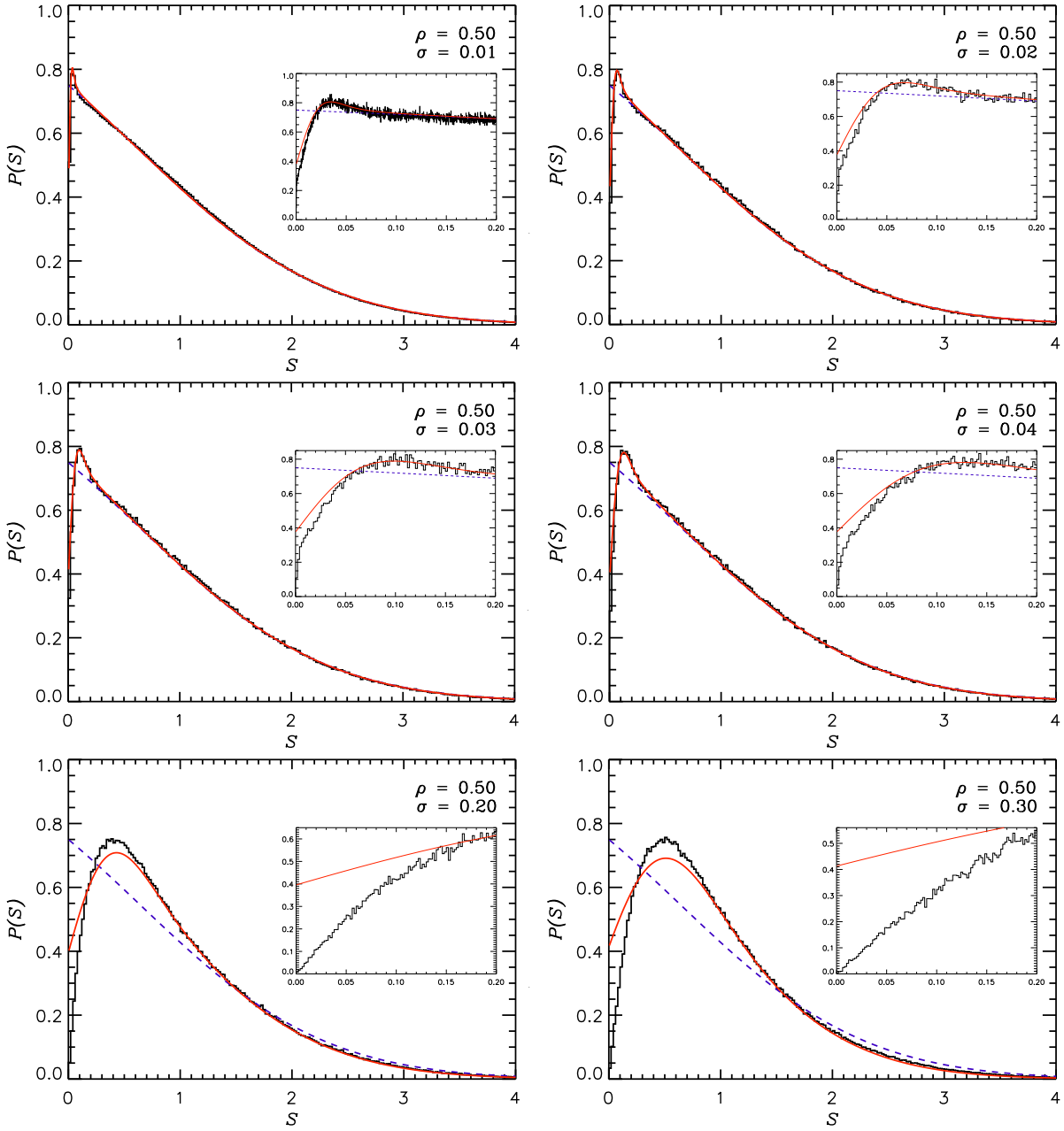

Figure 2.13: The same comparison of level spacing distributions as presented in Figs. 2.11 and 2.12, but now for the fixed $\rho = 0.5$ (equal for both the regular and the chaotic parts) and for other (smaller and larger) coupling $\sigma = 0.01, 0.02, 0.03, 0.04, 0.20, 0.30$ affected by tunneling. Again only cross couplings between the integrable and the chaotic eigenvalues are allowed. In the upper left plot with $\sigma = 0.01$ there appear 10 times more objects in the statistics.

2.6 Improvements on the tunneling-distorted BR distribution

Sec. 2.5.2 proves that the 2D model has certain disadvantages. This section represents two possible improvements to this model.

The formulation from Eq. (2.21), which presents the distribution of tunneling matrix elements, could be replaced by

$$g_b(b) = 2\rho(1-\rho)\frac{1}{\sigma\sqrt{2\pi}}\exp\left(-\frac{b^2}{2\sigma^2}\right) + [1-2\rho(1-\rho)]\frac{1}{\sigma_1\sqrt{2\pi}}\exp\left(-\frac{b^2}{2\sigma_1^2}\right), \quad (2.43)$$

where $\sigma_1 > 0$ phenomenologically represents the second order splitting in the regular block. This block is not fully regular here, so it is not proportional to $\delta(b)$. Since the splitting of the regular states is the second-order effect, σ_1 should be interpreted as being proportional to σ^2. So far we have not been able to establish an explicit relation between σ_1 and σ in this modification of the model. This is open for the future research.

To remove the degeneracies appearing due to the 2D model, one could use the 3×3 matrices, as proposed in (Stöckmann, 2007). These are chosen in such a way that they indicate the tunneling which couples two neighbouring regular states with the closest chaotic state: i.e. R-C-R tunneling. Since this coupling causes the repulsion of the regular levels, it also removes the degeneracies appearing in the regular sequence.

At this point we will select a mixed-type sequence on the basis of which we will develop the 3-level theory. Our Hamiltonian is written as

$$H^n = \left(\begin{array}{cc|c} E_{nR} & 0 & w_{1n} \\ 0 & E_{(n+1)R} & w_{2n} \\ \hline w_{1n} & w_{2n} & E_C \end{array}\right) - \frac{E_{nR}+E_{(n+1)R}}{2}\mathbf{1} = \left(\begin{array}{cc|c} \delta_n & 0 & w_{1n} \\ 0 & -\delta_n & w_{2n} \\ \hline w_{1n} & w_{2n} & \Delta_n \end{array}\right) \quad (2.44)$$

where n is the index of the regular levels whereas E_{nR}, $E_{(n+1)R}$ are the neighbouring regular levels with $E_{nR} \leq E_{(n+1)R}$ and E_C is the closest chaotic level. w_{1n} and w_{2n} are couplings of one regular and one chaotic level whereas $\delta_n = \frac{E_{nR}-E_{(n+1)R}}{2}$ and $\Delta_n = E_C - \frac{E_{nR}+E_{(n+1)R}}{2}$. The characteristic polynomial is thus expressed as

$$\chi(E) = det(H^n - E) = (E^2 - \delta_n^2)(E - \Delta_n) - (w_{1n}^2 + w_{2n}^2)E + (w_{1n}^2 - w_{2n}^2)\delta_n. \quad (2.45)$$

The chaotic level can lie above or below the mean of two neighbouring regular levels. Therefore Δ_n may have positive or negative values with equal probability and the mean $\langle\Delta_n\rangle_n$ (the average is calculated for all the regular levels) equals zero in this case. In addition, the averages $\langle w_{1n}^2\rangle_n = w_1^2$ and $\langle w_{2n}^2\rangle_n = w_2^2$ are equal.

Rigorously, this has to be applied to all the chaotic states affecting all the regular pairs. But, as presented at the end of Subsec. 2.5.1, the states that are far away from one another do not influence each other. In the first approximation we have therefore selected two neighbouring regular levels influenced by a close lying chaotic one. At this point we can make two additional approximations. Thus, we replace:
a) Δ_n with its mean $\langle\Delta_n\rangle_n = 0$. This indicates that the closest chaotic level lies in the very middle of two regular levels. This is not completely true since the chaotic levels would then obey the Poissonian statistics as well. Despite this the results obtained in this way could be useful.
b) $w_{1n}^2 - w_{2n}^2$ with its mean $\langle w_{1n}^2 - w_{2n}^2\rangle_n$, which results in $\langle w_{1n}^2\rangle_n - \langle w_{2n}^2\rangle_n = w_1^2 - w_2^2 = 0$. The final result will show whether the two approximations are meaningful.

By including the approximations into Eq. 2.45 we obtain

$$\chi(E) = (E^2 - \delta_n^2 - w_{1n}^2 - w_{2n}^2)E, \quad (2.46)$$

with the solutions

$$E_n^{I,II} = \pm\sqrt{\delta_n^2 + w_{1n}^2 + w_{2n}^2}, \quad E_n^{III} = 0. \tag{2.47}$$

Thus, the chaotic state does not change in any way whereas certain changes can be observed in the case of the two regular states. The distance between the latter equals

$$\Delta E_n = |E_n^I - E_n^{II}| = 2\sqrt{\delta_n^2 + w_{1n}^2 + w_{2n}^2}. \tag{2.48}$$

At this point we would like to learn how the regular spectrum changes if one follows the above procedure. For the spacing distribution of the regular levels $P_{Poisson}(x_1)$, where $x_1 = 2|\delta_n|$, we have chosen the distribution from Eq. (2.3), weighted by the fraction ρ of the N_{reg} regular levels appearing in the spectrum

$$P_{Poisson}(x_1) = \rho\, \exp(-\rho x_1). \tag{2.49}$$

The new distribution $P_{DPoisson}(x)$, which is termed the distorted Poisson distribution, reads

$$\begin{aligned}
P_{DPoisson}(x) &= \frac{1}{N_{reg}} \sum_{n=1}^{N_{reg}} \langle \delta\left(x - \Delta E_n\right)\rangle_{w_{1n},w_{2n}} \\
&= \frac{1}{N_{reg}} \sum_{n=1}^{N_{reg}} \left\langle \delta\left(x - 2\sqrt{\delta_n^2 + w_{1n}^2 + w_{2n}^2}\right)\right\rangle_{w_{1n},w_{2n}} \\
&= \frac{1}{N_{reg}} \sum_{n=1}^{N_{reg}} \int dx_1\, \delta\left(x_1 - 2|\delta_n|\right) \left\langle \delta\left(x - \sqrt{x_1^2 + 4(w_{1n}^2 + w_{2n}^2)}\right)\right\rangle_{w_{1n},w_{2n}} \\
&= \int dx_1\, \frac{1}{N_{reg}} \sum_{n=1}^{N_{reg}} \delta\left(x_1 - 2|\delta_n|\right) \left\langle \delta\left(x - \sqrt{x_1^2 + 4(w_{1n}^2 + w_{2n}^2)}\right)\right\rangle_{w_{1n},w_{2n}},
\end{aligned} \tag{2.50}$$

where $\delta(y)$ is the Dirac delta function of y whereas the average is calculated for all the off-diagonal elements w_{1n} and w_{2n}. By evaluating the sum over n in the limit of large N_{reg} we obtain

$$P_{DPoisson}(x) = \int dx_1\, P_{Poisson}(x_1) \left\langle \delta\left(x - \sqrt{x_1^2 + 4(w_1^2 + w_2^2)}\right)\right\rangle_{w_1,w_2}, \tag{2.51}$$

where w_1 and w_2 are the average couplings described above. Here we have assumed that w_1 and w_2 are Gaussian distributed (2.16), which was also the case in the 2×2 model: $g_b(w) = \frac{1}{\sigma\sqrt{2\pi}} \exp\left(-\frac{w^2}{2\sigma^2}\right)$ where w could either be w_1 or w_2, both with the same variance σ^2. If we incorporate this into (2.51), we obtain

$$P_{DPoisson}(x) = \frac{\rho}{2\pi\sigma^2} \int_0^\infty dx_1 e^{-\rho x_1} \int_{-\infty}^\infty dw_1 \int_{-\infty}^\infty dw_2\, e^{-\frac{w_1^2+w_2^2}{2\sigma^2}}\, \delta\left(x - \sqrt{x_1^2 + 4(w_1^2 + w_2^2)}\right). \tag{2.52}$$

If we introduce the polar coordinates: $w = w_1 \cos\varphi$, $w = w_1 \cos\varphi$, where $w \in [0, \infty)$ and $0 \leq \varphi \leq 2\pi$, we get

$$P_{DPoisson}(x) = \frac{\rho}{\sigma^2} \int_0^\infty dx_1 e^{-\rho x_1} \int_0^\infty w\, dw\, e^{-\frac{w^2}{2\sigma^2}}\, \delta\left(x - \sqrt{x_1^2 + 4\,w^2}\right). \tag{2.53}$$

By replacing $4\,w^2$ with z and by using the relation $\delta(x - \sqrt{x_1^2 + z}) = (x + \sqrt{x_1^2 + z})\,\delta(x^2 - x_1^2 - z)$, we get

$$P_{DPoisson}(x) = \frac{\rho}{8\sigma^2} \int_0^\infty dx_1 e^{-\rho x_1} \int_0^\infty dz\, e^{-\frac{z}{8\sigma^2}}\, \left(x + \sqrt{x_1^2 + z}\right) \delta\left(z - x^2 + x_1^2\right), \tag{2.54}$$

and by evaluating the integral with δ function

$$P_{DPoisson}(x) = \frac{\rho x}{4\sigma^2} \int_0^x dx_1\, e^{-\rho x_1}\, e^{-\frac{x^2 - x_1^2}{8\sigma^2}}. \tag{2.55}$$

If we calculate the integral from (2.55) with the *Mathematica*, we obtain

$$P_{DPoisson}(x) = \frac{\rho x}{4\sigma^2}\, e^{-2\rho^2\sigma^2 - \frac{x^2}{8\sigma^2}} \sigma\sqrt{2\pi} \left(\mathrm{erfi}\left(\rho\sigma\sqrt{2}\right) - \mathrm{erfi}\left(\frac{4\rho\sigma^2 - x}{2\sigma\sqrt{2}}\right)\right), \tag{2.56}$$

where $\mathrm{erfi}(z)$ is the imaginary error function of z: $\mathrm{erfi}(z) = -i\,\mathrm{erf}(iz)$. Due to normalisation the final result equals

$$P^n_{DPoisson}(x) = B_{DPoisson}\, P_{DPoisson}(B_{DPoisson} x), \quad \text{with} \quad B_{DPoisson} = \int_0^\infty y\, P_{DPoisson}(y)\, dy. \tag{2.57}$$

The normalised distorted Poisson distribution $P^n_{DPoissin}(x)$ is shown in Fig. 2.14. One clearly sees the disappearing of the degeneracies and the presence of the overshooting. The distribution quickly increases at small x values, which confirms our expectation. However, at very small x values there appears the quadratic level repulsion, i.e., by evaluating Eq. (2.55) for small x values, we obtain $P_{DPoissin}(x) \approx \rho x^2/4\sigma^2$, which is evident from Fig. 2.14. The $1/\sigma^2$ dependence of the $P_{DPoissin}(x)$ on the σ shows the expected behaviour of the second order effect contrary to the first order effect represented by Eq. (2.18). But the x^2 dependence on the regular spacing x is really surprising (or even unacceptable) since one has expected the linear level repulsion in this case. The reason for this may lie in one of our assumptions, which is, most probably, the assumption a).

Despite this one can conclude that the 3×3 CAT model could, in fact, improve the defect of the model for the level spacing distribution of the mixed systems. $P^n_{DPoissin}(x)$ has to be used instead of the 'true' Poissonian distribution function, so that there can emerge the new Berry-Robnik distribution function (see Sec. 2.1) followed by the new distorted Berry-Robnik distribution function (see Sec. 2.3).

If one applies Eqs. (2.55, 2.57) in this case, this can be pretty complicated due to numerical integrals. Instead, it might be better if the correct behaviour of Eq. (2.55) were represented via a simpler approximate analytic expression for the distorted Poisson

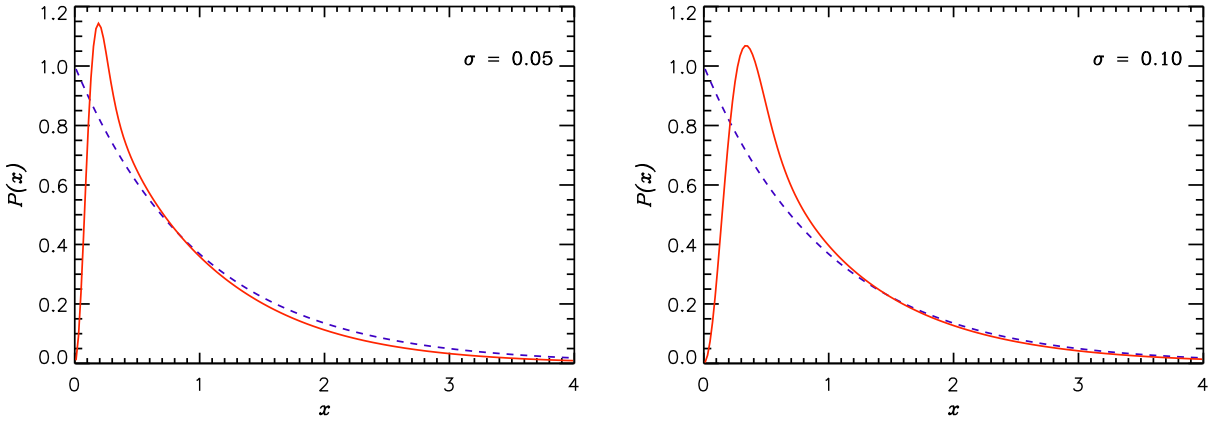

Figure 2.14: The comparison between two theoretical curves, i.e. the normalized distorted Poisson level spacing distribution $P^n_{DPoisson}$ (red line) from Eq. (2.57) and the 'true' Poissonian distribution function from Eq. (2.49) with $\rho = 1$ (blue dashed line) for two strengths of the level coupling σ, i.e. for $\sigma = 0.05, 0.1$. The normalisation factor $B_{DPoisson}$ equals 1.021 for the left curve and 1.074 for the right one.

distribution, which could be employed in a much easier way. This and the elimination of the quadratic level repulsion could be studied in the future.

At this point on could briefly mention an interesting work presented in (Leyvraz and Ullmo, 1996). Using the RMT model, similar to the one presented in this thesis, the authors (by neglecting the direct tunneling) calculated the distribution of the splittings ΔE (according to the CAT) of the exactly degenerate states in the systems with the discrete symmetry. This provides a simple analytic result, i.e. that the level splitting distribution in the cases where the chaotic part of the phase space is simple (i.e. without partial barriers etc.) is a Cauchy-Lorentz distribution one up to the border

$$P(\Delta E) = \frac{4v_t}{\Delta E^2 + 4\pi v_t^2} \qquad \Delta E < v_t \tag{2.58}$$

and zero afterwards, where v_t^2 is the average variance of the off-diagonal (tunneling) matrix elements (in the model represented here this would be σ^2). They have tested these results for the system of two coupled asymmetric quartic oscillators possessing the spatial symmetry, parity, where all the regular states appear in degenerate pairs. Our result presented in this section can be applied to all the systems where no spatial symmetries occur. This changes all the (particularly smaller) spacings S between the regular eigenvalues, not only the quasi-degenerate levels.

2.7 Dependence of the model on the matrix element statistics

This section studies how the model presented in this thesis is influenced by the statistics of the off-diagonal matrix elements for which only the Gaussian distribution with a given dispersion σ^2 has been employed up to this section.

For general *non-Gaussian* random matrix ensembles, which model fully chaotic systems, the statistics of local spectral fluctuations obey the universal Gaussian RMT in the

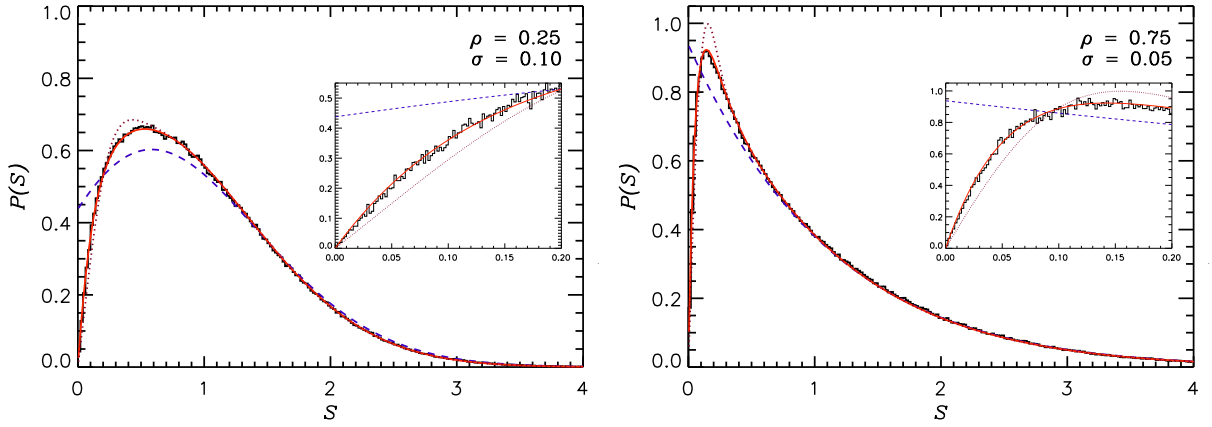

Figure 2.15: The comparison between the two theoretical curves for the normalised antenna-distorted BR level spacing distribution P^{An}_{DBR} resulting from the exponential and the Gaussian distributions of the off-diagonal elements and the histogram presented the P^{An}_{DBRN} from the numerical simulations with the matrices $N = 1000$, using the exponential distributions for all the off-diagonal matrix elements. The histogram agrees well with the 2D formula (solid curve), but both of them only slightly deviate from the Gaussian model (dotted curve). The figure also shows the BR distribution function with the same ρ (dashed curve). In the case of the Gaussian distribution with $N = 1000$ the result well agrees with the 2D formula represented in Figs. 2.8 (top-right) and 2.7 (bottom-left).

limit of large dimensions $N \to \infty$ (Hackenbroich and Weidenmüller, 1995), provided that the level density in this limit is smooth and confined to a finite interval. For 2D ensembles an explicit analytic theory has recently been performed (Grossmann and Robnik, 2007a,b) for a variety of matrix element distribution functions, including the exponential and the box (the uniform) distributions. Extensive numerical studies of such ensembles at high dimensions of the matrices (see Chap. 4) confirm the Hackenbroich-Weidenmüller prediction and show that the transition to the universal behaviour is pretty fast. If one or both of the Hackenbroich-Weidenmüller conditions are not fulfilled, e.g. for the Cauchy-Lorentz distribution of the matrix elements, there appear deviations from the GOE level spacing distribution.

Bearing in mind all this we would like to explore the sensitivity of the distorted BR level spacing distribution as regards the choice of the matrix element statistics. Thus, in addition to the Gaussian distribution treated earlier, as defined in (2.16), we will consider the box (the uniform) distribution

$$g_b(b) = \frac{\sqrt{3}}{6\sigma} \quad \text{if} \quad \mid b \mid \leq \sigma\sqrt{3} \quad \text{and zero, otherwise,} \tag{2.59}$$

and the exponential distribution

$$g_b(b) = \frac{\sqrt{2}}{2\sigma} \exp\left(-\frac{|b|\sqrt{2}}{\sigma}\right), \tag{2.60}$$

both with the variance σ^2.

It is obvious that the deviations from a Gaussian distribution are not as large as one might expect, which is clearly demonstrated in Figs. 2.15, 2.16, representing the results for the normalized antenna-distorted BR distribution $P^{An}_{DBRN}(S)$, for the Gaussian, for

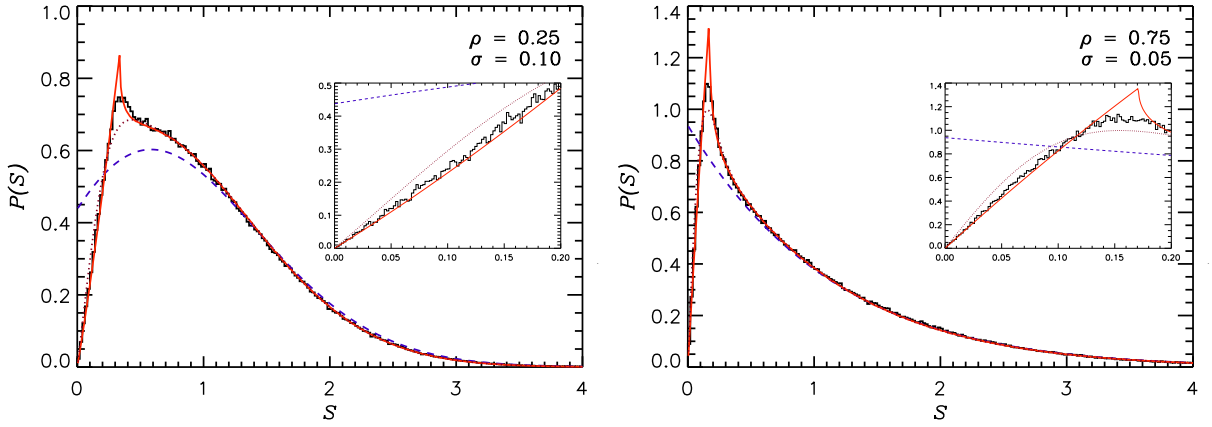

Figure 2.16: The same as Fig. 2.15 for the box (instead of the exponential) distribution of the off-diagonal matrix elements: the histogram from the numerical simulations with the matrices $N = 1000$ well agrees with the 2D formula (solid curve), but both of them only slightly deviate from the Gaussian model (dotted curve).

the exponential and for the box (the uniform) distribution with the same dispersion σ^2. These are various theoretical curves with the same σ^2. One should emphasise that no best curve fitting has been applied. One notices that the 2D theory for $P^{An}_{DBR}(S)$ from Sec. 2.3 is a suitable approximation for the random matrix ensembles of the dimension $N = 1000$. Nevertheless, the curves slightly differ from one another, especially in the central region of $0.3 \leq S \leq 0.6$ whereas the small S behaviour (the level repulsion) and the large S behavior (the tail) are in good agreement with the model where the $g_b(b)$ is the Gaussian distribution function. In fact, the tail for the exponential distribution is, analytically, the same as one for the Gaussian model (2.37). The ratio of the slopes at $S = 0$ for the exponential and the Gaussian case equals $\sqrt{\pi}$ whereas this ration equals $\sqrt{\pi/6}$ in the case of the box and the Gaussian distribution. This ration remains the same within 2% after one has rescaled the first moment to unity by using the stretch factor B_A. The agreement in the case of the Gaussian and the other ensembles is, therefore, quite satisfactory.

One intuitively expects that the statistical spectral properties of random matrix ensembles mostly depend on the variance of the matrix elements and not on other details of the ensemble unless these become singular in one way or another.

Some basic results from this chapter are tested in the following one.

Chapter 3

Dynamical tunneling in mushroom billiards

3.1 Mushroom billiard - classical

The mushroom billiard (shown in Fig. 3.1) was introduced in (Bunimovich, 2001). It is composed of a semicircle - the head, and a rectangle - the foot. We have used the rectangle for the foot although some other shapes, such as a triangle, etc., may be used instead. The mushroom billiard is a 2D autonomous system with the Hamiltonian $H(\mathbf{p},\mathbf{q}) = \mathbf{p}^2/2M + V(\mathbf{q})$, where $(\mathbf{q},\mathbf{p})$ are 2D coordinates and momenta of the particle whereas M is its mass and V is its potential. The potential is zero inside and infinite outside the billiard domain $\mathcal{D}$.

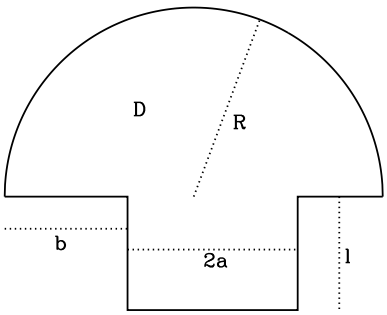

Figure 3.1: The geometry of the mushroom billiard: R = radius of the semicircle, $2a$ = width of the foot, l = height of the foot, b = position of the foot (the larger distance from the edge).

The energy is the only global constant of this billiard. There exists one additional local constant of motion for the orbits which do not enter the foot, i.e. the absolute value of the angular momentum. The orbits with the same angular momentum form a semicircular caustic. There is one critical caustic which rigorously separates the orbits into the regular and the chaotic ones. The orbits inside the head with a larger or equal caustic forever remain in the head whereas the other orbits eventually enter the foot, so they are chaotic (top two of Fig. 3.2). Since the billiard system has precisely one chaotic and one integrable component in the phase space, which are well separated from one

another (bottom of Fig. 3.2), this system is particularly attractive for analysis. Such a clear separation of the phase space first appeared in certain classical maps (Lee, 1989; Malovrh and Prosen, 2002).

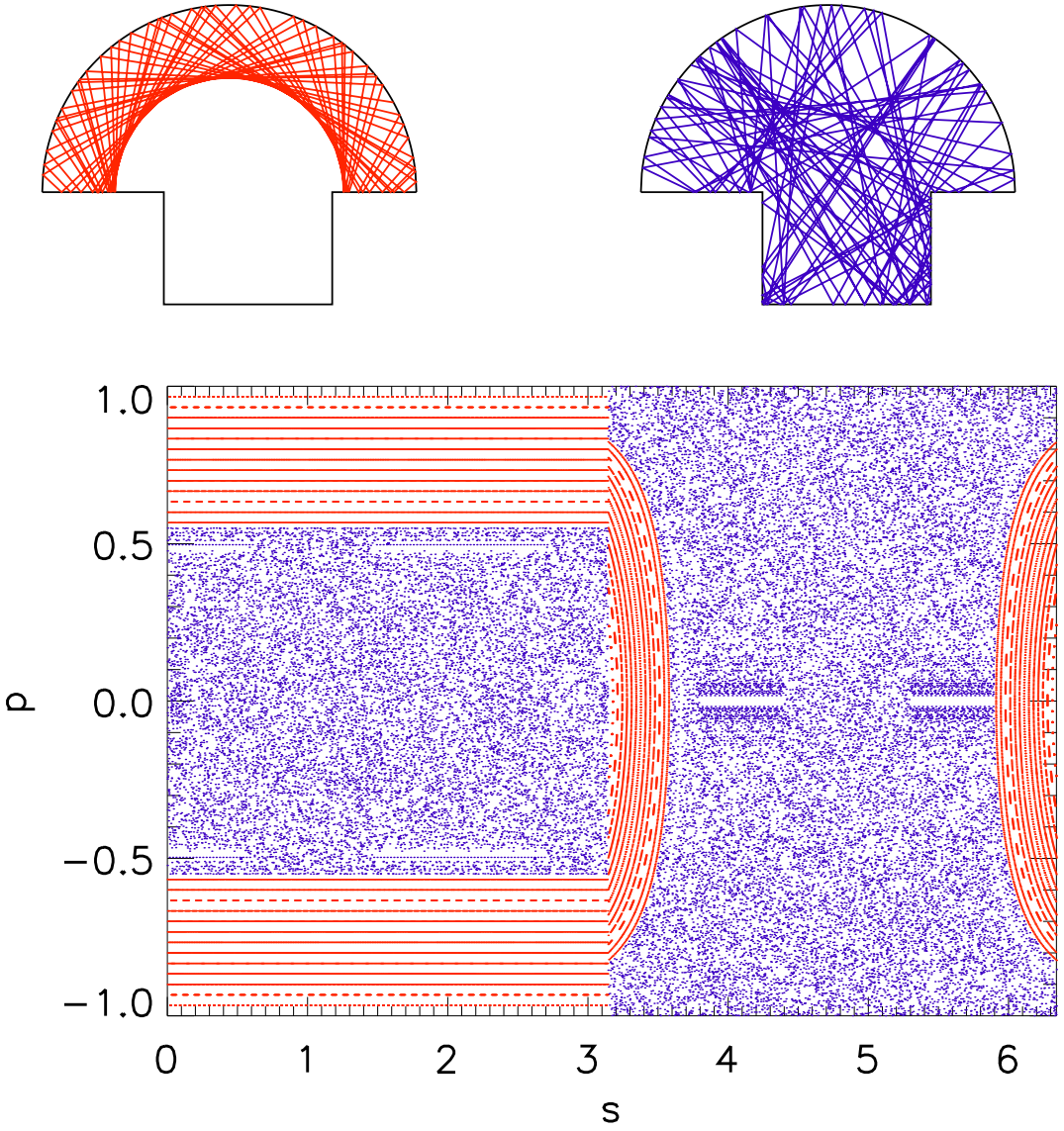

Figure 3.2: Top-left: Example of a regular (70 reflections) orbit in the mushroom billiard. Top-right: Example of a chaotic (100 reflections) orbit. Bottom: Phase space portrait. The abscissa is the border coordinate s (of the reflection point) beginning at the right $\frac{\pi}{2}$ corner of the semicircle whereas the ordinate p is the *sinus* of the reflection angle.

The regular part of the phase space of the mushroom billiard is simple since it consists of a single regular island. Due to this the volume of the regular (or the chaotic) part of the phase space can be calculated much easier than in the case of a KAM system. The group from Dresden, which was lead by R. Ketzmerick, derived an analytic expression for the effective chaotic area of the mushroom billiard with the central ($b = R - a$) foot

$$A_{ch} = 2\,la + \left[R^2 \arcsin\left(\frac{a}{R}\right) + a\sqrt{R^2 - a^2}\right], \tag{3.1}$$

where A_{ch} is the effective chaotic area of the configuration space of the mushroom billiard. If one wants to obtain the fraction ρ_2 of the chaotic component, the A_{ch} has to be divided by the entire area of the billiard, i.e. $A = 2\,la + \frac{\pi R^2}{2}$. If the foot is not in the central position ($b \neq R - a$), then instead of a in $[\dots]$ from Eq. (3.1) one employs a' defined as: $a' = 2a + b - R$. This calculation is represented and confirmed in Appendix A.

While the regular component of the phase space is very simple, the chaotic one consists of a complex distribution of families of marginally unstable periodic orbits (MUPOs). The first class of MUPOs corresponds to the orbits bouncing between the parallel walls in the foot of the mushroom billiard. Similar MUPOs can be found in many other billiards with parallel walls. The other, more interesting class of MUPOs, corresponds to periodic orbits in the chaotic region which remain trapped in the head of the mushroom billiard (Altmann et al., 2005, 2006). Since these sticky chaotic orbits, characterised by an almost regular motion and by the zero Lyapunov exponent, have measure zero, they do not affect the ergodicity of the system. Nevertheless, due to the MUPOs with long periods, one can understand certain dynamical properties of the system, such as the transport and the decay of correlations. As presented in (Altmann et al., 2005) these MUPOs result in an exponent $\gamma = 2$ for the asymptotic power-law decay of the commutative recurrence time distribution $Q(T) \propto T^{-\gamma}$. If $P(t)dt$ indicates the probability that the first return to the chosen region will happen at the time between t and $t + dt]$, N_T is the number of recurrences in that region with the recurrence time $t > T$ whereas N represents the total number of recurrences, so that then $Q(T) = \sum_{t=T}^{\infty} P(t) = \lim_{N\to\infty} \frac{N_T}{N}$. In fully chaotic hyperbolic systems $Q(T)$ decays exponentially. This definitely proves that the system discussed has the property of stickiness.

If one perturbs the system by employing the uniform transverse magnetic field (and inserts a charged particle) the situation changes. In this case there emerge the KAM tori whereas the phase space is not sharply divided anymore - now it exhibits the hierarchy of KAM-like islands and cantori which are surrounded by the chaotic sea.

3.2 Mushroom billiard - quantum

Quantum mechanically the billiard inside the domain $\mathcal{D}$ is described by the time-independent Schrödinger equation with the Hamiltonian $H(\mathbf{p}, \mathbf{q})$, the eigenenergies E_j and the eigenstates ψ_j

$$-\frac{\hbar^2\nabla^2}{2M}\psi_j(\mathbf{q}) = E_j\psi_j(\mathbf{q}), \tag{3.2}$$

where $\hbar$ is the Planck constant divided by 2π whereas ∇^2 is the Laplace operator; we use $2M = \hbar = 1$ in the following. In the case of hard walls represented in mushroom billiard the Dirichlet boundary conditions have to be applied: $\psi_n(\mathbf{q})|_{\partial\mathcal{D}} = 0$.

The eigenstates are either mainly regular or mainly chaotic, depending on the phase space region they concentrate on. One clearly sees (Fig. 3.4) the two types of wavefunctions which are already classified in (Percival, 1973). In this thesis we have used the desymmetrised mushroom billiard when the foot has been located in the central position, so that we would not have to deal with two symmetry classes of eigenstates.

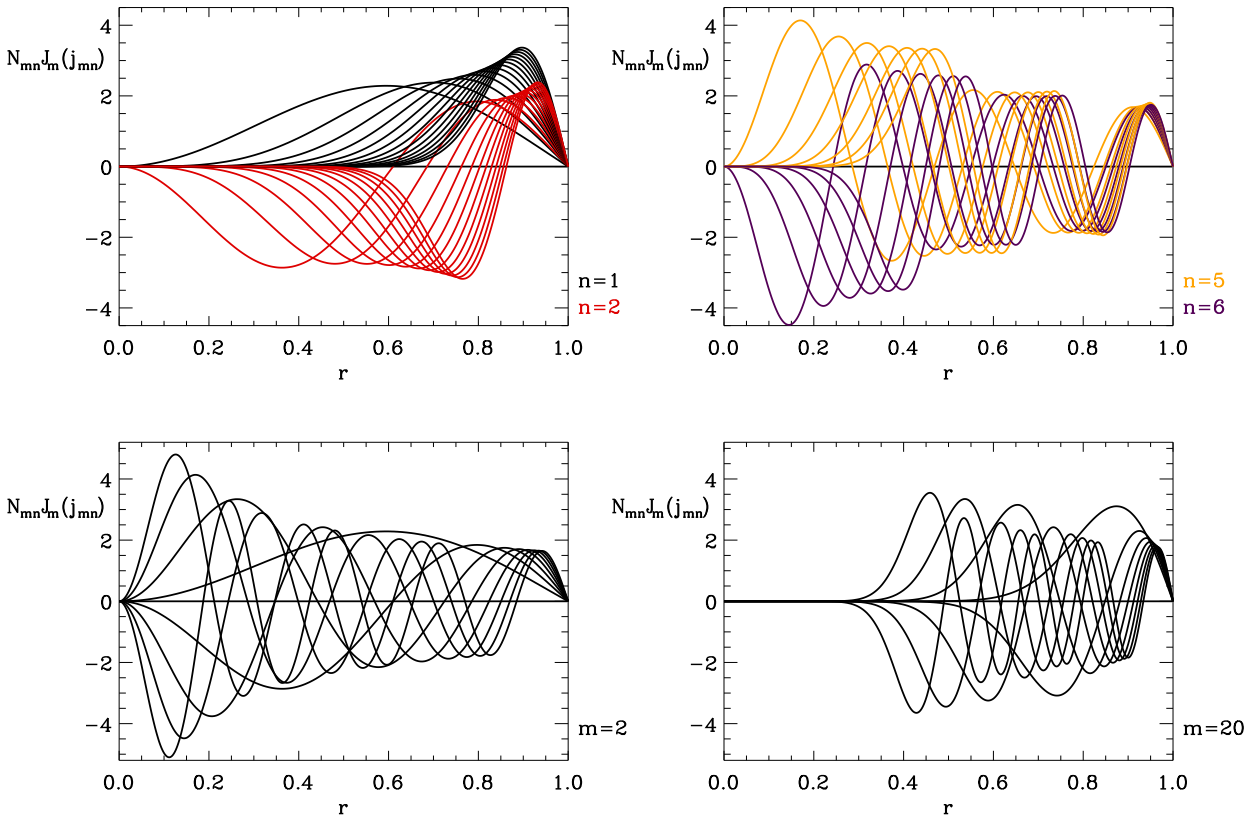

Figure 3.3: The radial part $N_{mn}J_m\,(j_{mn}r)$ of the quarter circle eigenfunctions from Eq. 3.3. The upper two plots show these functions for the fixed radial quantum numbers: $n = 1$ and $m = 2, 4, \ldots, 28$ on the upper left plot (black), $n = 2$ and $m = 2, 4, \ldots, 24$ on the upper left plot (red), $n = 5$ and $m = 2, 4, \ldots, 14$ on the upper right plot (orange), $n = 6$ and $m = 2, 4, \ldots, 12$ on the upper right plot (violet). The lower two plots represent the fixed azimuthal quantum numbers: $m = 2$ and $n = 1, 2, \ldots, 8$ the lower left and $m = 20$ and $n = 1, 2, \ldots, 8$ the lower right plot.

The regular wavefunctions resemble those of the Hamiltonian $H_{1/4}$ for the quarter circle. If $R = 1$, its eigenenergies and eigenfunctions, written in polar coordinates (r, φ) read

$$E_{1/4}^{mn} = j_{mn}^2 \quad \text{and} \quad \psi_{1/4}^{mn}(r \leq 1, \varphi) = N_{mn}J_m\,(j_{mn}r)\sin(m\varphi),\ \psi_{1/4}^{mn}(r > 1, \varphi) = 0 \quad (3.3)$$

These are characterized by the radial $(n = 1, 2, \ldots)$ and the azimuthal $(m = 2, 4, \ldots)$ quantum numbers. Here J_m is the m-th Bessel function whereas j_{mn} indicates its n-th root and $N_{mn} = -\sqrt{8/\pi}/J_{m-1}(j_{mn})$ is the normalisation constant. The radial part $N_{mn}J_m\,(j_{mn}r)$ of the quarter circle eigenfunctions is shown in Fig. 3.3.

In Fig. 3.4 (the right picture) we have resolved the quantum numbers (m, n) for a mushroom regular eigenstate and written down the energies of this regular and the neigbouring chaotic state; these energies are very close together. As evident from the following dynamical tunneling can, in fact, explain this small splitting.

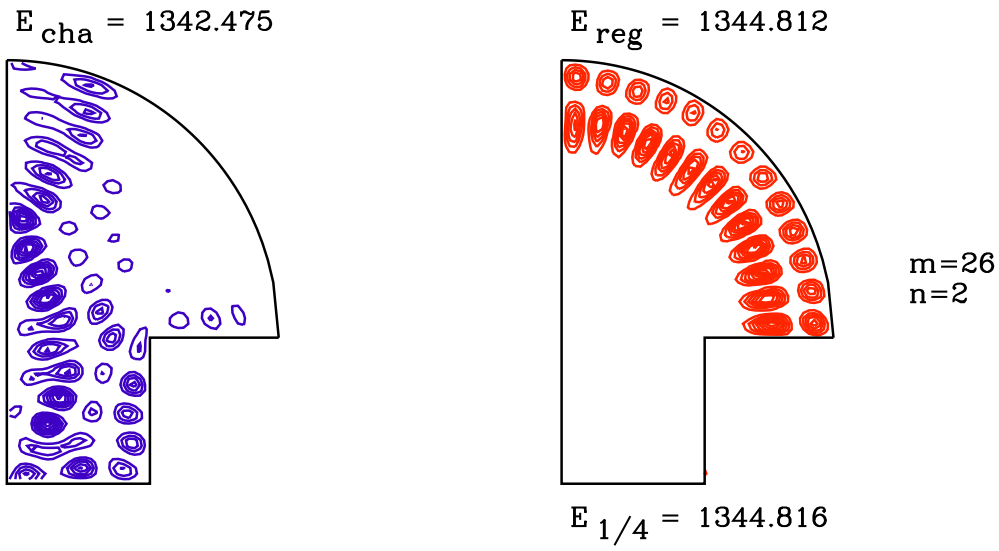

Figure 3.4: A neighbouring 'chaotic' and 'regular' state in the desymmetrised mushroom billiard. The probability density $|\psi(\mathbf{q})|^2$ is plotted.

3.3 Microwave experiments

3.3.1 The similarity between QM and ED

By first employing the Maxwell equations one obtains the Helmholtz equation for the propagation of electromagnetic waves (Jackson, 1982)

$$\nabla^2 \left\{ \begin{array}{c} \mathbf{E} \\ \mathbf{B} \end{array} \right\} + k^2 \left\{ \begin{array}{c} \mathbf{E} \\ \mathbf{B} \end{array} \right\} = 0, \tag{3.4}$$

with a wavenumber $k = \frac{2\pi\nu}{c}$, where ν is the frequency and c is the speed of light. Now one applies the cartesian coordinates and the cylindrical waveguide with walls from any ideal conductor, with any cross section oriented along the z direction. Using the ansatz

$$\left. \begin{array}{l} \mathbf{E}(x,y,z,t) \\ \mathbf{B}(x,y,z,t) \end{array} \right\} = \left\{ \begin{array}{l} \mathbf{E}(x,y)e^{i(\pm k_z z - 2\pi\nu t)} \\ \mathbf{B}(x,y)e^{i(\pm k_z z - 2\pi\nu t)} \end{array} \right. \tag{3.5}$$

Eq. (3.4) can be simplified to

$$\left[\nabla^2_{x,y} + k^2 - k_z^2\right] \left\{ \begin{array}{c} \mathbf{E} \\ \mathbf{B} \end{array} \right\} = 0. \tag{3.6}$$

The boundary conditions for the EM field at the ideal conducting boundary have to be taken into account: $E_{tang} = 0$ and $B_{norm} = 0$ where neither the electric field at the surface along the axis z nor the surface currents are allowed. If one encloses the infinite long waveguide at $z = 0$ and $z = d$, one gets the resonator of thickness d.

At this point we will select the components of the field parallel to the axis z (all the other components can be derived from them). The boundary conditions are written as

$$E_z(x,y,z)|_{Boundary} = 0, \qquad \frac{\partial B_z(x,y,z)}{\partial n}|_{Boundary} = 0. \tag{3.7}$$

In the z direction the condition $k_z = \frac{n\pi}{d}$ with $n = 0, 1, 2, \ldots$ has to be fulfilled as well. There are two classes of solutions: the transversal-electric (TE) and the transversal-magnetic (TM) modes. For both, respectively, one finds

$$\begin{aligned} B_z(x,y) &= \phi_B(x,y)\sin\left(\frac{n\pi z}{d}\right) \quad n = 1,2,3,\ldots, \quad E_z(x,y,z) = 0 \quad TE \\ E_z(x,y) &= \phi_E(x,y)\cos\left(\frac{n\pi z}{d}\right) \quad n = 0,1,2,\ldots, \quad B_z(x,y,z) = 0 \quad TM \end{aligned} \tag{3.8}$$

where $\phi_B(x,y)$ and $\phi_E(x,y)$ are scalar fields.

At lower frequencies $\nu < \nu_G = \frac{c}{2d}$ corresponding to the wavenumbers $k < \frac{\pi}{d}$, only TM modes with $n = 0$ ($k_z = 0$) appear whereas all the other modes are exponentially damped. Eq. (3.6) is reduced to

$$\left(\nabla^2_{x,y} + k^2\right)\phi_E(x,y) = 0 \tag{3.9}$$

with the Dirichlet boundary condition $\phi_E(x,y)|_{Boundary} = 0$. Thus, there exists a one-to-one correspondence between Eqs. (3.2) and (3.9) with the boundary conditions fulfilled as well. Due to this in the experimental studies of quantum billiards thin microwave cavities can be used instead of the quantum dots, which is experimentally realised in a simpler way. Studies of this type were initiated by H.-J. Stöckmann at the University of Marburg (Stöckmann and Stein, 1990).

3.3.2 Resonances

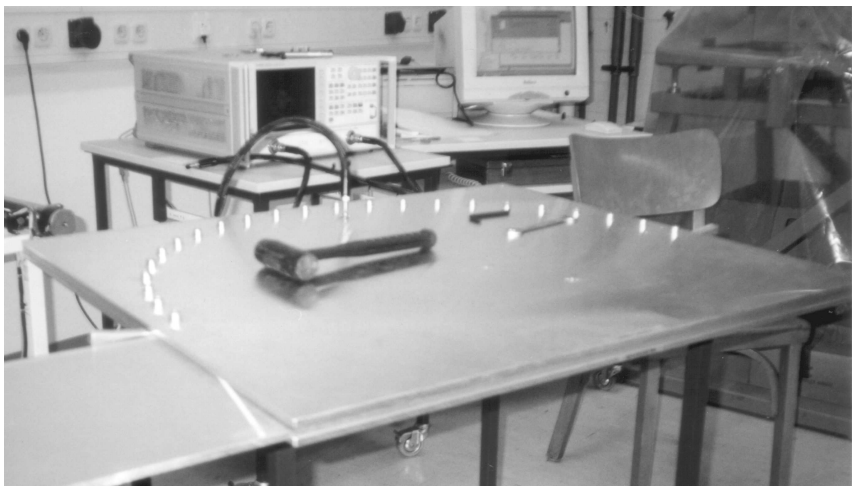

Figure 3.5: The measurement of the mushroom billiard resonances.

The eigenmodes were measured (Stöckmann, 1999) in such a way that the microwaves were fed into a resonator (Fig. 3.5) by means of an antenna which consists of a small wire with the radius $R_A = 0.2$ mm and which was introduced into the resonator through a small hole. The resonator with the thickness 8 mm was made of aluminium plates. Thickness was determined via the maximal possible frequency of microwaves, which was 18.61 GHz in this case. We measured in the range from 0.05 Ghz to the maximum in steps of 0.2 Mhz, so that about 93000 frequency points were treated in the end. In cases

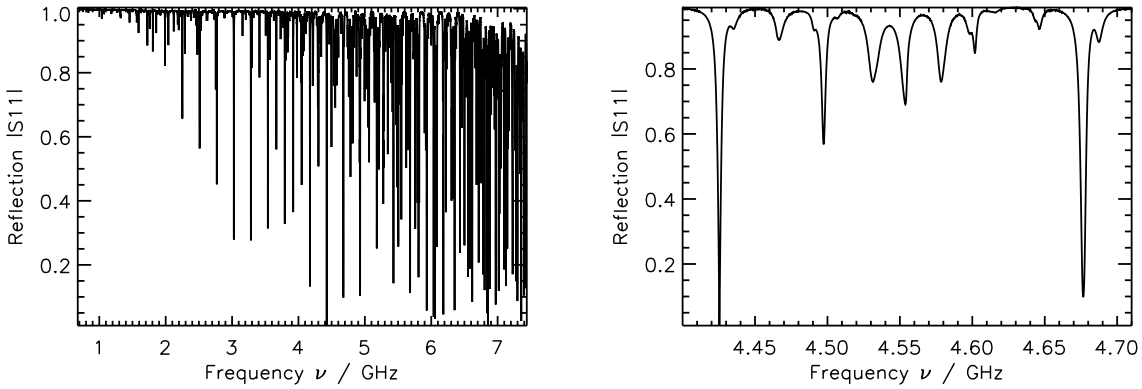

Figure 3.6: The absolute value of the reflection amplitude spectrum from Eq. (3.13). The mark '11' in $S11$ on the ordinate indicates that the waves are emitted and detected with the same antenna.

like the one presented the reflected microwave power is measured using the microwave bridge which separates the incoming and the outgoing waves, but various transmission measurements between two or more antennas can be employed as well.

The real and the imaginary part of the spectra have been measured with the help of Vector Network Analyzer by the company Agilent. The system has been calibrated with load, short and open standards. We have even performed the phase calibration to eliminate the antenna eigenfrequencies. Fig. 3.6 shows the absolute value of the measured reflection spectra of the mushroom billiard. Since energy is absorbed in the aluminium walls of the resonator at eigenfrequencies, each minimum in the reflected microwave power indicates an eigenmode.

The derivation in the previous subsection is exact only for ideal conducting walls of the resonator. In reality EM waves penetrate into the walls where they are damped due to the skin effect (Jackson, 1982). Thus, the energy loss in the walls causes the Lorentz broadening Γ_{0walls} of the resonances. The emitted electric scalar field at the frequency ν equals $\phi_E^{emitted}(t) = \phi_E(0)e^{-2\pi i\nu t}\Theta(t)$ which, in the vicinity of an eigenfrequency ν_0, after the reflection, transforms into $\phi_E^{received}(t) = S_0(\nu)\phi_E(0)e^{-2\pi i\nu t}\Theta(t)$. Here the $\Theta(t)$ is the Heaviside step function whereas $S_0(\nu)$ is the complex reflection amplitude for an isolated resonance, i.e.

$$S_0(\nu) = 1 - \frac{h_0}{\nu - \nu_0 - \Delta_0 + i\Gamma_0}, \tag{3.10}$$

where h_0 is the amplitude of the eigenfrequency while $\Delta_0 = \Delta_{0walls} + \Delta_0^A$ indicates its shift caused by the absorption in the walls and the coupling of the antenna with the resonator, so that the sum $\nu_0 + \Delta_0$ is the resonant frequency, i.e. the position of the Lorentzian in the spectrum. $\Gamma_0 = \frac{1}{\tau} = \Gamma_{0walls} + \Gamma_0^A$ is the width of the Lorentzian influenced by the walls and the coupling. [1] The higher the frequency, the stronger the coupling between the waves and the cavity; in such cases the (absolute) shifts and the widths increase as well. This results in (Stein et al., 1995)

[1] The index 0 is attached to the quantities of the isolated resonance. For the other resonances from the entire spectrum this index is replaced by the consecutive index j of the resonance.

$$\Delta_0^A = \Re(\alpha_0)|\psi_0(\mathbf{r})|^2 \qquad \text{and} \qquad \Gamma_0^A = \Im(\alpha_0)|\psi_0(\mathbf{r})|^2. \tag{3.11}$$

where α_0 is a complex coupling parameter which depends on the antenna shape as well as on the frequency of the microwaves, and $\psi_0(\mathbf{r})$ is the wavefunction at the antenna position $\mathbf{r}$.

How frequency increases in the coupling can be shown in the case of the ideal circular antenna with the radius R_A of the antenna which is much smaller than the wavelength $2\pi/k_0$ where one obtains (Stein et al., 1995)

$$\alpha_0 \approx \frac{2\pi}{\ln(k_0 R_A)}, \tag{3.12}$$

and $k_0 = 2\pi\nu_0/c$. This indicates that the shift Δ_0^A is negative and that its absolute value increases with the frequency whereas the Γ_0^A equals 0 (in this ideal case). Unfortunately (i) due to the non-ideal geometry of the antenna one does not obtain the α_0 values expected from the theory (ii) since the wavefunctions were not measured at all and (iii) since we cannot precisely determine the values for the shifts due to the absorption in the walls - presumably these values are small. This implies that the Δ_0 is a mere phenomenological parameter, so that by employing the fitting, one cannot determine the eigenfrequency ν_0 (which is our purpose) as precisely as if one used the analytic expression for the Δ_0 (Veble et al., 2000).

The resonant frequency ν_0 and the width Γ_0 of the Lorentzian are related via the resonator quality $Q = \frac{\nu_0}{\Gamma_0}$, which is usually between 10^3 and 10^4. This quality limits the total number of eigenfrequencies N_{max} (for a cubic cavity one gets $N_{max} = \frac{Q}{3}$) which can be determined experimentally. In our case N_{max} was about 600. The same experiments can be extended to the superconductive cavities (Gräf et al., 1992; Dietz et al., 2007) where quality factors up to 10^5 were obtained. These experiments result in a large number of extraordinarily sharp resonances.

If the nodal line of the wavefunction falls at the antenna position or if it approaches this position very closely, then resonances cannot be detected. One notices that if the resonances are measured only at one antenna position, the fraction of the missing resonances is quite large. For this reason we have measured and analysed the level dynamics (see Sec. 2.9) in order to determine where the levels expected are missing.

3.3.3 Harmonic inversion

If one wants to obtain useful information from the spectra, one has to determine the positions, the heights and the widths of the Lorentzians from (3.10) appearing in the spectra (see Fig. 3.6). A few years ago only the conventional fit procedure was used. In this procedure one first selects the starting parameters for each individual resonance and then one manually treats the entire spectrum to fit each individual resonance separately. This thesis employs a kind of automatization of the conventional fit, i.e the so-called harmonic inversion (HI) introduced in (Wall and Neuhauser, 1995) and improved in (Main et al., 2000).

The reflection amplitude spectrum (Fig. 3.6) is a superposition of the Lorentzians (Kuhl et al., 2008)

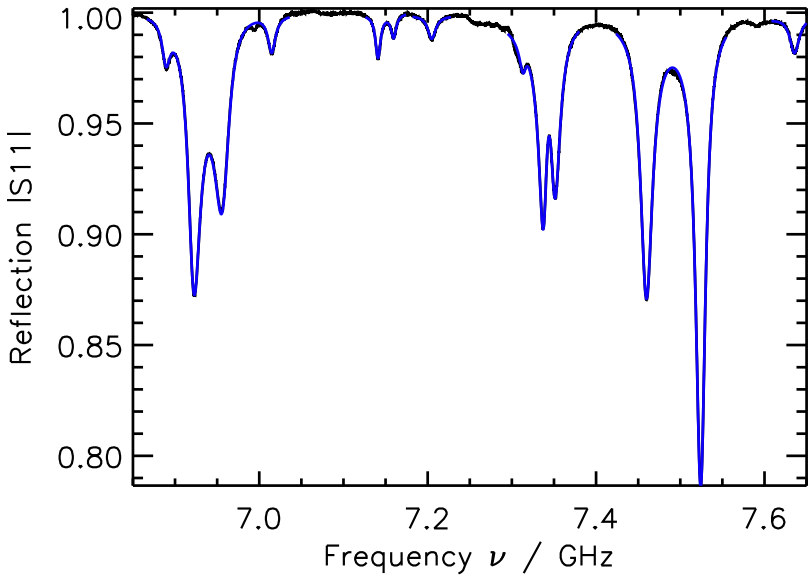

Figure 3.7: The harmonic inversion of a reflection spectrum: the rough spectrum (black) and harmonic inversion fit (blue). The two parameters for the harmonic inversion are $\Gamma_{max} = 60$ Mhz and $h_{min} = 0.005$. One can notice that there exists only a very slight difference between the signal and HI fit.

$$S(\nu) = 1 - \sum_j \frac{h_j}{\nu - \nu_j + i\Gamma_j} \tag{3.13}$$

for $\nu \geq 0$, and $S(\nu) = 0$ for $\nu < 0$, where h_j is the height, Γ_j the width and ν_j is the resonant frequency including the shift, and j in principle runs over all the resolvable resonances up to N_{max}. We have actually only evaluated a window of about $N_{HI} = 20$ resonances at once and, then, the solutions were glued together. If one decides to apply the HI technique, the spectrum from Eq. (3.13) has to be transformed to the time domain via the Fourier transform

$$\hat{S}(t) = \frac{1}{2\pi} \int_{-\infty}^{\infty} S(\nu)\, e^{-2\pi i(\nu_j - i\Gamma_j)t} d\nu = \delta(t) - \sum_j h_j\, e^{-2\pi i(\nu_j - i\Gamma_j)t} \tag{3.14}$$

for $t \geq 0$, and $\hat{S}(t) = 0$ for $t < 0$, with the amplitude h_j and the complex frequency $\nu_j - i\Gamma_j$ from the j-th state.

Since the measured data are presented in a discrete form, the second term of expression (3.14) has to be rewritten in a discrete form as well, which results in a system of nonlinear equations

$$\hat{S}(k\tau) = 1 - \sum_{j=1}^{N_{HI}} h_j\, e^{-2\pi i(\nu_j - i\Gamma_j)k\tau} = 1 - \sum_{j=1}^{N_{HI}} h_j\, z_j^k \qquad k = 0, 1, \ldots, 2N_{max} - 1. \tag{3.15}$$

Since we would like to solve the system for $z_j = e^{-2\pi i(\nu_j - i\Gamma_j)\tau}$ and h_j, we will apply the stable Decimated Linear Predictor method (Main et al., 2000). Normally one obtains a much greater number of solutions than the estimated number of eigenvalues in this window region represented by the Weyl formula (see the next section). If one wants to avoid the spurious solutions, one has to select the maximal suitable width Γ_{max} and the minimal suitable height h_{min} of the resonances. Then, one moves one time step τ to the left and recalculates the HI. Thus, one estimates the error and decides which calculated resonances are appropriate and which have to be rejected. The error has to be below a previously estimated value Err_{max}. One should emphasise, that (**i**) a cut-off of the modulus square $|\hat{S}(t)|^2$ of the Fourier transform has been employed, so that the constant background can be eliminated (Kuhl et al., 2008) and, (**ii**) the border of the window has not been taken into account due to the problems that could arise. We have used the procedure, which was implemented by R. Höhmann (Höhmann, 2004). Fig. 3.7 shows the reflection spectrum and its corresponding HI fit which only slightly differ from one another.

The advantages of the harmonic inversion are:

- The parameters of the Lorentzians can be determined for many resonances simultaneously even if these strongly overlap with each other, which, for example, happen when the width is 10 times larger than the mean resonance spacing, as recently presented in (Kuhl et al., 2008);
- The procedure is stable, so it can be applied to many data;
- No starting points are needed for this procedure. The determination of the starting points in the case of overlapping resonances is a big disadvantage of the conventional fit procedure. Therefore, HI can be applied in higher frequency region.

There are also certain disadvantages to the harmonic inversion such as:

- There appear certain the deviations if one tries to determine the pole positions in cases where two neighbouring resonances lie very close to one another and their amplitude is very large. Deviations also emerge with small resonances;
- The optimal filter parameters Γ_{max}, h_{min} and Err_{max} depend on the spectrum, so one has to select such parameters that one eventually obtains as many desired resonances as possible;
- There are some unresolved (about 15%) and a few redundant resonances. Therefore, after the calculation one has to check the entire spectrum and, additionally, fit the missing resonances by applying the conventional fit procedure and eliminate all the redundant ones.

3.4 Level Statistics

As soon as one has calculated the eigenfrequencies ν_j of the microwave billiard, one has already obtained the eigenenergies E_j of the corresponding QM system: $E_j = \frac{\hbar^2}{2M}k_j^2 = \frac{4\pi^2}{c^2}\nu_j^2$. At this point one should emphasise again that in microwave billiards the eigenfrequencies are systematically shifted to the left, i.e. microwave eigenvalues are slightly smaller than the QM ones (Stein et al., 1995).

Here we will consider the total number of states $N(E)$ of a 2D quantum billiard system below the energy E. This function is termed the spectral staircase function and it fluctuates about its average value $\langle N(E)\rangle$, which only depends on the area A, on the circumference L, on the curvature and on the edges of the billiard K. This dependence is represented by the generalised Weyl formula

$$\langle N(E)\rangle = \frac{1}{4\pi}\left(AE - L\sqrt{E}\right) + K. \tag{3.16}$$

If one wants to compare the fluctuations $N_{fluc} = N(E) - \langle N(E)\rangle$ in the regions with different $\langle N(E)\rangle$, one has to unfold the spectrum first, i.e. the spectrum has to be transformed in such way that the average density of states remains the same for all the states treated. e can be defined as $e \equiv \langle N(E)\rangle$ so that $N(e) = e + N_{fluc}(e)$, which means that the mean level spacing of $N(e)$ equals 1. The unfolded energy levels e_j are subject to the statistical analysis where the level spacing distribution $P(S)$, which was already discussed in Chap. 2, is chosen as the main statistical measure.

3.4.1 Level dynamics

If one wants to measure level dynamics, one has to change the parameter of the system and observe how its eigenvalues behave during the changes. In the experiment presented the position of the foot b was moved in 1 mm steps from the central to the outermost right position.

The motion of the energy eigenvalues, employed as a function of an external parameter, resembles the dynamics of the particles of a one-dimensional gas with the repulsive interaction (Pechukas, 1983; Yukawa, 1985; Stöckmann, 1999). Like in particle dynamics there also exists a conservation law for the eigenvalues employed as a function of an external parameter. The lower plot in Fig. 3.8 is obtained from the numerical calculation (described in detail in Sec. 3.5) where almost all the eigenvalues connect into the so-called spaghetti (Barth et al., 1999) appear. If, on the other hand, one measures the eigenfrequencies experimentally with only one antenna, spaghetti are broken due to the missing resonances (upper plot of Fig. 3.8) since the antenna hits the nodal lines of the wavefunctions. In the experiment presented here 37% of the resonances are missing. We believe that the missing resonances are randomly, not systematically, distributed. But there are no missing spaghetti, so one can identify the neighbouring eigenvalues, which is absolutely necessary if one wants to calculate the level spacing distribution. In this way the experiment is fully autonomous and it does not depend on the numerics.

Although the position of the foot of the mushroom billiard constantly changes, the total area and the circumference always remain constant, so all the spectra have the same mean density and the number of levels represented in Eq. (3.16). One can also notice that certain spaghetti are represented as mere straight lines up to a certain parameter value and as 'wavy' lines as soon as the parameter value is exceeded. Up to that parameter value these levels correspond to the regular levels. All the 'wavy' spaghetti correspond to the chaotic levels. Some straight-lined spaghetti are long whereas the others are short. This can be explained in terms of the radial quantum number n of the semicircle which counts the number of 'hills' of the absolute square of the wavefunction in the radial direction. The same quantum numbers can be attributed to the regular wavefunctions as well. Thus, the regular wavefunctions with smaller n (and larger m) 'survive' longer if one changes

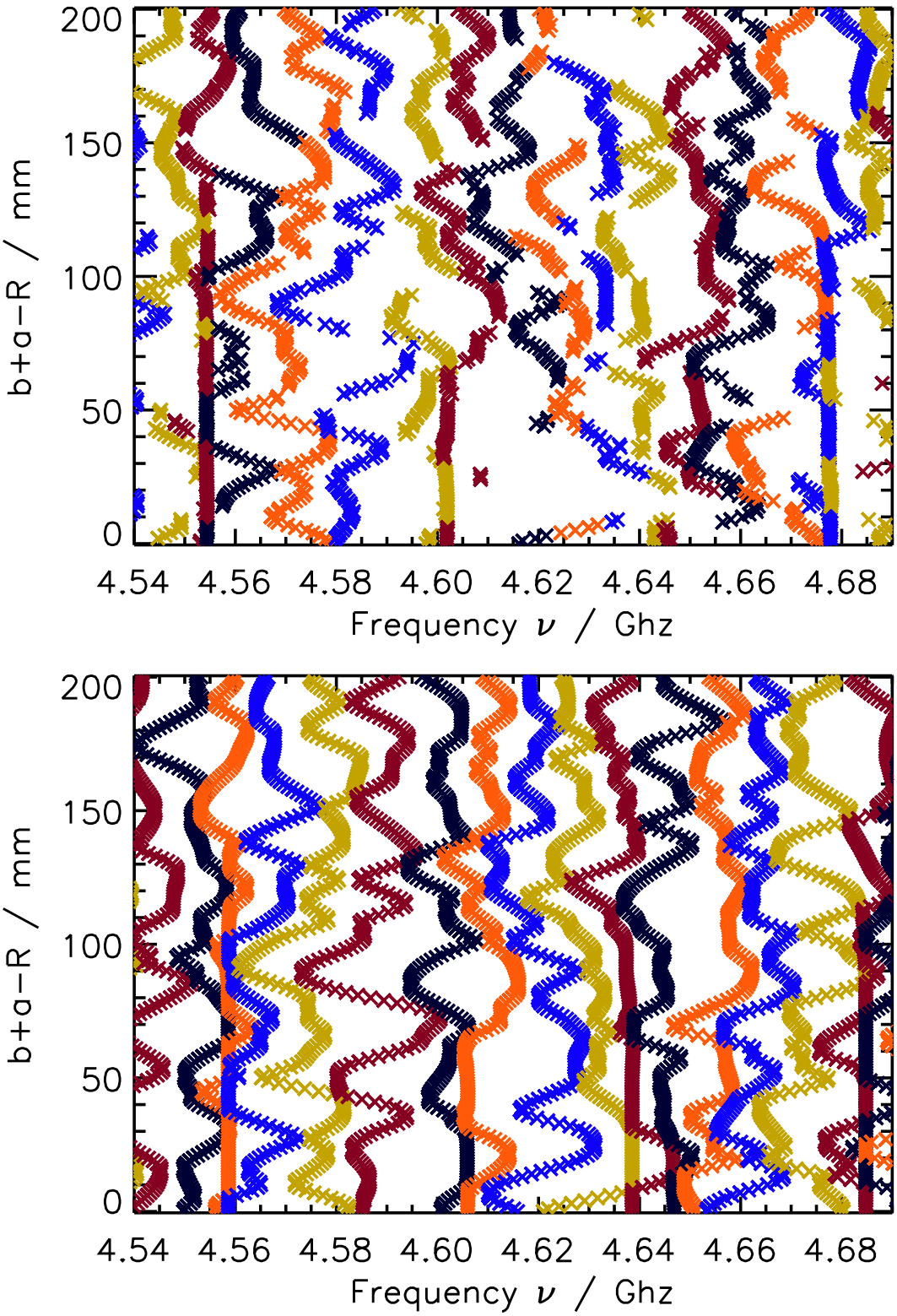

Figure 3.8: The microwave mushroom billiard levels from Fig. 3.1 with the foot moved in 1 mm steps. The radius of the semicircle equals $R = 400$ mm, which is the same as the diameter $2a$ of the foot where the depth $l = 100$ mm. There are 200 different positions from the central to the outermost right position. For the sake of better comparison the units in numerical plot are the same as the ones from the experimental plot although these are not real units in numerical calculations. All the details are explained in the text.

the position of the foot, which is due to the fact that these functions mainly 'live' in the vicinity of the border of the semicircle (see Fig. 3.3).

One has to admit that in level dynamics there also appear the misconnections, so one can wrongly determine the neighbouring eigenvalues. But this error is not as frequent as the eigenvalues disappearing from a single spectrum.

3.4.2 The level spacing distribution - comparison with the RMT prediction

Fig. 3.9 compares the mushroom experimental spectra (Fig. 3.8) with the RMT prediction treated in Chap. 2. One notices that the best fitting Gaussian model for P_{DBR}^{An} is very suitable for the experimental data. Similarly, the best fitting exponential model is of comparable quality. In both cases σ appears as the only fitting parameter whereas ρ is determined by classical dynamics.

For each experimental spectral data we have used 21 configurations by employing equidistant positions of the foot around the central values $b + a - R = 10$ mm (the upper plot) and 30 mm (the lower plot). For each configuration we have used the spectral stretches in the interval of 100-300 consecutive levels. The parameter ρ for these configurations varies up to $\pm 7.5\%$ (the upper plot) and $\pm 8.5\%$ (the lower plot) around the central values indicated in the plots. In the experimental spectra the level spacing distribution is affected by an antenna and by tunneling as well although, experimentally, the two effects cannot be separated. For the Fig. 3.9 we have chosen the best fitting plots although the curve may not fit so well in certain cases. One can, thus, conclude that this experiment, in fact, well agrees with our theory although it does not confirm it completely.

3.4.3 Absorber in the foot

As evident from Fig. 3.2 the classical chaotic orbits enter the foot whereas the regular ones remain outside of it. Due to this the regular and the chaotic eigenvalues can be separated by the microwave experiment. This can be achieved if a carbonate absorber is inserted into the bottom of the foot (Fig. 3.10). Thus one creates an open system, which absorbs the energy, so that the chaotic eigenstates disappear in the end. We have qualitatively obtained the expected results, i.e. the chaotic states are mainly absorbed whereas the regular ones remain intact (Fig. 3.11).

3.5 Expanded boundary integral method

We have calculated the numerical eigenvalues from Eq. (3.2) by using the expanded boundary integral method (EBIM), developed in (Veble et al., 2007) and based on the classical boundary integral method (BIM) described in (Bäcker, 2003). With the help of these two references one can describe the basic characteristics of the method. The method is general, so it can be applied to any billiard shape (which is its greatest advantage) although it is rather slow (which is its greatest disadvantage).

Eq. (3.2) can be represented by the k form:

$$(\nabla^2 + k^2)\psi(\mathbf{q}) = 0, \tag{3.17}$$

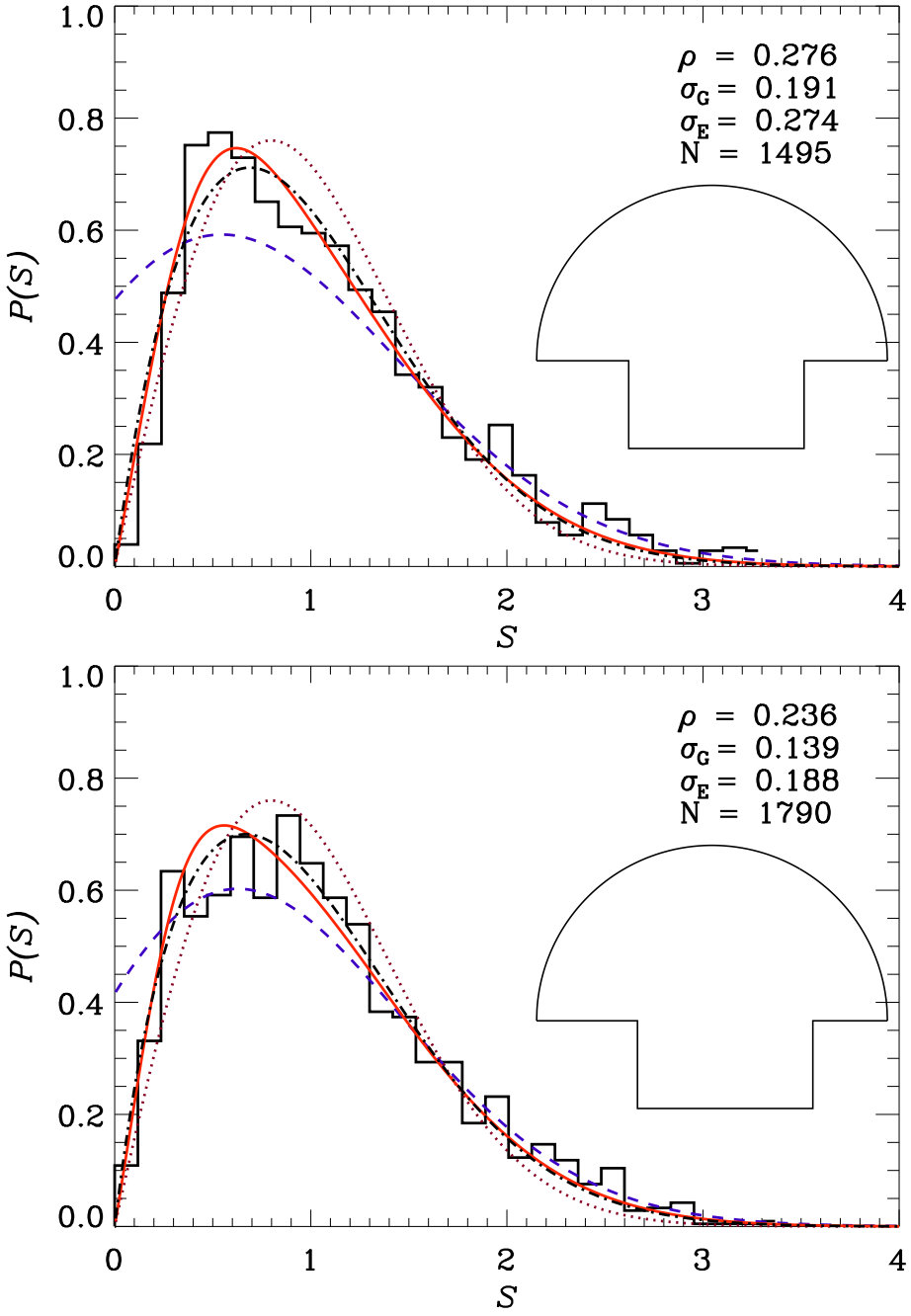

Figure 3.9: The comparison between the experimental data (histogram) and the best fitting theoretical curves for P^{An}_{DBRN}: The solid red curve represents the Gaussian model, the dash-dotted black curve indicates the exponential model, the dashed blue curve is the BR distribution (with the same ρ) whereas the dotted brown curve represents the Wigner distribution. σ_G and σ_E are the best fitting values of σ for the Gaussian and the exponential model respectively. N is the number of objects in the histogram. The experimental configuration is discussed below.

with $k^2 = E$ where the natural units $2M = \hbar = 1$ have been used. One can represent the wavefunction inside the billiard region $\mathcal{D} \setminus \partial\mathcal{D}$ by its normal derivative $u = \frac{\partial}{\partial n}\psi$ at the boundary $\partial\mathcal{D}$ (see Eq. (3.21)) where u must obey the integral equation

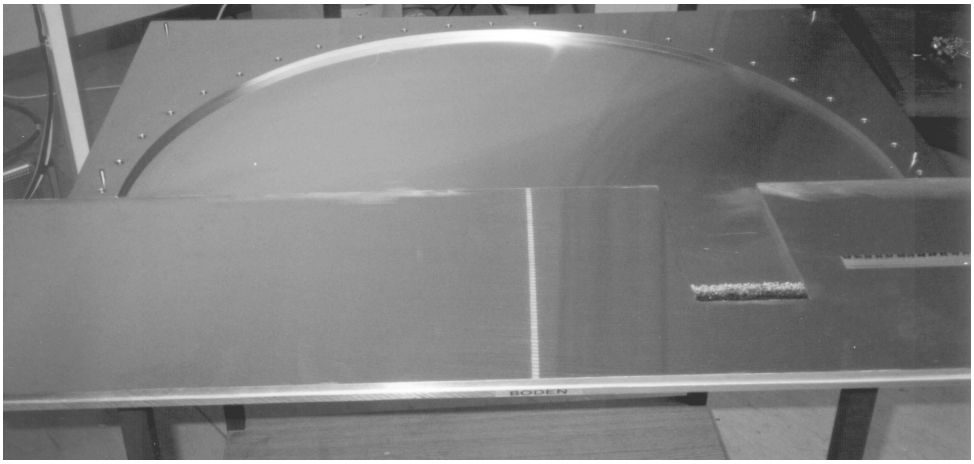

Figure 3.10: The experimental mushroom billiard with the absorber positioned at the bottom of the foot.

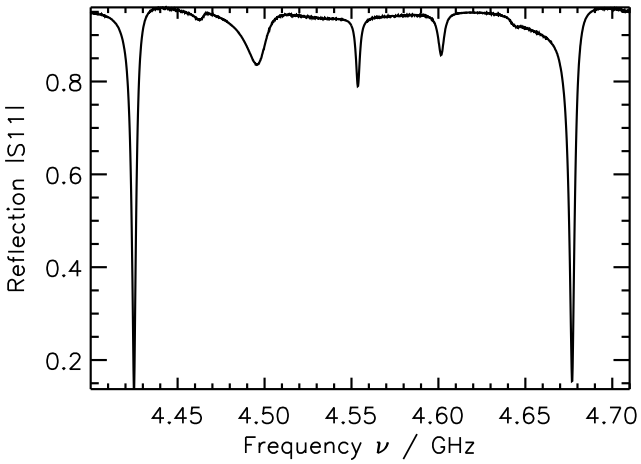

Figure 3.11: One part of the reflection microwave spectrum of the open mushroom billiard measured with the absorber. The same part of the spectrum is shown in the right plot of Fig. 3.6 for a closed system. The remaining resonances represent the regular resonances from the closed system.

$$u(s) = -2 \oint_{\delta\mathcal{D}} \frac{\partial}{\partial n} G_k(\mathbf{q}(s), \mathbf{q}(s')) u(s') ds'. \tag{3.18}$$

Here s denotes the arc-length parameter of the boundary whereas $\mathbf{n}$ represents the outward pointing normal vector and $\frac{\partial}{\partial n} G_k(\mathbf{q}, \mathbf{q}')$ the normal derivative of the Green function for the inhomogeneous case: $(\nabla^2 + k^2) G_k(\mathbf{q}, \mathbf{q}') = \delta(\mathbf{q} - \mathbf{q}')$. For the Green function one selects the complex Hankel function of the first kind: $G_k(\mathbf{q}, \mathbf{q}') = -i/4\, H_0^{(1)}(k|\mathbf{q} - \mathbf{q}'|) = -i/4\, (J_0(k|\mathbf{q} - \mathbf{q}'|) + i\, N_0(k|\mathbf{q} - \mathbf{q}'|)$.

One may discretise Eq. (3.18) on a finite set of points as determined by their arc-length parameters s_i which results in

$$[\mathbf{A}(k)\mathbf{u}]_i = \sum_j A_{ij}(k)u_j = 0. \tag{3.19}$$

where u_j is the value of the normal derivative at the point $\mathbf{q}(s_j)$. If there are corners at the boundary, the $\mathbf{q}(s_j)$ should not be positioned at the very corner otherwise the u_j could not be defined. [2] $A_{ij}(k)$ is a complex non-Hermitian matrix

$$A_{ij}(k) = \begin{cases} l_i\left(1 - \frac{l_i\kappa_i}{2\pi}\right), & i = j \\ \frac{ikl_il_j}{2}H_1^{(1)}(k\tau_{ij})\cos\phi_{ij}, & i \neq j \end{cases}, \tag{3.20}$$

where $\tau_{ij} = |\mathbf{q}(s_i) - \mathbf{q}(s_j)|$ is the distance between the points $\mathbf{q}(s_i)$ and $\mathbf{q}(s_j)$, $\cos\phi_{ij} = \mathbf{n}(s_i)\cdot(\mathbf{q}(s_i) - \mathbf{q}(s_j))/\tau_{ij}$ represents the angle between the normal $\mathbf{n}$ at the point $\mathbf{q}(s_i)$ and the distance vector between the two points whereas κ_i is the boundary curvature at the point $\mathbf{q}(s_i)$ which is defined in such a way that the convex parts of the boundary are indicated by the positive curvature, so that, for example, $\kappa_i = 1$ for the circle with the radius one. The arc-length parameter of the boundary section, which is centered at $\mathbf{q}(s_i)$, is denoted by l_i. The discretisation is characterised by the parameter $B = 2\pi N_p/(kL_b)$ where N_p is the number of the discretisation points whereas L_b is the total length of the billiard boundary. The parameter B indicates the number of discretisation points per wavelength; in our calculations $B = 12$ has been used.

The solutions of Eq. (3.19) provide suitable approximations for the eigenvalues ks and the eigenvectors $\mathbf{u}$s. From the latter, if necessary, the wavefunctions inside the billiard at a point $\mathbf{q} \in \mathcal{D} \setminus \partial\mathcal{D}$ can be calculated via the integration

$$\psi(\mathbf{q}) = \frac{1}{4}\oint_{\delta\mathcal{D}} Y_0(k|\mathbf{q} - \mathbf{q}(s)|)u(s)ds. \tag{3.21}$$

Now one has to solve Eq. (3.19). There are several possibilities for this; usually one tries to find the zeros of the determinant $det(\mathbf{A}(k))$, although, typically, certain levels, especially those close to degeneracy, disappear in this case. This problem can be solved by expanding the matrix $\mathbf{A}(k)$ in the Taylor series around a chosen reference value k_0 (Veble et al., 2007), so that one can determine the solution(s) k close to the reference value: $k = k_0 + \delta k$ where δk must be small. From the Eq. (3.19) one obtains

$$\left[\mathbf{A}(k_0) + \delta k\mathbf{A}'(k_0) + \frac{(\delta k)^2}{2}\mathbf{A}''(k_0) + \ldots\right]\mathbf{u} = 0, \tag{3.22}$$

where $\mathbf{A}'(k_0)$ and $\mathbf{A}''(k_0)$ are the first and the second derivative of the matrix $\mathbf{A}$ with respect to the k at the point k_0 which is obtained by calculating the derivatives of each matrix element. If only the first two terms on the left side are selected, one obtains the generalised eigenvalue problem

$$\mathbf{A}(k_0)\mathbf{u}_0 = -\delta k_0\mathbf{A}'(k_0)\mathbf{u}_0, \tag{3.23}$$

where $\mathbf{u}_0$ and δk_0 are the first orders of the expansions of $\mathbf{u}$ and δk respectively. In the case of the mushroom billiard the accuracy of Eq. (3.23) is, numerically, one order of magnitude higher than expected: if k_0 varies about the final solution, the eigenvalues

[2] The convex corners were treated in (Okada et al., 2005) by changing the starting Eq. (3.18).

from Eq. (3.23) are the third order polynomial in δk as opposed to the general second order polynomial that was expected.

Thus, Eq. (3.23), which was selected in the end, is very suitable in this case. After solving it, one has to decide which δks are good solutions. Larger δks are rejected since they do not agree with the starting assumption of the expansion. Each diagonalisation is characterised by a number of good solutions which also depend on the accuracy desired. In our calculation of the mushroom billiard from the ground state up to $k^2 = 5000$, there appear up to 3 appropriate eigenvalues per diagonalisation. While the accuracy of the method is of the third order in δk_0 (see Eqs. (3.22, 3.23) and the text below Eq.(3.23)) and the mean level spacing is proportional to $1/k_0$, we have chosen the steps of $\Delta k_0(k_0) = 0.05(\frac{k_0}{k_{0\,Start}})^{-1/3}$, so that similar errors in the units of the mean level spacing appear across the entire region of the calculation. Such a step dependence $\Delta k_0(k_0)$ might not be crucial and the constant $\Delta k_0 = 0.05$ would probably not be so inappropriate, but it was used and it applied well in (Veble et al., 2007) in the case of the Monza billiard, so we decided to use it for the mushroom billiard as well.

In the non-convex geometry the BIM can provide exterior solutions for the Neumann boundary conditions as well although this did not happen when EBIM was employed in the calculation of the mushroom billiard levels. If one wants to check the results roughly, one has to apply the Weyl formula and observe the difference $N(E) - \langle N(E) \rangle$ which should oscillate around zero. If there are too many or too few eigenvalues, $N(E) - \langle N(E) \rangle$ has a jump up or down, which immediately indicates that an eigenvalue is redundant (spurious) or that it is missing. In such cases one focuses on the critical region and repeats the calculation. Usually the shift in initial value k_0 suffices, so that one manages to obtain a missing level or eliminate a redundant one.

3.5.1 Corners and the accuracy of EBIM

The method and its accuracy have been tested on the 3/4 circle billiard with $R = 1$. The results of the comparison between the numerical and the exact (analytic) solutions are shown in Fig. 3.12 where the upper right plot corresponds to the equidistant points around the boundary. One can notice that the errors in units of the mean level spacing are not small. Since in our EBIM the boundary points must not be located at the corners, we believe that corners are the most important source of the errors. For all the corner, which are rational fractions p/q of π any eigenfunction can be expanded into a convergent series of the Fourier-Bessel functions

$$\psi(r,\theta) = \sum_{i=1}^{\infty} a_i J_{\frac{q\,i}{p}}(k_i r) \sin\left(\frac{q\,i}{p}\theta\right), \tag{3.24}$$

where r and θ are the polar coordinates starting at the corner whereas a_i are the expansion coefficients. If one expands the Bessel functions $J_{\frac{q\,i}{p}}(k_i r)$ for small r values (i.e. around the corner), one obtains $J_{\frac{q\,i}{p}}(k_i r) \propto r^{\frac{q\,i}{p}}$, which indicates the following: the smaller the exponent $\frac{q}{p}$, the larger the value of the $\psi(r,\theta)$ for small r values. The 3/4 circle is characterised by two $\pi/2$ corners and by a single $3\pi/2$ corner. Around the latter the wavefunction are larger which, consequently, influences the results in a larger extent than the $\pi/2$ corners. For this reason the points were condensed around the $3\pi/2$ corner; first with a 3 times larger constant density from the corner in the interval up to $0.2\,R$. Due

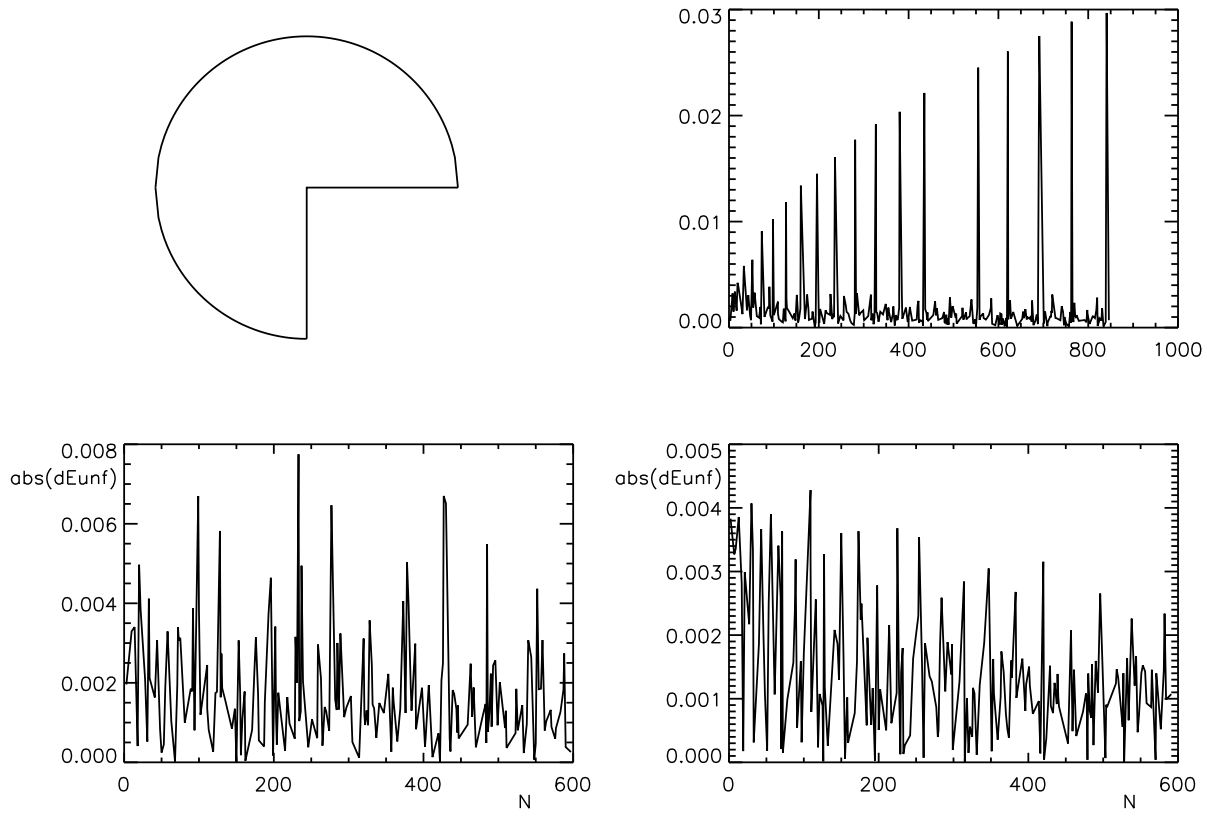

Figure 3.12: $|dEunf| = \left|\left\langle N(E_j^{numerics})\right\rangle - \left\langle N(E_j^{theory})\right\rangle\right|$ - eigenvalue errors numerically obtained for the 3/4 circle compared with the theoretical (zeros of Bessel functions) for the 1/4 circle (only) in units of the mean level spacing. The quantities in the upper right plot are the same as in the lower two plots. The Ns on the abscissa (alone in this plot) correspond to the consecutive indices js of the eigenvalues of the 3/4 circle. All the details are explained in the text.

to this, the results shown in the lower left plot of Fig. 3.12 are largely improved. If one increases the density of points, the calculation requires more time. Bearing in mind both the accuracy and the CPU time we have decided to employ a denser mesh of points by a factor 1 to 4 which linearly increases over an interval of length $0.4\,R$ away from the corner (the lower right plot from Fig. 3.12); the same procedure was followed in the case of the mushroom calculations as well.

Fig. 3.13 shows the first 9 lowest eigenstates of the mushroom billiard whereas Fig. 3.14 represents a few excited eigenstates with their regular, nonlocalised and localised chaotic (bouncing-ball or scarred) wavefunctions. In the upper plot from Fig. 3.15 one notices the difference between the eigenvalues calculated for $B = 12$ and those calculated for the three times larger $B = 36$ (for $l = a = \frac{10}{19}R$). Almost all the eigenvalues increase as soon as one applies a larger number of discretisation points per wavelength. The largest absolute difference is 0.0122 whereas the mean absolute difference equals 0.0023. The lower plots from Fig. 3.15 represent the eigenstates with the largest difference; one can see that the $3\pi/2$ corner is still problematic since these wavefunctions have large amplitudes around it.

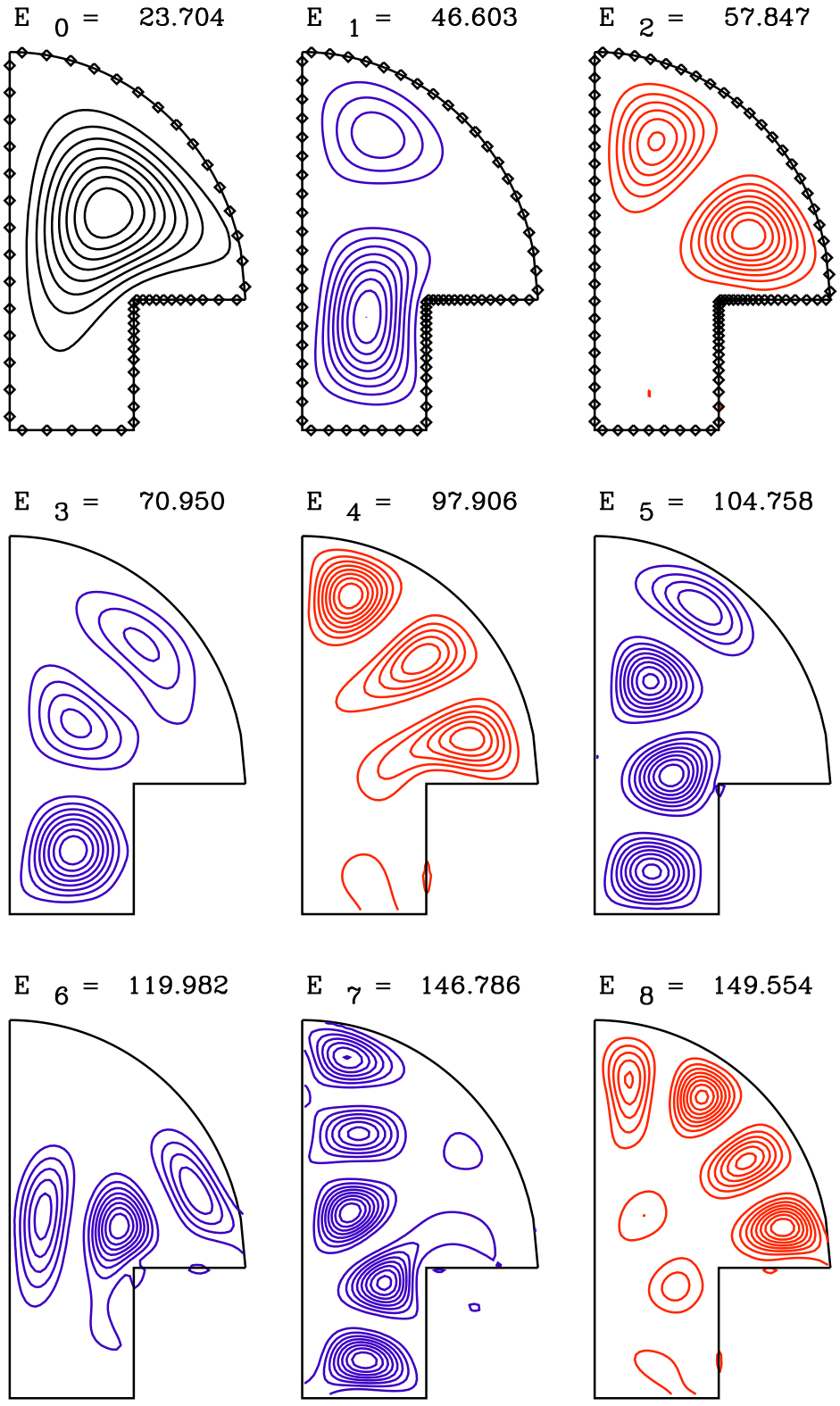

Figure 3.13: The lowest 9 wavefunctions of the mushroom billiard calculated with EBIM ($l = a = \frac{10}{19}R$). The regular states are red, the chaotic ones are blue whereas the ground state is black. The probability density with 8 equidistant contours from 0 up to the maximal value is plotted. The upper three plots also show the boundary points.

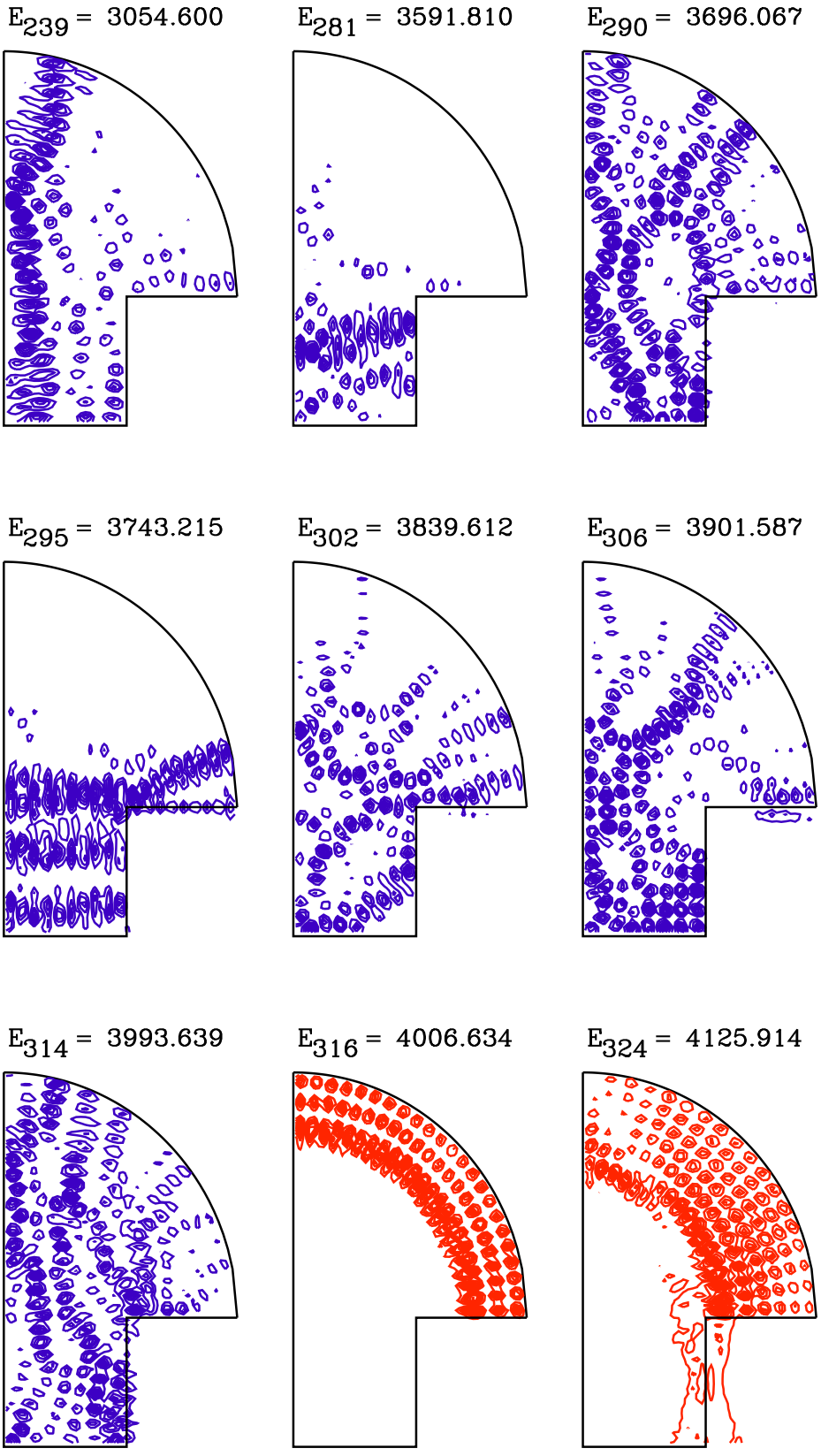

Figure 3.14: The same as Fig. 3.13, but here 9 higher exited states are represented.

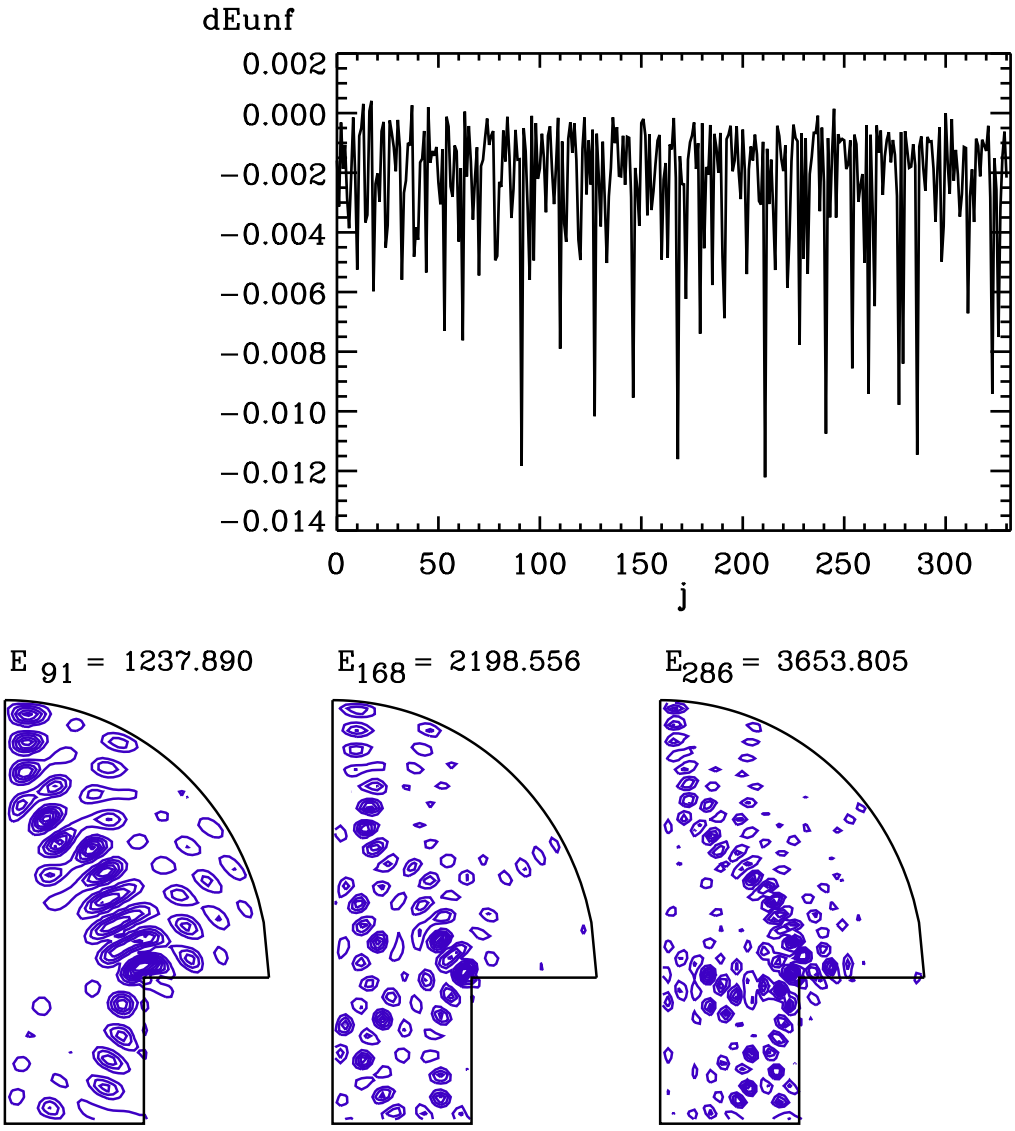

Figure 3.15: The upper plot: $dEunf = \left\langle N(E_j^{B12}) \right\rangle - \left\langle N(E_j^{B36}) \right\rangle$ - the difference between the numerically obtained eigenvalues for the mushroom billiard with the configuration $l = a = \frac{10}{19}R$ for two different numbers of discretisation points per wavelength, i.e. for $B = 12$ and for $B = 36$. The lower plots: the eigenstates with the largest eigenvalue errors.

In the next step all the eigenvalues with the difference ≥ 0.009 were tested one more time, with the six times bigger $B = 72$, which resulted in the maximal difference 0.0152. Bearing in mind all this the maximal numerical error of the calculation for $B = 12$ was estimated to **0.02** of the mean level spacing. One should be aware that this is the largest possible error whereas the mean error is more than 5 times smaller.

3.5.2 Level dynamics - increasing the depth l

In addition to level dynamics described in Subsec. 3.4.1 we have calculated another one, i.e. by deepening the foot of the mushroom billiard. This method is better since the regular eigenstates do not disappear in this case, which is indicated by a full-length

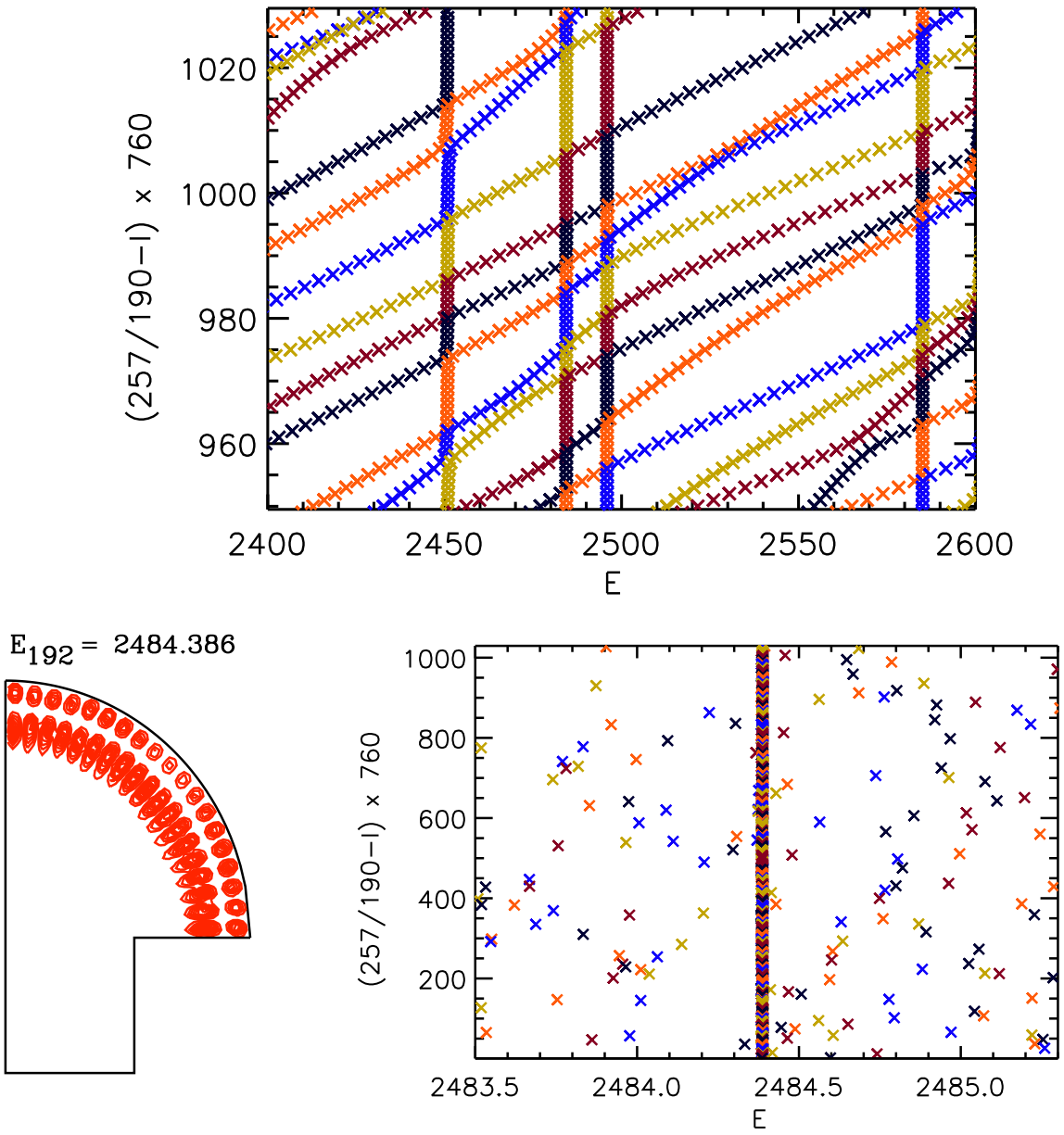

Figure 3.16: The numerically obtained levels for the central ($b = R-a$) desymmetrised mushroom billiards with the foot depth l increasing in steps of $\Delta l = 1/760 \approx 0.00139$. The radius of the semicircle is $R = 1$, the width $a = 10/19 \approx 0.526$. There are 1029 different positions, beginning with $l = 0$ and continuing equidistantly up to $l_{max} = 257/190 \approx 1.35263$. The energy $E = k^2$ is presented on the abscissa whereas the parameter, linearly dependent on the depth of the foot l, appears on the ordinate. The lower right plot represents the level dynamics around one regular state (showed in the lower left plot) for all possible parameter variations; the regular state is, in this case, surrounded by a cluster of chaotic levels.

vertical straight lines in the level dynamics plots (Fig. 3.16). This level dynamics was also presented by our second experiment which is described and used in Subsec. 3.7.2, although the experimental eigenvalues have not been connected into the spaghetti.

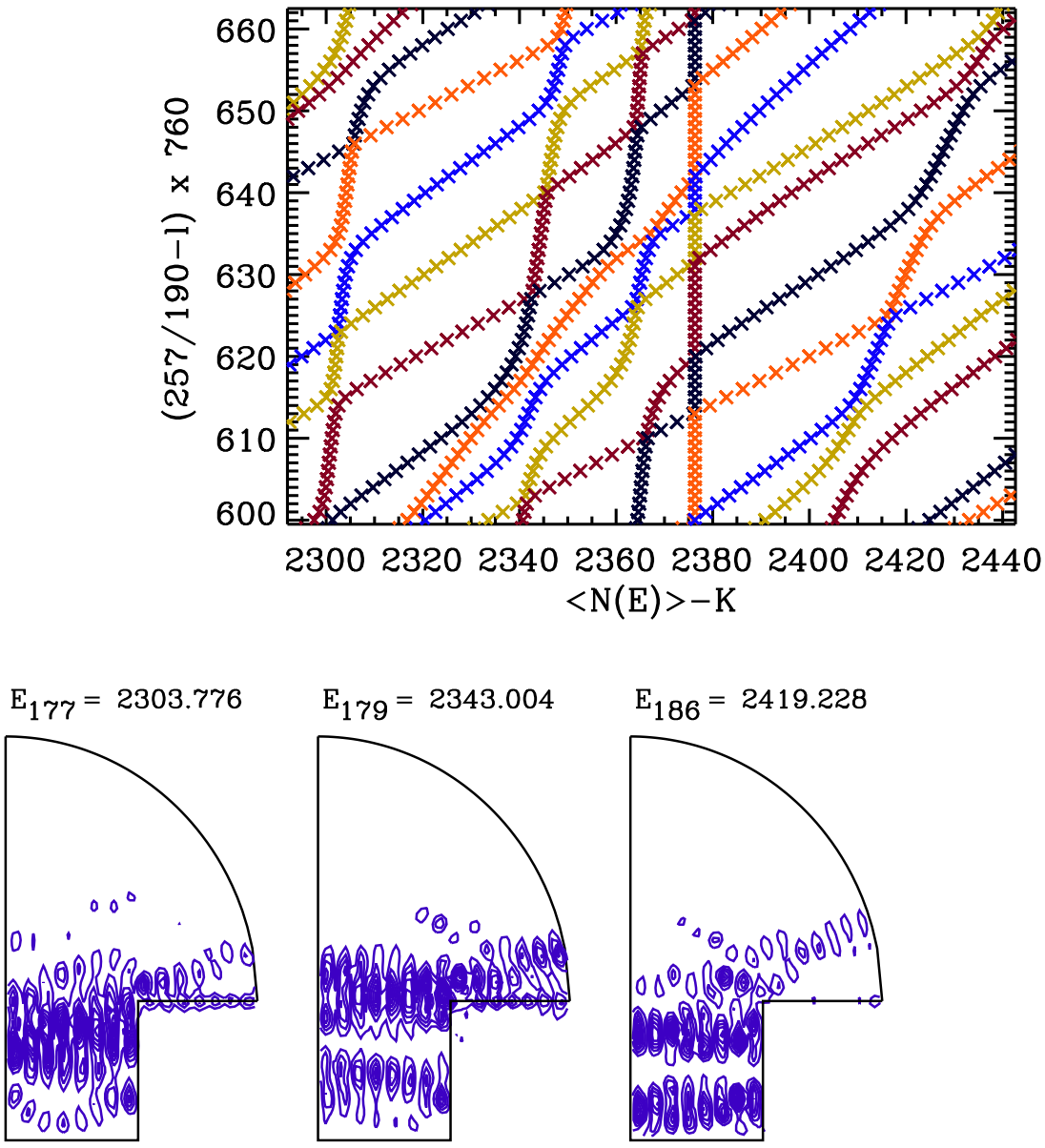

Figure 3.17: The upper plot: level dynamics showing the bouncing-ball states as bent, vertical structures. The lower plot: three bouncing-ball states for the parameters $l = a = \frac{10}{19}R$.

First, the eigenvalues were calculated for $l = l_{max}$ in each small interval Δk_0. In the next configuration with $l = l_{max} - \Delta l$ (where Δl indicates the step size), the eigenvalues from the previous step were used as initial eigenvalues. One can repeat this procedure until $l = 0$ is reached. Due to the decreased level density the eigenvalues were even shifted appropriately since, on average, the eigenvalues of the next configuration are larger than those from the previous one. In this way we have managed to improve our calculation to such an extent that it became faster by a factor of about 4.

At this point one should briefly mention the so-called bouncing-ball states which also appear in our system (the lower plots of Fig. 3.17). These states are localised along the classical parabolic periodic orbits. Contrary to the regular states their eigenvalues are

represented by bent vertical 'lines' (structures) in the level dynamics plot (the upper plot in Fig. 3.17), which indicates that they are not as strong as the regular states, but that they are, in fact, stronger in some positions and weaker in the others - this depends on the position of the foot of the mushroom billiard since these eigenstates may also be localised outside the foot. There exists a correlation between the slope of these vertical 'lines' and the strength of the bouncing-ball modes, i.e the stronger (or purer) a bouncing-ball mode the more vertical the corresponding 'line' in the level dynamics plot. We have also seen some scarred eigenstates (the upper left plot from Fig. 3.14) which are localised along the classical hyperbolic orbits and whose 'lines' in the level dynamics plot, as expected, are much more bent than the 'lines' indicating the bouncing-ball states.

3.5.3 The level spacing distribution - comparison with the RMT prediction

Figs. 3.18 - 3.22 show the results of the comparison between the mushroom numerical spectra (Fig. 3.16) and the tunneling RMT prediction treated in Chap. 2. One notices that the best fitting Gaussian model for P_{DBR}^{Tn} appropriately describes the numerical data. Similarly, the best fitting exponential model is suitable in this case as well. In both cases σ is the only fitting parameter whereas ρ is determined by classical dynamics.

We have employed sequential levels from j_{min} to j_{max} for 101 geometrical configurations of the equidistantly varied parameter l in steps of $\Delta l = 1/760 \approx 0.00139$ around the central position l_0. The parameter ρ for these configurations varies only up to 4% around the central value indicated in each plot.

The lower plot from Fig. 3.22 represents the enlarged interval for small S. Due to the numerical error 0.02 of the mean level spacing (see Subsec. 3.5.1) the histogram in the interval $S = [0, 0.04]$ is not reliable. Figs. 3.18 - 3.22 prove that the numerical histograms well agree with the best fitting theoretical curves describing the tunneling effects from Chap. 2. But in order to confirm the theory even more stronger, one should improve it and one should also obtain more precise numerical results for $S \Rightarrow 0$.

3.6 Avoided crossings

The narrowly avoided crossings, where ΔE indicates the separation at the closest approach (splitting), are especially interesting. Such crossings, for example, appear in the study of atomic systems perturbed by external fields, in the molecular systems employed as a function of the internuclear distance, etc.

Let us consider the level dynamics of the Hamiltonian written as

$$H = H_1 + \lambda H_2, \tag{3.25}$$

with the fixed Hamiltonian H_1 and with the parameter λ dependent second term λH_2. The parameter from a regular system is changed in such a way that the system remains regular, there only appear normal crossings but no avoided crossings appear. Thus, the distribution of the regular crossings can be represented by

$$P_{Regular}(\Delta E) = \delta(\Delta E). \tag{3.26}$$

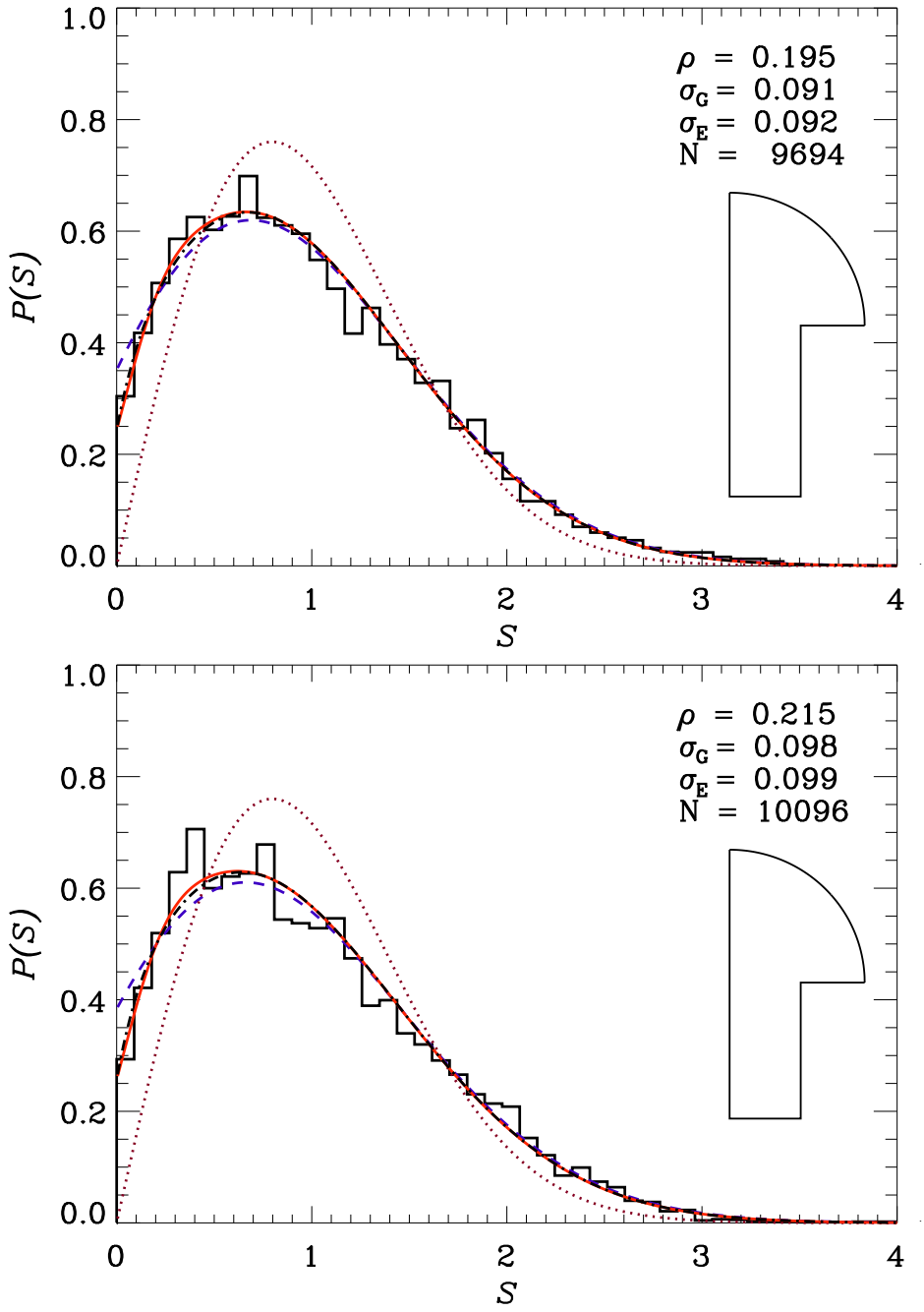

Figure 3.18: The comparison between the numerical data (histogram) for $(j_{min}, j_{max}) = (300, 400)$ (the upper plot) and $(j_{min}, j_{max}) = (200, 300)$ (the lower plot) and the best fitting theoretical curves for P^{Tn}_{DBRN}: The solid red curve represents the Gaussian model, the dash-dotted black curve is used for the exponential model, the dashed blue curve indicates the BR distribution (with the same ρ) and the dotted brown curve represents the Wigner distribution. σ_G and σ_E are the best fitting values of σ for the Gaussian and for the exponential model respectively. N is the number of objects in the histogram. The billiard parameters: $a = 10/19$, $R = 1$ (both plots), $l_0 = 1.287$ (the upper plot) and $l_0 = 1.024$ (the lower plot). All the details are explained in the text.

However, the avoided crossings appear if the H is strongly chaotic in the full energy range of varying λ. Here we have considered time reversal invariant systems obeying the

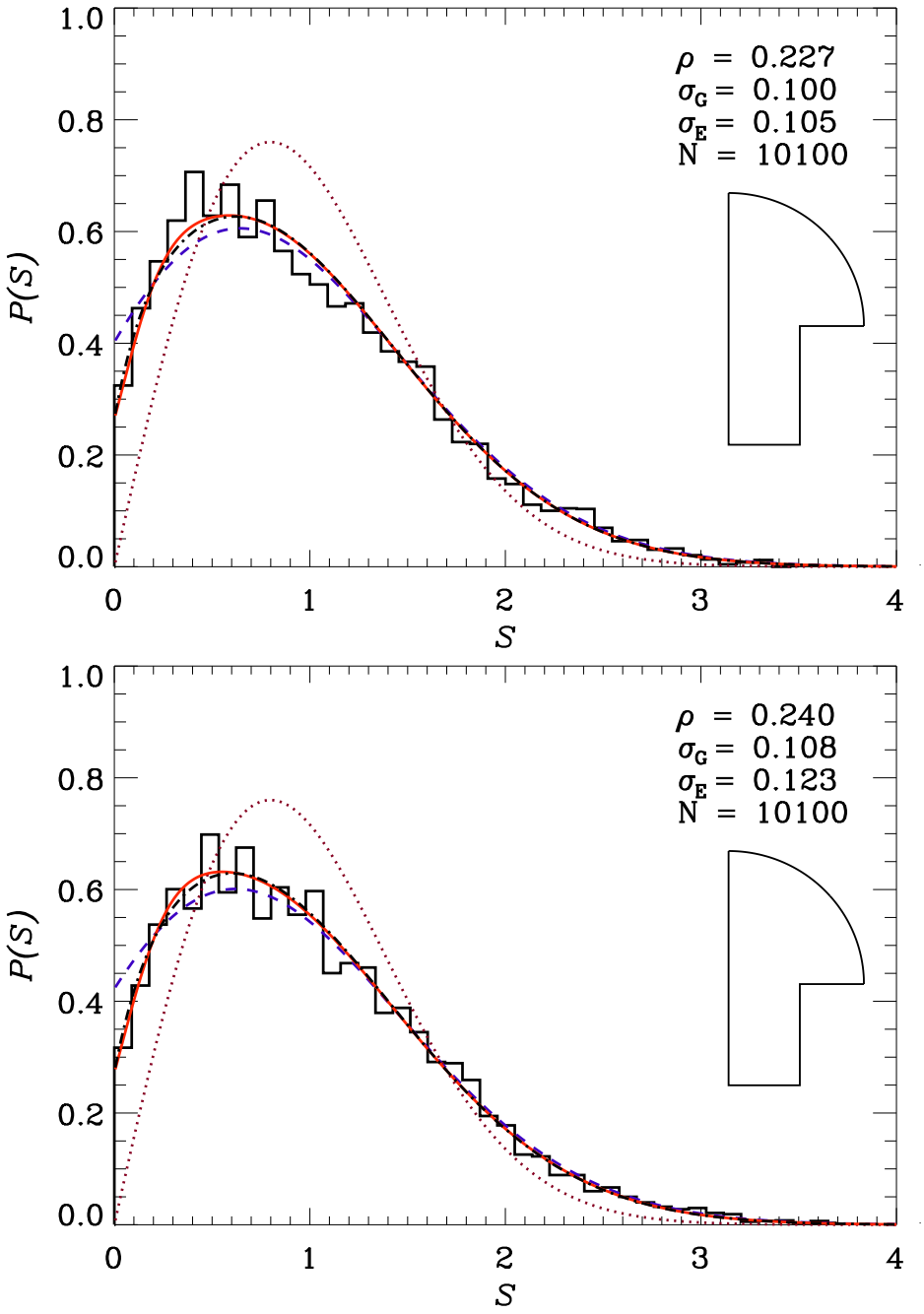

Figure 3.19: The same as Fig. 3.18 for $(j_{min}, j_{max}) = (200, 300)$ (both plots), $l_0 = 0.892$ (the upper plot) and $l_0 = 0.761$ (the lower plot).

GOE universality class, provided that the symmetry of the system does not change if one changes the parameter λ . On could, in fact, obtain a simple analytic formula for the avoided-crossing distribution if one assumed that such crossings are isolated, i.e. that the third level is so far away that one can neglect its influence, which means that each avoided crossing can be treated as a two-level mechanism. One may even make a weaker assumption, i.e. the multiple avoided crossings appear less frequently, so they are statistically insignificant. Then one may locally consider only two strongly interacting levels. Thus, one can select a two-dimensional subspace of two neighbouring levels which meet

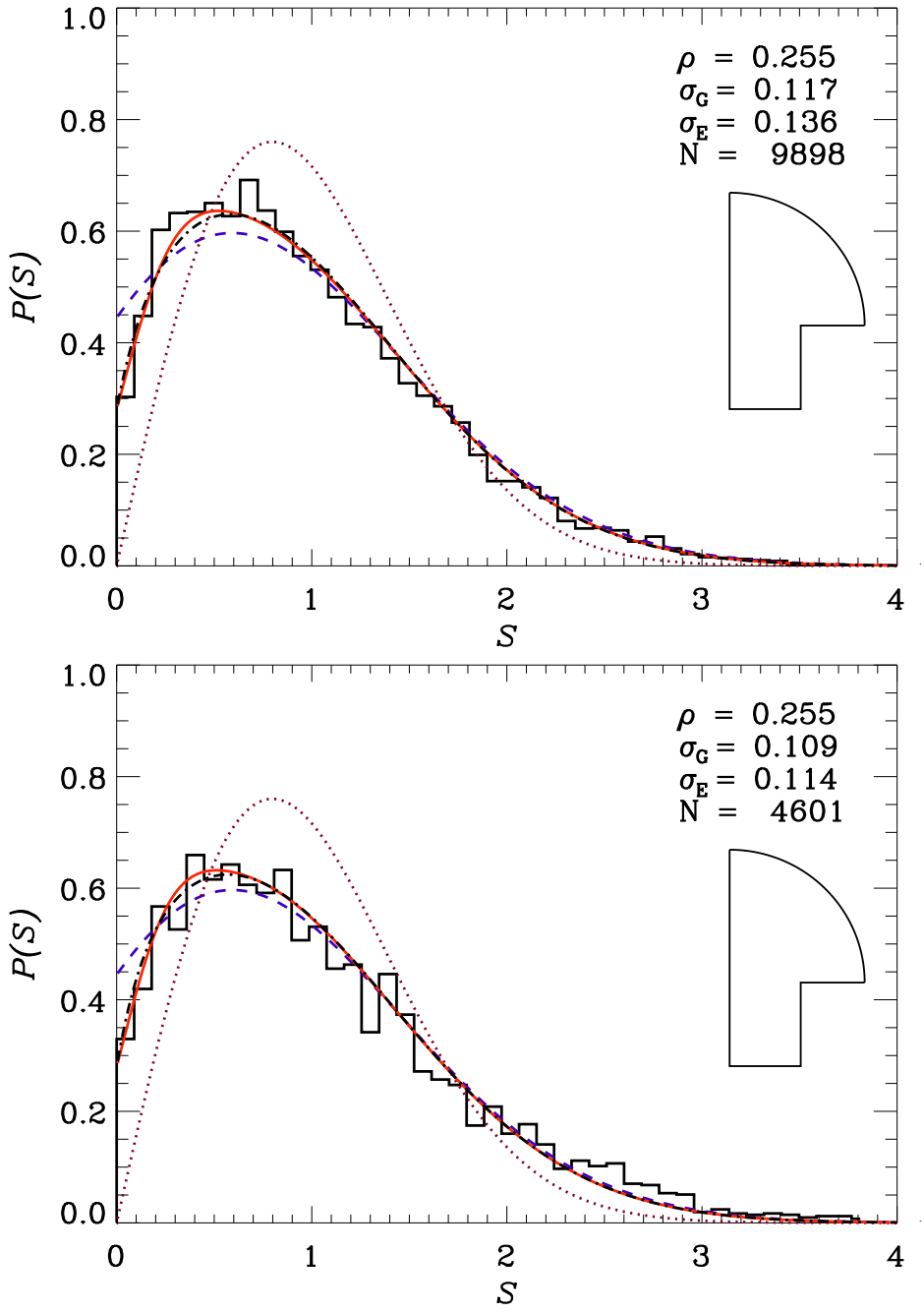

Figure 3.20: The same as Fig. 3.18 for $(j_{min}, j_{max}) = (100, 200)$ (the upper plot), $(j_{min}, j_{max}) = (300, 400)$ (the lower plot) and $l_0 = 0.629$ (both plots).

in the avoided crossing. In this subspace the effective Hamiltonian may be represented by the 2×2 matrix in the basis where H_2 is diagonal (Zakrzewski et al., 1993; Stöckmann, 1999). Thus, one obtains

$$H = \begin{pmatrix} a & b \\ c & d \end{pmatrix} + \lambda \begin{pmatrix} v_1 & 0 \\ 0 & v_2 \end{pmatrix}, \tag{3.27}$$

where a, b, c, v_1, v_2 are real numbers. A simple explicit calculation shows that the dependence of the levels on the parameter λ can be represented as a hyperbola whose two

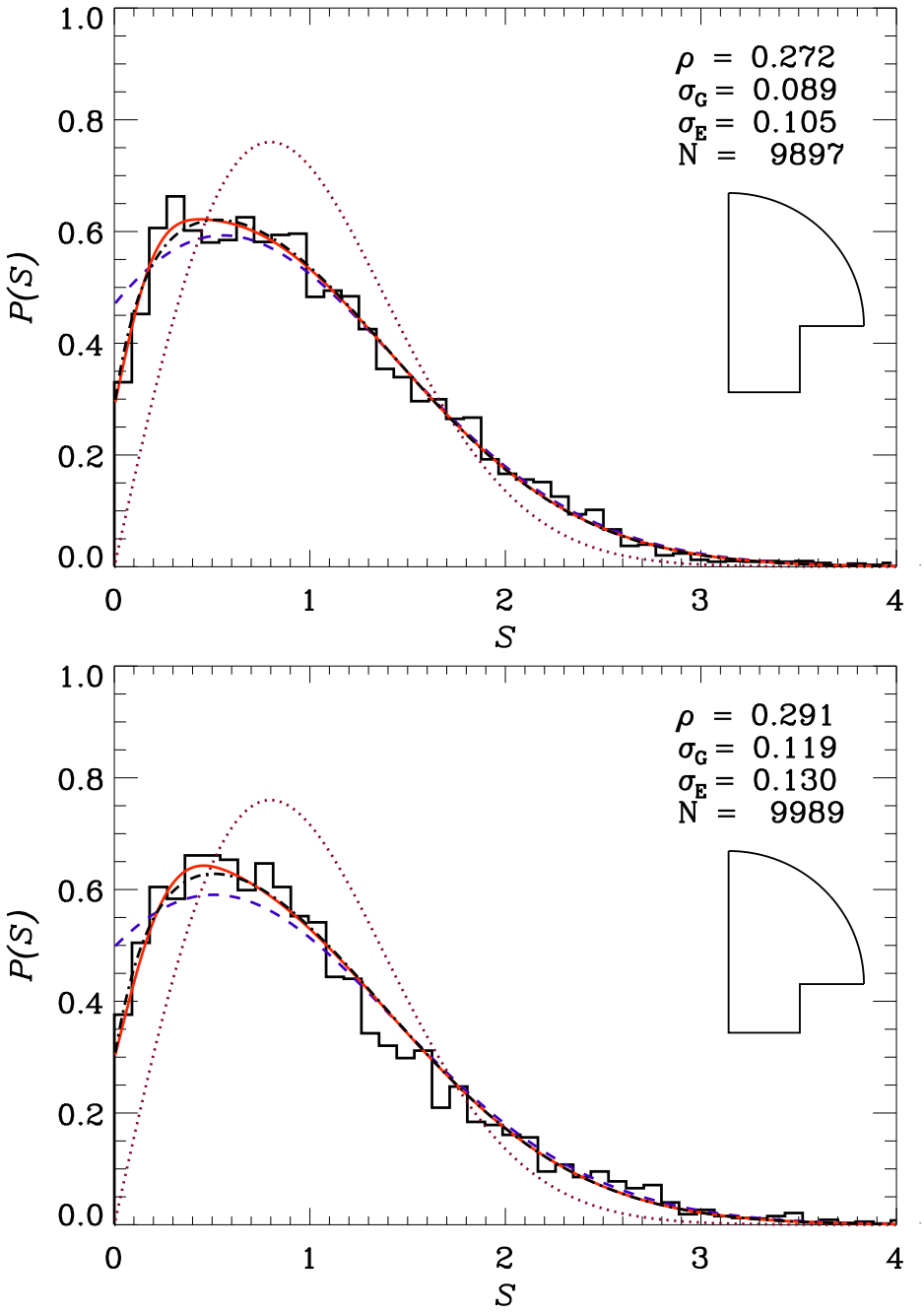

Figure 3.21: The same as Fig. 3.18 for $(j_{min}, j_{max}) = (100, 200)$, $l_0 = 0.497$ (the upper plot) and $(j_{min}, j_{max}) = (200, 300)$, $l_0 = 0.366$ (the lower plot).

branches $E_{1,2}(\lambda)$ can be calculated

$$E_{1,2}(\lambda) = \pm\frac{1}{2}\sqrt{((v_1 - v_2)\lambda + a - b)^2 + 4c^2} + \frac{1}{2}\left((v_1 + v_2)\lambda + a + b\right). \tag{3.28}$$

The minimal gap ΔE between the energy levels E_1 and E_2 as function of λ appears at $\lambda_0 = \frac{a-b}{v_1 - v_2}$ and equals $2\,|c|$. Since H obeys the GOE universally class, the matrix element c is normally distributed according to RMT. Due to this the probability distribution of avoided crossings reads $P(\Delta E) = \frac{1}{\alpha\sqrt{2\pi}} \exp\left(-\frac{\Delta E^2}{8\alpha^2}\right)$ where α is a free parameter. Since

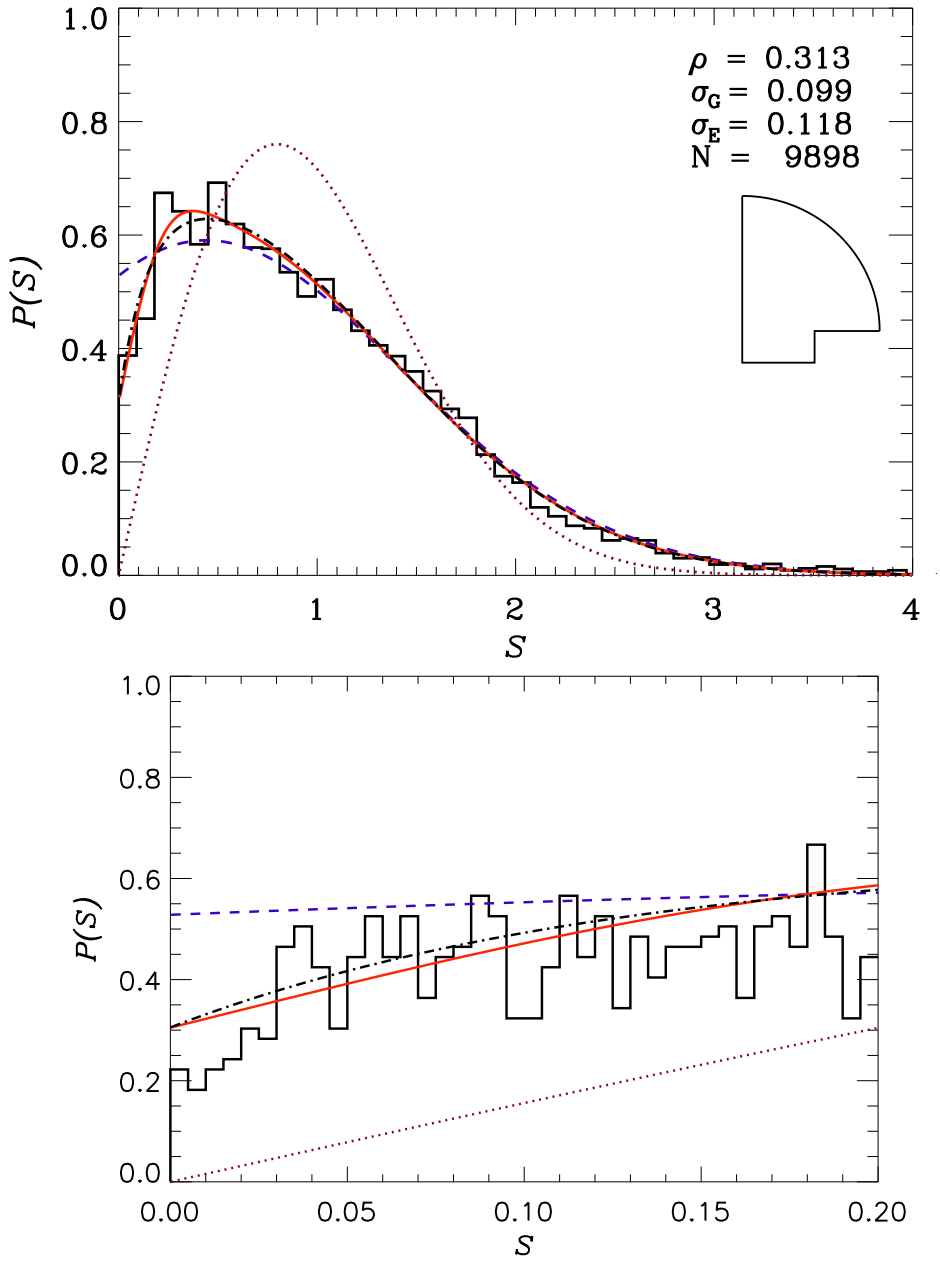

Figure 3.22: The same as Fig. 3.18 for $(j_{min}, j_{max}) = (100, 200)$, $l_0 = 0.234$ (the upper plot) and enlarged (the lower plot). All the details are explained in the text.

the ratio of the average avoided crossing to the average spacing is a system dependent quantity (Zakrzewski et al., 1993), one has to normalize $P(\Delta E)$ to unit average avoided crossing to obtain $\alpha = \frac{\sqrt{\pi}}{2\sqrt{2}}$, which results in

$$P_{GOE}(\Delta E) = \frac{2}{\pi} \exp\left(-\frac{\Delta E^2}{\pi}\right). \tag{3.29}$$

Since the crossings are non-generic, the probability of the level crossings in the chaotic systems with one system parameter equals zero. Due to this one has to change two or more system parameters to create a degeneracy. When only one parameter is varied, there appears a finite closest approach ΔE to the eigenvalues $E_1(\lambda)$ and $E_2(\lambda)$ rather

than a degeneracy. It was numerically confirmed that, for different systems, Eq. (3.29) appropriately describes what is happening in chaotic systems (Zakrzewski et al., 1993).

We would like to deal with the avoided crossings in the mixed-type systems, especially in the mushroom billiards in the case where one deepens the foot (see Subsec. 3.5.2). There exist two types of avoided crossings: the RC avoided crossings, which appear between a regular and a chaotic level, and the CC avoided crossings, which appear between two chaotic levels (Fig. 3.23). The RC avoided crossings appear due to tunneling, which affects the system; their size is employed as a tunneling measure. The two-hyperbola fit (see Fig. 3.23 - the upper and the middle plots) was applied to each (RC or CC) isolated avoided crossing. For practical reasons the two hyperbolas $E_{1,2}(\lambda)$ are described by a somewhat different set of five parameters a_0, a_1, a_2, a_3 and a_4: $E_{1,2}(\lambda) = \pm\sqrt{a_0^2(\lambda - a_2)^2 + a_1^2} + a_3 + a_4(\lambda - a_2)$ where the new parameters are simple functions of a, b, c, v_1, v_2 from Eqs. (3.27, 3.28). The minimal energy distance $\Delta E = 2\,|a_1|$ occurs at $\lambda_0 = a_2$. For the two-hyperbola fit we have used about 20 points whereas in the experimental data fewer points were often available due to the missing resonances.

If the density of states at the local scale does not vary much, one can apply the two-hyperbola fit on the energy or on the Weyl axes - one only switches the avoided-crossing distances to another scale if necessary. For the purpose of this section avoided-crossing distances have to be placed on the Weyl axes. Therefore, we have first unfolded the spectra up to the $E = 4200$ and, then, we have employed the two-hyperbola fit, so that we eventually devised the histogram of the splittings at the avoided crossings. For the sake of comparison with the theoretical prediction, the histogram has to be normalised to unit area and to unit average splitting at avoided crossings. The lower plot from Fig. 3.23 represents the avoided-crossing distribution of the mushroom billiard levels obtained numerically.

For the CC avoided-crossing distribution the results are in accordance with the theoretical prediction for fully chaotic systems. However, this does not happen in the case of larger crossings which cannot be adequately described by the 2×2 model since they cannot be treated as isolated pairs of levels. Another exception is the ratio of the mean avoided crossing to the mean level spacing $\langle \Delta E \rangle / \langle S \rangle$. In the Hamiltonian from Eq. (3.25) the mean level spacing explodes to infinity for a big λ . If one wants to avoid this explosion, the Hamiltonian has to be expressed by (Zakrzewski et al., 1993)

$$H = \cos(\lambda) H_3 + \sin(\lambda) H_4, \tag{3.30}$$

where H_3 and H_4 are GOE random matrices with the same mean level spacing. Then the mean level spacing of H from Eq. (3.30) does not dependent on λ any more. With this H the theoretical prediction results in $\langle \Delta E \rangle / \langle S \rangle = \sqrt{2} - 1 \approx 0.41$. Simulations with large ($N = 50$) GOE random matrices yield $\langle \Delta E \rangle / \langle S \rangle \approx 0.52$ (Zakrzewski et al., 1993). The results differ because the nonisolated avoided crossings are also treated in the GOE model. In real chaotic systems $\langle \Delta E \rangle / \langle S \rangle$ is a system dependent quantity, which is usually larger than the 2×2 RMT theoretical prediction. This equals 0.51 for the kicked-top model, 0.49 for the Africa billiard and 0.42 for the magnetised hydrogen atom (Zakrzewski et al., 1993). There appear certain discrepancies (**i**) because the avoided crossings in real systems cannot be regarded as isolated as well as (**ii**) due to the localised bouncing-ball and scarred eigenstates. If a bouncing-ball or a scarred eigenstate and another chaotic eigenstate, which create an avoided crossing, are dislocated from one another, so they do

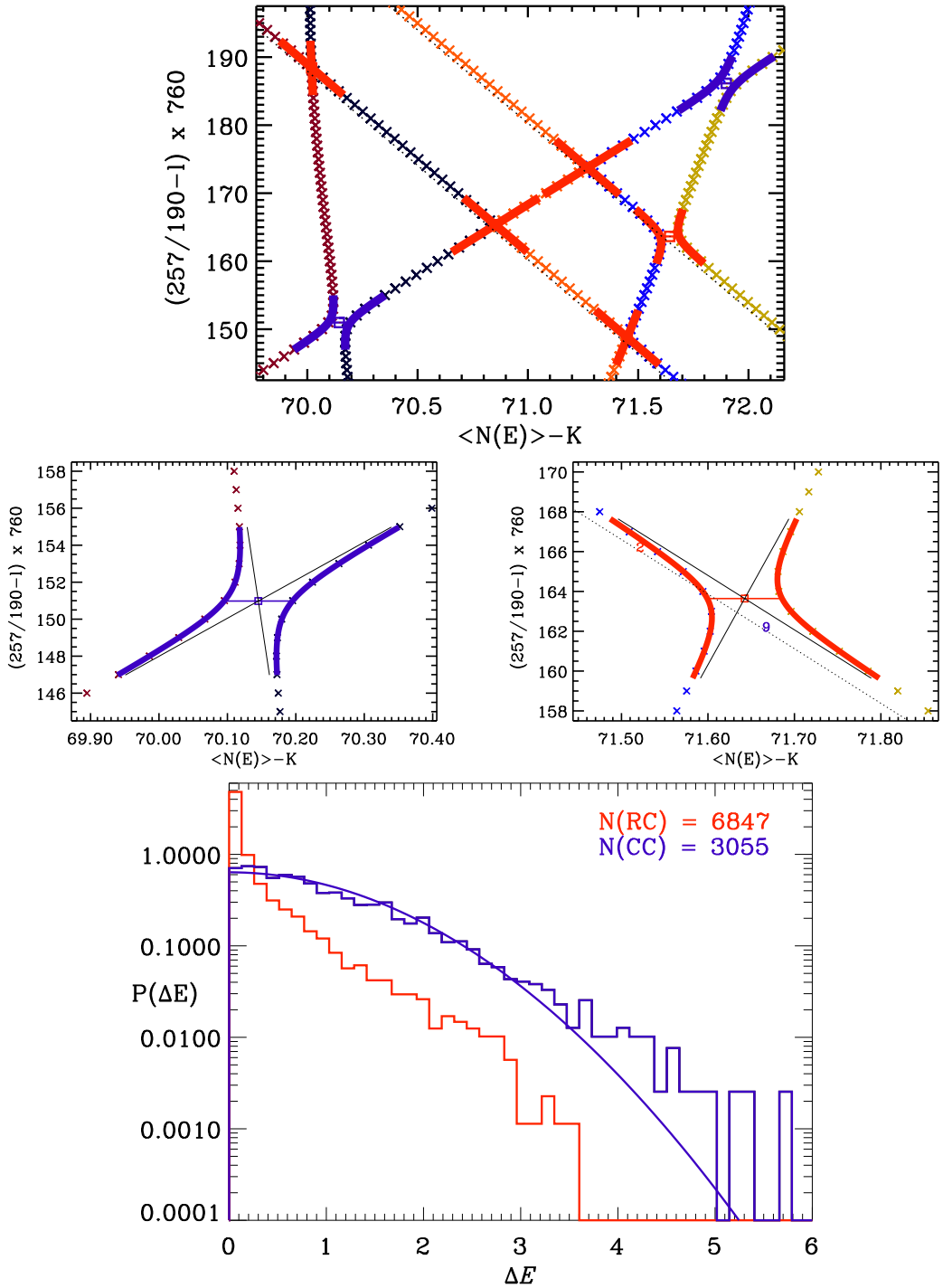

Figure 3.23: **The upper plot**: the avoided crossings in a numerically calculated level dynamics fitted on the Weyl axis; the RC crossings are indicated by the red colour whereas the CC ones are blue. The dotted lines represent the eigenvalues for the quarter circle. **The middle plots**: the magnification of a CC (blue) and a RC (red) avoided crossing where the closest distances are indicated by small horizontal coloured straight lines whereas the black straight lines represent the asymptotes of the hyperbolas. The blue number at a regular state indicates the azimuthal quantum number m divided by 2 whereas the red number is the radial quantum number n. **The lower plot**: the distribution of splittings for each of the cases, where the solid blue curve represents the Eq. (3.29). N(RC) and N(CC) are the numbers of objects included in each histogram. For the sake of comparison the first moment of the RC histogram is normalised with respect to the first moment of the CC histogram. K is defined in Eq. (3.16).

not overlap very strongly, which results in smaller splittings reducing the $\langle \Delta E \rangle / \langle S \rangle$.

In our system this ratio for the CC avoided crossings equals

$$\frac{\langle \Delta E \rangle_{CC}}{\langle S \rangle_{all}} \approx 0.27. \tag{3.31}$$

The value does not change if the quantities are scaled in the appropriate way, i.e. the mean level spacing $\langle S \rangle_{all}$ for the entire spectrum is scaled with the mean level spacing $\langle S \rangle_C$ for the chaotic states and the mean CC splittings with $\langle S \rangle_C$ as well since both quantities were divided by the same constant. Thus, the final result from (3.31) greatly differs from the theoretical 2×2 RMT prediction value (0.41) and, even more greatly, from the $N \times N$ value (0.52). We believe that the discrepancy occurs (**i**) due to the mixed-type nature of the system; the CC avoided crossings, their gaps and even their existence also depend on the neigbouring regular states; and (**ii**) due to several bouncing-ball and scarred eigenstates appearing. This could be studied in the future as well. Nevertheless, we are convinced that, due to this result, the validity of Eq. (3.29) could be extended to the mixed-type systems.

In the RC case (red) the average distances are much smaller than those from the CC case, and the ratio $\langle \Delta E \rangle_{RC} / \langle S \rangle_{all}$ of the mean avoided crossing and the mean level spacing of the entire spectrum is about 0.07. We have not managed to describe the RC histogram (for all the regular states) with an analytical function since we do not expect the universal behaviour. But, one can predict the tunneling rates for each regular state separately, which is discussed in the following section.

3.7 Tunneling rates

This section considers the tunneling rates in the mushroom billiard. First one should mention a typical example of tunneling under the barrier, i.e. the 1D double well problem (Landau and Lifshitz, 1989) with the symmetric potential

$$U(x) = \alpha \left(x^2 - x_0^2 \right)^2 . \tag{3.32}$$

Quantum mechanically, two quasi-modes with the same energy can be constructed: i.e. one, ψ_L, in the left well and the other, ψ_R, in the right well. The eigenstates are constructed if one employs a symmetric and an antisymmetric linear combination from $\psi_{L,R}$

$$\psi_+ = \frac{1}{\sqrt{2}} \left(\psi_L + \psi_R \right), \qquad \psi_- = \frac{1}{\sqrt{2}} \left(\psi_L - \psi_R \right) \tag{3.33}$$

with the energies E_S and E_A respectively. The splitting $\epsilon = E_S - E_A$ in the semiclassical limit is given by

$$\epsilon = \frac{\hbar \omega}{4 \pi M} \exp \left(-\frac{1}{\hbar} \int_{-x_1}^{+x_1} |p(x)| \, dx \right), \tag{3.34}$$

where the integral goes over the barrier, $\pm x_1$ are the two turning points of the trajectories from the right as well as those from the left well respectively, i.e. the points where the moment p vanishes (see Fig. 3.24) whereas ω corresponds to the angular frequency of the classical trajectory.

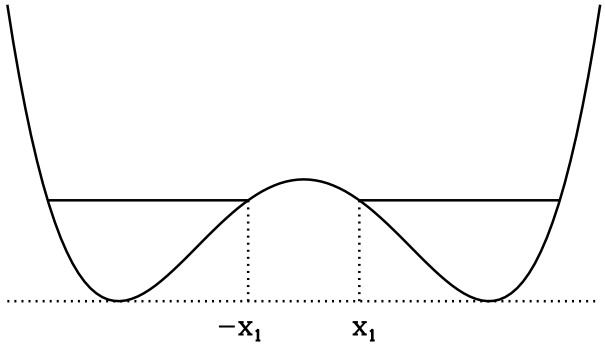

Figure 3.24: The double well potential $U(x)$ from Eq. (3.32).

If the initial state of the system is ψ_L, its time evolution $\hat{U}(t)\psi_L$ can be indicated by

$$\hat{U}(t)\psi_L = \frac{\sqrt{2}}{2}\hat{U}(t)(\psi_- + \psi_+) = \frac{\sqrt{2}}{2}e^{-iE_A t/\hbar}(\psi_- + e^{-i\epsilon t/\hbar}\psi_+). \tag{3.35}$$

Thus, its absolute square, the probability $|\hat{U}(t)\psi_L|^2$, oscillates between $|\psi_L|^2$ and $|\psi_R|^2$ with the time period $t_0 = \pi\hbar/\epsilon$, provided that the two-level approximation is justified. In the case of small splittings the time period t_0 is very long and this is why these modes are called quasi-modes.

Only two close-lying states were treated here. In the case of many (continuum) final close-lying states the qualitative behaviour of the system differs: there appears the exponential decay of the probability of the initial state, so one can apply Fermi's golden rule here. However, at times larger than the Heisenberg time $\tau_H = \frac{\hbar}{\Delta E}$, where ΔE is the mean level spacing of the discrete spectrum, there can occur quasi- or almost periodic oscillations which depend on the discrete energy specter.

3.7.1 Fermi's golden rule

Fermi's golden rule indicates the transition rates in systems with a perturbation. It is derived from the time-dependent perturbation theory although the perturbation appearing in Fermi's golden rule is time independent. The time-independent Hamiltonian is written as

$$H = H_0 + V, \tag{3.36}$$

where H_0 is the unperturbed Hamiltonian while V indicates the perturbation. If $|\psi_j^0\rangle$ and $|\psi_k^0\rangle$ are two different eigenstates of the H_0, their matrix elements of the perturbation may be represented in terms of the full Hamiltonian: i.e. $\langle\psi_j^0|V|\psi_k^0\rangle = \langle\psi_j^0|H|\psi_k^0\rangle$. As mentioned earlier the eigenstates $|\psi_j\rangle$ of the full Hamiltonian are either mainly regular or mainly chaotic. On the basis of these two types we have introduced purely regular $|\widetilde{\psi}_{\rm reg}\rangle$ and purely chaotic orthogonal states $|\widetilde{\psi}_{\rm ch}\rangle$ (Bäcker et al., 2008b) which in the first

approximation are the eigenstates of H_0. The Appendix B describes how these states can be calculated. One may doubt the existence of the H_0. Although H_0 cannot be explicitly represented as a slight variation of H, it is well defined by its eigenstates $|\psi_j^0\rangle$ and their corresponding eigenvalues E_j^0

$$H_0 = \sum_j E_j^0 |\psi_j^0\rangle\langle\psi_j^0|. \tag{3.37}$$

If one wants to obtain the E_j^0 eigenvalues, the spectrum of H has to be regarded as a function of l and every RC avoided crossing has to be replaced by an exact crossing whereas the CC avoided crossings remain intact.

The exponential tunneling decay $e^{-\gamma t}$ of a purely (unperturbed) regular state $|\widetilde{\psi}_{\rm reg}\rangle$ into the chaotic states $|\widetilde{\psi}_{\rm ch}\rangle$ is described by the tunneling rate γ. For the systems with a finite phase space (like ours) this exponential decay mostly occurs up to the Heisenberg time $t < \tau_H = \frac{\hbar}{\Delta_{ch}}$ where Δ_{ch} is the mean level spacing of the chaotic states. The central assumption of this formalism is that the chaotic states, which meet with one specific regular state in many avoided crossings, or the avoided crossings of this specific regular state themselves, are so dense, that they can, in fact, be regarded as a quasi-continuum. Thus, Fermi's golden can be applied to γ, which (if $\hbar = 1$) results in

$$\gamma = 2\pi\langle|v|^2\rangle\rho_{\rm ch}. \tag{3.38}$$

Here $\langle|v|^2\rangle$ is the averaged squared matrix element between the regular state and the chaotic states characterised by similar energy whereas $\rho_{\rm ch} = \frac{d\langle N(E)\rangle}{dE}$ is the density of the chaotic states in the vicinity of the regular state. According to Weyl's formula $\rho_{\rm ch} \approx \frac{A_{\rm ch}}{4\pi}$, where A_{ch} is the effective chaotic area, i.e. the area of the billiard times the fraction of the chaotic phase-space volume $1 - \rho_1$ (for the mushroom billiard see Appendix A). Note that one should consider level dynamics if one wants to observe how one regular state meets with many chaotic states. If only one billiard configuration were considered, there would not appear more than one (if any) avoided crossing per regular state. In this case no exponential decay would occur; one would rather notice true oscillations between the states (at avoided crossing) as in the case of 1D double potential well, provided that the Heisenberg time is larger than the oscillation time.

The theory for the tunneling rates γ_{mn} for any pure regular state $|\widetilde{\psi}_{\rm reg}\rangle = \psi_{1/4}^{mn}$ of the mushroom billiard from Eq. (3.3), was successfully derived by the group from Dresden (R. Ketzmerick, A. Bäcker and S. Löck) and it is discussed in Appendix B. The analytic result for $R = 1$ reads

$$\gamma_{mn} = \frac{8}{\pi} \sum_{s=1}^{\infty}{}' \frac{J_{m+\frac{2s}{3}}(j_{mn}a)^2}{J_{m-1}(j_{mn})^2}, \tag{3.39}$$

where the definitions are the same as in Sec. 3.2. The sum over s excludes all the multiples of 3 which is indicated by the prime, and this sum is rapidly converging. Its dominant contribution is $s = 1$, so if one uses $s \leq 2$, this is sufficiently accurate. The resulting γ_{mn}s, which are presented in Fig. 3.27, are connected by solid lines for fixed values of the radial quantum number n.

If one changes the foot height l and if ρ_{ch} is not too big (otherwise the flooding of regular islands (Bäcker et al., 2005, 2007) can occur), there appear the avoided crossings

between individual regular states and different chaotic states. If the full Hamiltonian is represented in the same way as in Eqs. (3.25) and (3.27), the splittings $\Delta E = 2|c|$ determine individual matrix elements for different billiards with varying ρ_{ch} where c equals v from this section. Thus, the average in Eq. (3.38) can also been applied to ρ_{ch}, provided that the regular-to-chaotic tunneling rate γ is a local property of the head region where the regular phase-space component resides, so it does not depend on the foot height. This results in

$$\gamma = \langle [\Delta E]^2 A_{\mathrm{ch}}/8 \rangle, \tag{3.40}$$

where A_{ch} varies from $0.5\,R^2$ to $1.2\,R^2$ if l increases from 0 to 25.7 cm at $R = 19$ cm (in experiment) and from 0 to 257/190 at $R = 1$ (in numerics).

3.7.2 Tunneling rates - the experiment

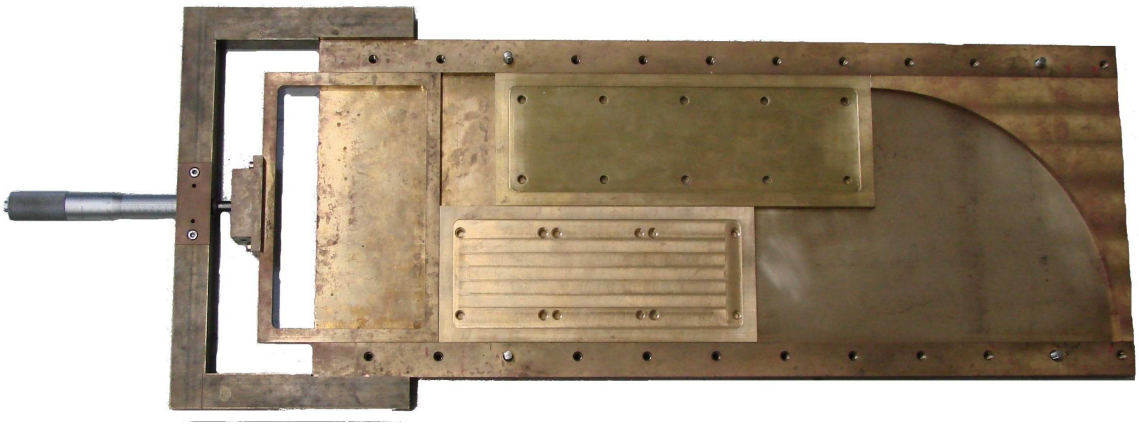

Figure 3.25: The desymmetrised experimental mushroom billiard with the radius $R = 19$ cm, the foot width $a = 10$ cm and the foot height $l = 0 \ldots 25.7$ cm. The antenna is located 4 cm left from the right corner and 0.75 cm above the horizontal wall.

Fig. 3.25 shows the mushroom billiard-shaped microwave cavity we have measured the tunneling rates with. The mushroom billiard with the radius $R = 19$ cm and the foot width $a = 10$ cm is made of brass. The spectra are (regarded as) a function of the foot height l of the mushroom billiard in the frequency regime from 3.0 to 13.5 GHz, which corresponds to the values of kR between 11.9 and 53.8.

Fig. 3.26 shows part of the spectra from a small $E = (kR)^2$ window. One should again emphasise that since the energy of the regular states from the quarter circle does not depend on the foot height, these states are indicated by straight vertical lines whereas the chaotic ones, with increasing foot height l, shift to the lower energies, which reflects the increasing density ρ_{ch} of chaotic states. For each of the regular states, described by Eq. (3.3), with the radial quantum numbers n between 1 and 5 and the azimuthal m even between 8 and 32, all the accessible splittings appearing at avoided crossings have been determined by means of the two-hyperbola fit (in this case the two-hyperbola fit was performed using full energy prior to spectral unfolding). Fig. 3.26 shows two such fits: a 'reliable' (red) and an 'unreliable' (yellow) one - these fits are explained at a later point but, for the time being, they are not treated separately. The tunneling rates γ_{mn}

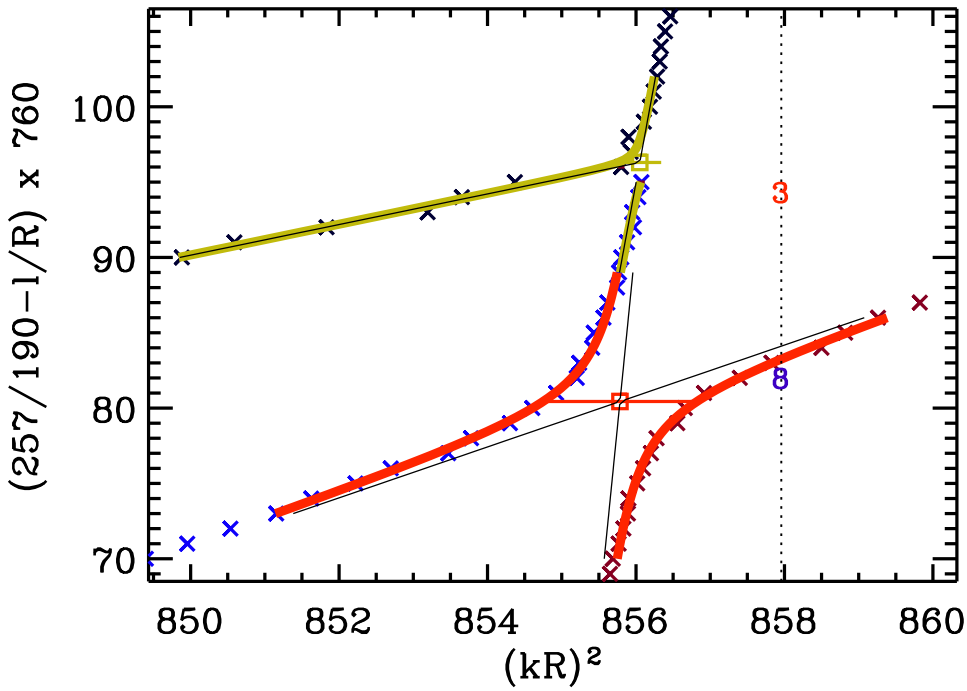

Figure 3.26: A small part of the evaluated experimental resonance spectra of the mushroom microwave billiard vs. the parameter, linearly dependent on the foot height l. The vertical lines indicate the eigenenergy of the quarter circle with the quantum numbers $m/2 = 8$ and $n = 3$. The RC two-hyperbola fits are red (the 'reliable' hyperbola; see the text) and yellow-green (the 'unreliable' hyperbola). All the other signatures are the same as in the middle plot from Fig. 3.23.

from the regular states (m, n) to the chaotic sea were determined in such a way that we employed the fixed values of (m, n) and averaged all the ΔEs by applying Eq. (3.40). The resulting γ_{mn} vs. the wavenumber k are presented in Fig. 3.27. The energy of regular states is represented as the square of the Bessel zero divided by R^2. Thus, if one wants to obtain the dimensionless units, the tunneling rates should be multiplied by R^2 whereas the wavenumber should be multiplied by R.

Apart from the deviations for $n = 1$ and for one or two points with $n = 2$ the results, including the error bars, are in very good agreement with the theoretical prediction, Eq. (3.39). Some points are missing; if two regular levels are very close to one another, it is not recommendable to fit and, thus, resolve their avoided crossings with the chaotic states since this would result in a 3-level mechanism which is not described by the theory employed.

The experimental resolution of the avoided crossings is limited by the line widths of the resonances caused by the wall absorption and the antenna coupling. In the frequency regime studied the line widths were about $\Delta\nu_w = 0.01$ GHz, which corresponds to $\Delta k_w R \approx 0.04$. From the hyperbola fit of the avoided crossings all the splittings ΔkR larger than $0.1\Delta k_w R$ could still be resolved, corresponding to the tunneling rates γ between 0.001 and 0.024. If one selects the average A_{ch} of $0.85\,R^2$, the estimated lower limit of the experimentally accessible rates in Fig. 3.27 is indicated by the dashed line.

Fig. 3.27 also represents the error bars indicating the standard error S_E of the mean tunneling rate $\gamma_0 (= \gamma_{mn})$ for the selected sample of the avoided crossings along one regular

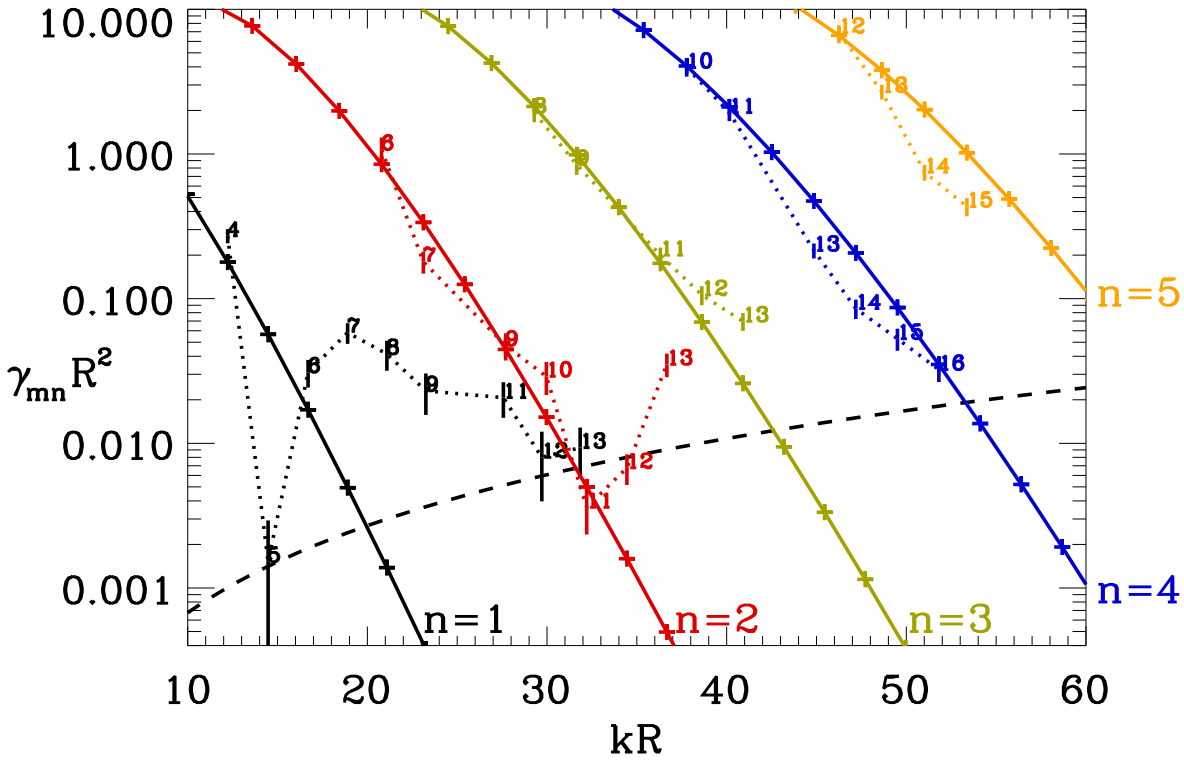

Figure 3.27: The dynamical tunneling rates from the regular region to the chaotic sea for the quantum numbers $n = 1$ to $n = 5$ vs. kR for the mushroom billiard with $a/R = 10/19$. The figure also represents the theoretical predictions ('+'s connected by solid lines for a fixed n, just to guide the eye) from Eq. (3.39) and from the experimental results. The quantum numbers $m/2$ are indicated in the figure and connected by dotted lines for a fixed quantum number n. In the experimental results the standard error bars are plotted as well. The dashed line denotes the lower limit of the experimental resolution of the resonance splittings.

line. The standard error indicates the uncertainty around the estimated mean measured value whereas the standard deviation σ_{meas} measures the spreading of the individual data points. The standard error and the standard deviation are related in the following way

$$S_E = \frac{\sigma_{meas}}{\sqrt{N}}, \tag{3.41}$$

where N is the sample size which, in this thesis, indicates the number of the avoided crossings obtained for a chosen (m, n).

In our study of the tunneling rates in the mushroom billiards, there appear two different types of errors: a) the statistical errors; its standard deviation is indicated by σ_{stat}. b) the fitting error; its standard deviation is denoted by σ_{fit}. Due to their independence the total, squared standard deviation is represented as the sum of the squares of both the standard deviations

$$\sigma^2_{meas} = \sigma^2_{stat} + \sigma^2_{fit}. \tag{3.42}$$

If the mean is represented by

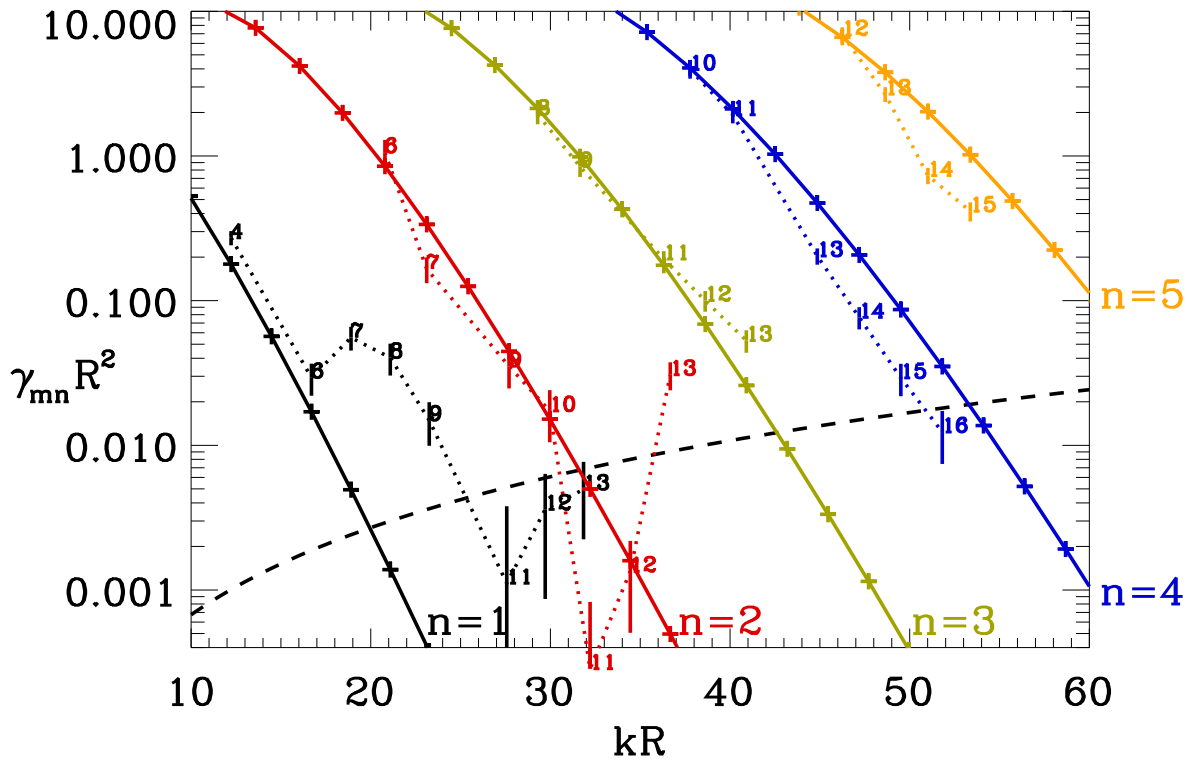

Figure 3.28: The same as Fig. 3.27 whereas the 'unreliable' hyperbolas are represented by the distance 0 and NOT by the fitted distance.

$$\gamma_0 = \sum_{i=1}^{N} \frac{([\Delta E]^2 A_{\mathrm{ch}})_i}{8N}, \tag{3.43}$$

the statistical error is written as

$$\sigma_{stat}^2 = \sum_{i=1}^{N} \frac{(([\Delta E]^2 A_{\mathrm{ch}})_i/(8N) - \gamma_0)^2}{N}. \tag{3.44}$$

Due to the uncertainty δE_i of each individual avoided crossing ΔE_i the fitting error can be calculated as:

$$\begin{aligned} \gamma_0 \pm \sigma_{fit} &= \sum_{i=1}^{N} \frac{([\Delta E \pm \delta E]^2 A_{\mathrm{ch}})_i}{8N} \\ &= \sum_{i=1}^{N} \frac{([\Delta E]^2 A_{\mathrm{ch}})_i}{8N} \pm 2 \sum_{i=1}^{N} \frac{(\Delta E \delta E A_{\mathrm{ch}})_i}{8N} + \sum_{i=1}^{N} \mathcal{O}([\delta E]_i^2) \end{aligned} \tag{3.45}$$

with

$m/2$	n	N_{hypALL}	N_{hypREL}	$\frac{N_{hypREL}}{N_{hypALL}}$	$\sigma_{fit}/\sigma_{stat}$	S_E/γ_0
4	1	3	3	100%	0.31	11.2%
5	1	3	/	/	1.10	93.1%
6	1	10	8	80%	0.54	21.6%
7	1	12	11	92%	0.25	16.3%
6	2	17	16	94%	0.08	21.3%
8	1	14	10	71%	0.22	23.5%
7	2	23	16	70%	0.35	17.3%
9	1	21	9	43%	0.24	31.8%
11	1	20	1	5%	0.48	27.6%
9	2	29	12	41%	0.40	21.3%
8	3	38	35	92%	0.05	14.3%
12	1	17	3	18%	0.29	50.4%
10	2	28	9	32%	0.44	25.7%
9	3	40	37	92%	0.06	15.1%
13	1	18	3	17%	0.19	37.7%
11	2	23	1	4%	0.39	35.1%
12	2	50	5	10%	0.31	23.9%
11	3	63	44	70%	0.12	12.9%
13	2	56	23	41%	0.22	18.6%
10	4	65	61	94%	0.05	13.5%
12	3	73	42	58%	0.18	15.0%
11	4	74	65	88%	0.06	12.7%
13	3	77	32	42%	0.23	14.2%
13	4	99	57	58%	0.13	11.8%
12	5	84	70	83%	0.05	12.7%
14	4	102	38	37%	0.18	15.3%
13	5	110	90	82%	0.07	11.6%
15	4	105	19	18%	0.21	17.4%
14	5	121	77	64%	0.08	12.5%
16	4	111	9	8%	0.33	17.9%
15	5	122	65	53%	0.10	14.3%

Table 3.1: The number counting all and only the 'reliable' hyperbolas with their fraction for the experimental data for various quantum numbers (m, n) plotted in Figs. 3.27 and 3.28. The 6th column shows the ratio of two different errors whereas the last column indicates the relative error. The quantum numbers selected are ordered according to increasing energy.

$$\sigma_{fit}^2 = \frac{1}{16}\left(\sum_{i=1}^{N}\frac{(\Delta E \delta E A_{\mathrm{ch}})_i}{N}\right)^2 . \tag{3.46}$$

For this reason one needs to calculate the uncertainty δE_i which is obtained from the least square fit procedure and which is equal to the square root of its χ^2, i.e. the sum of the squares of the distances between the hyperbola and the fitted points divided by M

which indicates the number of the fitted points reduced by the number of the free (5 in our case) parameters of the hyperbola. If one follows this procedure, one can calculate the correct (standard) error for each individual tunneling rate γ_{mn} indicated by the error bars in Fig. 3.27. The entire (standard) error represents about $10 - 30\%$ of the mean, which implies that the procedure selected is reliable. In Tab. 3.1 one notices that the statistical error is much more important (larger) than the fitting one, so one might even disregard the latter one.

The standard error of the individual hyperbola can be obtained from its uncertainty: $\delta E_i/(M-5)$. A hyperbola is classified as 'reliable' if its standard error is by at least a factor 1.5 smaller than the standard error of the two-straight lines fit describing the hyperbolas in infinity.

Tab. 3.1 shows the hyperbolas employed. About one half of these hyperbolas are characterised as the 'unreliable' ones. From all the 1256 points, since it was not possible to fit all the hyperbolas, some distances (appearing at avoided crossings) have been determined manually (15 such points) and treated as the 'reliable' ones whereas some of them have been determined with the distance 0 (3 such points) and treated as the 'unreliable' ones. So far (Fig. 3.27) the results for all the hyperbolas have been presented. However, in Fig. 3.28 the results are presented in such a way that the 'unreliable' hyperbolas have been taken with the distance 0. One can learn from Tab. 3.1 that all the hyperbolas are 'unreliable' at the missing point $(m/2, n) = (5, 1)$. The difference between the results is significant for the lower values of the tunneling rates where some points even fall below the experimental resolution. This happens because the majority of the 'unreliable' hyperbolas are characterised by small splittings. So if one selects the splitting 0, this changes the result, which is clearly seen in the logarithmic scale. For this reason γ_{mn}s for $(m/2, n) = (5, 1), (11, 1), (12, 1), (13, 1), (11, 2), (12, 2), (16, 4)$ might not be taken into account.

Another complication arises due to the antenna which causes an additional splitting (see Chap. 2). The size of this splitting is proportional to the absolute value of the product $|\psi^{mn}_{1/4}(\mathbf{q}_a)\psi_{ch}(\mathbf{q}_a)|$ of the wavefunctions at the antenna position $\mathbf{q}_a$ (see Subsec. 2.5.1). For the points $(m/2, n) = (7, 1), (8, 1), (9, 1)$ and $(13, 2)$ $|\psi^{mn}_{1/4}(\mathbf{q}_a)|$ is considerably larger than $|\psi^{m'n}_{1/4}(\mathbf{q}_a)|$ for $m/2 > m'/2$, which could probably explain the deviations between the experimental results and the theoretical prediction (see Figs. 3.27 and 3.28).

Tab. 3.1 shows that the higher the energy of a regular state, the more avoided crossings are formed. The fraction of the 'unreliable' hyperbolas increases with the increasing m at a fixed n. The avoided distances are in many cases small, which can be explained by the fact that many Bessel functions have larger values at a larger radius, so the hyperbolas resemble straight lines.

Thus, this is the very first experimental confirmation of any theoretical prediction of tunneling rates in billiards without the fitting parameter, with the agreement extending over more than 2 orders of magnitude. This is the most important result in our study of the dynamics of the avoided crossings in the mushroom billiard.

3.7.3 Tunneling rates - the numerics

With the numerically obtained levels the tunneling rates have been calculated in the same way as the experimental tunneling rates and their errors; the eigenvalues are the same as the ones employed in the analysis of the level spacing distribution model treated

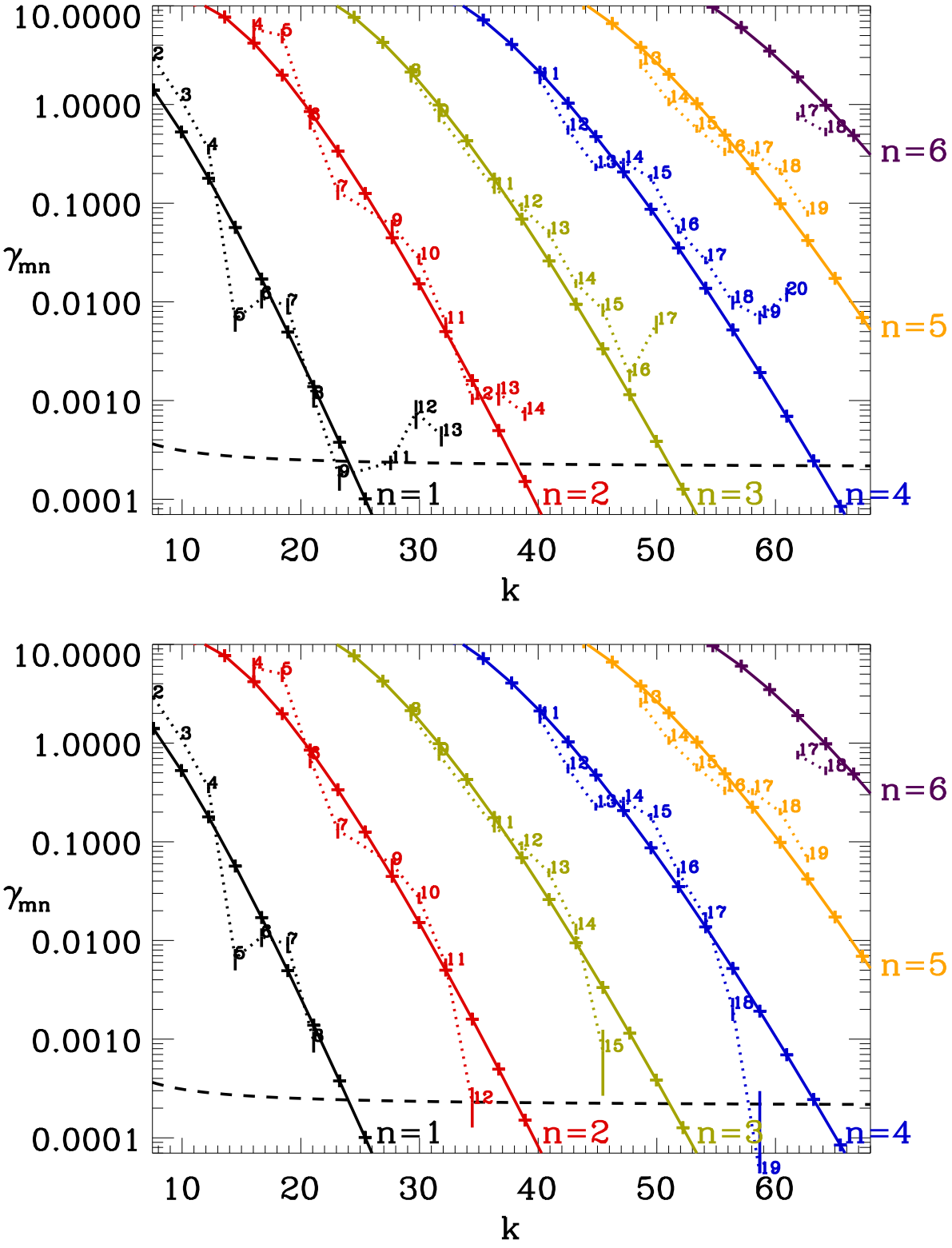

Figure 3.29: The same as Figs. 3.27 and 3.28 for numerically calculated levels with EBIM. The upper plot represents all the hyperbolas considered whereas in the lower plot the distance 0 is applied to the 'unreliable' hyperbolas. The 'numerical resolution' of an avoided crossing is indicated by the horizontal dashed line.

in this thesis. (see Subsecs. 3.5.2 and 3.5.3). The results are presented in Fig. 3.29 and Tabs. 3.2 and 3.3. Obviously, the numerical results confirm the theoretical findings up to 4 orders of magnitude, which indicates that the agreement in this case is by a 1.5 order of magnitude better than it was in the experiment case.

The dashed horizontal line indicates the error which appeared when we tried to resolve a gap at an individual avoided crossing by our method, which is estimated to be 0.004 in units of the mean level spacing (see Subsec. 3.5.1). This error corresponds to the tunneling rate γ of about 0.0003 where k changes from 7.5 to 68. In this case all the gaps ΔE larger than $0.1 \times 2\,\Delta E_{error}$ (see Subsec. 3.7.2) could still be resolved via the two-hyperbola fit of the avoided crossings where ΔE_{error} is the error of a single level prior to unfolding.

As expected, one notices that the ratio of the fitting and the statistical error is smaller than the one from the experimental study. Due to this and due to a larger number of hyperbolas the standard error is smaller than the one obtained in the experiment. As evident from Tabs 3.2 and 3.3 some (m, n)s contain only the 'unreliable' hyperbolas, so, consequently, these are not presented in the lower plot from Fig. 3.29. We believe that all these γ_{mn}s and, at least, also $(m/2, n) = (19, 4)$ should not be considered in our analysis. In an extreme situation one might select the distance zero for the 'unreliable' hyperbolas, although it would probably be better if one chose the mean of the fitted distance and the distance zero (namely $\Delta E/2$), however, such an approach is not necessarily useful.

Numerical accuracy is a large problem here since (as already mentioned above) the corners, especially the non-convex corner of $3\pi/2$, are the main sources of errors.

After all the eigenvalues had been calculated, there emerged a completely new, a very efficient and highly accurate numerical method, especially adapted for the mushroom billiard (Barnett and Betcke, 2007). This method is based on a set of basis functions ξ_i, which are termed particular solutions. These obey the Helmholz equation (3.2) or (3.9) although they do not individually fulfil the Dirichlet boundary condition. For this reason one should obtain such values for E_j, that the specific linear combination of the corresponding basis functions would disappear at the boundary. These linear combinations would, then, be regarded as good approximations for the eigenfunctions whereas the E_js for the eigenvalues. The authors of the method employed the previously-mentioned Fourier-Bessel functions represented by

$$\xi_i = J_{\frac{2\,i}{3}}(\sqrt{E}r)\sin\left(\frac{2\,i}{3}\theta\right), \tag{3.47}$$

as a set of basis functions. The non-convex corner is selected as the center of the coordinate system. These functions accurately capture the behaviour at the corner.

Since the group from Dresden had already calculated the energy spectra using the new method, we have not performed our own calculation with this method. Their calculation and the results for the tunneling rates are briefly represented in Appendix C. The results agree with the theory at over 18 orders of magnitude, which indicates an extremely strong confirmation.

Even if we tried to improve our EBIM method by treating the influence of the corners more precisely, the agreement would probably not be improved for more than a few orders of magnitude. We have solved the problem by using a general numerical method which is, consequently, slower and less accurate. Nevertheless, we can conclude that the theoretical prediction has also been confirmed by the numerical results.

$m/2$	n	N_{hypALL}	N_{hypREL}	$\frac{N_{hypREL}}{N_{hypALL}}$	$\sigma_{fit}/\sigma_{stat}$	S_E/γ_0
2	1	2	2	100%	0.13	4.1%
3	1	3	3	100%	0.79	0.9%
4	1	3	3	100%	0.10	11.9%
5	1	9	8	89%	0.04	24.3%
4	2	6	6	100%	0.01	25.8%
6	1	12	12	100%	0.02	21.4%
5	2	13	13	100%	0.006	17.1%
7	1	15	14	93%	0.06	19.0%
6	2	21	20	95%	0.007	20.4%
8	1	20	14	70%	0.09	19.8%
7	2	25	24	96%	0.01	17.9%
9	1	25	/	/	0.43	28.3%
11	1	37	/	/	0.31	17.0%
9	2	37	31	84%	0.02	14.0%
8	3	41	40	98%	0.01	14.6%
12	1	43	/	/	0.55	32.5%
10	2	45	36	80%	0.08	13.3%
9	3	47	45	96%	0.02	13.3%
13	1	52	/	/	0.46	23.2%
11	2	50	33	66%	0.10	13.3%
12	2	59	7	12%	0.25	12.7%
11	3	66	54	82%	0.04	11.2%
13	2	68	/	/	0.36	25.2%
12	3	77	65	84%	0.05	9.9%
14	2	78	/	/	0.35	15.9%
11	4	76	72	95%	0.02	12.2%
13	3	84	68	81%	0.06	10.1%
12	4	85	80	94%	0.05	11.0%
14	3	95	58	61%	0.11	10.2%
13	4	100	91	91%	0.04	8.6%
15	3	98	18	18%	0.38	15.2%
14	4	102	89	87%	0.03	9.5%
16	3	108	/	/	0.24	15.2%
13	5	91	89	98%	0.06	11.2%
15	4	109	96	88%	0.03	8.6%
17	3	122	/	/	0.30	20.7%
14	5	113	106	94%	0.05	9.8%
16	4	130	84	65%	0.17	9.4%
15	5	132	119	90%	0.05	9.3%
17	4	140	64	46%	0.40	8.8%
16	5	122	106	87%	0.05	9.5%

Table 3.2: The same as Tab. 3.1 for the numerical data.

$m/2$	n	N_{hypALL}	N_{hypREL}	$\frac{N_{hypREL}}{N_{hypALL}}$	$\sigma_{fit}/\sigma_{stat}$	S_E/γ_0
18	4	137	32	23%	0.26	16.1%
17	5	143	129	90%	0.08	7.9%
19	4	154	1	1%	0.23	15.8%
18	5	165	126	76%	0.09	7.9%
20	4	166	/	/	0.30	16.7%
17	6	150	140	93%	0.03	10.0%
19	5	195	127	65%	0.18	7.2%
18	6	134	117	87%	0.06	9.9%

Table 3.3: Continuation of the previous table.

Chapter 4

Numerical studies of non-Gaussian real symmetric random matrices

4.1 2D real symmetric random matrices

Here we refer to Sec. 2.2 where the 2×2 symmetric matrices $A = (A_{ij})$ ($i, j = 1$ or 2) have been considered and where their level spacing distribution $P(S)$ from Eq. (2.13), which is expressed in terms of the distribution function of the diagonal $g_a(a)$ and the off-diagonal $g_b(b)$ matrix elements of A, has been calculated.

As mentioned earlier the distribution (2.13) is normalised by construction, $\langle 1 \rangle = 1$, but this is not true for the first moment where $\langle S \rangle \neq 1$. If this distribution is selected as the model distribution for real, experimental spectra after the spectral unfolding, it must be normalised to unit mean level spacing $\langle S \rangle = 1$. Such a normalised distribution function is denoted by $P^n(S)$ and it can be easily obtained if one rescales the argument of $P(S)$ by the scale factor B, i.e.

$$P^n(S) = B\ P(BS), \quad \text{with} \quad B = \int_0^\infty x\ P(x)\ dx. \tag{4.1}$$

In this section we will introduce four non-Gaussian 2D random matrix ensembles and their results for the level spacing distribution, following the reference (Grossmann and Robnik, 2007b). First we will test the analytic results and, in the next step, we will generalise them to the higher dimensions of matrix A.

4.1.1 Box (uniform) distribution

The distribution functions of matrix elements are defined as

$$g_a(a) = \frac{1}{2a_0}, \quad \text{if } |a| \leq a_0, \quad 0 \quad \text{otherwise}, \tag{4.2}$$

$$g_b(b) = \frac{1}{2b_0}, \quad \text{if } |b| \leq b_0, \quad 0 \quad \text{otherwise}. \tag{4.3}$$

Without any loss of generality one can assume that $b_0 \leq a_0$. In this case the exact result for the level spacing distribution is written as

$$P(S) = \begin{cases} \frac{\pi S}{8a_0b_0}, & \text{if } S \le 2b_0 \le 2a_0, \\ \frac{S}{4a_0b_0}\arcsin\frac{2b_0}{S}, & \text{if } 2b_0 \le S \le 2a_0, \\ \frac{S}{4a_0b_0}\left(\arcsin\frac{2b_0}{S} - \arccos\frac{2a_0}{S}\right), & \text{if } 2a_0 \le S \le 2\sqrt{a_0^2+b_0^2}, \\ 0, & \text{if } S \ge 2\sqrt{a_0^2+b_0^2}. \end{cases} \tag{4.4}$$

If one selects $b_0 \ge a_0$ instead of $b_0 \le a_0$, one should only interchange a_0 and b_0 in the above formulae.

4.1.2 Exponential distribution

The distribution functions of matrix elements are defined as

$$g_a(a) = \frac{\lambda_a}{2}e^{-\lambda_a|a|}, \quad g_b(b) = \frac{\lambda_b}{2}e^{-\lambda_b|b|}. \tag{4.5}$$

For the level spacing distribution function one obtains

$$P(S) = \frac{\lambda_a\lambda_b}{4}\ S\int_0^{\pi/2} d\varphi\ \exp\left(-\frac{S}{2}(\lambda_a\cos\varphi + \lambda_b\sin\varphi)\right), \tag{4.6}$$

which cannot be analytically evaluated in a closed form. For small values of S the linear level repulsion law is recovered, i.e.

$$P(S) \approx \frac{\pi\lambda_a\lambda_b}{8}\ S. \tag{4.7}$$

For large values of S we use $\lambda_a\cos\varphi + \lambda_b\sin\varphi = \hat{A}\sin(\varphi+\phi)$, with $\phi = \arctan(\lambda_a/\lambda_b)$, and $\hat{A} = \sqrt{\lambda_a^2+\lambda_b^2}$. Then the integration variable φ is substituted by $\chi = \varphi + \phi$ which now runs from ϕ to $\phi + \pi/2$. This transforms $P(S)$ into

$$P(S) = \frac{\lambda_a\lambda_b}{4}\ S\int_\phi^{\phi+\pi/2} d\chi\ e^{-\frac{S}{2}\hat{A}\sin\chi}. \tag{4.8}$$

Since the integrand is continuous and bounded, the mean value theorem can be applied in this case, indicating that there is a value $\chi_0(S)$ in the interval between ϕ and $\phi+\pi/2$, so that the level spacing distribution can be presented as

$$P(S) = \frac{\pi\lambda_a\lambda_b}{8}\cdot S\cdot e^{-\frac{S}{2}\hat{A}\sin\chi_0(S)}, \tag{4.9}$$

where, as expected, $\chi_0(S)$ is only weakly dependent on S. Due to this the tail of $P(S)$ is roughly exponential.

4.1.3 Cauchy-Lorentz distribution

The normalized probability densities for matrix elements are defined by

$$g_a(a) = \frac{1}{\pi a_0(1+\frac{a^2}{a_0^2})}, \quad g_b(b) = \frac{1}{\pi b_0(1+\frac{b^2}{b_0^2})}\ . \tag{4.10}$$

The level spacing distribution is given by

$$P(S) = \frac{S}{4\pi^2 a_0 b_0} \int_0^{2\pi} \frac{d\varphi}{(1+\frac{S^2}{4a_0^2}\cos^2\varphi)(1+\frac{S^2}{4b_0^2}\sin^2\varphi)} \ . \tag{4.11}$$

The integral for $S \to 0$ results in 2π, so that, at small values of S, $P(S) \approx S/(2\pi a_0 b_0)$, which well agrees with Eq. (2.14). The integral in (4.11) can be calculated analytically, resulting in

$$P(S) = \frac{S}{2\pi a_0 b_0} \cdot \frac{\alpha^2\sqrt{1+\beta^2} + \beta^2\sqrt{1+\alpha^2}}{(\alpha^2+\beta^2+\alpha^2\beta^2)\sqrt{1+\alpha^2}\sqrt{1+\beta^2}} \ , \tag{4.12}$$

where $\alpha^2 = S^2/(4a_0^2)$ and $\beta^2 = S^2/(4b_0^2)$. The asymptotic behaviour of $P(S)$ at large S is characterised as an inverse quadratic power law,

$$P(S) \approx \frac{4(a_0+b_0)}{\pi S^2}, \tag{4.13}$$

implying that, due to divergence, $P(S)$ does not have the first moment.

4.1.4 Singular times exponential distribution

The normalized singular distributions are defined as

$$g_a(a) = C_a|a|^{-\mu_a} e^{-\lambda_a|a|}, \quad g_b(b) = C_b|b|^{-\mu_b} e^{-\lambda_b|b|}, \tag{4.14}$$

with the normalization constants

$$C_i = \lambda_i^{1-\mu_i}/(2\Gamma(1-\mu_i)). \tag{4.15}$$

Here $i = a, b$ and the exponents $\mu_i < 1$ whereas $\Gamma(x)$ is the gamma function. These distribution functions are singular but integrable power laws for $a, b \to 0$ and they decay nearly exponentially in the tails. For the level spacing distribution it follows

$$P(S) = C_a C_b \ S\left(\frac{S}{2}\right)^{-(\mu_a+\mu_b)} \int_0^{\pi/2} \frac{d\varphi \ \exp\left(-\frac{S}{2}(\lambda_a\cos\varphi + \lambda_b\sin\varphi)\right)}{\cos^{\mu_a}\varphi \ \sin^{\mu_b}\varphi}, \tag{4.16}$$

but this formulae still have no analytical solutions. One can evaluate it for small argument S where the exponential can be approximated by 1. This results in the following level repulsion law, i.e. the fractional exponent power law

$$P(S) = C_a C_b \ S\left(\frac{S}{2}\right)^{-(\mu_a+\mu_b)} \frac{\Gamma(\frac{1}{2}-\frac{\mu_a}{2})\Gamma(\frac{1}{2}-\frac{\mu_b}{2})}{2\Gamma(1-\frac{\mu_a}{2}-\frac{\mu_b}{2})}. \tag{4.17}$$

The power law distribution of matrix elements leads to the power law repulsion in the level spacing distribution.

4.1.5 Comparison with numerics

Fig. 4.1 shows the numerically evaluated $P(S)$ for 2D random matrices defined by the four ensembles mentioned above and compared to the theoretical curves. An excellent agreement is observed for certain typical parameter values.

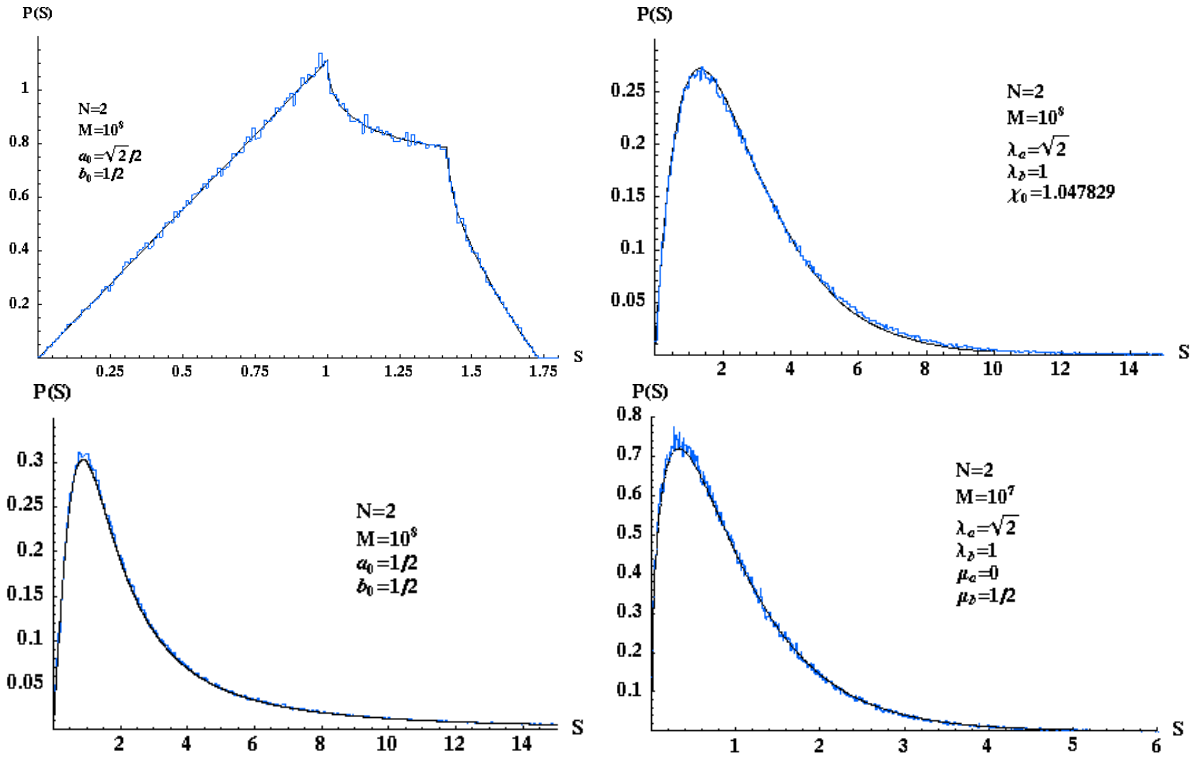

Figure 4.1: The numerical histograms are compared with the theoretical curves for the four ensembles from Sec. 4.1 (not unfolded, except for the singular times exponential case). M is the number of matrices taken from the ensemble. Top-left: Box distribution, $a_0 = \sqrt{2}/2$, $b_0 = 1/2$, $M = 10^8$. Top-right: Exponential distribution, $\lambda_a = \sqrt{2}$, $\lambda_b = 1$, $M = 10^8$. Bottom-left: Cauchy-Lorentz distribution $a_0 = 1/2$, $b_0 = 1/2$, $M = 10^8$. Bottom-right: Singular times exponential distribution: $\lambda_a = \sqrt{2}$, $\lambda_b = 1$, $\mu_a = 0$, $\mu_b = 1/2$, $M = 10^7$; this distribution is unfolded.

4.2 Numerical calculations with higher dimensional non-Gaussian random matrices

We have generalized the random matrix ensembles from Sec. 4.1 from $N = 2$ to the higher dimension N by applying the distribution $g_a(a)$ for all the diagonal elements of the N-dimensional real symmetric matrix and the distribution $g_b(b)$ for all the off-diagonal matrix elements.

This study primarily intends to determine whether there exists the transition (in the cases 4.1.1 and 4.1.2), or maybe there is not any (in the cases 4.1.3 and 4.1.4), from the nonuniversal behaviour at small N values to the Hackenbroich-Weidenmüller (HW) universal GOE behaviour at $N = \infty$. In the numerical studies of the spectra we have used two different types of spectral unfolding which is necessarily approximate due to the finite dimension of the spectra. For small matrices we have calculated the level spacings for the M representatives from the given ensemble (M is the number of matrices drawn from the ensemble). The spacings obtained have then been divided by the mean spacing calculated for the entire set. In the case of large matrices this rule does not make sense since the density of eigenvalues is strongly non-uniform. Therefore, in the case of larger matrices, we have applied the phenomenological rule (see Subsec. 2.5.1), which means that we have selected a certain number of the nearest neighbours (typically **unf** = 20 for

$N = 120$), so that the local mean level spacing has been calculated by averaging the entire set. One should emphasise that $N = 120$ and **unf** $= 20$ in the phenomenological unfolding procedure means $120 - 20 = 100$ effective energy levels (for comparison: in Sec. 2.5 only the effective points have been treated). The two unfolding procedures differ in the mean used; this mean can be either global or local, so it is sometimes hard to decide which type of mean is to be applied in the calculation. The results (unavoidably) depend on the unfolding method selected although, in most cases, its influence is not as large as one might expect at first sight.

4.2.1 Box (uniform) distribution

As observed in Fig. 4.2 the transition from $N = 2$ to GOE is quite fast since for $N = 3, 4$ one still notices certain deviations from the GOE (approximated by the Wigner distribution) whereas at $N = 7$ the agreement with the Wigner distribution is already perfect despite the fact that we have used the unfolding procedure for small matrices in this case (the procedure is described in the previous section). At the dimension $N = 120$ one observes perfect agreement with the GOE distribution for both the unfolding procedures, i.e. for small matrices as well as for the 20 neighbours-rule. This demonstrates that, at least in this case, the final results relatively weakly depend on the unfolding procedure. The last plot in Fig. 4.2 shows the eigenvalue distribution for the dimension $N = 120$, so one clearly sees that the limiting distribution is smooth and confined to a finite interval. Since the assumptions from the HW theorem are fulfilled in this case, the transition to the GOE behaviour is expected (see the plots from Fig. 4.2).

4.2.2 Exponential distribution

In comparison with the previous subsection the transformation of the level spacing distribution as a function of N is relatively slower here, but it completes at $N = 120$, which confirms the theoretical prediction (as observed in Fig. 4.3). The level spacing distribution approaches the Wigner distribution already at $N = 4$. Then the value of N increases from 7 to 10 and 20 so that the agreement is almost perfect. The last plot in Fig. 4.3 re-confirms this for the dimension $N = 120$. Like in the case of the box distribution the distribution of the eigenvalues for $N = 120$ is smooth and confined to a finite interval (but this is not shown in the figure).

4.2.3 Cauchy-Lorentz distribution

The Cauchy-Lorentz distribution is interesting, since its first moment diverges. One also knows that according to Eq. (4.13) the tail of $P(S)$ for $N = 2$ is proportional to $1/S^2$, so it does not have the first moment either. In the limit of very large Ns, such as $N = 120$, one clearly sees (Fig. 4.4) that the density of the eigenvalues is not confined to a finite interval. Thus, one of the assumptions from the HW theory is not fulfilled in this case, so in the limit $N \to \infty$ one might expect certain deviations from the universal GOE behaviour. This is indeed what one notices in Fig. 4.4, which shows the level spacing distribution for $N = 120$ for the unfolding procedure with **unf** $= 20$ neighbours. At smaller Ns, such as $N = 3$, 4, 7 and, also, at $N = 120$ if one uses the unfolding procedure typical of small matrices, we have observed an unusual behaviour of $P(S)$ which differs

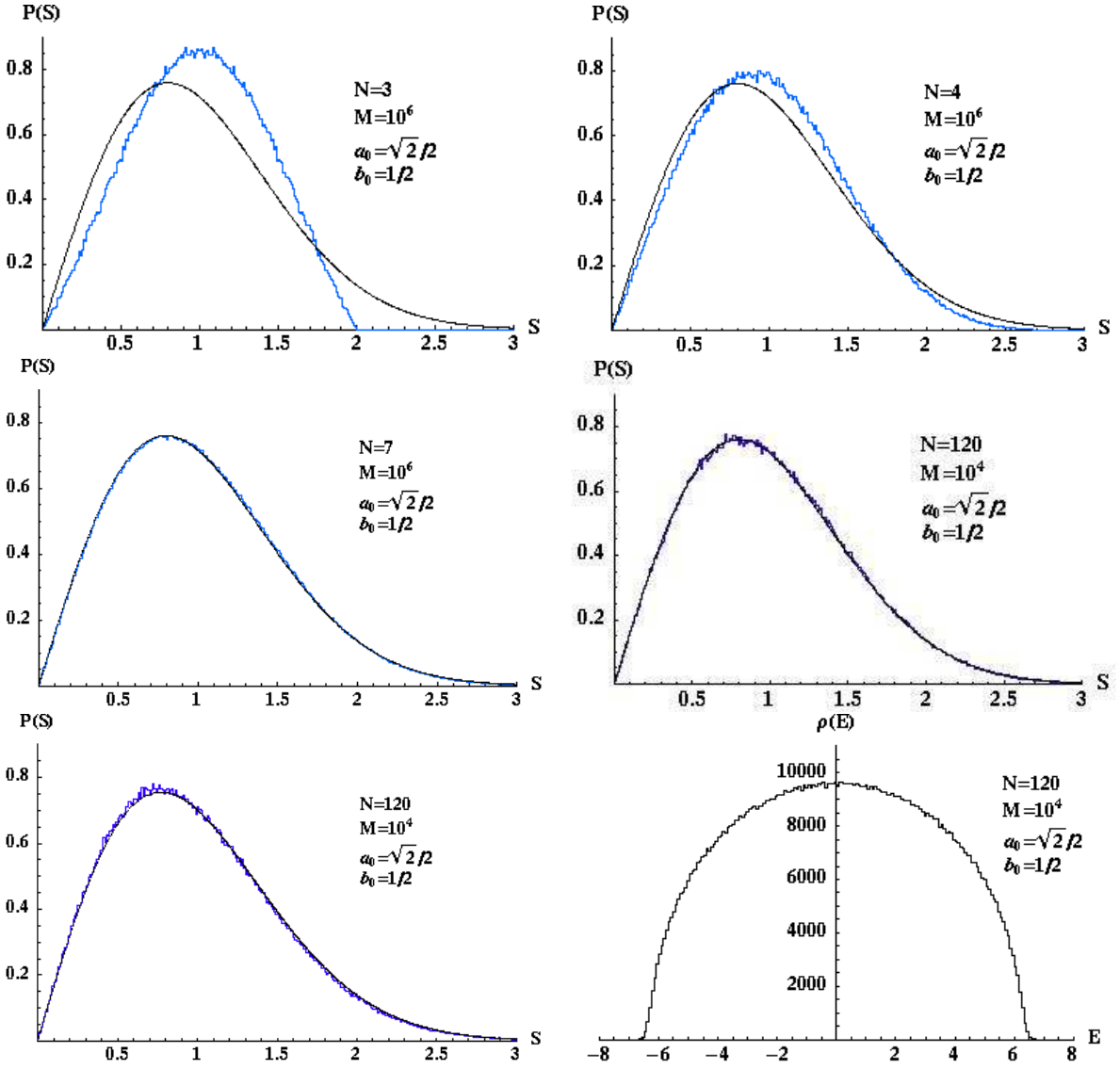

Figure 4.2: The numerical histograms compared with the Wigner curve for the ensemble with **the box distribution** for $a_0 = \sqrt{2}/2$, $b_0 = 1/2$. M is the number of matrices from the ensemble. Top-left: $N = 3$, $M = 10^6$, unfolding for small matrices. Top-right: $N = 4$, $M = 10^6$, unfolding for small matrices. Middle-left: $N = 7$, $M = 10^6$, unfolding for small matrices. Middle-right: $N = 120$, $M = 10^4$, unfolding for small matrices. Bottom-left: $N = 120$, $M = 10^4$, unfolding with **unf** $= 20$ neighbours. Here the curve represents the exact GOE result. Bottom-right: the eigenvalue distribution for $N = 120$, $M = 10^4$, showing that the distribution is smooth and confined to a finite interval.

in each case; clearly, this behaviour is influenced by the fact that the mean energy level spacing approaches infinity when $N \to \infty$. If certain singularities of the Cauchy-Lorentz distribution of the matrix elements are eliminated (by cutting off the tails at a large but finite a, b), one observes the immediate transition to the GOE behaviour, which well agrees with the HW theory (see Fig. 4.4). The cutting is realised via the transformation from the uniform distributed random numbers a_{box}, b_{box} to the Cauchy-Lorentz distributed random numbers a, b. This transformation is represented by

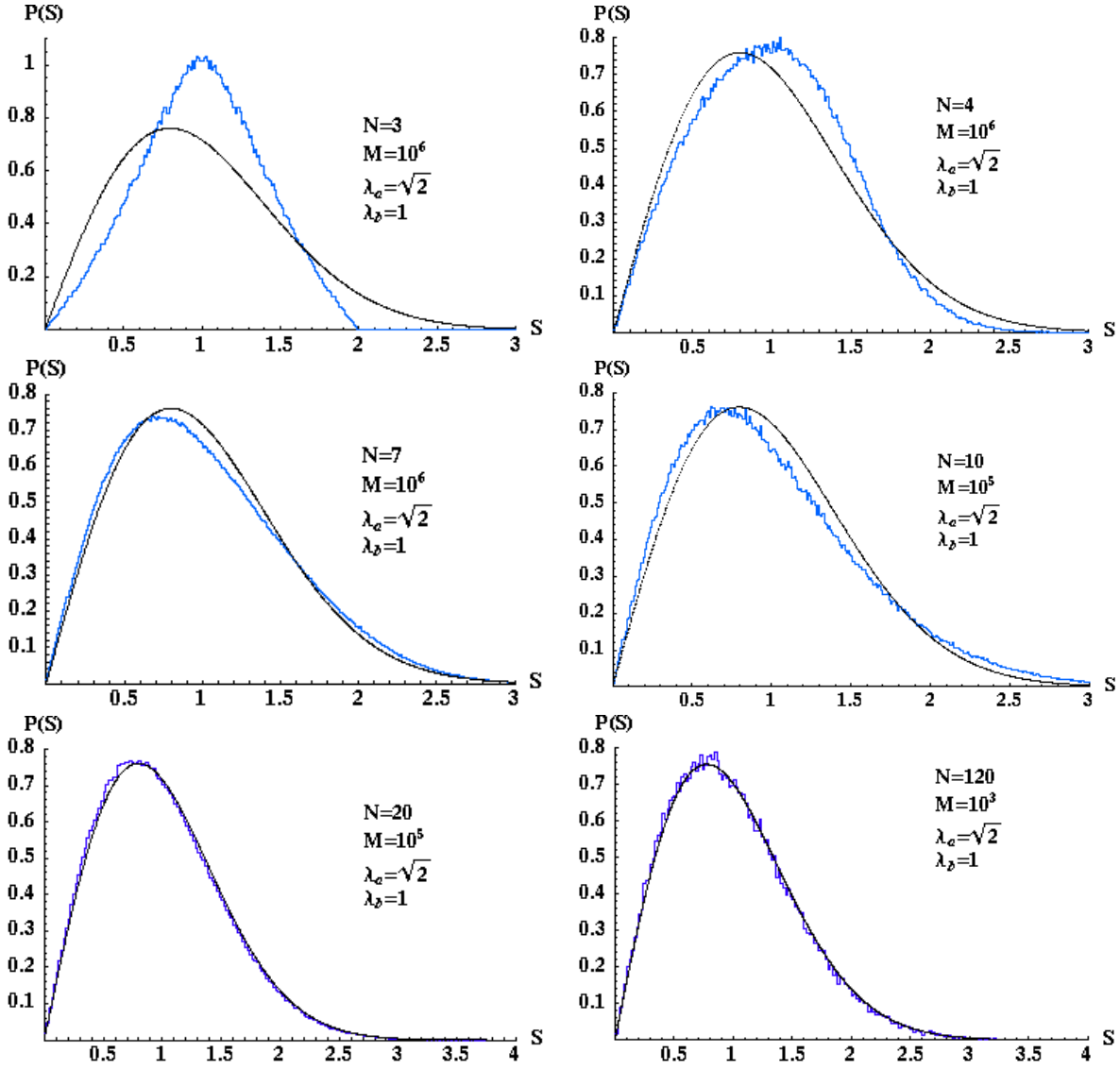

Figure 4.3: The numerical histograms compared with the Wigner curve for the ensemble with **the exponential distribution** for $\lambda_a = \sqrt{2}$, $\lambda_b = 1$. M is the number of matrices from the ensemble. Top-left: $N = 3$, $M = 10^6$, unfolding for small matrices. Top-right: $N = 4$, $M = 10^6$, unfolding for small matrices. Middle-left: $N = 7$, $M = 10^6$, unfolding for small matrices. Middle-right: $N = 10$, $M = 10^5$, unfolding for small matrices. Bottom-left: $N = 20$, $M = 10^5$, unfolding with **unf** $= 6$ neighbours. Bottom-right: $N = 120$, $M = 10^3$, unfolding with **unf** $= 20$ neighbours. Here the curve represents the exact GOE result.

$$a = a_0 \tan\left(\frac{\pi}{2}\frac{a_{box}}{a_0}\right), \qquad b = b_0 \tan\left(\frac{\pi}{2}\frac{b_{box}}{b_0}\right), \tag{4.18}$$

where a_{box}, b_{box} are uniformly distributed on the intervals $[-a_0(1-\epsilon), a_0(1-\epsilon)]$ and $[-b_0(1-\epsilon), b_0(1-\epsilon)]$ respectively. Thus, a, b are Cauchy-Lorentz distributed with $g_a(a)$, $g_b(b)$ from Subsec. 4.1.3 up to the border $a_{cut} = a_0 \tan\left(\frac{\pi}{2}(1-\epsilon)\right)$ and $b_{cut} = b_0 \tan\left(\frac{\pi}{2}(1-\epsilon)\right)$ where $|a| \leq a_{cut}$ and $|b| \leq b_{cut}$. The value $\epsilon = 0.01$ has been chosen for the last plot from Fig. 4.4.

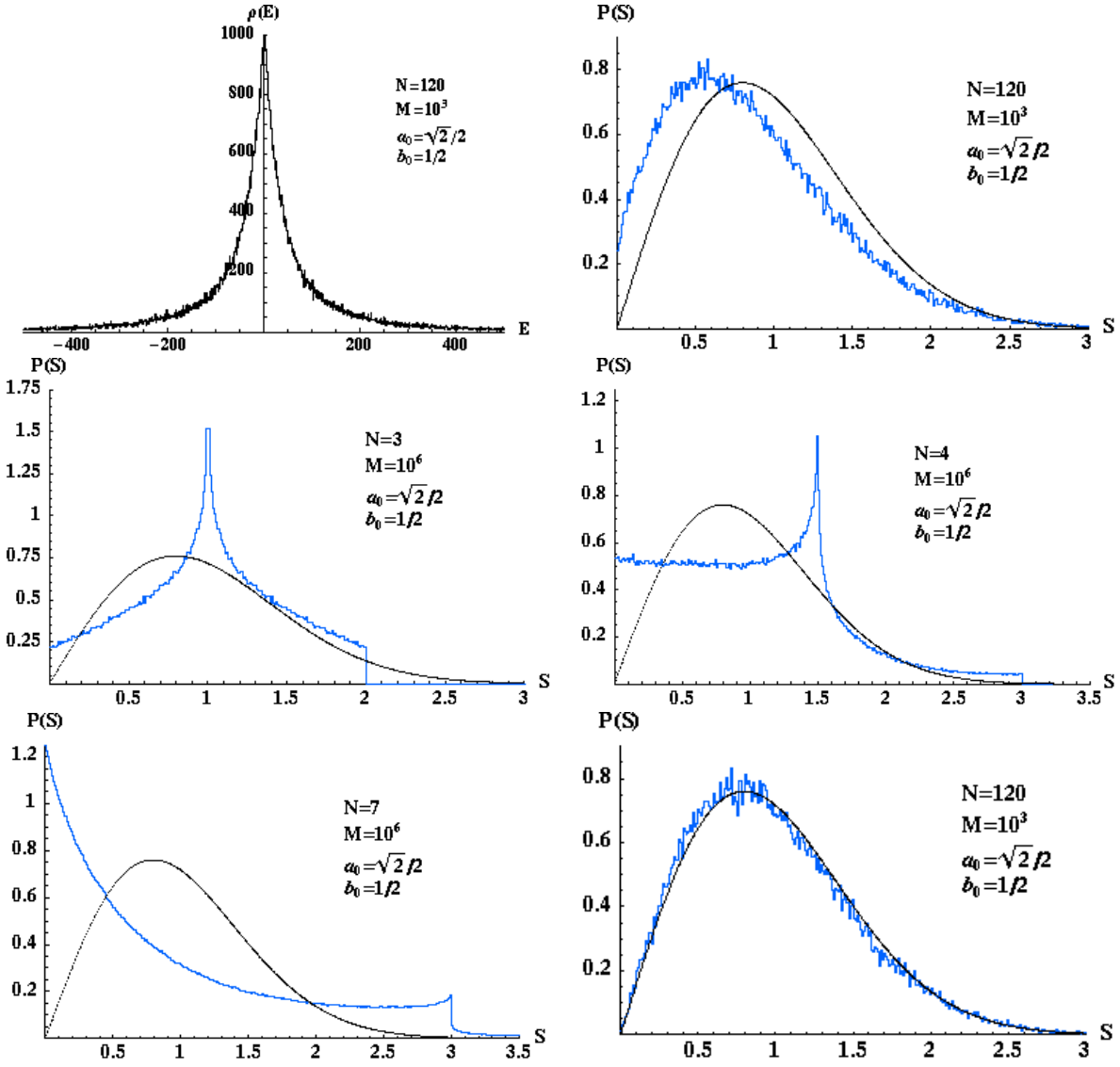

Figure 4.4: The numerical data for the ensemble with **the Cauchy-Lorentz distribution** for $a_0 = \sqrt{2}/2$, $b_0 = 1/2$. M indicates the number of matrices selected from the ensemble. For the sake of comparison the thin curve represents the Wigner distribution. Top-left: the density of the eigenvalues for $N = 120$, $M = 10^3$ which is obviously not confined to a finite interval. Top-right: $N = 120$, $M = 10^3$, unfolding with **unf** $= 20$ neighbours, the smooth curve is the Wigner distribution for the sake of comparison. Middle-left: $N = 3$, $M = 10^6$, unfolding for small matrices. Middle-right: $N = 4$, $M = 10^6$, unfolding for small matrices. Bottom-left: $N = 7$, $M = 10^6$, unfolding for small matrices. Bottom-right: $N = 120$, $M = 10^3$, unfolding with **unf** $= 20$ neighbours. Here the tails of the matrix element distribution function have been cut off at the specific value of $\epsilon = 0.01$, due to which the level spacing distribution immediately approaches the GOE behaviour.

4.2.4 Singular times exponential distribution

The singular (times exponential) distribution from Sec. 4.1.4 (4.14) at the dimension $N = 2$ might trigger off a completely new phenomenon, i.e. the fractional power law level repulsion (see Fig. 4.1). Surprisingly, if this ensemble is generalised to the higher

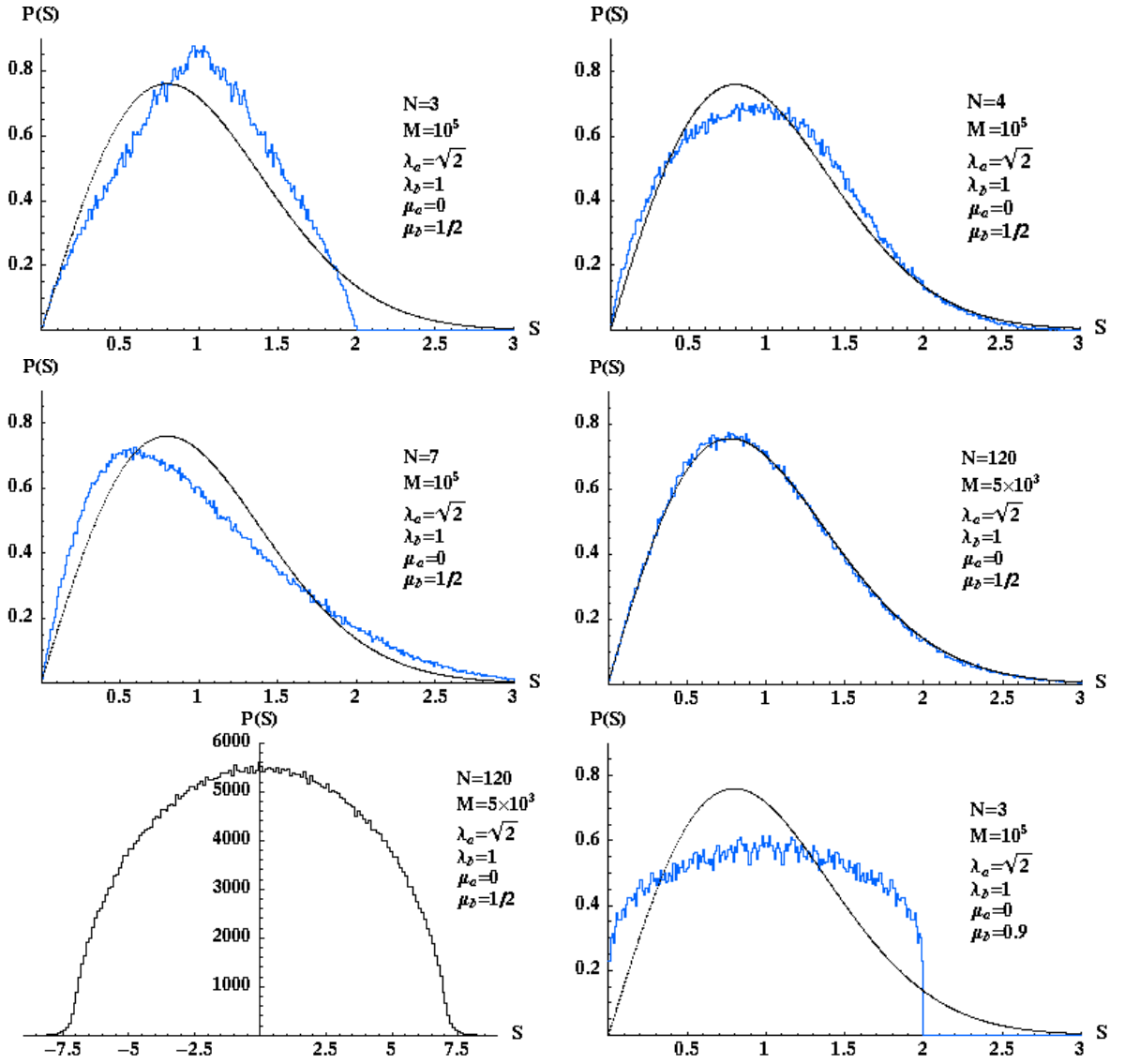

Figure 4.5: The numerical histograms compared with the Wigner curve (except for $N = 120$ where the exact GOE appears) for the ensemble with **the singular times exponential distribution** for $\lambda_a = \sqrt{2}$, $\lambda_b = 1$, $\mu_a = 0$, and $\mu_b = 1/2$, except in the last plot (bottom-right) where $\mu_b = 0.9$. M indicates the number of matrices chosen from the ensemble. Top-left: $N = 3$, $M = 10^5$, unfolding for small matrices. Top-right: $N = 4$, $M = 10^5$, unfolding for small matrices. Middle-left: $N = 7$, $M = 10^5$, unfolding for small matrices. Middle-right: $N = 120$, $M = 5 \times 10^3$, unfolding with **unf** $= 20$ neighbours. Here the curve represents the exact GOE result. Bottom-left: $N = 120$, $M = 5 \times 10^3$, the eigenvalue density. Bottom-right: $N = 3$, $M = 10^5$, unfolding for small matrices.

dimensions of $N > 2$, for $\mu_a = 0$ and $\mu_b = 1/2$, one observes a transition to the linear level repulsion already at the dimension $N = 3$. Fig. 4.5 shows a relatively fast transition to the GOE distribution appearing with the increasing values of N. One can verify that the level density for $N = 120$ is confined to a finite interval, so the HW prediction applies in this case. If one increases the value of μ_b to $\mu_b = 0.9$, i.e. closer to the nonintegrable singularity $\mu_b = 1$, this influences the $P(S)$ behaviour so strongly that the fractional power law level repulsion can be observed in the end.

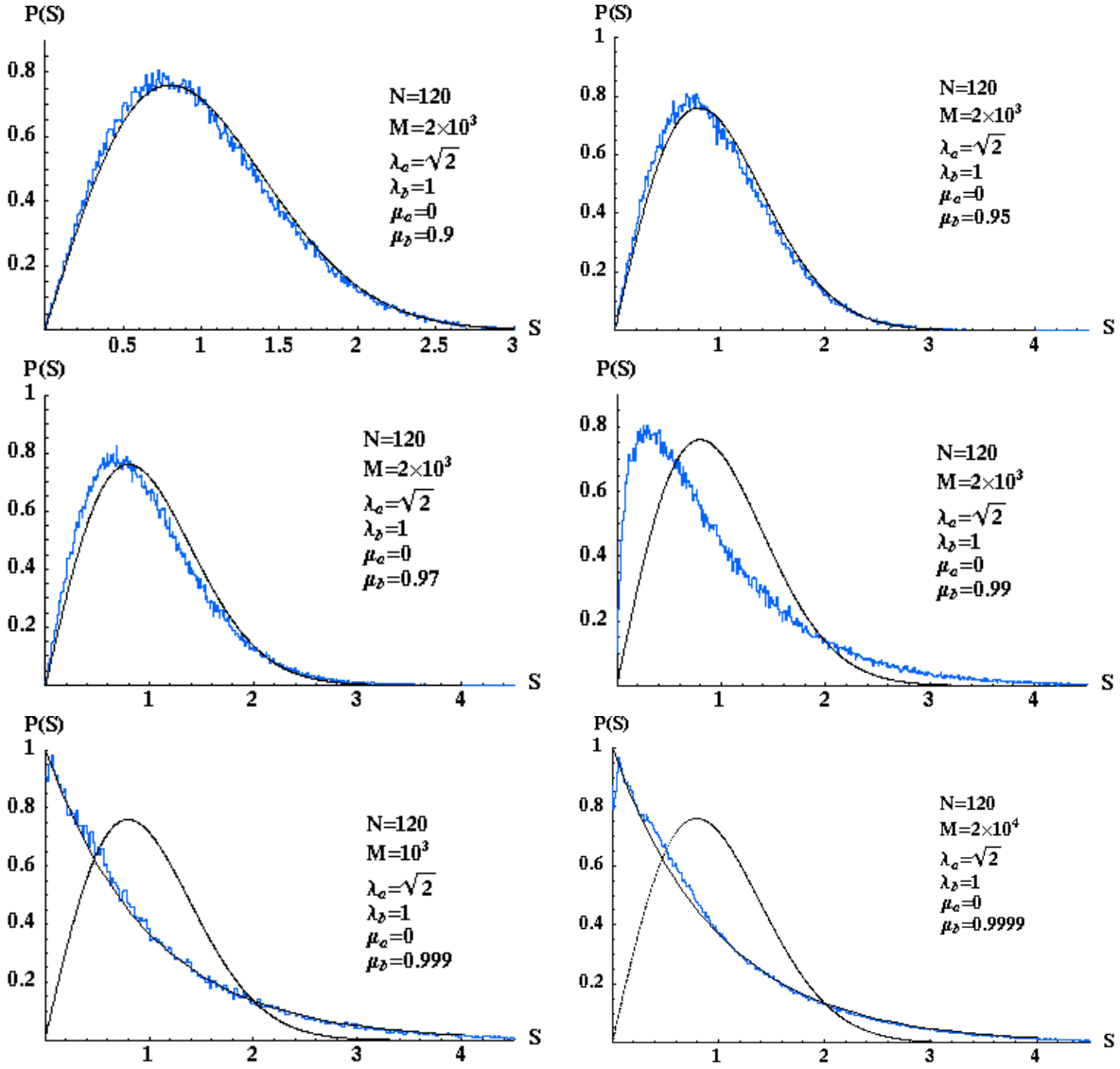

Figure 4.6: The numerical histograms compared with the Wigner curve for the ensemble with **the singular times exponential distribution** for $\lambda_a = \sqrt{2}$, $\lambda_b = 1$, $\mu_a = 0$, and μ_b varying from 0.9 to 0.9999. In all the cases the dimension of the matrices was $N = 120$ and the unfolding was calculated via **unf** $= 20$ neighbours. M indicates the number of matrices chosen from the ensemble. Top-left: $\mu_b = 0.9$, $N = 120$, $M = 2 \times 10^3$. Top-right: $\mu_b = 0.95$, $N = 120$, $M = 2 \times 10^3$. Middle-left: $\mu_b = 0.97$, $N = 120$, $M = 2 \times 10^3$. Middle-right: $\mu_b = 0.99$, $N = 120$, $M = 2 \times 10^3$. Bottom-left: $\mu_b = 0.999$, $N = 120$, $M = 10^3$, one can also observe the Poissonian curve $P(S) = \exp(-S)$. Bottom-right: $\mu_b = 0.9999$, $N = 120$, $M = 2 \times 10^4$ and the Poissonian curve $P(S) = \exp(-S)$ as well.

However, as the exponent μ_b increases and approaches the nonintegrable singularity $\mu_b = 1$, in the case of large matrices with $N = 120$ there appears the transition from the GOE (at smaller values of μ_b) to the Poissonian (exponential) if μ_b is sufficiently close to the value 1 (see Fig. 4.6). At the intermediate values of μ_b, such as $\mu_b \approx 0.99$, we have conjectured the fractional power law level repulsion, althoug additional analytical as well as numerical analysis is needed to provide more quantitative predictions and descriptions.

Chapter 5

Summary and conclusions

This thesis mainly discusses dynamical tunneling (a concept introduced in (Davis and Heller, 1981)) in the systems with the mixed (i.e. regular-chaotic) type dynamics. We have considered two different aspects: (**i**) we have studied the level spacing distribution for a general mixed-type system and tested the theory for the mushroom billiard levels and (**ii**) we have analysed the tunneling rates as well as the avoided-crossing distribution for the mushroom billiard. Additionally, we have calculated the level spacing distribution for the random matrices of non-Gaussian ensembles in order to model the fractional power-law level repulsion.

In Chap. 2 we have devised a new random matrix model which describes the distorted Berry-Robnik level spacing distribution affected by the tunneling between the regular and the chaotic states, denoted by $P^{Tn}_{DBRN}(S)$. We have derived a two-level analytic formula for $P^{Tn}_{DBR}(S)$ which agrees with the results for higher dimensional random matrices at not too large values of the coupling parameter. We have also developed an analytic two-level model creating the level spacing distribution $P^{An}_{DBR}(S)$ for the all-to-all level couplings, which well applies in the cases of general perturbation such as the presence of an antenna in a microwave resonator. Since this all-to-all two dimensional model, where all the levels are coupled, perfectly agrees with the N-dimensional simulations denoted by $P^{An}_{DBRN}(S)$, this is, certainly, a very successful model. Its exact integral representation $P^{A}_{DBR}(S)$ can be analytically expressed in a closed form for small as well as for large values of S. The same applies for the tunneling-distorted Berry-Robnik distribution $P^{Tn}_{DBR}(S)$ where only the regular and the chaotic levels are coupled. However, an overall good, simple analytic approximation has not been devised yet. We have also shown that the non-Gaussian models for the all-to-all couplings (i.e. the exponential and the box distributions for the off-diagonal matrix elements) well agree with the Gaussian model although they deviate from it significantly a the intermediate values of S. However, they almost perfectly agree with the corresponding two-dimensional model.

The experimental and the numerical data for the mushroom billiard (see Chap. 3) can be well described by the theoretical models employed. If the energy increases towards infinity (the semiclassical limit), σ should approach zero (and there appears the BR behaviour), which does not necessarily happen quickly and monotonously. We have noticed that σ somehow decreased (but not monotonously), but this cannot be confirmed by the results obtained, so one cannot make any definite conclusions at this point. The reason, presumably, lies mainly in the theory since two important things were not taken into account, i.e (**i**) the splittings of regular states due to the presence of chaotic states and

(**ii**) localisation effects. There may be other reasons as well, i.e. the experimental and the numerical inaccuracy of the mushroom levels or, even, the specific properties of the very mushroom billiard, such as scarred (Dietz et al., 2007) or bouncing-ball eigenfunctions. In the future we intend to improve the theory in the way discussed in Sec. 2.6, so that it can be tested in other systems, billiards or maps, or even in the recalculated mushroom billiard levels with the new method of particular solutions. In the case of the mushroom billiard the semiclassical limit is reached very quickly, i.e. already after a few thousands of levels. For the numerical level dynamics in this high lying regime one should definitely apply the method of particular solutions since the EBIM would be too slow in this case. Experimentally, without using the superconducting cavity - in (Dietz et al., 2007) the authors resolved the first 938 resonances and some additional ones as well, but they did not reach more resonances since they only measured one billiard configuration at different antenna positions whereas we reached the 600th branch in the level dynamics measurement - obviously, this semiclassical limit is unreachable.

According to the overall picture of the level spacings in the mixed-type systems (Robnik and Prosen, 1997), there exists the regime of linear level repulsion at small S whereas the regime of the fractional power law level repulsion appears at larger S followed by the Berry-Robnik tail. Thus, the theoretical approach presented seems to be very promising. The linear level repulsion, which always exists due to tunneling, is a very robust phenomenon indeed (Grossmann and Robnik, 2007b).

Recently, V.A. Podolskiy and E.E. Narimanov have tried to correct the Berry-Robnik level spacing distribution by modelling the tunneling effects in another way, which has resulted in the formula presented in (Podolskiy and Narimanov, 2003b) and based on (Podolskiy and Narimanov, 2003a). However, this derivation is incomplete and inconsistent since it does not incorporate the normalisation and since the physical grounds and the results are questionable, so this approach is not discussed in any further details.

Localisation effects should cause the fractional power law level repulsion, as captured by the Brody-like distribution (Prosen and Robnik, 1994a,b). We have tried to model localisation in Chap. 4 of the thesis where we have numerically studied four non-Gaussian ensembles of real symmetric random matrices for various dimensions N, from $N = 2$ to $N = 120$, defined by (a) the box, (b) the exponential, (c) the Cauchy-Lorentz and (d) the singular times exponential distribution. We have studied the transition to the universality regime at $N \to \infty$, precisely described by the GOE from the random matrix theory, as predicted in (Hackenbroich and Weidenmüller, 1995), provided that two conditions are fulfilled, i.e. (**i**) the limiting eigenvalue distribution is smooth, and (**ii**) it is confined to a finite interval.

In the first two cases (a) and (b) the two conditions are fulfilled, so the HW prediction is confirmed whereas in the case (c) the level spacing distribution clearly deviates from the GOE curve since the eigenvalue distribution is not confined to a finite interval. At the intermediate values of N the behaviour of $P(S)$ is quite unusual indeed. In the case (d), for the singular times exponential distribution of the off-diagonal matrix elements, only a partial deviation from the HW theorem and the two conditions presented can be observed. This happens at those values of μ_b which closely approach to the nonintegrable singularity $\mu_b = 1$. Thus, surprisingly, the fractional power law level repulsion, which is clearly manifested in the two-dimensional theory (Grossmann and Robnik, 2007b) and in its simulation, does not appear at the higher dimensions $N > 2$, except, possibly, for the case of a specific interval of μ_b approaching the nonintegrable value 1, e.g. at $\mu_b \approx 0.99$.

However, only additional numerical and analytical studies could explain the behaviour of singular random matrix ensembles in more details. Indeed, the Hamilton operators of nearly integrable systems (slightly perturbed integrable systems in the KAM scenario) in the basis of the integrable part are quantally represented as sparsed matrices, which should exhibit singular distribution of matrix elements (Prosen and Robnik, 1993a).

Chap. 3 experimentally and numerically studies the tunneling rates γ_{mn} in the mushroom billiards. Fermi's golden rule is applied to all possible eigenstates $\psi_{1/4}^{mn}$ of the quarter circle which are also termed 'pure regular states of the mushroom billiard' and which decay into the neighbouring chaotic states. The results have confirmed the theory especially devised for the mushroom billiard. We have observed a very good agreement without any free parameters including the error bars, which is unprecedented for billiards. On average an eigenstate of the quarter circle with quantum numbers (m, n) decays by about one order of magnitude slower than the one with quantum numbers $(m, n + 1)$. This result could be, potentially, applied in the field of microlasers, optical fibres, etc.

Surprisingly, Fermi's golden rule which is derived for the continuum distribution of levels, well applies in closed systems, i.e. in systems with the discrete distribution of levels. Strictly speaking, this rule should be applied only in the case of the open mushroom billiard where the depth of the mushroom foot is infinite, but it is, obviously, suitable in this case as well.

In theory, the approach using a fictitious integrable system could, hopefully, be applied to other generic billiards where it is much more challenging and difficult to determine an appropriate H_{reg}. In the experiment presented the unavoidable coupling to the environment was preferred for small tunneling rates; however Fig. 3.27 shows that in the microwave experiment the coupling by the antenna is actually negligible beyond three orders of magnitude. This is a promising aspect for future experimental studies of more complex systems, especially in the cases where the numerical and theoretical results are not available yet.

Similarly, the tunneling rates could also be studied in the full chaotic systems, such as the Sinai or the stadium billiard. Here, one could study the decay rates of the bouncing-ball states into the (pure) eigenstates. In this way, one could learn a lot about the strength of interaction between the bouncing-ball modes and the eigenstates, one could, for example, determine how localisation influences the splittings at avoided crossings, to determine the relationship between tunneling and localisation. Similarly, this could also be studied in the mushroom billiard.

Chap. 3 also presents the results of the numerical study of the avoided-crossing distribution in the mushroom billiard. Both types of splittings, i.e. splittings at CC avoided crossings and splittings at RC avoided crossings, were studied separately. In the case of CC splittings we have found very good agrement with the 2×2 RMT prediction. However, one still cannot explain a ratio of the mean splitting and the mean level spacing which is smaller than predicted. Due to these new results, the RMT prediction may eventually be generalised to the CC splittings from the mixed-type systems.

Bibliography

Abramowitz, M. and Stegun, I. A. (1970). *Handbook of Mathematical Functions with Formulas, Graphs, and Mathematical Tables*. Dover, New York, ninth edition.

Abul-Magd, A. Y. and Simbel, M. H. (2000). High-order level-spacing distributions for mixed systems. *Phys. Rev. E*, **62**:4792–4798.

Altmann, E. G., Motter, A. E., and Kantz, H. (2005). Stickiness in mushroom billiards. *Chaos*, **15**(3):033105, 1–7.

Altmann, E. G., Motter, A. E., and Kantz, H. (2006). Stickiness in Hamiltonian systems: From sharply divided to hierarchical phase space. *Phys. Rev. E*, **73**:026207, 1–10.

Arnold, V. I. (1989). *Mathematical Methods of Classical Mechanics*. Springer, New York, second edition.

Bäcker, A. (2003). Numerical aspects of eigenvalue and eigenfunction computations for chaotic quantum systems. *Lecture Notes in Physics*, **618**:91–144.

Bäcker, A., Ketzmerick, R., Löck, S., Robnik, M., Vidmar, G., Höhmann, R., Kuhl, U., and Stöckmann, H.-J. (2008a). Dynamical tunneling in mushroom billiards. *Phys. Rev. Lett.*, **100**:174103.

Bäcker, A., Ketzmerick, R., Löck, S., and Schilling, L. (2008b). Regular-to-chaotic tunneling rates using a fictitious integrable system. *Phys. Rev. Lett.*, **100**:104101.

Bäcker, A., Ketzmerick, R., and Monastra, A. G. (2005). Flooding of chaotic eigenstates into regular phase space islands. *Phys. Rev. Lett.*, **94**:054102.

Bäcker, A., Ketzmerick, R., and Monastra, A. G. (2007). Universality in the flooding of regular islands by chaotic states. *Phys. Rev. E*, **75**:066204, 1–11.

Bäcker, A. and Schubert, R. (2002). Amplitude distribution of eigenfunctions in mixed systems. *J. Phys. A: Math. Gen.*, **35**:527–538.

Barnett, A. H. and Betcke, T. (2007). Quantum mushroom billiards. *Chaos*, **17**(4):043125.

Barth, M., Kuhl, U., and Stöckmann, H.-J. (1999). Global versus local level dynamics: the limits of universality. *Phys. Rev. Lett.*, **82**:2026.

Berry, M. V. (1977). Regular and irregular semiclassical wavefunctions. *J. Phys. A: Math. Gen.*, **10**:2083–2091.

Berry, M. V. (1985). Semiclassical theory of spectral rigidity. *Proc. Roy. Soc. Lond. A*, **400**:229–251.

Berry, M. V. (2002). Statistics of nodal lines and points in chaotic quantum billiards: perimeter corrections, fluctuations, curvature. *J. Phys. A: Math. Gen.*, **35**:3025–3038.

Berry, M. V. and Robnik, M. (1984). Semiclassical level spacings when regular and chaotic orbits coexist. *J. Phys. A: Math. Gen.*, **17**:2413–2421.

Berry, M. V. and Robnik, M. (1986). Statistics of energy levels without time-reversal symmetry: Aharonov-Bohm chaotic billiards. *J. Phys. A: Math. Gen.*, **19**:649–668.

Berry, M. V. and Tabor, M. (1977). Level clustering in the regular spectrum. *Proc. Roy. Soc. Lond. A*, **356**:375–394.

Betcke, T. and Trefethen, L. N. (2005). Reviving the method of particular solutions. *SIAM Review*, **47**:469–491.

Bohigas, O., Boosé, D., Egydio de Carvalho, R., and Marvulle, V. (1993a). Quantum tunneling and chaotic dynamics. *Nucl. Phys. A*, **A560**:197–210.

Bohigas, O., Giannoni, M. J., and Schmit, C. (1984). Characterization of chaotic quantum spectra and universality of level fluctuation laws. *Phys. Rev. Lett.*, **52** (1):1.

Bohigas, O., Tomsovic, S., and Ullmo, D. (1990). Dynamical quasidegeneracies and separation of regular and irregular levels. *Phys. Rev. Lett.*, **64**(13):1479.

Bohigas, O., Tomsovic, S., and Ullmo, D. (1993b). Manifestations of classical phase space structures in quantum mechanics. *Phys. Rep.*, **223**(2):43–133.

Brodier, O., Schlagheck, P., and Ullmo, D. (2001). Resonance-assisted tunneling in near-integrable systems. *Phys. Rev. Lett.*, **87**:064101.

Brodier, O., Schlagheck, P., and Ullmo, D. (2002). Resonance-assisted tunneling. *Ann. Phys.*, **300**:88–136.

Bunimovich, L. A. (1974). On ergodic properties of certain billiards. *Funct. Anal. Appl.*, **8**(3):254–255.

Bunimovich, L. A. (2001). Mushrooms and other billiards with divided phase space. *Chaos*, **11** (4):802–808.

Casati, G., Guarneri, I., and Valz-Gris, F. (1980). On the connection between quantization of nonintegrable systems and statistical theory of spectra. *Lette. Nuovo Cimento*, **28**:279.

Davis, M. J. and Heller, E. J. (1981). Quantum dynamical tunneling in bound states. *J. Chem. Phys.*, **75**:246.

Dembowski, C., Gräf, H.-D., Heine, A., Hofferbert, R., Rehfeld, H., and Richter, A. (2000). First experimental evidence for chaos-assisted tunneling in a microwave annular billiard. *Phys. Rev. Lett.*, **84**(5):867.

Dietz, B., Friedrich, T., Miski-Oglu, M., Richter, A., and Schäfer, F. (2007). Spectral properties of Bunimovich mushroom billiards. *Phys. Rev. E*, **75**:035203(R), 1–4.

Dietz, B., Friedrich, T., Miski-Oglu, M., Richter, A., Seligman, T. H., and Zapfe, K. (2006). Nonperiodic echoes from mushroom billiard hats. *Phys. Rev. E*, **74**:056207, 1–8.

Doron, E. and Frischat, S. D. (1995). Semiclassical description of tunneling in mixed systems: case of the annular billiard. *Phys. Rev. Lett.*, **75**(20):3661.

Eltschka, C. and Schlagheck, P. (2005). Resonance- and chaos-assisted tunneling in mixed regular-chaotic systems. *Phys. Rev. Lett.*, **94**:014101.

Feist, J., Bäcker, A., Ketzmerick, R., Rotter, S., Huckestein, B., and Burgdörfer, J. (2006). Nanowires with surface disorder: giant localization lengths and quantum-to-classical crossover. *Phys. Rev. Lett.*, **97**:116804.

Frischat, S. D. and Doron, E. (1998). Dynamical tunneling in mixed systems. *Phys. Rev. E*, **57**(2):1421–1443.

Gräf, H.-D., Harney, H. L., Lengeler, H., Lewenkopf, C. H., Rangacharyulu, C., Richter, A., Schardt, P., and Weidenmüler, H. A. (1992). Distribution of eigenmodes in a superconducting stadium billiard with chaotic dynamics. *Phys. Rev. Lett.*, **69**(9):1296.

Grossmann, S. and Robnik, M. (2007a). On level spacing distributions for 2D non-normal Gaussian random matrices. *J. Phys. A: Math. Theor.*, **40**:409–421.

Grossmann, S. and Robnik, M. (2007b). Some generic properties of level spacing distributions of 2D real random matrices. *Zeitschrift für Naturforschung A*, **62**:471–482.

Guhr, T., Müller-Gröling, A., and Weidenmüller, H. A. (1998). Random matrix theories in quantum physics: Common concepts. *Phys. Rep.*, **299**:189–425, cond-mat/9707301.

Haake, F. (2001). *Quantum signatures of chaos*. Springer, Heidelberg, New York, second edition.

Haake, F., Kuś, M., Šeba, P., Stöckmann, H.-J., and Stoffregen, U. (1996). Microwave billiards with broken time reversal invariance. *J. Phys. A: Math. Gen.*, **29**:5745–5757.

Hackenbroich, G. and Weidenmüller, H. (1995). Universality of random-matrix results for non-Gaussian ensembles. *Phys. Rev. Lett.*, **74**:4118.

Hanson, J., Ott, E., and Antonsen, T. (1984). Influence of finite wavelength on the quantum kicked rotator in the semiclassical regime. *Phys. Rev. A*, **29**:819–825.

Hensinger, W., Häffner, H., Browaeys, A., Heckenberg, N., Helmerson, K., McKenzie, C., Milburn, G., Phillips, W., Rolston, S., Rubinsztein-Dunlop, H., and Upcroft, B. (2001). Dynamical tunneling of ultracold atoms. *Nature*, **412**:52.

Heusler, S., Müller, S., Braun, P., and Haake, F. (2004). Universal spectral form factor for chaotic dynamics. *J. Phys.A: Math. Gen.*, **37**:L31–L37.

Höhmann, R. (2004). *Untersuchung von Billiards mit symmetrischer Unordnung*. University of Marburg. BS thesis.

Ishikawa, A., Tanaka, A., and Shudo, A. (2007). Quantum suppression of chaotic tunneling. *J. Phys. A: Math. Theor.*, **40**:F1–F9.

Izrailev, F. M. (1989). Intermediate statistics of the quasi-energy spectrum and quantum localisation of classical chaos. *J. Phys. A: Math. Gen.*, **22**:865–878.

Izrailev, F. M. (1990). Simple models of quantum chaos: spectrum and eigenfunctions. *Phys. Rep.*, **196**:299.

Jackson, J. D. (1982). *Klassische Elektrodynamik*. Gruyter, Berlin, second edition.

Jacquod, P. and Amiet, J.-P. (1995). Evidence for the validity of the Berry-Robnik surmise in a periodically pulsed spin system. *J. Phys. A: Math. Gen.*, **28**(17):4799–4811.

Kaufmann, Z., Kormányos, A., Cserti, J., and Lambert, C. J. (2006). Quantized invariant tori in Andreev billiards of mixed phase space. *Phys. Rev. B*, **73**:214526, 1–4.

Ketzmerick, R., Hufnagel, L., Steinbach, F., and Weiss, M. (2000). New class of eigenstates in generic Hamiltonian systems. *Phys. Rev. Lett.*, **85**(6):1214.

Kuhl, U., Höhmann, R., Main, J., and Stöckmann, H.-J. (2008). Resonance widths in open microwave cavities studied by harmonic inversion. *Phys. Rev. Lett.*, **100**:254101.

Landau, L. D. and Lifshitz, E. M. (1989). *Quantum mechanics (Non-relativistic Theory)*. Butterworth-Heinemann, Oxford, third edition.

Lee, K.-C. (1989). What makes chaos border sticky? *Physica D*, **35**:186–202.

Lehman, R. S. (1959). Developments at an analytic corner of solutions of elliptic partial differential equations. *J. Math. Mech.*, **8**:727–760.

Leyvraz, F. and Ullmo, D. (1996). The level splitting distribution in chaos-assisted tunneling. *J. Phys. A: Math. Gen.*, **29**:2529–2551.

Lin, W. A. and Ballentine, L. E. (1990). Quantum tunneling and chaos in a driven anharmonic oscillator. *Phys. Rev. Lett.*, **65**(42):2927.

Lin, W. A. and Ballentine, L. E. (1992). Quantum tunneling and regular and irregular quantum dynamics of a driven double-well oscillator. *Phys. Rev. A*, **45**(6):3637–3645.

Main, J., Dando, P. A., Belkić, D., and Taylor, H. S. (2000). Decimation and harmonic inversion of periodic orbit signals. *J. Phys. A: Math. Gen.*, **33**:1247–1263.

Malovrh, J. and Prosen, T. (2002). Spectral statistics of a system with sharply divided phase space. *J. Phys. A: Math. Gen.*, **35**:2483–2490.

Markarian, R. (1993). New ergodic billiards: exact results. *Nonlinearity*, **6**:819–841.

Mehta, M. L. (1991). *Random Matrices*. Academic Press, New York, San Diego, second, revised and enlarged edition.

Meyer, H.-D. (1985). Theory of the Liapunov exponents of Hamiltonian systems and a numerical study on the transition from regular to irregular classical motion. *J. Chem. Phys.*, **84**(6):3147–3160.

Mouchet, A., Miniatura, C., Kaiser, R., Grémaud, B., and D., D. (2001). Chaos-assisted tunneling with cold atoms. *Phys. Rev. E*, **64**:016221, 1–15.

Müller, S., Heusler, S., Braun, P., Haake, F., and Altland, A. (2004). Semiclassical foundation of universality in quantum chaos. *Phys. Rev. Lett.*, **93**:014103.

Narimanov, E. and Stone, A. (1999). Quantum chaos in quantum wells. *Physica*, **131**:221–246.

Okada, Y., Shudo, A., Tasaki, S., and Harayama, T. (2005). On the boundary element method for billiards with corners. *J. Phys. A: Math. Gen.*, **38**:6675–6688.

Pechukas, P. (1983). Distribution of energy eigenvalues in the irregular spectrum. *Phys. Rev. Lett.*, **51**:943.

Percival, I. C. (1973). Regular and irregular spectra. *J. Phys. B: Atom. Mol.*, **6**(9):L229–L232.

Pineda, C. and Prosen, T. (2007). Universal and nonuniversal level statistics in a chaotic quantum spin chain. *Phys. Rev. E*, **76**:061127.

Podolskiy, V. A. and Narimanov, E. E. (2003a). Semiclassical description of chaos-assisted tunneling. *Phys. Rev. Lett.*, **91**(26):263601.

Podolskiy, V. A. and Narimanov, E. E. (2003b). Universal level spacing distribution in quantum systems. *arXiv:nlin/0310034v1 [nlin:CD]*, pages 1–4.

Press, W. H., Flannery, B. P., Teukolsky, S. A., and Vetterling, W. T. (1986). *Numerical Recipes: The Art of Scientific Computing*. Cambridge University Press, Cambridge, etc.

Prosen, T. (1995). Quantum surface-of-section method: demonstration of semiclassical Berry-Robnik energy level-spacing distribution in a generic two-dimensional Hamiltonian system. *J. Phys. A: Math. Gen.*, **28**:L349–L355.

Prosen, T. (1998a). Berry-Robnik level statistics in a smooth billiard systems. *J. Phys. A: Math. Gen.*, **31**:7023–7029.

Prosen, T. (1998b). A new class of completely integrable quantum spin chains. *J. Phys. A: Math. Gen.*, **31**:L397–L403.

Prosen, T. and Robnik, M. (1993a). Energy level statistics and localization in sparsed banded matrix ensemble. *J. Phys. A: Math. Gen.*, **26**:1105–1114.

Prosen, T. and Robnik, M. (1993b). Energy level statistics in the transition region between integrability and chaos. *J. Phys. A: Math. Gen.*, **26**:2371–2387.

Prosen, T. and Robnik, M. (1994a). Numerical demonstration of the Berry-Robnik level spacing distribution. *J. Phys. A: Math. Gen.*, **27**(13):L459–L466.

Prosen, T. and Robnik, M. (1994b). Semiclassical energy level statistics in the transition region between integrability and chaos: transition from Brody-like to Berry-Robnik behaviour. *J. Phys. A: Math. Gen.*, **27**(24):8059–8077.

Prosen, T. and Robnik, M. (1999). Intermediate E(k,L) statistics in the regime of mixed classical dynamics. *J. Phys. A: Math. Gen.*, **32**:1863–1873.

Robnik, M. (1983). Classical dynamics of a family of billiards with analytic boundaries. *J. Phys. A: Math. Gen.*, **16**:3971–3986.

Robnik, M. (1986). Antiunitary symmetries and energy level statistics. *Lecture Notes in Physics*, **263**:120–130.

Robnik, M. and Berry, M. V. (1986). False time-reversal violation and energy level statistics: the role of anti-unitary symmetries. *J. Phys. A: Math. Gen.*, **19**:669–682.

Robnik, M., David, H. M., Vidmar, G., and Romanovskiy, V. (2007). Numerical studies of non-Gaussian real symmetric matrices: confirmation of the Hackenbroich-Weidenmüller theory. Preprint at CAMTP.

Robnik, M. and Prosen, T. (1997). Comment on energy level statistics in the mixed regime. *J. Phys. A: Math. Gen.*, **30**:8787–8793.

Robnik, M. and Veble, G. (1998). On spectral statistics of classically integrable systems. *J. Phys. A: Math. Gen.*, **31**:4669–4704.

Sheinman, M., Fishman, S., Guarneri, I., and Rebuzzini, L. (2006). Decay of quantum accelerator modes. *Phys. Rev. A*, **73**:052110, 1–12.

Shudo, A. and Ikeda, K. S. (1995). Complex classical trajectories and chaotic tunneling. *Phys. Rev. Lett.*, **74**:682.

Sieber, M. and Richter, K. (2001). Correlations between periodic orbits and their role in spectral statistics. *Physica Scripta*, **T90**:128–133.

Sinai, Y. G. (1970). Dynamical systems with elastic reflections; ergodic properties of dispersing billiards. *Russian Math. Surveys*, **25**:137.

Steck, D., Oskay, W., and Raizen, M. (2001). Observation of chaos-assisted tunneling between islands of stability. *Science*, **293**:274.

Stein, J., Stöckmann, H.-J., and Stoffregen, U. (1995). Microwave studies of billiard Green functions and propagators. *Phys. Rev. Lett.*, **75**(1):53.

Stöckmann, H.-J. (1999). *Quantum Chaos: An Introduction*. Cambridge University Press.

Stöckmann, H.-J. (2007). Private comunication.

Stöckmann, H.-J. and Stein, J. (1990). Quantum chaos in billiards studied by microwave absorption. *Phys. Rev. Lett.*, **64**(19):2215.

Tanaka, A. and Shudo, A. (2006). Recurrence time distribution in mushroom billiards with parabolic hat. *Phys. Rev. E*, **74**:036211, 1–5.

Tomsovic, S. and Ullmo, D. (1994). Chaos-assisted tunneling. *Phys. Rev. E*, **50**(1):145–162.

Veble, G., Kuhl, U., Robnik, M., Stöckmann, H.-J., Liu, J., and Barth, M. (2000). Experimental study of generic billiards with microwave resonators. *Prog. of Theor. Ph. Suppl. Num.*, **139**:283–300.

Veble, G., Prosen, T., and Robnik, M. (2007). Generalized scaling method and chaotic time-reversal doubles in quantum billiards. *New Journal of Physics*, **9**:15, 1–17.

Vidmar, G., Stöckmann, H.-J., Robnik, M., Kuhl, U., Höhmann, R., and Grossmann, S. (2007). Beyond the Berry-Robnik regime: a random matrix study of tunneling effects. *J. Phys. A: Math. Theor.*, **40**:13883–13905.

Šeba, P., Haake, F., Kus, M., Barth, M., Kuhl, U., and Stöckmann, H.-J. (1997). Distribution of the wave function inside chaotic partially open systems. *Phys. Rev. E*, **56**:2680–2686.

Wall, M. R. and Neuhauser, D. (1995). Extraction, through filter-diagonalisation, of general quantum eigenvalues or classical normal mode frequencies from a small number of residues or a short time segment of a signal. I. theory and application to a quantum-dynamics model. *J. Chem. Phys.*, **102**:8011.

Wiersig, J. and Hentschel, M. (2008). Combining directional light output and ultralow loss in deformed microdisks. *Phys. Rev. Lett.*, **100**:033901.

Wilkinson, M. (1986). Tunneling between tori in phase space. *Physica*, **21D**:341–354.

Wilkinson, M. (1987). Narrowly avoided crossings. *J. Phys. A: Math. Gen.*, **20**(3):635–645.

Yukawa, T. (1985). New approach to the statistical properties of energy levels. *Phys. Rev. Lett.*, **54**:1883.

Zakrzewski, J., Delande, D., and Buchleitner, A. (1998). Ionization via chaos assisted tunneling. *Phys. Rev. E*, **57** (2):1458–1474.

Zakrzewski, J., Delande, D., and Kuś, M. (1993). Parametric motion of energy levels in quantum chaotic systems. II. avoided-crossing distribution. *Phys. Rev. E*, **47** (3):1665–1676.

Appendix A

ρ_1 calculation for the mushroom billiard

The group from Dresden has analytically derived the classical effective chaotic area of the desymmetrised mushroom billiard for the central position of the foot: $b = R - a$. The derivation is presented in this appendix together with our numerical results.

The fraction ρ_2 of the chaotic part of the classical phase space volume of the 2D billiard system can be generally represented as

$$\rho_2 = \frac{\Omega_{PSC}}{\Omega_{PS}} = \frac{\int d\mathbf{q}\, d\mathbf{p}\, \chi_{ch}(\mathbf{q},\mathbf{p})\, \delta\left(E - H(\mathbf{q},\mathbf{p})\right)}{\int d\mathbf{q}\, d\mathbf{p}\, \delta\left(E - H(\mathbf{q},\mathbf{p})\right)}, \tag{A.1}$$

where Ω_{PS} is the volume of the whole classical phase space and Ω_{PSC} is the volume of the chaotic part of the classical phase space; $\chi_{ch}(\mathbf{q},\mathbf{p})$ equals 1 if the trajectory with the coordinate $\mathbf{q}$ and the momentum $\mathbf{p}$ is chaotic, but if this trajectory is regular, $\chi_{ch}(\mathbf{q},\mathbf{p})$ equals 0. Due to the relation $H(\mathbf{q},\mathbf{p}) = \frac{p^2}{2M} = E$ in billiards the Ω_{PS} is written as

$$\Omega_{PS} = \int d\mathbf{q}\, d\mathbf{p}\, \delta\left(E - \frac{p^2}{2M}\right). \tag{A.2}$$

The integration over the space coordinates provides the area A of the billiard. By replacing the double integral over the momenta with the integral over the energy one gets

$$\Omega_{PS} = 2\pi M A \int dE\, \delta\left(E - \frac{p^2}{2M}\right). \tag{A.3}$$

The remaining integral equals 1, which results in

$$\Omega_{PS} = 2\pi M A. \tag{A.4}$$

The phase space of the mushroom billiard (Fig. A.1) is given by $\{(r,\varphi,\vartheta) : (r,\varphi) \in \mathcal{D}, \vartheta \in [0, 2\pi]\}$, where (r,φ) are the polar coordinates of the position of the particle, $\mathcal{D}$ is the domain of the billiard and ϑ is the angle determining the direction of the particle's momentum. The Ω_{PSC} is written as

$$\begin{aligned}
\Omega_{PSC} &= \int d\mathbf{q}\, d\mathbf{p}\, \chi_{ch}(\mathbf{q},\mathbf{p})\, \delta\left(E - \frac{p^2}{2M}\right) \\
&= \int d\mathbf{q}\, p\, dp\, d\vartheta\, \chi_{ch}(\mathbf{q},\vartheta)\, \delta\left(E - \frac{p^2}{2M}\right) \\
&= M \int d\mathbf{q}\, dE\, d\vartheta\, \chi_{ch}(\mathbf{q},\vartheta)\, \delta\left(E - \frac{p^2}{2M}\right) \\
&= M \int d\mathbf{q}\, d\vartheta\, \chi_{ch}(\mathbf{q},\vartheta) \\
&= 2\pi M A_{ch},
\end{aligned} \tag{A.5}$$

where the last integration introduces the so-called effective chaotic area: $A_{ch} = 1/(2\pi) \int d\mathbf{q}\, d\vartheta\, \chi_{ch}(\mathbf{q},\vartheta)$.

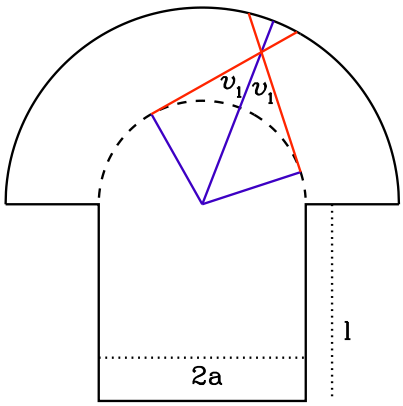

Figure A.1: The mushroom billiard with the central position of the foot. This figure shows the entire billiard whereas the derivation has been done for its desymmetrised part.

All the trajectories are chaotic in the foot and in the hat for $r < a$. Additionally, the region $r > a$ is characterised by regular and chaotic dynamics. Its contribution to A_{ch}, called I should be calculated as

$$A_{ch} = la + \frac{1}{4}\pi a^2 + I, \tag{A.6}$$

where

$$I = \frac{1}{2\pi} \int_0^{\frac{\pi}{2}} d\varphi \int_a^R r\, dr \int_0^{2\pi} d\vartheta\, \chi_{ch}(r,\varphi,\vartheta). \tag{A.7}$$

Only the radial coordinate r determines whether there appear chaotic trajectory in the hat for $r > a$ (see Fig. A.1). If one considers the trajectories crossing the point (r,φ) with $r \in [a,R]$, all the chaotic ones lie inside the red zone since they have crossed and/or they will cross the small circle with $r = a$, which results in

$$I = \frac{1}{2\pi} \int_0^{\frac{\pi}{2}} d\varphi \int_a^R r\, dr\, 4 \int_0^{\vartheta_1(r)} d\vartheta, \tag{A.8}$$

where $\vartheta_1(r)$ is represented by trigonometric relations as $\vartheta_1(r) = \arcsin(\frac{a}{r})$. One gets

$$\begin{aligned} I &= \int_0^{\frac{\pi}{2}} d\varphi \int_a^R \frac{2}{\pi} \arcsin\left(\frac{a}{r}\right) r\, dr \\ &= \int_a^R \arcsin\left(\frac{a}{r}\right) r\, dr \\ &= \frac{1}{2}R^2 \arcsin\left(\frac{a}{r}\right) + \frac{1}{2}a\sqrt{R^2 - a^2} - \frac{1}{4}\pi a^2. \end{aligned} \tag{A.9}$$

If one inserts this into Eq. (A.6), one obtains

$$A_{ch} = la + \frac{1}{2}\left[R^2 \arcsin\left(\frac{a}{R}\right) + a\sqrt{R^2 - a^2}\right], \tag{A.10}$$

which is the equation occurring in Sec. 3.1. The fraction of the regular phase space can be calculated directly from Eq. (A.10)

$$\rho_1^{analytic} = \frac{A - A_{ch}}{A} = \frac{\frac{1}{4}\pi R^2 - \frac{1}{2}\left[R^2 \arcsin\left(\frac{a}{R}\right) + a\sqrt{R^2 - a^2}\right]}{la + \frac{1}{4}\pi R^2}. \tag{A.11}$$

l	$\rho_1^{analytic}$	$\Delta\rho_1 \times 10^5$
0.011	0.3597	3.1
0.063	0.3475	-1.2
0.116	0.3362	-0.9
0.474	0.2750	1.8
0.526	0.2678	-0.9
0.579	0.2610	3.1
0.711	0.2454	-3.0
0.763	0.2397	-0.5
0.816	0.2342	-10.2
0.947	0.2216	-11.0
1.000	0.2169	-17.1
1.053	0.2124	-15.7
1.247	0.1973	3.5
1.300	0.1936	-0.6

Table A.1: The regular fraction of the classical phase space volume ρ_1 for various lengths l of the foot, obtained via the analytic formula (A.11) and via numerical calculations. The last column represents the difference $\Delta\rho_1 = \rho_1^{analitic} - \rho_1^{numerical}$. The width of the foot and the radius of the circle are the same for all the configurations analysed: i.e. $a = \frac{10}{19}$ and $R = 1$.

We have numerically tested this formula by using the standard calculation of the classical phase space volume of the regular and the chaotic region described in (Meyer,

1985). For the surface of section (SOS) (the lower plot in Fig. 3.2), the sine of the reflection angle has been selected as the momentum while the arc-length parameter has been used as the coordinate. We have also calculated the average return times.

The comparison between the analytic and the numerical calculation is shown in Tab. A.1. There exists a good agreement within the relative fraction of 10^{-4}, which confirms the analytic expression (A.11) as well as the general reliability, accuracy and efficiency of the numerical calculation of the classical ρ_1 (or ρ_2) parameter.

Appendix B

Theoretical analysis of the tunneling rates in the mushroom billiard

The group from Dresden has also derived the formula for the tunneling rates for the desymmetrised mushroom billiard. For the sake of completeness this appendix discusses this excellently devised derivation.

If one wants to derive the formula for the tunneling rates for a general billiard, one faces a general problem. The matrix element v, appearing in Eq. (3.38), cannot be calculated from the nominally regular and chaotic eigenstates of H, since those, in fact, include small admixtures of the other type of states. This is clearly visible near avoided crossings where the identity of the eigenstates is even exchanged under parameter variation. Due to this fact v was then determined via the fictitious regular and chaotic billiard systems H_{reg} and H_{ch} with purely regular and purely chaotic eigenstates respectively, which extends the approach for 1D quantum maps (Bäcker et al., 2008b). H_{reg} has to be chosen in such a way that its classical dynamics resembles the classical which has to correspond to H within the regular region as closely as possible. The eigenstates $|\psi_{\mathrm{reg}}\rangle$ of H_{reg} are localized in the regular region and continue to decay into the chaotic sea. The eigenstates $|\psi_{\mathrm{ch}}\rangle$ of H_{ch} 'live' in the chaotic region of H and decay into the regular islands. Since $|\psi_{\mathrm{reg}}\rangle$ and $|\psi_{\mathrm{ch}}\rangle$ are the eigenstates of different operators, H_{reg} and H_{ch}, they are not necessarily orthogonal, $\langle\psi_{\mathrm{ch}}|\psi_{\mathrm{reg}}\rangle = \chi$ with $0 \leq |\chi| \ll 1$. In order to apply Fermi's golden rule the orthonormalised states were introduced $|\widetilde{\psi}_{\mathrm{reg}}\rangle = |\psi_{\mathrm{reg}}\rangle$, $|\widetilde{\psi}_{\mathrm{ch}}\rangle = (|\psi_{\mathrm{ch}}\rangle - \chi^*|\psi_{\mathrm{reg}}\rangle)/\sqrt{1-|\chi|^2}$, leading to $\langle\widetilde{\psi}_{\mathrm{ch}}|\widetilde{\psi}_{\mathrm{reg}}\rangle = 0$.

For the coupling matrix element $v = \langle\widetilde{\psi}_{\mathrm{ch}}|V|\widetilde{\psi}_{\mathrm{reg}}\rangle = \langle\widetilde{\psi}_{\mathrm{ch}}|H|\widetilde{\psi}_{\mathrm{reg}}\rangle$ it follows

$$\begin{aligned} v &= \langle\widetilde{\psi}_{\mathrm{ch}}|H - H_{\mathrm{reg}}|\widetilde{\psi}_{\mathrm{reg}}\rangle + \langle\widetilde{\psi}_{\mathrm{ch}}|H_{\mathrm{reg}}|\widetilde{\psi}_{\mathrm{reg}}\rangle \\ &= \frac{1}{\sqrt{1-|\chi|^2}}\langle\psi_{\mathrm{ch}}|H - H_{\mathrm{reg}}|\psi_{\mathrm{reg}}\rangle - \frac{\chi}{\sqrt{1-|\chi|^2}}\langle\psi_{\mathrm{reg}}|H - H_{\mathrm{reg}}|\psi_{\mathrm{reg}}\rangle + 0. \end{aligned} \quad \text{(B.1)}$$

The leading order in χ for billiards is represented by

$$v = \int_{\Omega} \psi^*_{\mathrm{ch}}(x,y)(H - H_{\mathrm{reg}})\psi_{\mathrm{reg}}(x,y)\,\mathrm{d}x\,\mathrm{d}y + \mathcal{O}(x). \quad \text{(B.2)}$$

Eqs. (3.38) and (B.2) can be used if one wants to determine the dynamical tunneling rates in billiards. Here one should emphasise that H_{reg} and $|\psi_{\mathrm{reg}}\rangle$ have to be selected very carefully, which is a difficult task in the case of a general billiard.

This approach can now be applied to the desymmetrised mushroom billiard composed of a quarter circle and a rectangular foot (see Fig. B.1a) where we have chosen $R = 1$ in the following analysis. For the regular system H_{reg} the quarter-circle billiard $H_{1/4}$ is a natural choice (with its eigenvalues $E^{mn}_{1/4}$ and the eigenstates $\psi^{mn}_{1/4}$ represented in Eq. (3.3)).

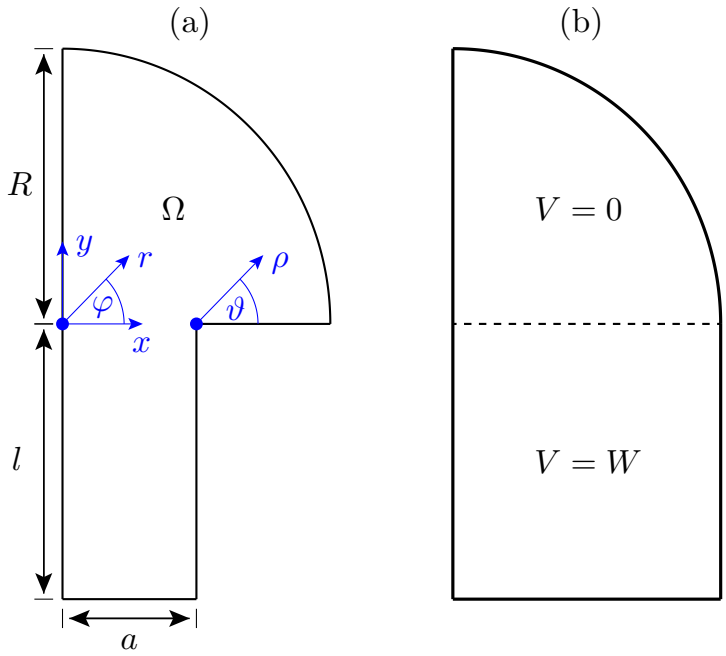

Figure B.1: The desymmetrised mushroom billiard: (a) Schematic picture of the coordinate systems used in the theoretical derivation. (b) The auxiliary billiard $H^W_{1/4}$.

After evaluating Eq. (B.2) one obtains the undefined product of $H - H_{1/4} = -\infty$ and $\psi^{mn}_{1/4}(x, y) = 0$, for $y \leq 0$. Therefore, the auxiliary billiard $H^W_{1/4}$ is introduced (see Fig. B.1b) with a large but finite potential $V(x, y \leq 0) = W \gg E$, characterised by the eigenstates $\psi^{mn}_{1/4,W}$. Eq. (B.2) is evaluated in the limit $W \to \infty$ where $H^W_{1/4}$ approaches $H_{1/4}$, which leads to

$$
\begin{aligned}
v &= \lim_{W\to\infty} \int_0^a \mathrm{d}x \int_{-l}^0 \mathrm{d}y\, \psi_{\mathrm{ch}}(x,y)(-W)\psi^{mn}_{1/4,W}(x,y) \\
&= -\int_0^a \mathrm{d}x \lim_{W\to\infty} W\psi^{mn}_{1/4,W}(x,y=0) \int_{-l}^0 \mathrm{d}y\, \psi_{\mathrm{ch}}(x,y) \exp(\sqrt{W - E^{mn}_{1/4}}\, y) \\
&= -\int_0^a \mathrm{d}x \lim_{W\to\infty} \frac{\partial\psi^{mn}_{1/4,W}}{\partial y}(x,y=0) \frac{W}{\sqrt{W - E_{mn}}} \int_{-l}^0 \mathrm{d}y\, \psi_{\mathrm{ch}}(x,y) \exp(\sqrt{W - E^{mn}_{1/4}}\, y) \\
&= -\int_0^a \mathrm{d}x \frac{\partial\psi^{mn}_{1/4}}{\partial y}(x,y=0) \int_{-l}^0 \mathrm{d}y\, \psi_{\mathrm{ch}}(x,y) \lim_{W\to\infty} \sqrt{W} \exp(\sqrt{W - E^{mn}_{1/4}}\, y) \\
&= -\int_0^a \mathrm{d}x \frac{\partial\psi^{mn}_{1/4}}{\partial y}(x,y=0) \int_{-l}^0 \mathrm{d}y\, \psi_{\mathrm{ch}}(x,y)\, 2\,\delta(y) \\
&= -\int_0^a \mathrm{d}x \frac{\partial\psi^{mn}_{1/4}}{\partial y}(x,y=0)\, \psi_{\mathrm{ch}}(x,y=0) \\
&= -N_{mn} \int_0^a \mathrm{d}x\, \frac{m}{x}\, J_m(j_{mn}x)\, \psi_{\mathrm{ch}}(x,y=0),
\end{aligned}
\tag{B.3}
$$

where the y-integration was performed on $\psi^{mn}_{1/4,W}(x,y) = \psi^{mn}_{1/4,W}(x,y=0)\exp(\sqrt{W-E^{mn}_{1/4}}\,y)$, obtained from the Schrödinger equation for $y<0$ and the continuity at $y=0$. Furthermore $\frac{\partial\psi^{mn}_{1/4,W}}{\partial y}(x,y=0) = \sqrt{W-E^{mn}_{1/4}}\,\psi^{mn}_{1/4,W}(x,y=0)$ has been used, obtained from the continuity of the derivative at $y=0$ and $\lim_{W\to\infty}\sqrt{W}\exp(\sqrt{W-E^{mn}_{1/4}}y)$ was replaced by the Dirac delta function; N_{mn} is the normalisation defined in Sec. 3.2.

One should observe that the value of the chaotic eigenstates $|\psi_{\mathrm{ch}}\rangle$ is only needed on the line $y=0$. For these eigenstates a random wave decomposition (RWD) (Berry, 1977) was employed. Recently, the RWD has been generalised to the systems with the mixed phase space (Bäcker and Schubert, 2002). While this description accurately describes the behavior inside the billiard, it does not incorporate the effect of the boundary, e.g. near the corner, which, for $m\geq 2$, largely influences the (final) integral from Eq. (B.3). Therefore, the RWD model (Berry, 2002) was extended to the case of the corner with the angle $3\pi/2$ using the eigenstates with the Dirichlet boundary conditions (Lehman, 1959),

$$\psi_{\mathrm{ch}}(\rho,\vartheta) \approx \sqrt{\frac{8}{3A_{\mathrm{ch}}}}\sum_{s=1}^{\infty} c_s J_{\frac{2s}{3}}\left(\sqrt{E}\rho\right)\sin\left(\frac{2s}{3}\vartheta\right), \tag{B.4}$$

where the polar coordinates (ρ,ϑ) at the corner are related to (x,y) by $x=a+\rho\cos(\vartheta)$ and $y=\rho\sin(\vartheta)$ (see Fig. B.1a). The coefficients c_s of this ensemble are independent Gaussian random variables with $\langle c_s\rangle = 0$ and $\langle c_s c_t\rangle = \delta_{st}$. The normalization is performed in such a way that $\langle|\psi_{\mathrm{ch}}(\rho,\vartheta)|^2\rangle = 1/A_{\mathrm{ch}}$ holds far away from the corner. In this case the chaotic states need not decay into the regular islands since Eq. (B.3) is an integral along a line of the billiard where the phase space is fully chaotic. If one inserts Eq. (B.4) for $\vartheta=\pi$ and $E=E^{mn}_{1/4}$ into Eq. (B.3), one can determine the averaged squared matrix element, $\langle|v|^2\rangle$, and by using Eq. (3.38) one obtains

$$\gamma_{mn} = m^2 N^2_{mn}\langle\left[\int_0^a \frac{\mathrm{d}x}{x} J_m(j_{mn}x)\sum_{s=1}^{\infty}{}' c_s J_{\frac{2s}{3}}(j_{mn}[x\text{-}a])\right]^2\rangle, \tag{B.5}$$

where the sum over s excludes all the multiples of 3, which is indicated by the prime. The average runs over all the chaotic states, i.e. all the possible c_ss, which results in

$$\gamma_{mn} = m^2 N^2_{mn}\sum_{s=1}^{\infty}{}'\left[\int_0^a \frac{\mathrm{d}x}{x} J_m(j_{mn}x) J_{\frac{2s}{3}}(j_{mn}[a\text{-}x])\right]^2. \tag{B.6}$$

The remaining integral can be calculated analytically (Abramowitz and Stegun, 1970, Eq. (11.3.40)), to that one obtains the final result

$$\gamma_{mn} = \frac{8}{\pi}\sum_{s=1}^{\infty}{}' \frac{J_{m+\frac{2s}{3}}(j_{mn}a)^2}{J_{m-1}(j_{mn})^2} \tag{B.7}$$

for the tunneling rates from any of the regular states $\psi^{mn}_{1/4}$ in the mushroom billiard. The sum over s is rapidly converging. The term with $s=1$ is by far the most important (large) in the sum, so if one employs the sum for $s\leq 2$, this is sufficiently accurate.

At this point one should remark that a very plausible estimate of the tunneling rate can be obtained if one calculates the averaged square of the regular wave function on the circle with the radius a, i.e. the boundary to the fully chaotic phase space, which results in $\gamma^0_{mn} = N^2_{mn} J_m(j_{mn}a)^2/2$. This quantity is equivalent to Eq. (B.7) with the single term $s = 0$ and the additional factor $1/2$. Surprisingly, this is for just about the factor of 2 larger for the parameters studied. Ref. (Barnett and Betcke, 2007) proposes a related quantity, given by the integral of the squared regular wave function over the quarter circle with the radius a. This quantity, however, is for a factor of the order 100 too small for the parameters under consideration.

Appendix C

Numerics with particular solutions for the tunneling rates in the mushroom billiard

The eigenvalues and the eigenfunctions of the mushroom billiard have also been numerically determined via the improved method of particular solutions (Betcke and Trefethen, 2005; Barnett and Betcke, 2007). Due to its superior computational efficiency one can determine the energies E with the relative error $\approx 10^{-14}$. The tunneling rates from Eq. (3.40) were deduced via the analysis of the avoided crossings of the preselected regular state with typically 30 chaotic states. One should observe that certain pairs of regular levels lie very near together, e.g. $E_{20,1} - E_{16,2} \approx 10^{-4}$, so that their avoided crossings overlap with the chaotic levels. Due to these overlaps the numerically calculated smaller tunneling rates do not comply with the theoretical approach presented. Fig. C.1 shows the tunneling rates γ_{mn} for the fixed radial quantum numbers $n = 1, 2, 3$ and for the increasing azimuthal quantum number m, by comparing the theoretical prediction (3.39) with the numerical results obtained by the method of particular solutions. One can observe an excellent agreement for tunneling rates γ_{mn} over 18 orders of magnitude.

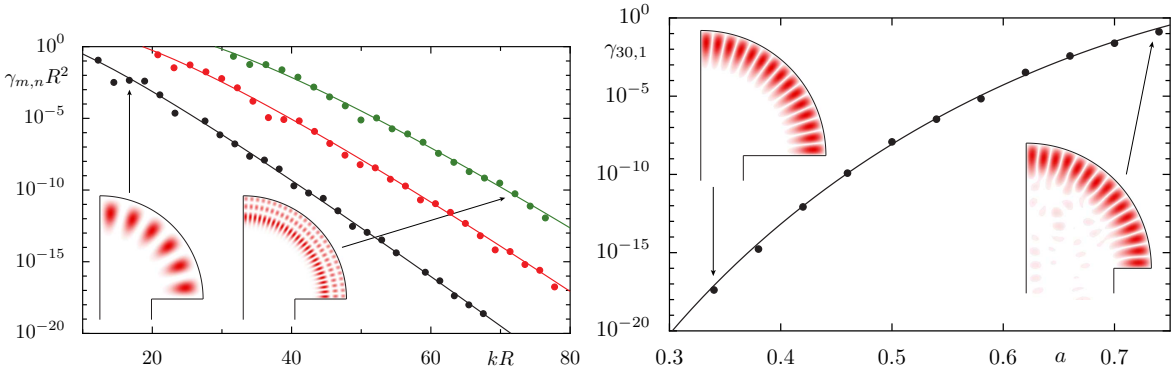

Figure C.1: Left plot: The tunneling rates from the regular states with the quantum numbers $n = 1$, 2 and 3 vs kR for $a/R = 0.5$ comparing the theoretical prediction from Eq. (3.39) (connected by solid lines) and the numerical data (dots). The insets show the regular eigenfunctions $\psi_{\mathrm{reg}}^{12,1}(x, y)$ and $\psi_{\mathrm{reg}}^{54,3}(x, y)$. Right plot: the tunneling rates with the varying foot width a. The insets show the regular eigenfunction $\psi_{\mathrm{reg}}^{30,1}(x, y)$.

Daljši slovenski povzetek

Tipični sistemi v naravi so mešanega tipa med regularnimi in kaotičnimi ter posedujejo regularno gibanje za določene in kaotično za komplementarne začetne pogoje. Priročni za študij dinamike gibanja so biljardni sistemi. Dandanes poznamo 3 popolnoma integrabilne in 3 dokazano popolnoma kaotične biljarde. Drugi biljardi so mešanega tipa, med katerimi prevladujejo tisti tipa KAM s fraktalno strukturo otokov stabilnosti, obdanih s kaotičnim morjem. V tej disertaciji študiramo gobasti biljard (Bunimovich, 2001), ki ima to (lepo) lastnost, da nima kompleksne KAM strukture, ampak je njegov fazni prostor ostro ločen v natanko eno regularno in eno kaotično komponento.

Študij kvantne mehanike klasično kaotičnih sistemov imenujemo kvantni kaos. Lastna stanja sistema mešanega tipa v semiklasični limiti klasificiramo kot regularna ali kaotična (Percival, 1973), odvisno od tega, kje 'živijo' v kvantnem faznem prostoru. Ker so poskusi s kvantnimi biljardi tehnično zahtevni, lahko zaradi formalne podobnosti Schrödingerjeve in drugih valovnih enačb fizike, študiramo valovne sisteme. Med njimi so najpomemnbejše eksperimentalno orodje v zadnjih letih postali mikrovalovni eksperimenti (Stöckmann, 1999) lastnih stanj in pripadajočih lastnih energij mikrovalov v 'mikrovalovnih' biljardih (resonatorjih).

Medtem ko so v klasični mehaniki območja regularnega in kaotičnega gibanja dobro ločena, so v kvantni mehaniki povezana s tuneliranjem. Temu tuneliranju, ki poteka med dvema dinamično (in ne nujno prostorsko) ločenima stanjema in je popolnoma drugačno od običajno poznanega tuneliranja skozi potencialno bariero, rečemo 'dinamično' tuneliranje (Davis and Heller, 1981). Dinamično tuneliranje se lahko odvija med dvema simetrijsko ločenima regularnima stanjema (kvazistanjema) kot direktno tuneliranje ali posredno preko kaotičnih stanj, kar imenujemo CAT (ang. *chaos-assisted tunneling*). Izkazalo se je (Bohigas et al., 1993b), da je prisotnost kaosa pogosto ključna pri jakosti tuneliranja. Dinamično tuneliranje poteka tudi med posamezno regularno komponento faznega prostora in kaotičnim morjem. V tem primeru je vpliv tuneliranja najbolj viden v primeru dveh degeneriranih lastnih vrednosti, pri čemer ena pripada regularnemu in druga kaotičnemu lastnemu stanju.

Kvantitativne napovedi dinamičnega tuneliranja so zaenkrat zelo redke in še te vključujejo dodatne parametre. V tej disertaciji predstavljamo določitev tunelskih parametrov za tuneliranje iz 'čistih' regularnih stanj v gobastem biljardu. Delo (Bäcker et al., 2008a) je bilo narejeno tako eksperimentalno kot tudi numerično, s čimer smo želeli potrditi teoretično izpeljano formulo skupine R. Ketzmericka v Dresdenu, predstavljeno v istem članku. Dinamično tuneliranje močno vpliva tudi na statistiko in dinamiko spektrov sistemov mešanega tipa. V semiklasični limiti za statistiko velja teorija Berryja in Robnika (Berry and Robnik, 1984), za statistiko nižje ležečih stanj pa še ni ustreznega opisa. Zato smo s pomočjo teorije naključnih matrik razvili 2- in N-nivojski model, ki opiše defor-

macijo porazdelitve Berryja in Robnika po razmikih med sosednjimi nivoji (**I**) zaradi sklopitve vseh nivojev z vsemi in (**II**) zaradi tuneliranja oziroma medsebojne sklopitve samo regularnih in kaotičnih nivojev ter ga testirali na energijskih nivojih za gobasti biljard (Vidmar et al., 2007). Poleg tega smo si za gobasti biljard ogledali tudi porazdelitev razdalj v izognjenih križanjih med enim regularnim in enim kaotičnim (RC) ter dvema kaotičnima (CC) stanjema.

V primeru, ko nismo v semiklasični limiti, na dogajanje vpliva tudi lokalizacija. Poskus modeliranja le-te v porazdelitvi razmikov med sosednjimi nivoji s singularno krat eksponentno porazdelitvijo matričnih elementov, kot tudi nekaterih drugih porazdelitev, ki niso v povezavi z lokalizacijo, predstavljamo v zadnjem delu te disertacije.

i Deformirana porazdelitev Berryja in Robnika po razmikih med sosednjimi nivoji

Porazdelitev Berryja in Robnika (BR) (Berry and Robnik, 1984) po razmikih med sosednjimi nivoji za sistem mešanega tipa v semiklasični limiti je

$$P_{BR}(S) = e^{-\rho_1 S}\left\{e^{-\frac{\pi\rho_2^2 S^2}{4}}\left(2\rho_1\rho_2 + \frac{\pi\rho_2^3 S}{2}\right) + \rho_1^2 \mathrm{erfc}\left(\frac{\sqrt{\pi}\rho_2 S}{2}\right)\right\}, \tag{i}$$

kjer ρ_1 in $\rho_2 = 1 - \rho_1$ merita delež regularne in kaotične komponente faznega prostora, kjer smo privzeli samo eno kaotično komponetno. $P_{BR}(S)$ je izpeljana kot drugi odvod verjetnosti za energijsko vrzel po razmikih med sosednjimi nivoji. Osnovna ideja BR slike je, da je verjetnost za energijsko vrzel enaka produktu uteženih verjetnosti za energijsko vrzel posebej za regularni in posebej za kaotični del spektra, kjer za regularnega velja Poissonska statistika (Berry and Tabor, 1977), za kaotičnega pa vzamemo Wignerjevo porazdelitev, ki je dober približek za eksaktno GOE statistiko (Bohigas et al., 1984). $P_{BR}(S)$ in njen prvi moment sta normalizirana. Njena značilnost je, da je eksaktno uporabna samo v semiklasični limiti. Ne upošteva namreč (**I**) linearnega odbijanja med sosednjimi nivoji zaradi tuneliranja, saj je $P_{BR}(S=0) = 1 - \rho_2^2$, kar je v primeru mešanega sistema večje od 0, in (**II**) potenčnega odbijanja med sosednjimi nivoji z eksponentom manjšim kot 1, za kar je odgovorna lokalizacija.

Vpliv tuneliranja in posledično deformacijo porazdelitve $P_{BR}(S)$ modeliramo tukaj. Zato najprej obravnavamo realno simetrično 2×2 matriko $A = (A_{ij})$ z $i, j = 1$ ali 2

$$A = \begin{pmatrix} a & b \\ b & -a \end{pmatrix}, \tag{ii}$$

kjer sta a in b realni števili s porazdelitvijo $g_a(a)$ in $g_b(b)$. Če za $g_a(a)$ vzamemo porazdelitev BR

$$g_a(a) = P_{BR}(2a) \tag{iii}$$

in Gaussovo porazdelitev s skopitvenim parametrom σ za $g_b(b)$

$$g_b(b) = \frac{1}{\sigma\sqrt{2\pi}} \exp\left(-\frac{b^2}{2\sigma^2}\right), \tag{iv}$$

potem za porazdelitev po razmikih med sosednjimi nivoji sledi

$$P^A_{DBR}(S) = \frac{S}{\sigma\sqrt{2\pi}} \int_0^{\pi/2} d\varphi \; P_{BR}\left(S\cos\varphi\right) \; \exp\left(-\frac{S^2\sin^2\varphi}{8\sigma^2}\right). \tag{v}$$

Enačbo (v) poimenujemo splošno deformirana porazdelitev Berryja in Robnika po razmikih med sosednjimi nivoji. [1] Tu imamo sklopitev vseh (regularnih in kaotičnih) nivojev z vsemi, kar odraža realno situacijo pri eskperimentih lastnih frekvenc mikrovalovnih resonatorjev zaradi prisotnosti antene, zato oznaka A (ang. *antenna-distorted* ali *all-to-all*) v P^A_{DBR}. Standardna deviacija σ je mera za jakost sklopitve. Gaussovo porazdelitev za izvendiagonalne matrične elemente upravičimo z univerzalnostjo RMT statistike lokalnih spektralnih fluktuacij (Hackenbroich and Weidenmüller, 1995), čeprav tukaj nimamo čiste RMT situacije, saj imajo izvendiagonalni elementi drugačno porazdelitev kot diagonalni. Glavni lastnosti nove porazdelitvene funkcije $P^A_{DBR}(S)$ sta linearno odbijanje nivojev, predvideno v sistemih mešanega tipa (Robnik and Prosen, 1997)

$$P^A_{DBR}(S) \approx \frac{S\sqrt{\pi}P_{BR}(0)}{2\sigma\sqrt{2}}, \tag{vi}$$

ter konvergenca k porazdelitvi BR za velike S

$$P^A_{DBR}(S) \approx P_{BR}(S). \tag{vii}$$

$P^A_{DBR}(S)$ je avtomatsko normalizirana, njen prvi moment pa je potrebno dodatno normalizirati z uvedno parametra B_A, da dobimo rezultat (slika i)

$$P^{An}_{DBR}(S) = B_A \; P^A_{DBR}(B_A S), \quad \text{z} \quad B_A = \int_0^\infty x \; P^A_{DBR}(x) \; dx. \tag{viii}$$

Ker imamo v primeru tunelskih procesov (samo) sklopitev regularnih nivojev s kaotičnimi, porazdelitveno funkcijo za izvendiagonalne elemente $g_b(b)$ rahlo spremenimo in dobimo tunelsko deformirano porazdelitev Berryja in Robnika po razmikih med sosednjimi nivoji

$$P^T_{DBR}(S) = 2\rho(1-\rho)P^A_{DBR}(S) + [1-2\rho(1-\rho)]P_{BR}(S), \tag{ix}$$

ki je uteženo povprečje nedeformirane in splošno deformirane porazdelitve BR. Njen prvi moment normaliziramo s parametrom B_T in dobimo končni rezultat 2×2 modela

$$P^{Tn}_{DBR}(S) = B_T \; P^T_{DBR}(B_T S), \quad \text{z} \quad B_T = \int_0^\infty x \; P^T_{DBR}(x) \; dx. \tag{x}$$

Integrale v enačbah (v), (viii) in (x) izračunamo numerično. B_A-ji se za izbrana parametra ρ in σ gibljejo na intervalu med 1 in 1.2, B_T-ji pa med 1 in 1.1. Porazdelitev $P^{Tn}_{DBR}(S)$ je za različne parametre prikazana na sliki ii s polno rdečo črto. Vidimo, da sicer ni odbijanja sosednjih nivojev, je pa zmanjšanje vrednosti nove porazdelitve pri $S = 0$ glede na vrednost porazdelitve BR pri $S = 0$. V limiti velikih S se $P^{An}_{DBR}(S)$ asimptotsko, skrčena za faktor B_A, približuje porazdelitve BR (slika i desno spodaj), kar velja tudi za $P^{Tn}_{DBR}(S)$.

[1] Ang. '*antenna-distorted*' ali '*all-to-all*' prevajamo s 'splošno deformirana', ker gre za splošno sklopitev vseh nivojev z vsemi.

ii Simulacije z naključnimi matrikami

Tu bomo predstavili rezultate simulacij z N dimenzionalnimi matrikami, z Gaussovo naključno porazdelitvijo izvendiagonalnih in porazdelitvijo Berryja in Robnika diagonalnih elementov. Z diagonalizacijo take matrike in razgrnitvijo lastnih vrednosti dobimo N dimenzionalno splošno in tunelsko deformirano porazdelitev BR po razmikih med sosednjimi nivoji: $P^{An}_{DBRN}(S)$ in $P^{Tn}_{DBRN}(S)$. V primeru splošne deformacije imajo Gaussovo porazdelitev z isto varianco σ^2 vsi izvendiagonalni elementi dane matrike, v primeru tunelske pa le dva pravokotna bloka elementov, ki predstavljajo sklopitev med regularnimi in kaotičnimi lastnimi vrednostmi. Enako kot v 2D primeru v porazdelitvenih funkcijah nastopata dva parametra: BR parameter ρ in sklopitveni parameter σ. Pričakujemo, da bomo s $P^{Tn}_{DBRN}(S)$ dobili ustrezen opis porazdelitve po razmikih med sosednjimi nivoji v sistemih mešanega tipa. Naredili smo obsežne izračune z matrikami dimenzije $N = 1000$, pri čemer smo za razgrnitev nivojev uporabili fenomenološko pravilo **unf** $= 30$ sosedov, 15 gor in 15 dol in vsako konfiguracijo ponovili 1000 krat. Optimalno število sosedov **unf** pri razgrnitvi smo poiskali tako s χ^2 testom kot s primerjavo z eksaktno GOE razgrnitvijo v primeru $\rho = 0$. Izkazalo se je, da je odvisnost rezultatov od števila **unf** zelo šibka. Lahko bi vzeli **unf** ≥ 14 in bi dobili skoraj enak rezultat. Tudi odvisnost rezultatov od velikosti matrike N je zelo majhna.

Rezultati za splošno deformacijo so predstavljeni na sliki i za tunelsko pa na sliki ii. Histogram predstavlja rezultat N dimenzionalne simulacije, medtem ko rdeča krivulja predstavlja 2-dimenzionalni model. Vidimo, da je v primeru splošne deformacije ujemanje za majhne σ^2 in vse ρ izredno dobro. Očitno pa je, da 2D model deluje samo dokler so izvendiagonalni elementi majhni v primerjavi s povprečnim razmikom med nivoji. To vidimo na sliki i spodaj desno, kjer predstavimo primer z večjo sklopitvijo $\sigma = 0.3$.

V primeru tunelske deformacije je ujemanje zadovoljivo, opogumljajoče, a so odstopanja očitna predvsem okrog $S = 0$. Medtem ko imamo pri N dimenzionalnem modelu linearno odbijanje nivojev, pri 2D modelu odbijanja ni. To opažanje odraža dejstvo, da se v 2D modelu naključne degeneracije v regularnem delu pojavljajo generično, medtem ko so v N dimenzionalnem modelu eliminirane. V slednjem sicer ni direktnih tunelskih matričnih elementov, obstaja pa efektivno tuneliranje drugega reda, ki indirektno sklaplja dve regularni stanji z enim ali več kaotičnimi stanji. Zaradi tega 2D model tukaj odpove.

Imamo dva predloga odprave defekta 2D modela. Pri prvem porazdelitev izvendiagonalnih elementov (iv) zamenjamo z

$$g_b(b) = 2\rho(1-\rho)\frac{1}{\sigma\sqrt{2\pi}}\exp\left(-\frac{b^2}{2\sigma^2}\right) + [1-2\rho(1-\rho)]\frac{1}{\sigma_1\sqrt{2\pi}}\exp\left(-\frac{b^2}{2\sigma_1^2}\right) \ , \qquad \text{(xi)}$$

kjer $\sigma_1 > 0$ fenomenološko upošteva razcep drugega reda v regularnem delu spektra. Pri drugem vsak trojček dveh sosednjih regularnih in enega najbližjega kaotičnega nivoja obravnavamo s 3×3 matriko, pri čemer je sklopljen samo kaotični nivo z vsakim od obeh regularnih (Stöckmann, 2007). Oboje je še v delu.

Pogledali smo si tudi, kaj dobimo, če je porazdelitev izvendiagonalnih elementov škatlasta ali eksponentna. Izkaže se, da se rezultat spremeni samo nekoliko, večjih spremembnb pa ni. Kot smo že intuitivno pričakovali, so statistične lastnosti spektrov odvisne predvsem od variance in ne toliko od drugih detajlov porazdelitvene funkcije izvendiagonalnih elementov dane matrike.

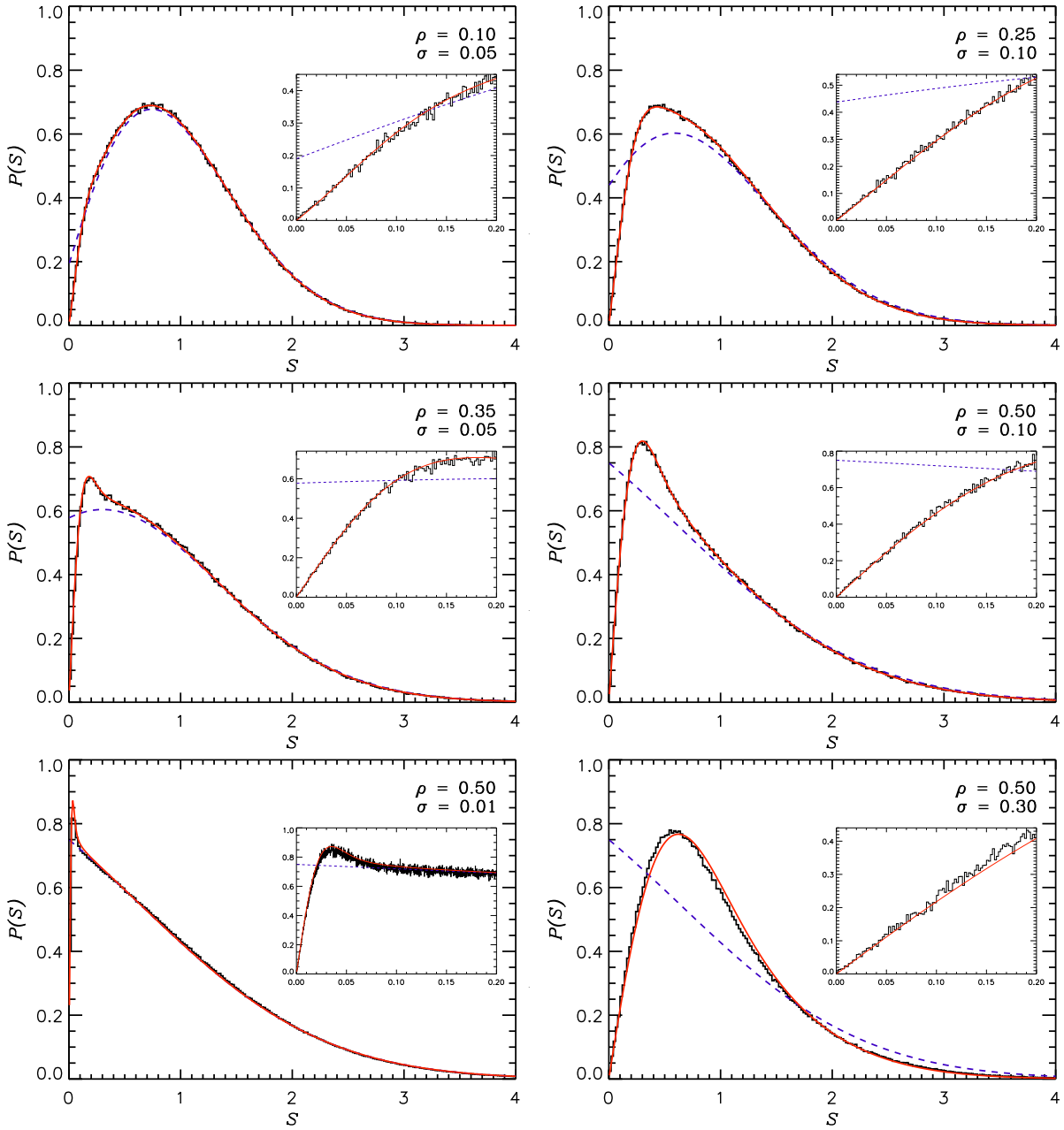

Slika i: Rezultati za splošno deformirano porazdelitev BR po razmikih med sosednjimi nivoji $P^{An}_{DBR}(S)$ (rdeča krivulja) in $P^{An}_{DBRN}(S)$ (histogram) za različne parametre σ in ρ. Vsi nivoji so sklopljeni. Za primerjavo črtkasta modra črta predstavlja porazdelitev BR. Pri obeh krivuljah smo pri izračunu BR uporabili eksaktno GOE porazdelitev. Pri povečavah prikažemo obnašanje histograma in krivulj za majhne S. N dimenzionalni (numerični) in 2D (analitični) rezultati so v primeru $\sigma = 0.01$, 0.05 in 0.1 praktično identični, krivulja BR pa se razlikuje znatno. Pri velikih $\sigma = 0.3$ pa vidimo razliko med modeloma. Tam je lepo vidno tudi odstopanje modelov od BR za velike S, ki nastopi zaradi skrčitve oziroma raztegnitve modelskih funkcij, kot smo razložili v tekstu. Pri majhnih S ta efekt ni viden. V primeru s $\sigma = 0.01$ imamo 10-krat več objektov v histogramu.

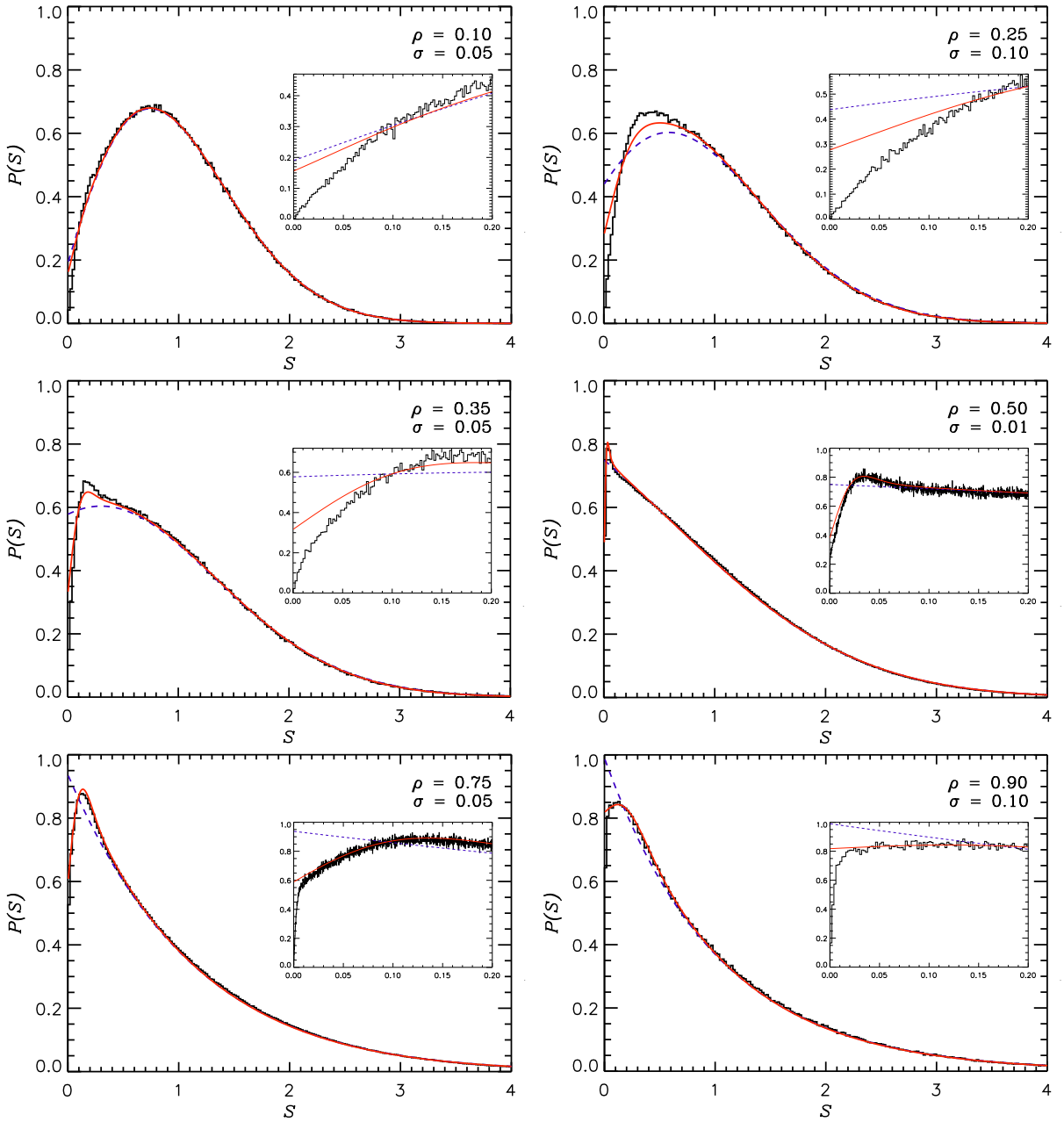

Slika ii: Rezultati za tunelsko deformirano porazdelitev BR po razmikih med sosednjimi nivoji $P^{Tn}_{DBR}(S)$ (rdeča krivulja) in $P^{Tn}_{DBRN}(S)$ (histogram) za različne parametre σ in ρ. Sklopljeni so samo regularni in kaotični nivoji. Za primerjavo črtkasta modra črta predstavlja porazdelitev BR. Pri povečavah prikažemo obnašanje histograma in krivulj za majhne S. N dimenzionalni (numerični) in 2D (analitični) rezultati se relativno ujemajo zadovoljivo, razlikujejo se predvsem okrog $S = 0$. Na srednji desni in spodnji levi sliki imamo 10-krat več objektov v histogramu.

iii Gobasti biljard

Gobasti biljard (Bunimovich, 2001) je sestavljen iz polkrožne glave in pravokotne noge (slika iii).

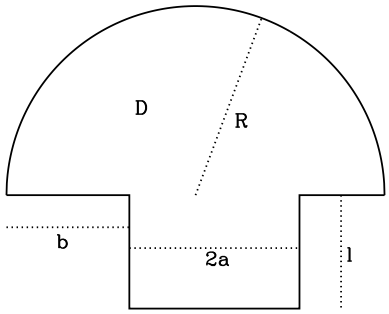

Slika iii: Geometrija gobastega biljarda: R = radij polkroga, $2a$ = širina noge, l = višina noge, b = pozicija noge (daljša razdalja do roba).

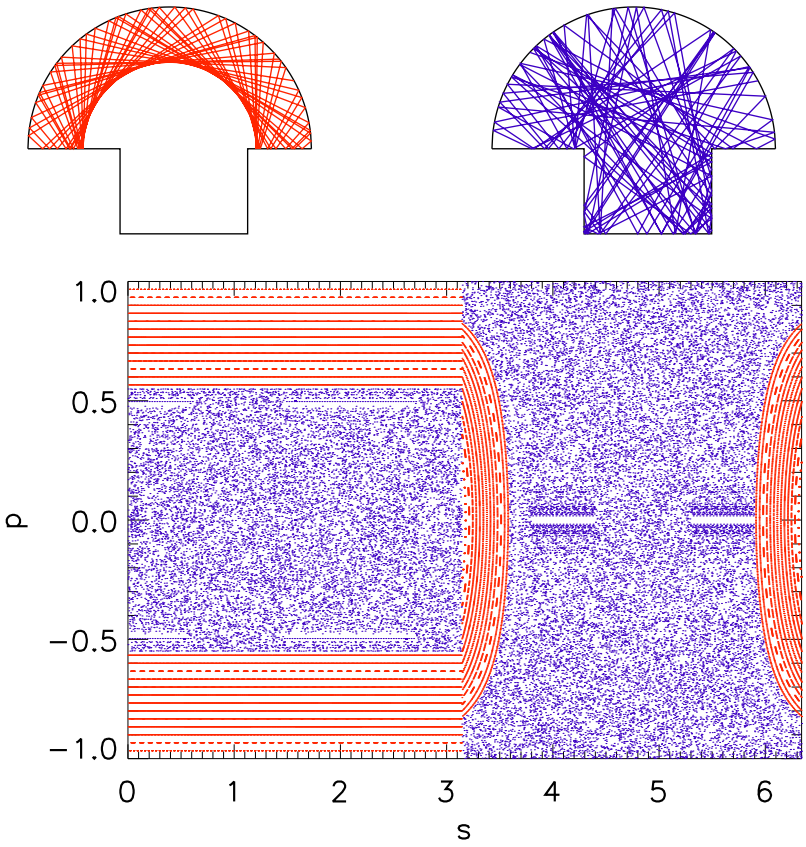

Slika iv: Zgoraj levo: primer regularne orbite z 70 odboji. Zgoraj desno: primer kaotične orbite z 100 odboji. Spodaj: fazni portret. Abscisa je koordinata roba s pri odboju, medtem ko je ordinata p *sinus* odbojnega kota.

Posebna lastnost gobastega biljarda je ostra ločenost faznega prostora v natanko eno kaotično in eno regularno komponento (slika iv spodaj), zato je ta biljard posebej privlačen

za analize. Orbite, ki pridejo enkrat v nogo, so kaotične, vse ostale so regularne (slika iv zgoraj). Regularne orbite se nahajajo v polkrožnem kolobarju nad polkrožno kavstiko z najmanjšim dovoljem radijem $2a + b - R$. Ta kavstika ostro loči regularne orbite od kaotičnih.

Regularni del klasičnega faznega prostora je zelo preprost. Zato je volumen regularnega (ali kaotičnega) dela faznega prostora enostavneje izračunati kot pri KAM sistemih. V skupini R. Ketzmericka v Dresdenu jim je uspelo dobiti analitičen izraz za efektivno kaotično površino gobastega biljarda s centralno pozicijo noge ($b = R - a$)

$$A_{ch} = 2\,la + \left[R^2 \arcsin\left(\frac{a}{R}\right) + a\sqrt{R^2 - a^2}\right], \tag{xii}$$

kjer za delež regularne komponente faznega prostora sledi

$$\rho_1^{analitic} = \frac{A - A_{ch}}{A} = \frac{\frac{1}{4}\pi R^2 - \frac{1}{2}\left[R^2 \arcsin\left(\frac{a}{R}\right) + a\sqrt{R^2 - a^2}\right]}{la + \frac{1}{4}\pi R^2}. \tag{xiii}$$

Ta rezultat smo potrdili z numeričnim izračunom z relativno natančnostjo 0.0002.

Medtem ko je regularni del faznega prostora enostaven, pa je kaotični del bolj kompleksen. Ta poleg odbijajočih stanj (ang. *bouncing balls*) vsebuje tudi druge družine marginalno nestabilnih periodičnih orbit (Altmann et al., 2005, 2006), t. i. 'lepljive' orbite.

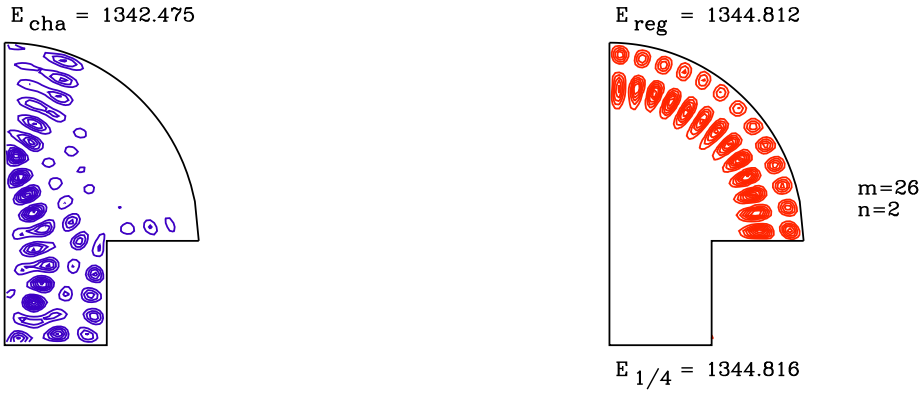

Slika v: Verjetnostna gostota sosednjih kaotičnega in regularnega stanja.

Kvantnomehansko biljard opišemo s časovno neodvisno Schrödingerjevo enačbo s hamiltonko $H(\mathbf{p}, \mathbf{q})$, lastnimi energijami E_j in lastnimi stanji ψ_j. V našem primeru imamo Dirichletove robne pogoje: $\psi_n(\mathbf{q})|_{\partial\mathcal{D}} = 0$. Lastna stanja lahko razvrstimo kot v glavnem regularna ali v glavnem kaotična (slika v). Regularne valovne funkcije in pripadajoče energije so podobne lastnim fukcijam in energijam polkroga, kjer pri $R = 1$ v polarnim koordinatah (r, φ) dobimo

$$E_{1/4}^{mn} = j_{mn}^2 \quad \text{and} \quad \psi_{1/4}^{mn}(r \le 1, \varphi) = N_{mn} J_m\left(j_{mn} r\right) \sin(m\varphi),\ \psi_{1/4}^{mn}(r > 1, \varphi) = 0. \tag{xiv}$$

Tukaj je J_m m-ta Besslova funkcija ($m = 2, 4, \dots$), j_{mn} njena n-ta ničla ($n = 1, 2, \dots$) in $N_{mn} = -\sqrt{8/\pi}/J_{m-1}(j_{mn})$ normalizacijska konstanta.

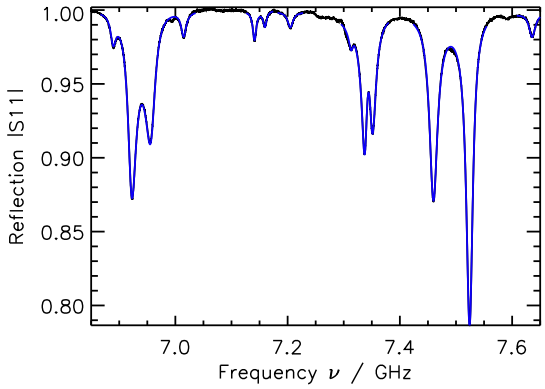

Slika vi: Absorbcijski EM spekter, nad katerim smo izvedli harmonično inverzijo. Med spektrom (črna) in rezultatom harmonične inverzije (modra krivulja) skorajda ni razlike.

iv Mikrovalovni eksperimenti in numerična metoda EBIM

Izkaže se, da je enačba za z komponento električnega polja stoječih elektromagnetih valov v tankem resonatorju enaka Schrödingerjevi enačbi za 2D biljard vključno z robnimi pogoji (Stöckmann, 1999). To nam omogoča bogato eksperimentalno raziskovanje.

Z eno anteno, ki mikrovalove hkrati oddaja in sprejema, smo merili realni in imaginarni del odbojnega spektra (**I**) aluminijastega in (**II**) medeninastega resonatorja v obliki gobastega biljarda in dobili absorbcijske resonance (slika vi) pri (nekoliko zmanjšanih) lastnih frekvencah. Zaradi absorbcije mikrovalov v stenah resonatorja so resonance razširjene, medtem ko je za njihov premik odgovorna prisotnost antene.

Z metodo harmonične inverzije iz spektra dobimo lastne frekvence (Kuhl et al., 2008). S Fourierovo transformacijo spektra, zapisanega s kompleksno vsoto prispevkov posameznih resonanc, in diskretizacijo dobimo sistem nelinearnih enačb, ki ga rešimo z metodo decimalnega linearnega prediktorja (Main et al., 2000). S to metodo harmonične inverzije dobimo veliko večino (cca. 85%) resonanc (slika vi), preostale moramo poiskati s fitanjem vsake resonance posebej, kar pa je veliko zamudnejše. Naj dodamo, da premik resonanc zaradi prisotnosti antene predstavlja sistemsko napako meritve, saj ga iz rezultatov ne moremo izločiti.

Numerične lastne vrednosti pa smo računali z metodo integriranja po robu EBIM (ang. *expanded boundary integral method*) (Veble et al., 2007). Metoda je splošna in ima to prednost, da je uporabna za vsako obliko biljarda, njena slabost pa je počasnost. Pri tej metodi Schrödingerjevo enačbo za lastne energije in lastne funkcije prepišemo v integral normalnega odvoda po robu biljarda. Slednjega diskretiziramo in izračunamo numerično tako, da dobljeno matriko, ki je odvisna od lastnega valovnega števila k, razvijemo okrog vnaprej izbranega k_0. V našem primeru zadošča že prvi red razvoja, saj je iste natančnosti kot formalni drugi red.

Po k osi se premikamo po korakih $\Delta k_0(k) = 0.05(\frac{k}{k_{Start}})^{-1/3}$ od k_{Start} do $k = \sqrt{5000}$. Pri vsakem koraku izračunamo poslošen diagonalizacijski problem lastnih vrednosti in vektorjev, iz katerih dobimo tudi lastne valovne funkcije, če jih potrebujemo. Pri vsaki diagonalizaciji dobimo največ 3 dobre lastne vrednosti začetnega problema, vse ostale

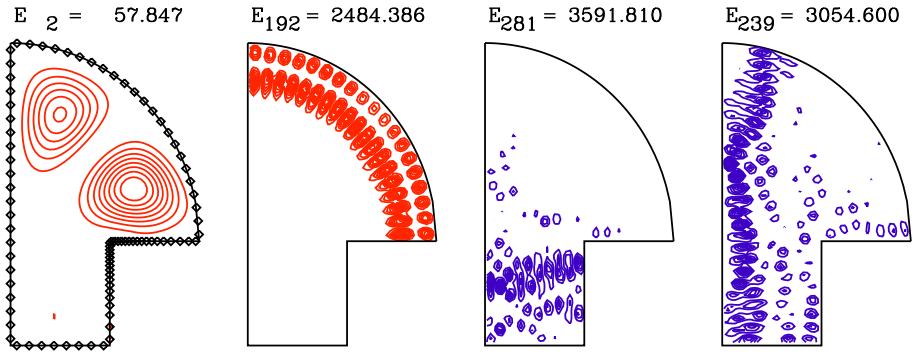

Slika vii: Valovne funkcije gobastega biljarda izračunane z EBIM ($l = a = \frac{10}{19}R$). Narisana je verjetnostna gostota z 8-ekvidistantnimi izohipsani od 0 do največje vrednosti. Na levi sliki so označene tudi robne točke.

zavržemo, ker ne ustrezajo izhodiščni ideji razvoja v Taylorjevo vrsto. Dobljeno število lastnih vrednosti testiramo z Weylovo formulo. V primeru računanja dinamike lastnih energij zadošča, da prejšnjo lastno vrednost od sosednje konfiguracije vzamemo za izhodiščno vrednost nove konfiguracije, kar za približno faktor 4 poveča hitrost numeričnega računa.

Metodo smo testirali na 3/4 krogu z $R = 1$, kjer smo ugotovili, da je nekonveksni kot $3\pi/2$ največji izvor napake, zato smo okrog njega linearno zgostili točke od faktorja 1 do 4 na intervalu 0.4 stran od vogala, kar je bistveno izboljšalo natančnost. To smo potem uporabili tudi na gobastem biljardu, kjer smo napako metode z 12 robnimi točkami na valovno dolžino ocenili na maksimalno 0.02 srednjega razmika med sosednjimi nivoji. Na sliki vii je prikazanih nekaj lastnih stanj.

v Dinamika lastnih energij gobastega biljarda

Merili smo dinamiko lastnih energij gobastega biljarda s premikanjem pozicije noge od sredine do desnega roba. Rezultati so prikazani na sliki viii levo, kjer so lastne vrednosti povezane v t. i. 'špagete' ali veje lastnih vrednosti. Valoviti 'špageti' ustrezajo kaotičnim, pokončni in ravni pa regularnim lastnim stanjem. Pri meritvah smo izgubili 37 % lastnih vrednosti. Vendar to ne moti, saj dobljene povežemo med seboj, pri čemer je napaka pri povezovanju relativno majhna. Tako dobimo vse 'špagete' in ni manjkajočih, zato so ekperimentalni rezultati popolnoma avtonomni. Enak eksperiment smo naredili tudi z absorberjem v nogi biljarda. Rezultati potrjujejo, da vse kaotične valovne funkcije živijo tudi v nogi biljarda, zato v dinamiki lastnih stanj od tega eksperimenta vsa kaotična stanja izginejo, ostanejo samo regularna.

Za ta tip dinamike lastnih energij smo naredili tudi izračun, ki pa se je izkazal za premalo natančnega, zato ga v nadaljevanju ne uporabljamo. Smo pa naredili izračun za drugo dinamiko, ko poglabljamo nogo gobe. Izračunane lastne energije so prikazane na sliki viii desno. V tem primeru nagnjeni 'špageti' (veje lastnih vrednosti) ustrezajo kaotičnim, pokončni pa regularnim lastnim stanjem. Pri numeriki ne izgubimo nobenega stanja. Poleg regularnih pokončnih 'špagetov', dobimo kot skoraj pokončne ali nekoliko nagnjene tudi tiste, ki ustrezajo stanjem odbijajočih žogic (and. *bouncing-ball modes*), tisti, ki ustrezajo lastnih funkcijam brazgotin, pa so zelo nagnjeni. Za enake konfiguracije smo izvedli tudi eksperiment, ki ga bomo predstavili v nadaljevanju.

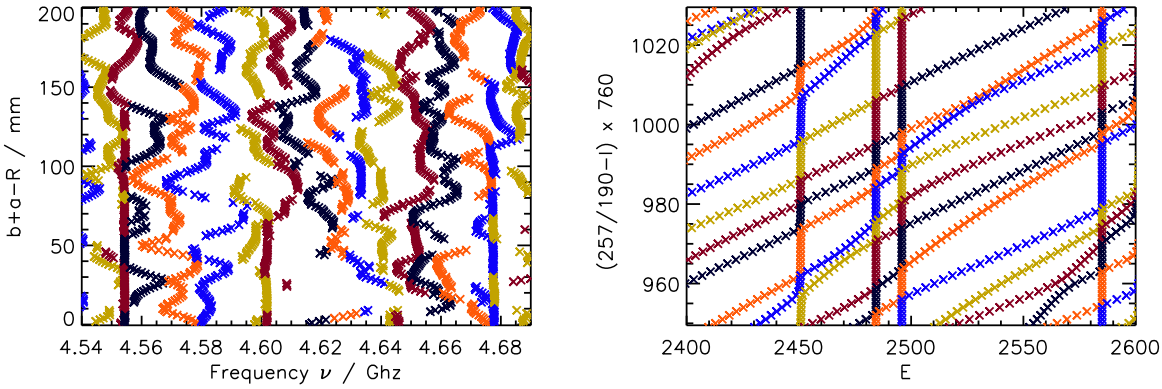

Slika viii: Levo: energijski nivoji mikrovalovnega gobastega biljarda, pri katerem premikamo nogo v korakih po 1 mm, $R = 2a = 400$ mm in $l = 100$ mm. Merili smo 200 različnih konfiguracij, od centralne do skrajno desne pozicije noge. Desno: energijski nivoji desimetriziranega gobastega biljarda s centralno pozicijo noge ($b = R - a$) izračunani z EBIM, pri katerem smo poglabljali nogo v korakih po $\Delta l = 1/760 \approx 0.00139$, $R = 1$ in $a = 10/19 \approx 0.526$. Računali smo 1029 različnih konfiguracij, začenši z $l = 0$ ekvidistantno do $l_{max} = 257/190 \approx 1.35263$. Na abscisi imamo $E = k^2$, na ordinati pa parameter, linearno odvisen od globine noge l.

Porazdelitev po razmikih med sosednjimi nivoji - primerjava z RMT napovedjo

Če želimo spektre primerjati med seboj, jih moramo najprej razgrniti - prevesti na konstantno povprečno gostoto energijskih nivojev. Na razgrnjenih spektrih računamo različne statistične količine, v našem primeru bo to porazdelitev po razmikih med sosednjimi nivoji $P(S)$.

Na sliki ix zgoraj so prikazani rezultati primerjave eksperimentalnih rezultatov in teoretične napovedi P^{An}_{DBR}, spodaj pa je primerjava numeričnih rezultatov in teoretične napovedi P^{Tn}_{DBR}. Oboji se relativno dobro ujemajo s teorijo. Pri eksperimentalnih spektrih smo vzeli 21 sosednjih konfiguracij iz dinamike lastnih energij, pri numeričnih pa 101 le-teh (slika viii). ρ_1 je klasični parameter, ki ga dobimo iz enačbe (xii) in se spreminja za $\pm 7.5\,\%$ (zgornja) in $\pm 3\,\%$ (spodnja slika) okrog srednjih vrednosti ρ, vpisanih na obeh slikah. Edini prilagoditveni (ang. *fitting*) parameter je sklopitev σ. Vidimo, da so tako ekperimentalni kot tudi numerični rezultati dobra, a seveda ne dokončna potrditev naše teorije. Zato v primeru P^{Tn}_{DBR} potrebujemo večjo natančnost izračunanih nivojev, ko $S \Rightarrow 0$, izboljšanje teorije in seveda tudi izračun lastnih energij kakšnega drugega sistema mešanega tipa.

vi Izognjena križanja in tuneliranje

Veje lastnih stanj se lahko križajo ali pa tudi ne, v tem primeru dobimo t. i. izognjena križanja dveh vej z najbližjo razdaljo ΔE. V regularnem sistemu izognjenih križanj ni, v popolnoma kaotičnem sistemu pa so vsa križanja izognjena. Če ima tak sistem simetrijo na obrat časa, je v njem porazdelitev razcepov v izognjenih križanjih Gaussova, kar sledi iz 2×2 GOE modela naključnih matrik za izolirano izognjeno križanje (Zakrzewski et al., 1993). Normalizirana na enotski povprečni razcep se porazdelitev glasi:

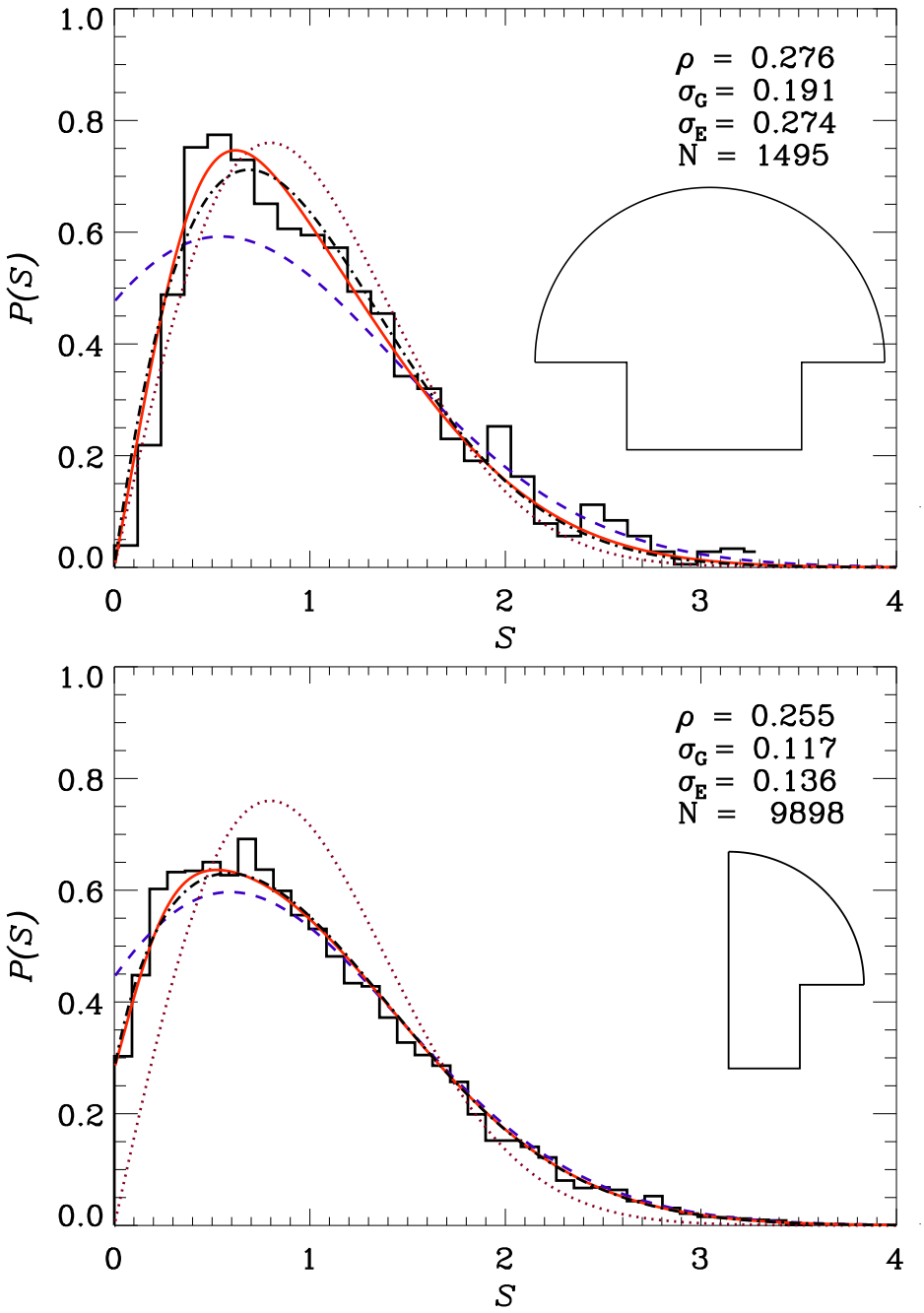

Slika ix: Primerjava eksperimentalnih podatkov (histogram) z najbolj prilegajočo se teoretično krivuljo P^{An}_{DBRN} (zgornja) in numeričnih z najbolj prilegajočo se teoretično krivuljo P^{Tn}_{DBRN} (spodnja slika), kjer je rdeča krivulja za Gaussov, pikčasto črtkasta črna za eksponentni model, črtkasta modra za BR porazdelitev z istim ρ in pikčasta rjava za Wignerjevo porazdelitev. σ_G in σ_E sta vrednosti najboljših fitov za σ za Gaussov in eksponentni model. N je število objektov v vsakem histogramu. Na zgornji sliki imamo nivoje na intervalu $(j_{min}, j_{max}) = (100, 300)$, na spodnji pa na intervalu $(j_{min}, j_{max}) = (100, 200)$.

$$P_{GOE}(\Delta E) = \frac{2}{\pi} \exp\left(-\frac{\Delta E^2}{\pi}\right). \tag{xv}$$

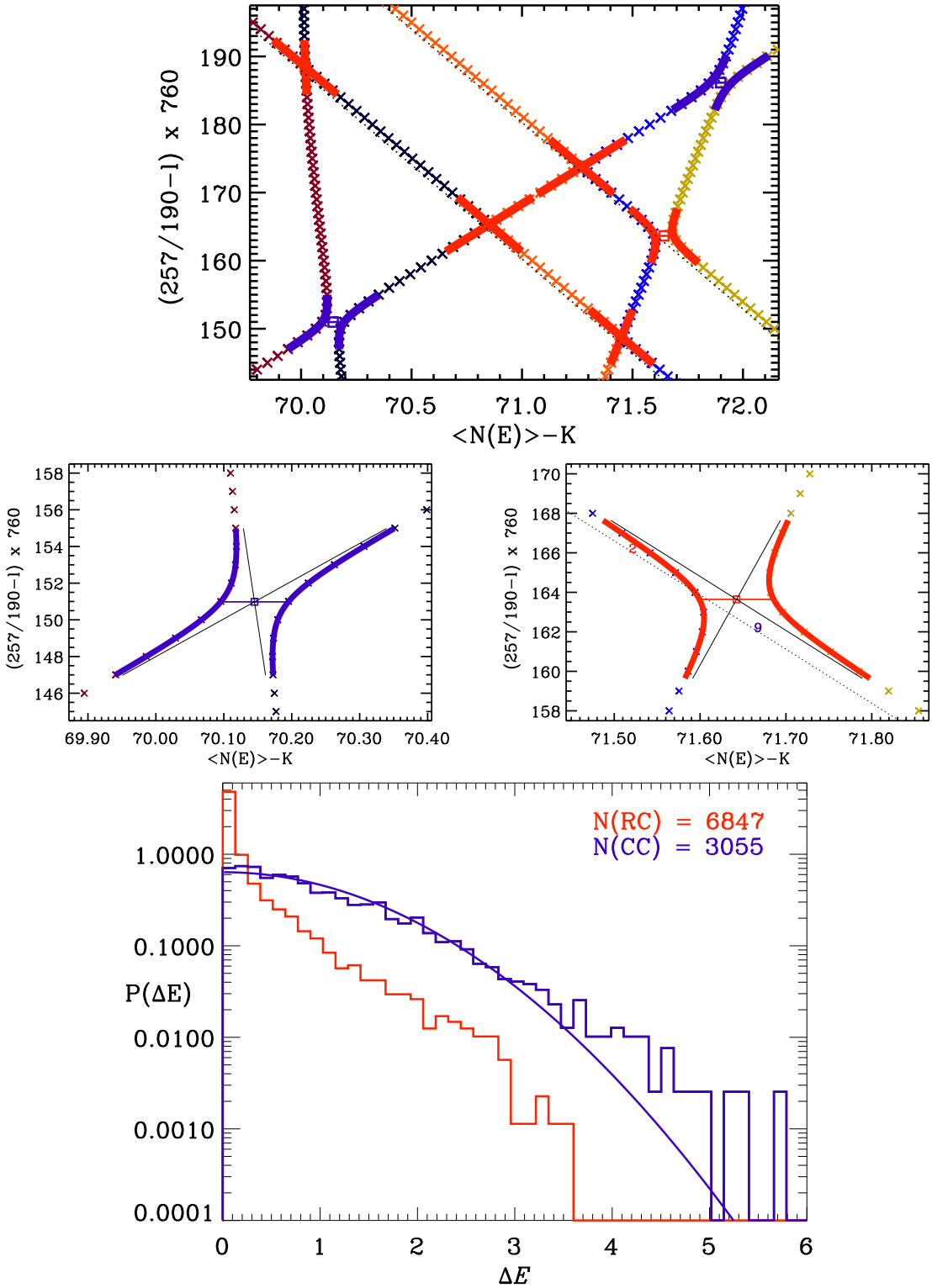

Slika x: **Zgornja slika**: izognjena križanja v numeričnem izračunu dinamike lastnih energij do $k^2 = 4200$ na Weylovi osi; RC hiperbole so označene rdeče, CC pa modro. Črtkaste črte označujejo lastne vrednosti četrtkroga. **Srednji sliki**: povečava enega CC in enega RC izognjenega križanja; najbližje razdalje so označene s horizontalno barvno črtico, črne ravne črte pa so asimptote hiperbol. Pri regularnem stanju je modra številka azimutalno kvantno število m deljeno z 2, rdeča pa radialno kvantno število n. **Spodnja slika**: porazdelitev razcepov za vsak tip izognjenih križanj, kjer polna modra črta predstavlja izraz (xv). N(RC) in N(CC) sta števili objektov v posameznem histogramu. Zaradi primerjave je prvi moment RC histograma normaliziran glede na prvi moment CC histograma. K je definiram v formuli (3.16).

Veji lastnih energij E_1 in E_2 v odvisnosti od zunanjega parametra sistema λ imata v bližini izognjenega križanja obliko hiperbol

$$E_{1,2}(\lambda) = \pm\sqrt{a_0^2(\lambda - a_2)^2 + a_1^2} + a_3 + a_4(\lambda - a_2), \tag{xvi}$$

parametriziranih z a_0, a_1, a_2, a_3 in a_4. Najmanjša razdalja med njima $\Delta E = 2\,|a_1|$ je pri $\lambda_0 = a_2$.

Nas zanimajo izognjena križanja pri gobastem biljardu, do katerih pride med podaljševanjem globine noge l. Tu obstajata dva tipa izognjenih križanj: CC izognjena križanja so med sosednjima kaotičnima stanjema, RC pa med regularnim in sosednjim kaotičnim stanjem. RC izognjena križanja so neposredna posledica tuneliranja v sistemu, njihova najmanjša razdalja pa je mera za tuneliranje. Vsako izognjeno križanje, v primeru numeričnih podatkov smo uporabili okrog 10 točk za vsako vejo, smo po razgrnitvi spektra 'pofitali' z dvema hiperbolama iz enačbe (xvi), glej slika x.

Izvrednotili smo izognjena križanja do $k^2 = 4200$, izračunali histogram razcepov in ga normalizirali na enotski razcep. Tako se za CC izognjena križanja histogram dobro ujema z 2×2 teoretično napovedjo za popolnoma kaotične sisteme, kar nakazuje možno razširitev veljavnosti enačbe (xv) na sisteme mešanega tipa. Neskladje je pri velikih razcepih, ki jih seveda ne moremo popisati z izoliranimi izognjenimi križanji, ter pri kvocientu povprečnega razcepa in povprečne razdalje med sosednjima stanjema, ki je precej manjši od tistega, ki ga napoveduje 2×2 model.

Pri RC-jih je razcep v povprečju veliko manjši kot pri CC-jih, pri njihovi porazdelitvi pa ne pričakujemo univerzalnosti. So pa RC izognjena križanja idelna za kvantitativno analizo dinamičnega tuneliranja. Če bi obravnavali eno samo izognjeno križanje danega regularnega stanja, kar pomeni 'srečanje' tega regularnega stanja s kaotičnim, ki ima podobno energijo, bi dobili oscilacije verjetnostne gostote iz enega stanja v drugo in nazaj. Tukaj bomo obravnavali koeficiente tuneliranja iz določenega regularnega stanja, upoštevajoč dinamiko lastnih stanj in posledična srečanja tega regularnega stanja s sosednjo vejo kaotičnih stanj. V tem primeru uporabimo Fermijevo zlato pravilo.

Fermijevo zlato pravilo

Fermijevo zlato pravilo pove velikost prehoda med stanji v sistemu s perturbacijo. Tak je tudi naš sistem, le da njegove hamiltonke ne moremo zapisati kot vsote nezmotenega dela in motnje. Eksponentni tunelski razpad $e^{-\gamma t}$ čistega (nezmotenega) regularnega stanja v kaotična stanja, ki traja do Heisenbergovega časa t_H, opišemo s koeficientom tuneliranja

$$\gamma = 2\pi\langle|v|^2\rangle\rho_{\mathrm{ch}}, \tag{xvii}$$

kjer je $\langle|v|^2\rangle$ povprečni matrični element med tem regularnim in kaotičnimi stanji s podobno energijo, ρ_{ch} pa gostota kaotičnih stanj v okolici regularnega stanja. Za gobasti biljard so v skupini v Dresdenu (R. Ketzmerick, A. Bäcker in S. Löck) izračunali teoretične koeficiente tuneliranja γ_{mn} za vsako čisto regularno stanje gobastega biljarda iz enačbe (xiv) in dobili

$$\gamma_{mn} = \frac{8}{\pi}\sum_{s=1}^{\infty}{}' \frac{J_{m+\frac{2s}{3}}(j_{mn}a)^2}{J_{m-1}(j_{mn})^2}. \tag{xviii}$$

Vsota po s izključuje večkratnike od 3 in konvergira zelo hitro. γ_{mn} so predstavljeni na sliki xi.

Ker je razcep v izognjenem križanju direktno preko $\Delta E = 2|v|$ povezan z matričnim elementom v iz (xvii) in smemo pri ne preveliki kaotični komponenti faznega prostora povprečenje razširiti čez $\rho_{\rm ch}$ oziroma $A_{\rm ch}$ iz (xii), dobimo

$$\gamma = \langle [\Delta E]^2 A_{\rm ch}/8 \rangle. \tag{xix}$$

Koeficienti tuneliranja - eksperiment in numerika

Pri poglabljanju noge smo poleg numeričnega izračuna naredili tudi eksperiment. Za vsako regularno stanje pri eksperimentu s kR med 11.9 in 53.8 in numeriki s k med 11.9 in 67 smo obravnavali vsa izognjena križanja in dobili njihove razcepe v enotah energije pred razgrnitvijo. Z uporabo formule xviii smo dobili koeficiente tuneliranja pri eksperimentalni in numerični obravnavi, rezultati so prikazani na sliki xi. Zaradi velikega deleža nezanesljivih hiperbol pri fitanju, ki so posledica eksperimentalne oziroma numerične ločljivosti in prisotnosti antene pri eksperimentu, točke $(m/2, n) = (5, 1)$, $(7, 1)$, $(8, 1)$, $(9, 1)$, $(11, 1)$, $(12, 1)$, $(13, 1)$, $(11, 2)$, $(12, 2)$, $(13, 2)$ in $(16, 4)$ izločimo iz končne obravnave. Preostale točke se s teorijo ujemajo zelo dobro, zato lahko rečemo, da je to prva eksperimentalna potrditev teorije koeficientov tuneliranja brez dodatnega parametra z ujemanjem, ki je večje od dveh redov velikosti.

Pri numeriki iz istih razlogov (razen prisotnosti antene) zavržemo točke $(m/2, n) = (9, 1)$, $(11, 1)$, $(12, 1)$, $(13, 1)$, $(13, 2)$, $(14, 2)$, $(16, 3)$, $(17, 3)$, $(19, 4)$ in $(20, 4)$. Preostale se s teorijo ujemajo zelo dobro, s čimer smo tudi z numeričnim računom potrdili teorijo in to na 4 rede velikosti natančno.

vii Numerična študija negausovskih realno simetričnih matrik

Izhodišče za to študijo je simetrična matrika $A = (A_{ij})$ $(i, j = 1$ ali $2)$ iz enačbe (ii) s porazdelitveno funkcijo $g_a(a)$ diagonalnih ter $g_b(b)$ izvendiagonalnih matričnih elementov. Tej matriki smo za različne porazdelitvene funkcije izračunali porazdelitev po razmikih med sosednjima lastnima vrednostima $P(S)$ in opazovali njeno obnašanje. Kot že omenjeno, je taka $P(S)$ pri normaliziranih $g_a(a)$ in $g_b(b)$ avtomatično normalizirana, medtem ko njen prvi moment ni in ga dodatno normaliziramo

$$P^n(S) = B\ P(BS), \quad \text{z} \quad B = \int_0^\infty x\ P(x)\ dx. \tag{xx}$$

Uvedli smo škatlasto (enakomerno)

$$g_a(a) = \frac{1}{2a_0}, \quad \text{če } |a| \le a_0, \quad \text{sicer} \quad 0, \tag{xxi}$$

$$g_b(b) = \frac{1}{2b_0}, \quad \text{če } |b| \le b_0, \quad \text{sicer} \quad 0, \tag{xxii}$$

eksponentno

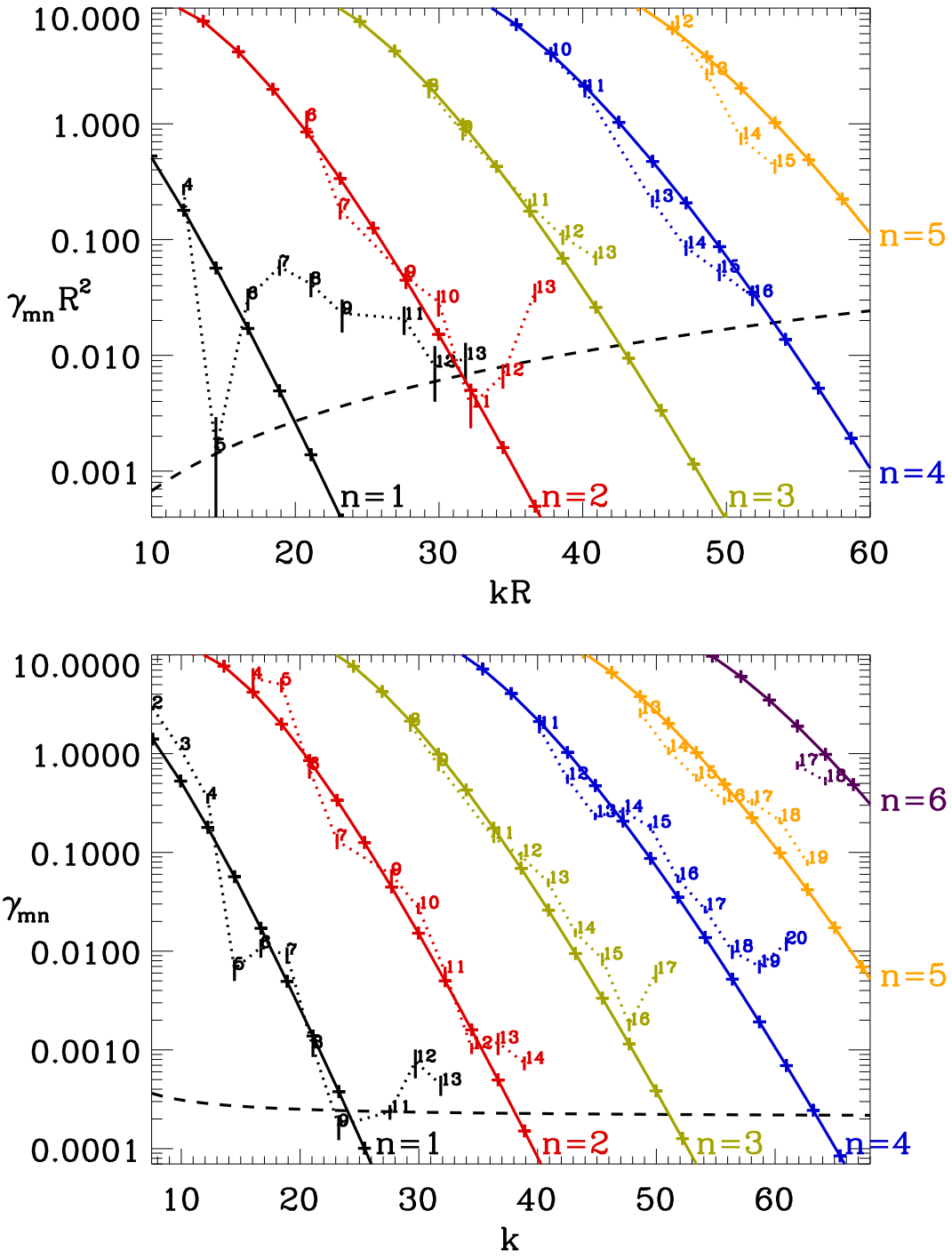

Slika xi: Koeficienti dinamičnega tuneliranja iz regularnega stanja $(m/2, n)$ v kaotično morje za kvantna števila $n = 1$ do $n = 5$ (eskperiment) in $n = 6$ (numerika) versus kR za gobasti biljard z $a/R = 10/19$. Prikazana je teoretična napoved ('+'-i, povezani v krivuljo za fiksen n) iz enačbe (xviii) in eksperimentalni (zgornja) oziroma numerični rezultati (spodnja slika). Predstavljeni so na način, da so kvantna števila $m/2$ izpisana na sliki in povezana s pikčasto črto za fiksno kvantno število n. Pri eksperimentalnih in numeričnih rezultatih so vrisane tudi napake, ki pomenijo standardne napake povprečja. Črtkasta črta na vsaki sliki označuje eksperimentalno oziroma numerično resolucijo za γ.

$$g_a(a) = \frac{\lambda_a}{2} e^{-\lambda_a |a|}, \quad g_b(b) = \frac{\lambda_b}{2} e^{-\lambda_b |b|}, \tag{xxiii}$$

Cauchy-Lorentzovo

$$g_a(a) = \frac{1}{\pi a_0 (1 + \frac{a^2}{a_0^2})}, \quad g_b(b) = \frac{1}{\pi b_0 (1 + \frac{b^2}{b_0^2})} \tag{xxiv}$$

ter singularno krat ekponentno porazdelitev matričnih elementov

$$g_a(a) = C_a |a|^{-\mu_a} e^{-\lambda_a |a|}, \quad g_b(b) = C_b |b|^{-\mu_b} e^{-\lambda_b |b|}, \tag{xxv}$$

z normalizacijsko konstanto $C_i = \lambda_i^{1-\mu_i}/(2\Gamma(1-\mu_i))$. Z numeričnih testom na 2×2 matrikah smo potrdili analitične rezultate (Grossmann and Robnik, 2007b).

Problem smo posplošili na večje matrike z dimenzijo $N = 120$. Hoteli smo testirati HW obnašanje (Hackenbroich and Weidenmüller, 1995), ki pravi, da pri (**I**) končnih in (**II**) omejenih porazdelitvenih funkcijah $g_a(a)$ in $g_b(b)$ vedno dobimo univerzalno GOE obnašanje, ne glede na podrobnosti porazdelitev. V primeru škatlaste in eksponentne porazdelitve smo potrdili napoved in za $P(S)$ dobili Wignerjevo porazdelitev oziroma njen eksakten ekvivalent v ∞ dimenzijah. Pri škatlasti porazdelitvi matričnih elementov je prehod zelo hiter in se zgodi že do $N = 7$, medtem ko je pri eksponentni počasnejši, a je pri $N = 120$ že popolnoma končan. Zanimiva je Cauchy-Lorentznova porazdelitev (xxiv), ki nima prvega momenta in posledično njene lastne vrednosti niso omejene na končen interval (slika xii levo). Tu ne dobimo GOE obnašanja, kar vidimo na sliki xii desno. Če pa porazdelitvenim funkcijam v (xxiv) pri izbranih a in b odrežemo repe, se takoj pojavi GOE obnašanje. Oboje je v skladu z napovedjo (Hackenbroich and Weidenmüller, 1995).

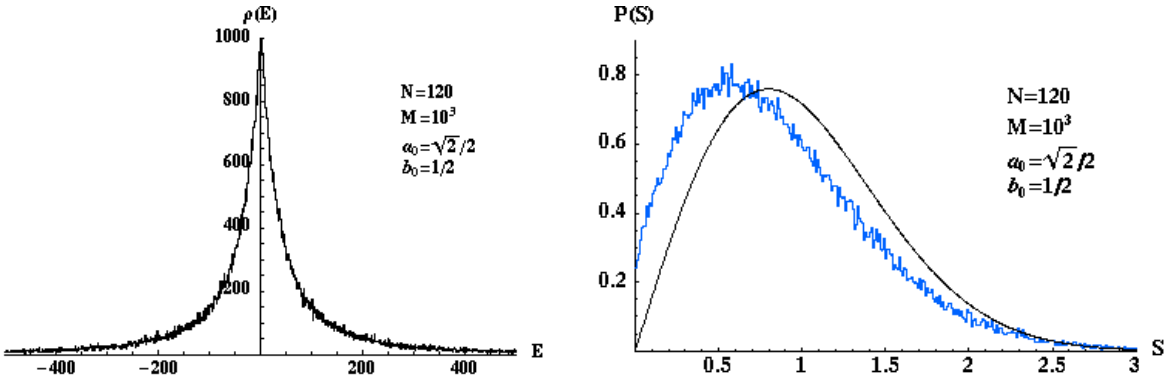

Slika xii: Numerični rezultati za ansamble s **Cauchy-Lorentzovo** porazdelitvijo matričnih elementov iz enačbe (xxiv) z $a_0 = \sqrt{2}/2$ in $b_0 = 1/2$. M je število matrik tega ansambla. Levo: gostota lastnih vrednosti za $N = 120$, $M = 10^3$, kjer je jasno vidno, da ni omejena na končen interval. Desno: porazdelitev po sosednjih razgrnjenih lastnih vrednostih za $N = 120$, $M = 10^3$, kjer je razgrnitev narejena s fenomenološkim pravilom **unf** $= 20$. Tanka krivulja je Wignerjeva porazdelitev za primerjavo.

Še bolj zanimivo pa je obnašanje v primeru singularne krat eksponentne porazdelitve matričnih elementov iz enačbe (xxv), ki že pri $N = 2$ za $\lambda_a = \sqrt{2}$, $\lambda_b = 1$, $\mu_a = 0$ in $\mu_b = 1/2$ (slika xiii zgoraj levo) obljublja nov pojav, imenovan potenčno odbijanje sosednjih nivojev z eksponentom manjšim od 1 (ang. *fractional power law level repulsion*).

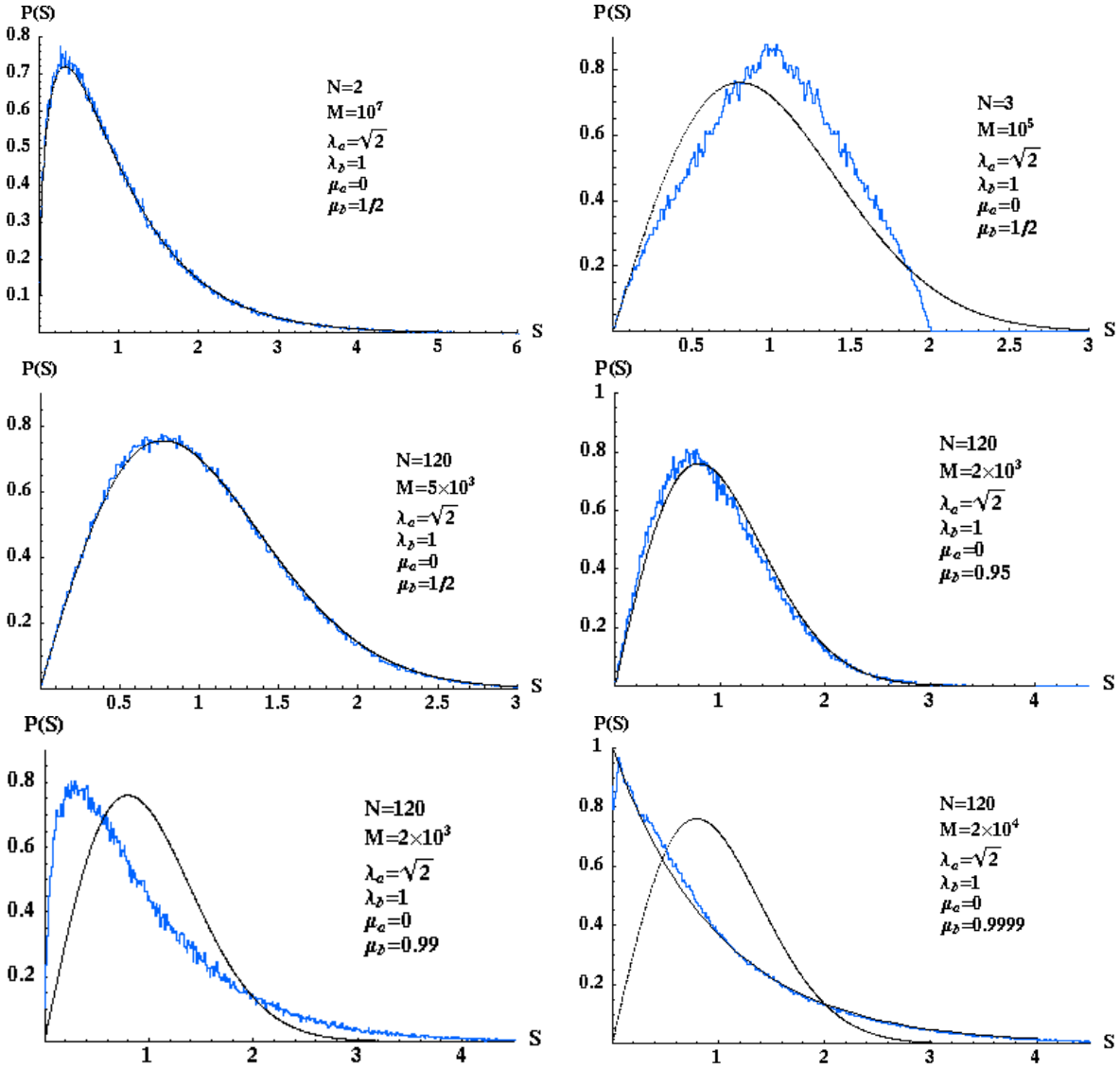

Slika xiii: Numerični rezultati za ansamble s **singularno krat eksponentno** porazdelitvijo matričnih elementov iz enačbe (xxv) z $\lambda_a = \sqrt{2}$, $\lambda_b = 1$, $\mu_a = 0$ in $\mu_b = 1/2$. M je število matrik tega ansambla. Levo zgoraj: $N = 2$ in $M = 10^7$, kjer je razgrnitev narejena s povprečjem po obeh lastnih vrednostih (vrisana je tudi teoretična vrednost (Grossmann and Robnik, 2007b)). Desno zgoraj: $N = 3$ in $M = 10^5$, kjer je razgrnitev narejena s povprečjem po vseh treh lastnih vrednostih. Sredina levo: $N = 120$ in $M = 5 \times 10^3$, razgrnitev s fenomenološkim pravilom **unf** $= 20$. M je število matrik tega ansambla. Sredina desno: $\mu_b = 0.95$ in $M = 2 \times 10^3$, sicer isto kot na srednji levi sliki. Spodaj desno: $\mu_b = 0.99$ in $M = 2 \times 10^3$, sicer isto kot na srednji levi sliki. Spodaj desno: $\mu_b = 0.9999$ in $M = 2 \times 10^4$, sicer isto kot na srednji levi sliki. Za lažjo primerjavo rišemo tudi Wignerjevo in na zadnji sliki Poissonovo porazdelitev.

Presenetljivo je, da pri istih parametrih že pri $N = 3$ opazimo prehod v linearno odbijanje nivojev in posledično v Wignerjevo porazdelitev pri $N = 120$, pri čemer je porazdelitev lastnih vrednosti polkrožna (ang. *semicircle law*), kar izpolnjuje pogoje HW napovedi.

Ko povečujemo μ_b proti neintegrabilni singularnosti $\mu_b = 1$, se $P(S)$ spreminja zelo močno in zdi se, da je spet prisotno potenčno odbijanje sosednjih nivojev z eksponentom manjšim od 1. Opazimo prehod $P(S)$ od GOE pri majhnih vrednostih μ_b k Poissonovi

(eksponenti) porazdelitvi, ko smo dovolj blizu μ_b (slika xiii). V vmesnem območju pa se nakazuje željeno potenčno odbijanje.

Izjava o avtorstvu

Izjavljam, da sem v predloženi doktorski disertaciji uporabljal rezultate lastnega raziskovalnega dela.

Ljubljana, 29. september 2008. Gregor Vidmar